Mathematical modelling of urethral and similar flows

Stephen E. Glavin

Department of Mathematics
UCL

A thesis submitted for the degree of
Doctor of Philosophy

Supervisors

Professor Frank Smith and Professor Guo-Xiong Wu

October 2011

I, Stephen Glavin, confirm that the work presented in this thesis is my own. Where information has been derived from other sources, I confirm that this has been indicated in the thesis.

Abstract

Flows in flexible tubes and vessels have been studied extensively in the past with particular application to the cardiovascular and respiratory systems. However there have been few treatments of the lower urinary tract, which consists of the bladder and urethra. This thesis concentrates specifically on the urethra with the aim of giving insight into the evolving flow characteristics within the vessel and mechanical responses of the vessel which give rise to fluid structure interactions. Urethral modelling is an important area of research given the social and economic costs involved in lower urinary tract dysfunction. In the modelling, examination is given to slow and fast opening vessels where certain exact analytical solutions are found along with numerical results. Following this, fast and slow responses of the walls of the vessels are considered, where the response is defined as the relative change in cross-sectional area for relatively varying transmural pressure. These features are important for pathologies that alter the characteristics of the vessel wall such as bladder outlet obstruction. A change in the distensibility along the vessel resulting from pathologies or normal transition through the various sections of the urethra is studied both in terms of developing jump conditions based on a localised Euler region and also over a comparatively short length scale giving rise to the Burgers equation; small amplitude instabilities are studied through the derivation of the KdV equation. Following on from these mostly two-dimensional treatments, three-dimensional systems are then studied. Consideration is given to the secondary flow effects driven by the tortuosity of a vessel in three dimensions. We study cases of three-dimensional constriction, with main interest in the effects of benign prostate hyperplasia or urethral stricture on the flow, where pressure drops are demonstrated. Finally an appendix deals with the effects concerned with a wide population, focusing on an allied problem of consumer choice.

Acknowledgements

My gratitude goes to Professor Frank Smith for all his support, advice, guidance and encouragement. This work would not have been possible without his enthusiasm and expertise. I would also like to thank Professor Guo-Xiong Wu for his advice and discussions on modelling, to Professor Alan Cottenden for all his useful discussions on the biology and mechanics of the lower urinary tract, to Professor Jean-Marc Vanden Broeck for his expertise and advice on free-surface problems and to Dr Abhijit Sengupta for his supervision and enthusiasm during my internship.

I am grateful to the Department of Mathematics and Department of Mechanical Engineering for their funding throughout this PhD and also to Unilever UK and the Knowledge Transfer Network in industrial mathematics (sponsered by EPSRC) for their funding during my six month internship at Unilever.

Finally I would like to give my thanks to my wife, family and friends for their enouragement and support and also to the postgraduates of the Mathematics department at UCL, in particular Dr Alex White, Dr Hannah Fry and Dr Marios Tziannaros.

Contents

List of Figures

List of Tables

Chapter 1

Introduction

We begin with a discussion on urology, an excellent discussion of which is given in [87] and proceeds in slightly modified form as follows.

Urinary incontinence and bladder instability are of major importance. The number of patients with this problem and the potential economic impact are staggering. In the USA alone there are an estimated 17 million people with bladder control problems which costs around $ 26 billion per year to manage, namely suggesting estimated costs of £1.4 billion per year to the National Health Service in the UK (at 1990 prices) [14].

The micturition process, the process of voiding urine from the body, can be visualised as a complex of neural circuits in the brain and spinal cord that coordinate the activity of smooth muscle in the bladder and urethra, the vessel connecting the bladder neck to the outside world. These circuits act like on-off switches to alternate the lower urinary tract (LUT) between two modes of operation, storage and elimination. The LUT is defined as the combination of bladder and urethra and so its main function is storage and voiding of urine as opposed to the upper urinary tract which is made up of the kidneys and ureters whose function is to extract urine from the blood and transfer it to the bladder. Injuries or diseases of the nervous system in adults can disrupt

voluntary control of micturition resulting in bladder instability and so-called urge incontinence [87]. Because of the complexity of the central nervous control of the lower urinary tract urge incontinence can occur as a result of a variety of neurological disorders. Urge incontinence may also be due to intrinsic detrusor myogenic abnormalities, resulting in motor detrusor instability [87].

Urethral dysfunction can also be a cause of urinary incontinence. Increased bladder outlet urethral resistance (essentially the pressure required to open the urethra as a result of the material properties of the vessel) in men with benign prostatic hyperplasia (enlargement of the prostate gland) and in young men and women with detrusor-sphincter dyssynergia (spinal cord injuries, multiple sclerosis) causes alteration of the bladder. Increased bladder outlet resistance causes bladder remodelling and results in urge incontinence. It can also be speculated that in patients with mixed stress and urge incontinence, stress can cause urge incontinence. Leakage of urine into the urethra (stress incontinence) may stimulate urethral effects that induce involuntary voiding reflex (urge incontinence).

1.1 Relevant anatomy and biomechanics.

The bladder can be divided into two parts, first the body lying above the ureteral orifices and second a base consisting of the trigone (a smooth triangular region internal to the bladder with vertices formed of the two ureteral orifices and the internal urethral orifice) and bladder neck. The construction of the bladder wall differs from the discrete circular and longitudinal smooth muscle layers in the ureter or gastrointestinal tract, being composed of myofibrils (elongated bundles of contractile protein) which are arranged into fascicles (bundles of skeletal muscle) in random directions.

The bladder outlet is composed of the bladder base, urethra and external

urethral sphincter (a circular muscle which constricts the urethra when contracted; see figures 1.1 - 1.3). The urethra begins at the internal meatus (a meatus is an opening or passage) of the bladder and extends to the external meatus. In the male, four segments are readily identified. The first is the preprostatic portion, or bladder neck. The prostatic urethra then extends throughout the length of the gland, terminating at its apex. The membranous urethra extends from the prostatic apex through the pelvic floor musculature until it becomes the bulbous and penile urethra at the base of the penis. In women, the urethra extends throughout the distal third of the anterior vaginal wall from the bladder neck to the meatus. The urethra is comprised of tissues that aid continence rather than a single discrete and visible sphincter. A network of vascular subepithelial tissue (layer of tissue beneath the surface or epithelial layer) in women contributes to a urethral seal effect.

It is debatable whether the detrusor or trigone muscles project into the proximal urethra. Embryologic data support the concept of a separate origin for muscles of the bladder and urethra. Histologic studies show that longitudinal muscle of the bladder base extends into the urethra to form an inner longitudinal layer. Striated and smooth muscle coalesce in the urethra and interdigitate (interlock) with the fibrous prostatic capsule (tissue surrounding the prostate gland). Conversely, there exists a complete and competent ring of smooth muscle at the male bladder neck. Maintenance of continence in men and some women with destruction of the opening of the bladder neck argues that the bladder neck may not be the site of urinary continence.

The contractile properties of bladder smooth muscle cells are well suited for either urine storage or release. Filling the bladder at a slow physiological rate (approximately 1.4 ml min^{-1} [50]) maintains an intravesical pressure (pressure within the vessel) of less than 10 cm H_2O. Acute denervation (loss of nerve supply) of the bladder does not appreciably alter the low filling pressure. This

concept has been used to support a hypothesis that the intrinsic myogenic or viscoelastic properties of cellular and extracellular components are major contributors to low pressure bladder filling and compliance. Conversely neural input is required for the rapid and sustained smooth muscle contraction accompanying voiding.

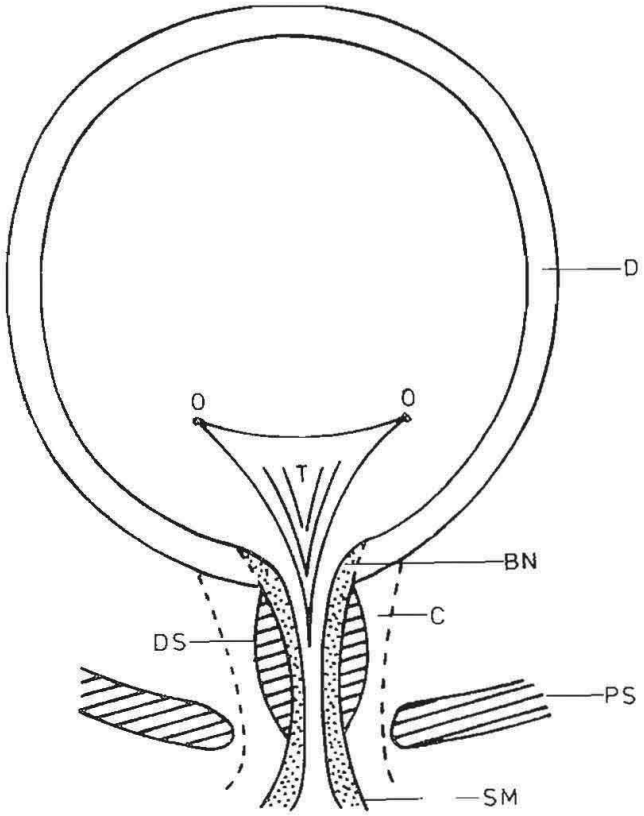

Figure 1.1: Sketch of the lower urinary tract for females viewed from the front. Labels are D, detrusor smooth muscle; T, trigone; SM, urethral smooth muscle; DS, distal intrinsic urethral sphincter; PS, periurethral sphincter; BN, bladder neck; O, ureteral orifices; C, connective tissue. This diagram is adapted from that found in [40].

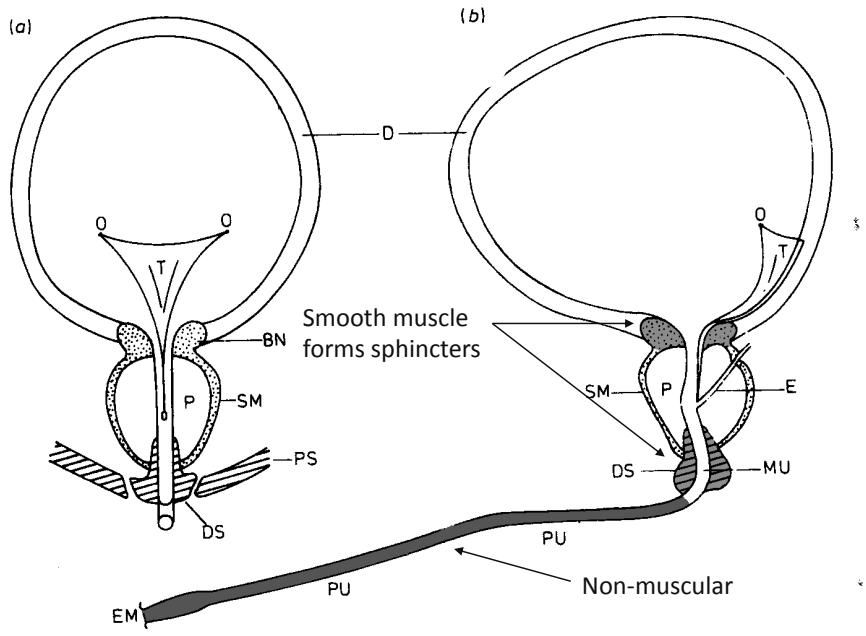

Figure 1.2: Sketch of the lower urinary tract for males viewed from the front and left side respectively. Labels are D, detrusor smooth muscle; T, trigone; SM, smooth muscle; DS, distal intrinsic urethral sphincter; PS, periurethral sphincter; BN, bladder neck; P, prostate gland; MU, membraneous urethra; PU, penile urethra; EM, external meatus; E, ejaculatory duct; O, ureteral orifices. This diagram is adapted from that found in [40].

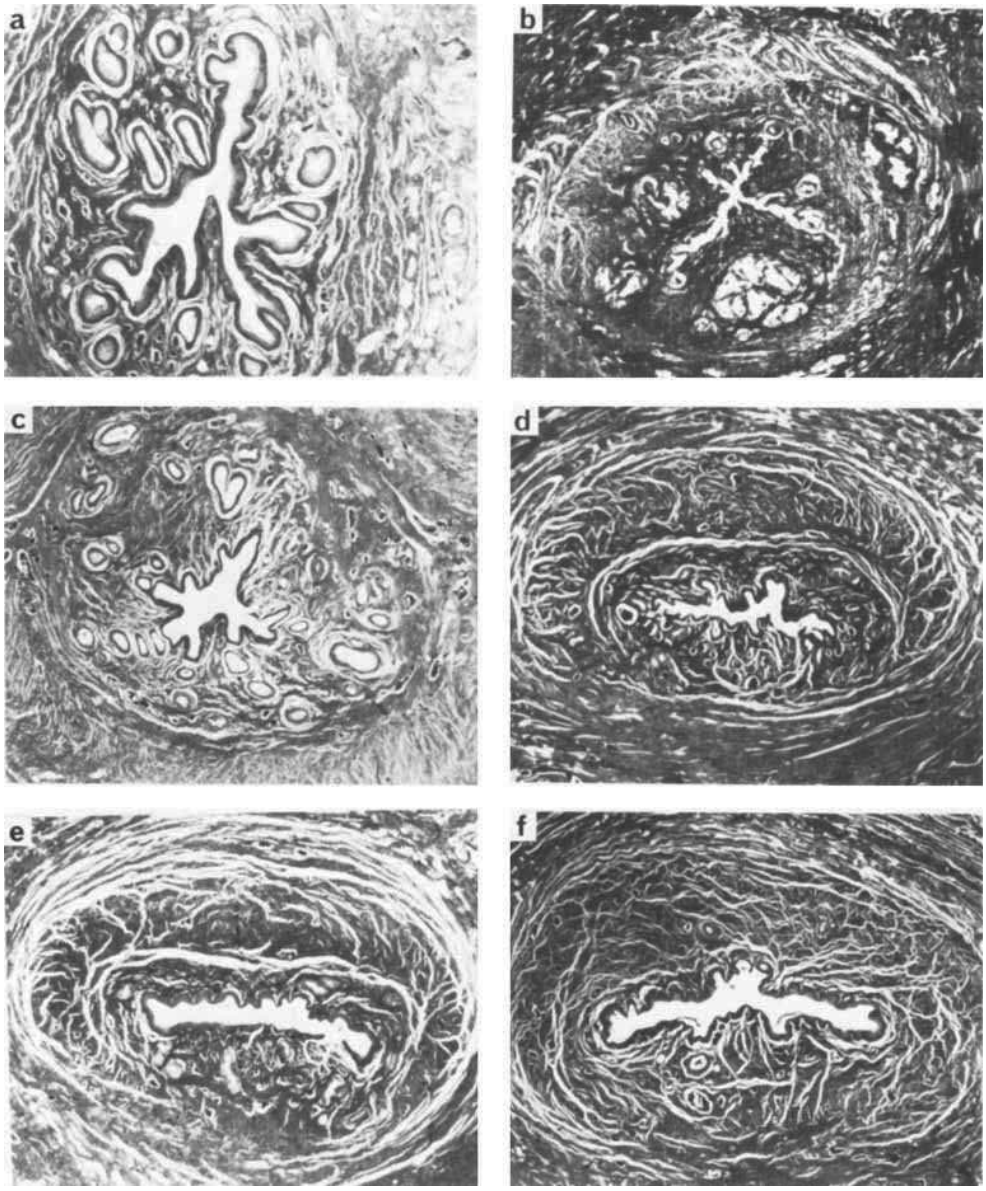

Figure 1.3: Cross-sections of a human female urethra taken from [64] illustrating the changes in shape of the urethra from the external meatus (a) to the bladder neck (f).

1.2 The structure of the male urethra

The following comes from [16], [57], [13] and [3], in a slightly modified form due to the author. The male urethra is approximately 20 cm in length and a sketch can be seen in figure 1.2 taken from [40]. The urethra consists of four regional parts, as mentioned earlier, the preprostatic, prostatic, membranous and spongiose parts. Except during the passage of fluid along it, the urethral canal is a mere slit. In the prostatic part the slit is transversely arched, in the membranous portion it is stellate (a cross-section that is star shaped), in the spongiose portion it is transverse and at the external orifice it is sagittal (a slit at right angles to the transverse shape). The urethra passes downwards except at the spongiose part where it turns forward in the bulb of the penis resulting in an abrupt angulation.

1.2.1 Preprostatic part

The preprostatic part has a stellate lumen and is approximately 1-1.5 cm long. It extends almost vertically from the bladder neck to the base of the prostatic gland. The smooth muscle bundles surrounding the bladder neck and preprostatic urethra are arranged as a distinct circular collar which becomes continuous distally with the capsule of the prostate gland.

1.2.2 Prostatic part

Approximately 3-4 cm long, it is the widest and most dilatable part of the urethra [3]. It tunnels through the substance of the prostate closer to the anterior than the posterior surface (closer to the front than the back) of the gland. It is continuous above with the preprostatic part and emerges from the prostate slightly anterior to its apex. Throughout most of its length the posterior wall possesses a midline ridge, the urethral crest (also known as the

verumontanum), which projects into the lumen, the wall of the urethra, causing it to appear crescent shaped in transverse section, see chapter 6. At the midpoint of the bladder neck and the prostate apex it encounters an abrupt anterior angulation of its posterior wall, the angle of deviation being approximately 35 degrees [3]. It is widest at the middle and narrowest below this where it joins the membraneous part.

1.2.3 Membraneous part

This is the shortest and least dilatable part. It has a stellate cross-section (star shaped). Except for external orifice, the exit of the urethra, it is the narrowest section. It descends with a slight vertical concavity from prostate to the bulb of the penis and is approximately 2 cm in length. The wall consists of a muscle coat separated from the epithelial lining, the surface of the vessel wall, by a narrow layer of fibroelastic connective tissue. It is the site of sphincteric activity in the male urethra.

1.2.4 Spongiose part

Contained in the corpus spongiosum penis, this part is approximately 15 cm in length. It extends from the end of the membranous urethra to the external urethral orifice on the glans penis. It has a narrow lumen with a uniform diameter of approximately 6 mm and forms a transverse slit. The proximal part is surrounded by the bulbospongiosus muscle, commonly known as the bulb of the urethra. Contraction of this muscle assists in emptying the urethra at the end of voiding. Sphincteric activity in the male urethra is traditionally attributed to a sphincter derived from fibres of the levator ani which surrounds the membranous urethra as it penetrates the pelvic floor. However, although fibres from the levator ani form a peri-urethral sling this does not constitute a

complete muscle ring. The main contribution to the distil sphincter mechanism is from muscles within the urethral wall itself. As well as the inner layer of smooth muscle, the urethral musculature has an outer circular layer of striated muscle fibres (rhabdosphincter); these fibres are designed for prolonged tonic contraction (slow twitch fibres). Although the peri-urethral sling of pelvic floor muscles is not capable of sustained contraction it can contract rapidly to constrict the urethra for short periods (fast twitch fibres). This may contribute to continence during the sudden rise in intravesical pressure seen, for example, with coughing or straining. The distal sphincter mechanism exerts a higher closure pressure than the bladder needs and is a more potent sphincter in terms of maintaining closure.

1.3 The structure of the female urethra

The following description of the female urethra may be found in the 2ndinternational consultation on incontinence [3]. The female urethra is between 3 and 4 cm in length, beginning at the internal meatus of the bladder and terminating at the external meatus just above the vaginal opening. A sketch of the urethra can be seen in figure 1.1 and is taken from [40]. Five regions can be identified, each approximately one fifth of the total length. The first fifth is surrounded by the vesical neck or bladder neck. The next two fifths are encircled by the sphincter urethrae (also known as the external sphincter) and smooth muscle. The fourth section contains the compressor urethrae (an arch shaped muscle structure which generally does not completely encircle the urethra) and urethrovaginal sphincter (a muscle structure that surrounds the urethra and vagina). The final section of the urethra lacks contractile tissue.

The striated sphincter, consisting of the sphincter urethrae, compressor urethrae and urethrovaginal sphincter, can be contracted to increase urethra clo-

sure during times of urgent need [3]. Micturition occurs when bladder pressure exceeds urethral pressure, produced by the simultaneous contraction of the detrusor muscle within the bladder wall and relaxation of striated and smooth sphincters.

Smooth muscle appears in the urethral wall, beneath the outer striated muscle layer previously described. The majority of this tissue is orientated longitudinally and appears to be active during micturition with the effect of shortening and widening the urethral lumen (opening through which the urine travels), aiding in the voiding of urine [3].

A cross-section of a female urethra can be seen in figure 1.3 taken from [64] and helps to illustrate the changing and non-uniform nature of the lumen cross-section.

1.4 Aim of the thesis

The urethra, in males, is a long winding and distensible tube whose physical properties can have profound influences over the efficiency of voiding. A rise in the resistance offered by the urethra can have profound effects on the whole LUT. The present study addresses the fluid-structure interaction associated with the urethral resistance and urinary flow.

Current urodynamic tests tend to be invasive [2], [13] and so it is helpful to produce mathematical models that help validate current tests and identify underlying pathologies. Typical urodynamic examinations involve the measuring of bladder pressure through the use of a catheter which passes through the urethra or through the abdominal and bladder walls [40]. A measurement of abdominal pressure taken through the rectum serves to recover a detrusor pressure applied at the bladder wall. During the examination the bladder is slowly filled with X-ray contrast medium via a catheter whilst measurements

of pressure are made. Once the bladder is full the clinician will ask the patient to micturate into a device to measure the flow rates and volumes. Pressures and shapes within the bladder and urethra may be recorded at the same time in order to examine pathologies (urethral profile profilometry [1]). Important quantities, for a urologist, are pressure, volume and flow rate. It is also clear that it is also therefore important that informative noninvasive diagnostic techniques be devised in order to avoid discomfort for patients.

The main aim of the present work is to understand the physical properties of the LUT, in particular the urethra (a companion study [85] on the modelling of the bladder has been simultaneously carried out by Marios Tziannaros at UCL) and the corresponding flow behaviour in order to gain better insight and also to aid development of new predictive tests. Although the male urethra has been kept in mind during this work with regard to a relatively long, distensible and tortuous tube, in principle the ideas can be applied to the female urethra also. Studied are the effects of urethral length, tortuosity and variable cross-sectional dimensions on the contained fluid flow as well as the effects of distensible walls. It should be noted here also that measurements of pressure within the bladder and urethra can be affected by the measuring catheter itself as has been noted in [35] and [65], although this effect is not considered in this work.

1.5 Distensibility

The urethra is a distensible tube such that, when filled with fluid, the cross-sectional area of the lumen depends on the pressure [40] and so a mathematical relation is taken to exist between the fluid pressure and cross-sectional area. A typical relation for a uniform thin walled elastic tube can be seen in figure 1.4 which holds for many such tubes, for example large arteries [62] or latex tubes. The relation is for a thin walled elastic tube with undisturbed radius

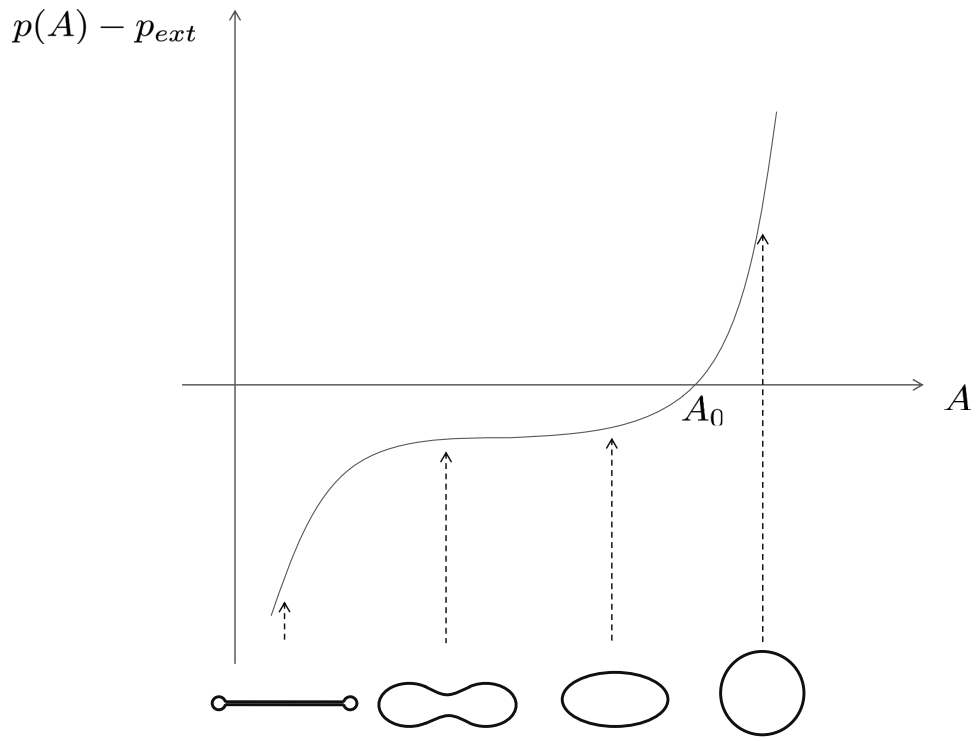

Figure 1.4: Sketch of a tube law (pressure-area relation) for a thin walled elastic tube with approximate (simplified) wall shapes. [40],[62],[71].

r_0 and wall thickness h. An excess pressure p_e within the tube must generate a circumferential tension $r_0 p_e$ per unit length of the tube. This circumferential tension pulls on an area h of the tube material per unit length, giving a circumferential tension stress (force pulling on unit area normal to that force) $r_0 p_e / h$. For a thin walled tube ($h \ll a$) the magnitude of the circumferential stress greatly exceeds the magnitude of the radial stress. The corresponding circumferential strain is written $r_0 p_e / \bar{E} h$ where the elastic behaviour of the tube material under small stress is represented by modulus $\bar{E}$.

1.6 Typical values

Typical values in SI units of the quantities just mentioned are

$$h_0 = 5 \times 10^{-4}\text{m}, \tag{1.1}$$

$$\bar{E} = 10^4\text{N m}^{-2}, \tag{1.2}$$

$$\nu = 0.5, \tag{1.3}$$

$$A_0 = 3 \times 10^{-5}\text{m}^2, \tag{1.4}$$

where h_0 and A_0 are the vessel wall thickness and cross-sectional area when the tube is at rest, $\bar{E}(x)$ is Young's modulus and ν is the Poisson ratio of the vessel wall [18].

The dynamic viscosity and density of urine are both similar to that of water [17], giving approximate values of

$$\rho = 10^3\text{kg m}^{-3}, \tag{1.5}$$

$$\mu = 10^{-3}\text{kg m}^{-1}\text{s}^{-1}, \tag{1.6}$$

respectively.

From Griffiths [40], the bladder volume is approximately 350-500 ml and typical maximum outflow is 25ml s^{-1} with an approximate urethra radius of 3mm. A typical urethral velocity is given by

$$u_0 \approx 1\text{m s}^{-1}. \tag{1.7}$$

In tests carried out by Griffiths he found upper limits on flow speed to be approximately 2.1-2.2ms^{-1} with a max flow rate of 25.5($\pm$1) ml s^{-1} [38]. He also found [39] that over much of a micturition there is little variation of flow rate (being about 20-40ml s^{-1}) which is also independent of initial volume. Also found was an opening/closing pressure of approximately 25cmh_2O (2500Pa).

If we now define the Reynolds number Re for the urethra as

$$Re = \frac{\rho u_0 L}{\mu}, \tag{1.8}$$

we then find an approximate Reynolds number of

$$Re = 7000, \tag{1.9}$$

See also [40], [64].

1.7 Review

There have been numerous computational studies of cardiovascular flows and a large number of analytical studies of the same subject [47], [58], [59], [41], [72], [61], [71], [62]. There have also been a fair number of experimental studies and measurements concerning the lower urinary tract (LUT) and its various different aspects [17], [3], [2], [64], [40]. As far as we know however the present work taken together with the concurrent investigation of the bladder in the thesis of [85] is the first to bring a combined analytical and computational effort to bear on the LUT. The present work has the additional aim of advancing models and techniques within the area, in a sense. This study is centred on an applied mathematical basis and takes account spatially of both two-dimensional and three-dimensional unsteady flow features. It is built upon the pioneering work of Griffiths [40] on two-dimensional and axisymmetric modelling.

We hope the present work will open up the subject further and lead on to more investigations along similar lines for the general area, whether from an experimental, computational or applied-mathematical viewpoint, or indeed from an interdisciplinary mixture of those viewpoints.

Interesting reviews are by: Grotberg and Jensen [41] as well as [73] including discussions of soft walled tubes and steady flow; Oates [58], on large amplitude waves [59] application; and Jensen on airways [47]. These are only loosely connected with the current study, in contrast with the review of Griffiths [40] as described earlier in the introduction.

1.8 Structure of the present thesis

The thesis is divided into two parts, the first being dedicated to a mathematical model of the urethra and its fluid-structure interactions. The second part departs from the physical model and examines, instead, heterogeneous populations with the aim of application being the decision of treatment by GPs or surgeons for an individual displaying a set of symptoms. The link between the two parts is discussed later in the thesis.

Part one begins with the derivation of a quasi-one dimensional model for inviscid flow through a long distensible vessel valid for relatively small tortuosity. The pressure-area relation is introduced in chapter 2 and then solutions are sought for both abrupt and gradual openings of an initially closed or undisturbed vessel. Following this, short-scale alterations in tube distensibility are considered, leading to the consideration of an Euler-region and corresponding jump conditions.

The quasi-one dimensional model is further studied in chapter 3 for gradual openings with an aim to developing a numerical scheme. In almost all cases of real concern throughout this study the governing equations are nonlinear and computational investigation is called for but this is complemented by analysis involving exact solutions (which tend to be illuminating in general) and asymptotic solutions (which open up wider application). Within the framework of gradual openings, the special cases of relatively rapid openings, fast-response and slow-response vessels are examined asymptotically in chapter 3 as these turn out to be of much interest and lead on to further progress subsequently. Two-dimensionality is tackled next for both fast and slow response vessels with new solutions being found as a result.

Chapter 4 concerns fully numerical solutions and begins with a simple finite-difference scheme which suffices to find solutions for the quasi-one dimensional model of chapters 2 and 3. Changes in distensibility are again examined, re-

sulting in a forced Burgers equation for which numerical solutions are obtained and analysed.

Chapter 5 moves on to three-dimensional effects, initially in a longitudinal system with a first attempt at understanding the influences of vessel tortuosity and subsequently in both longitudinal vortex systems and three-dimensional interactive inviscid boundary layer systems for fast-response walls.

Chapter 6 looks at the important case of a constriction in three dimensions which may be taken as an approximation to the prostatic part of the male urethra, see section 1.2. Solutions are found numerically for a number of test cases.

The second part of the thesis is described in chapter 7. Here a different approach at modelling is taken, concerned more with the decision making involved for a heterogenous population displaying different pathologies. The work can be seen as modelling choice or perhaps the probabilities of operations.

Finally in chapter 8 we have a discussion of the work set out in this study as well as recommendations for further study.

Part I

The Physical Model

Chapter 2

Derivation of the long-tube equations

2.1 Dimensional equations.

In dimensional terms the derivation of a long tube approximation, where cross-sectional length scales are much smaller than the typical longitudinal length scale, can be obtained in the following way which is similar to that in [71]. The flow-structure interactions discussed in this chapter are essentially two-dimensional or axisymmetric. We consider a vessel of length L with centreline curve $s(\mathbf{x})$ and cross-sectional area $A(s,t)$, where $\mathbf{x}$ is the Cartesian coordinate vector in three dimensions and t is time. The cross-sectional area A here generally varies with time, i.e. evolves, as well as being dependent on position. Assuming the local curvature to be sufficiently small the axial direction and distances may in fact be described by the Cartesian coordinate x as shown in figure (2.1), with say $x = 0$ representing the left-hand entry position of the fluid flow.

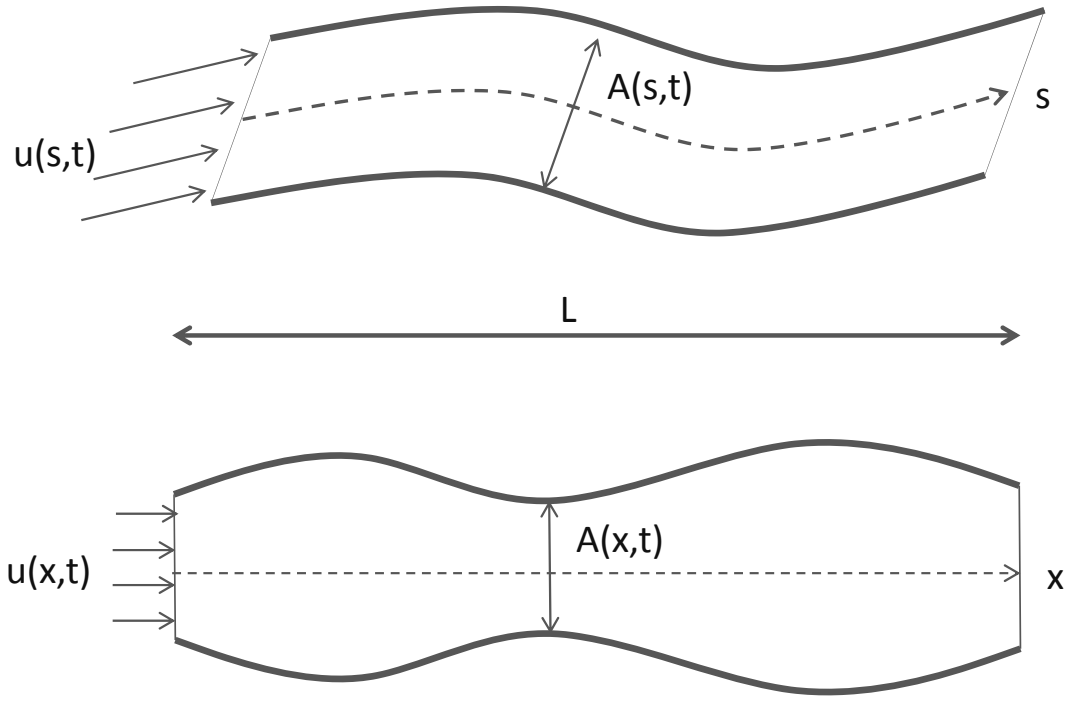

Figure 2.1: The "one-dimensional vessel". Above, the original slowly varying vessel (not to scale), and below, the one-dimensional orientation. Figure adapted from [71].

Now the unknown cross-sectional area can be defined by

$$A(x,t) = \iint_S \mathrm{d}y\mathrm{d}z, \tag{2.1}$$

where $S(x,t) = \{(r,\theta,t) : 0 \leqslant r < R(x,t), 0 \leqslant \theta < 2\pi\}$ gives the cross-section of the tube at an axial position x at time t with $R(x,t)$ being the unknown representative radius of the tube. As a first approximation the tube is taken to be axisymmetric (i.e. a circular cross-section although in reality the urethra has in general a non-circular cross-section, see sections 1.1 - 1.3). Then equation (2.1) simplifies to

$$A(x,t) = \pi R^2(x,t). \tag{2.2}$$

The average velocity and pressure, taken over a cross-section, may also be defined with

$$u(x,t) = \frac{1}{A(x,t)} \iint_S \hat{u}(x,y,z,t)\, dydz, \tag{2.3}$$

$$p(x,t) = \frac{1}{A(x,t)} \iint_S \hat{p}(x,y,z,t)\, dydz, \tag{2.4}$$

where $\hat{u}(x,y,z,t)$ and $\hat{p}(x,y,z,t)$ are the unknown axial velocity and pressure within the tube. A new independent variable can also be introduced, namely the volume flux given by

$$Q(x,t) = A(x,t)u(x,t) = \iint_S \hat{u}(x,y,z,t)\, dydz. \tag{2.5}$$

There are therefore three variables, either (A,u,p) or (A,Q,p), and so three governing equations are required. These are derived from conservation of mass and conservation of momentum along with a constitutive equation relating the local cross-sectional area to the local internal pressure. The fluid is assumed to be incompressible and Newtonian, and so its density ρ and viscosity μ are constant.

2.1.1 Mass conservation.

For a control volume, for which we take the segment where x is in the range $\in (0, L)$ as shown in figure (2.1), conservation of mass requires that the rate of change of mass within the control volume is equal to the net mass flux into that volume. Thus the balance implied here is

$$\rho \frac{\mathrm{d}V(t)}{\mathrm{d}t} = \rho Q(0,t) - \rho Q(L,t), \tag{2.6}$$

where V is the volume of the control volume and the right-hand side stands for the net mass flux. This balance may be rewritten in terms of the integrated area and the flux gradient as

$$\rho \frac{d}{dt} \left\{ \int_0^L A(x,t)\, \mathrm{d}x \right\} = -\rho \int_0^L \frac{\partial Q}{\partial x}\, \mathrm{d}x, \tag{2.7}$$

and so after rearrangement the equation

$$\rho \int_0^L \left(\frac{\partial A}{\partial t} + \frac{\partial Q}{\partial x} \right) \mathrm{d}x = 0 \tag{2.8}$$

follows.

As the control volume is arbitrary (2.8) must hold for any length L and so the integrand there must be identically zero. The one-dimensional mass conservation equation is therefore obtained,

$$\frac{\partial A}{\partial t} + \frac{\partial Q}{\partial x} = \frac{\partial A}{\partial t} + \frac{\partial (uA)}{\partial x} = 0, \tag{2.9}$$

using also the identification of Q with uA.

2.1.2 Momentum balance.

Considering again the same control volume, conservation of momentum states that the rate of change of momentum within the control volume plus the net flux of momentum out of the control volume must equal the applied forces on the control volume.

Firstly, the rate of change of momentum in the volume is given by

$$\frac{\mathrm{d}}{\mathrm{d}t}\left\{\int_0^L\left(\iint_S \rho\hat{u}\,\mathrm{d}y\mathrm{d}z\right)\,\mathrm{d}x\right\} = \frac{\mathrm{d}}{\mathrm{d}t}\left\{\int_0^L \rho Q\,\mathrm{d}x\right\} = \int_0^L \rho\frac{\mathrm{d}Q}{\mathrm{d}t}\,\mathrm{d}x. \tag{2.10}$$

Secondly the net flux of momentum out of the control volume is given by

$$\iint_S \rho\hat{u}^2\left(L,y,z,t\right)\,\mathrm{d}y\mathrm{d}z - \iint_S \rho\hat{u}^2\left(0,y,z,t\right)\,\mathrm{d}y\mathrm{d}z, \tag{2.11}$$

recalling that the ends are at $x = 0, L$. However, a momentum flux correction factor 'α' which accounts for the nonlinearity of the sectional integration in terms of the local velocity $\hat{u}$ is introduced such that

$$\iint_S \rho\hat{u}^2\left(x,y,z,t\right)\,\mathrm{d}y\mathrm{d}z = \rho A\left(x,t\right)u^2\left(x,t\right)\alpha\left(x,t\right), \tag{2.12}$$

which defines α as the ratio of actual momentum flux to the momentum flux of the equivalent one dimensional system with $\alpha \geqslant 1$. So equation (2.11) becomes

$$\rho\left\{\left(\alpha u^2 A\right)_{x=L} - \left(\alpha u^2 A\right)_{x=0}\right\} = \rho\left\{\left(\alpha\frac{Q^2}{A}\right)_{x=L} - \left(\alpha\frac{Q^2}{A}\right)_{x=0}\right\}. \tag{2.13}$$

Finally here the applied forces are contributed to by both viscous and pressure forces as given by

$$\left(pA\right)_{x=0} - \left(pA\right)_{x=L} + \int_0^L\left(\int_{\partial S}\hat{p}n_x\,\mathrm{d}s\right)\,\mathrm{d}x + \int_0^L f\,\mathrm{d}x. \tag{2.14}$$

Here the third term is the contribution at the wall with ∂S denoting the boundary of the cross-section S and n_x the x-component of the surface normal, while f is the frictional force per unit length. Constant cross-sectional pressure and axisymmetry mean that, in (2.14),

$$\int_0^L\int_{\partial S}\hat{p}n_x\,\mathrm{d}s\mathrm{d}x = \int_0^L p\frac{\partial A}{\partial x}\,\mathrm{d}x. \tag{2.15}$$

Combining equations (2.10), (2.13) and (2.14) the momentum conservation for the control volume in the form

$$\begin{aligned}\int_0^L \rho\frac{\mathrm{d}Q}{\mathrm{d}t}\,\mathrm{d}x + \left(\rho\alpha\frac{Q^2}{A}\right)_{x=L} - \left(\rho\alpha\frac{Q^2}{A}\right)_{x=0} = \\ \left(pA\right)_{x=0} - \left(pA\right)_{x=L} + \int_0^L p\frac{\partial A}{\partial x}\,\mathrm{d}x + \int_0^L f\,\mathrm{d}x\end{aligned} \tag{2.16}$$

is obtained.

Using next

$$\left(\rho\alpha\frac{Q^2}{A}\right)_{x=L} - \left(\rho\alpha\frac{Q^2}{A}\right)_{x=0} = \int_0^L \frac{\partial}{\partial x}\left(\rho\alpha\frac{Q^2}{A}\right)\,\mathrm{d}x \tag{2.17}$$

and

$$(pA)_{x=0} - (pA)_{x=L} = -\int_0^L \frac{\partial\,(pA)}{\partial x}\,\mathrm{d}x, \tag{2.18}$$

as well as the fact that the control volume is arbitrary, equation (2.16) gives conservation of momentum as

$$\frac{\mathrm{d}Q}{\mathrm{d}t} + \frac{\partial}{\partial x}\left(\alpha\frac{Q^2}{A}\right) = -\frac{A}{\rho}\frac{\partial p}{\partial x} + \frac{f}{\rho}, \tag{2.19}$$

a form which is used later.

2.1.3 Pressure-area relationship (wall law).

In order to close the system a relationship between pressure and area is now needed. A direct functional relationship of the simple form $p = p(A)$ is assumed [61]. From this functional form a definition of distensibility can be defined,

$$D = \frac{1}{A}\frac{\mathrm{d}A}{\mathrm{d}p}. \tag{2.20}$$

A simple representative wall law is

$$p = p_{\text{ext}} + \beta\,(x)\,(A^n - A_0^n)\,, \tag{2.21}$$

where the coefficient of proportionality is dependent on the x location,

$$\beta\,(x) = \frac{\sqrt{\pi}h_0\,(x)\,\bar{E}\,(x)}{(1-\nu^2)\,A_0\,(x)}, \tag{2.22}$$

and p_{ext}, A_0, n are constants. A function of this form has been used to describe elastic vessels such as large blood vessels ([71], [61]) as well as a similar form for the urethra in [40] and [78]. In [71] a value of one half was chosen for the

power n as a consequence of Laplace's law, but a value of $n > 1/2$ may be used [19] in order to account for a non-linear stress-strain response so that the cross-sectional area changes slower at higher pressures. Faster and slower rates of wall response are studied later in this thesis, in chapter 3. Also here h_0 and A_0 are the vessel wall thickness and cross-sectional area when the tube is at rest such that $(p, u) = (p_{\text{ext}}, 0)$, whereas $\bar{E}(x)$ is Young's modulus (which is the ratio of tensile stress to tensile strain), p_{ext} is the external pressure and ν is the Poisson ratio, which is taken to be close to one half since biological tissue is practically incompressible [71], giving a material close to rubber. It can be seen from equation (2.20) that, for a fixed cross-sectional area, an increase in β will result in a less distensible tube. From the typical values found in section 1.6 it can be seen that typically

$$\beta \sim 10^6, \tag{2.23}$$

which is similar to the elastic constant value of 10^5 dyn cm^{-2} used by Griffiths [37].

2.1.4 Governing equations for the (u, A) system.

Equations (2.9), (2.19) and (2.21) form the governing equations for the (p, A, Q) system; however, the equations may be rewritten to form governing equations for the (u, A) system. Firstly equation (2.19) is written in the form

$$\begin{aligned} u\left\{\frac{\partial A}{\partial t} + \frac{\partial\left(uA\right)}{\partial x}\right\} + u\frac{\partial\left(\left(\alpha-1\right)uA\right)}{\partial x} \\ + A\left\{\frac{\partial u}{\partial t} + \alpha u\frac{\partial u}{\partial x}\right\} = -\frac{A}{\rho}\frac{\partial p}{\partial x} + \frac{f}{\rho}. \end{aligned} \tag{2.24}$$

By use of equation (2.9) the first bracket is zero. The assumption of inviscid flow means usually in the absence of incoming vorticity that we will have plug flow and so have values of $\alpha = 1$ to account for a flat velocity profile while

$f = 0$ due to lack of viscous forces. Our dimensional system is thus now

$$\frac{\partial A}{\partial t} + \frac{\partial (uA)}{\partial x} = 0, \tag{2.25}$$

$$\frac{\partial u}{\partial t} + u\frac{\partial u}{\partial x} = -\frac{1}{\rho}\frac{\partial p}{\partial x}, \tag{2.26}$$

$$p = p_{\text{ext}} + \beta\left(A^n - A_0^n\right), \tag{2.27}$$

in full.

For β constant, equations (2.26) and (2.27) are combined to give

$$\frac{\partial u}{\partial t} + u\frac{\partial u}{\partial x} = -\frac{n\beta}{\rho}A^{n-1}\frac{\partial A}{\partial x}, \tag{2.28}$$

for u,A as functions of x and t. The (u, A) system is thus (2.25) with (2.28). We prescribe boundary conditions at the start of the vessel to be taken as outflow from the bladder, with the vessel initially closed.

We should mention in passing that the position of the front of the opened urethra model is to be determined. Also reference is appropriate to other works including Huppert [44] plus related papers on gravity currents and fronts.

2.1.5 Characteristic system for constant β.

A system of characteristics is now sought. Letting

$$\underline{U} = \begin{pmatrix} A \\ u \end{pmatrix}, \tag{2.29}$$

$$\underline{\underline{H}} = \begin{pmatrix} u & A \\ \frac{n\beta}{\rho}A^{n-1} & u \end{pmatrix}, \tag{2.30}$$

the system (2.25), (2.28) can be written in the form

$$\frac{\partial \underline{U}}{\partial t} + \underline{\underline{H}}\frac{\partial \underline{U}}{\partial x} = 0. \tag{2.31}$$

The matrix $\underline{\underline{H}}$ here has two eigenvalues given by

$$C_{\pm} = u \pm \sqrt{\frac{n\beta}{\rho}A^n}, \tag{2.32}$$

which are also the characteristics. In order to decouple equations (2.31) the matrix $\underline{\underline{H}}$ is diagonalised such that $\underline{\underline{H}} = \underline{\underline{L}}^{-1}\underline{\underline{\Lambda}}\underline{\underline{L}}$, where

$$\underline{\underline{\Lambda}} = \begin{pmatrix} C_+ & 0 \\ 0 & C_- \end{pmatrix}, \tag{2.33}$$

and it is found that

$$\underline{\underline{L}} = \begin{pmatrix} \frac{1}{A}\sqrt{\frac{n\beta}{\rho}A^n} & 1 \\ -\frac{1}{A}\sqrt{\frac{n\beta}{\rho}A^n} & 1 \end{pmatrix} \tag{2.34}$$

after some working.

Now introducing a change of variables $\frac{\partial \underline{W}}{\partial \underline{U}} = \underline{\underline{L}}$ where $\underline{W} = (W_+ W_-)^T$ and multiplying equation (2.31) by $\underline{\underline{L}}$ there are obtained two decoupled wave equations:

$$\frac{\partial W_+}{\partial t} + C_+\frac{\partial W_+}{\partial x} = 0, \tag{2.35}$$

$$\frac{\partial W_-}{\partial t} + C_-\frac{\partial W_-}{\partial x} = 0. \tag{2.36}$$

The Riemann invariants for the system are therefore given by $\underline{W}$ and these are found to be

$$\begin{aligned} W_\pm &= \int_{u_0}^{u} \mathrm{d}u \pm \int_{A_0}^{A} \frac{1}{A}\sqrt{\frac{n\beta}{\rho}A^n}\mathrm{d}A \\ &= u - u_0 \pm \sqrt{\frac{4\beta}{n\rho}}\left(A^{\frac{n}{2}} - A_0^{\frac{n}{2}}\right). \end{aligned} \tag{2.37}$$

We may take $u_0 = 0$ as we define A_0 to be the cross-sectional area taken by the vessel when at rest. The significance of the Riemann invariants here is that they are conserved values along each characteristic curve.

2.2 Non-dimensionalisation

We may now non-dimensionalise our governing equations (2.25)-(2.27). This is done by introduction of non-dimensional variables given by $x = L\bar{x}$, $u = U\bar{u}$,

$p = P\bar{p}$, $A = \hat{A}\bar{a}$ and $t = \frac{L}{U}\bar{t}$ with bars denoting order one dimensionless variables. Here L is our long axial length scale (which can be taken as 17 cm say, the average urethral length in males as discussed - chapter 1), U is a characteristic axial velocity (taken as 1-4ms^{-1} say, a velocity calculated based on the length of the urethra and average micturition time), P is a typical wall-effect pressure and $\hat{A}$ a typical cross-sectional area. Equation (2.26) suggests that $P = \rho U^2$ in order to maintain balance of terms. If we now non-dimensionalise β such that $\beta = B\bar{\beta}$ for $\bar{\beta}$ of $O(1)$, we find from equation (2.27) a balance for $B = \frac{U^2}{\hat{A}^n}$. The non-dimensional governing equations are therefore given by

$$\bar{a}_{\bar{t}} + (\bar{u}\bar{a})_{\bar{x}} = 0, \tag{2.38}$$

$$\bar{u}_{\bar{t}} + \bar{u}\bar{u}_{\bar{x}} = -\bar{p}_{\bar{x}}, \tag{2.39}$$

$$\bar{p} = \bar{p}_{\text{ext}} + \bar{\beta}\left(\bar{a}^n - \bar{a}_0^n\right), \tag{2.40}$$

with constants $\bar{p}_{\text{ext}} = \frac{p_{\text{ext}}}{P}$ and $\bar{a}_0 = \frac{A_0}{\hat{A}}$ and subscripts denoting partial derivatives. For convenience bars are now removed and rewriting equations (2.38) to (2.40) yields

$$a_t + (ua)_x = 0, \tag{2.41}$$

$$u_t + uu_x = -p_x, \tag{2.42}$$

$$p = p_{\text{ext}} + \beta\left(a^n - a_0^n\right). \tag{2.43}$$

2.3 Early times; the opening of the vessel.

In order to gain some insight into the system we first examine the governing equations for small time ($t \ll 1$). In particular we are thinking of the start of micturition, with the vessel beginning to open from the neck of the bladder. In the following we examine two cases, one in which the vessel's cross-sectional area is of order one and the other with the vessel's cross-sectional area opening

on a scale t^k, thus opening more gradually than the first case if k is positive and more abruptly if k is negative. In the following we take β to be a constant.

2.3.1 Similarity solutions for abrupt openings.

It is assumed here that the effective area, tube width or gap width a is of $O(1)$ for all time. Taking equations (2.41) to (2.43) we find that in order to balance terms we must have $a \sim 1$, $u \sim 1$ and $x \sim t$ (here we are thinking $u^2 \sim a^n$). Solutions of the following form are therefore sought,

$$a = a_1(\eta) + O(t^m), \tag{2.44}$$

$$u = u_1(\eta) + O(t^m), \tag{2.45}$$

where the unknown power $m > 0$ and we define

$$\eta = \frac{x}{t} \quad \text{of} \quad O(1), \tag{2.46}$$

at this point we can see that (2.46) agrees with the characteristics (2.32) found above in section 2.1.5. Substitution into equations (2.41) to (2.43) and combining the latter two equations gives to leading order the two coupled nonlinear ordinary differential equations which form a nonlinear pair,

$$-\eta a_1' + (u_1 a_1)' = 0, \tag{2.47}$$

$$-\eta u_1' + u_1 u_1' + n\beta a_1^{(n-1)} a_1' = 0, \tag{2.48}$$

where primes denote differentiation with respect to the similarity variable η. Dropping subscripts and making a substitution $\hat{u} = u - \eta$, equations (2.47) and (2.48) become respectively

$$\hat{u}a' + (\hat{u}' + 1)\, a = 0, \tag{2.49}$$

$$(\hat{u}' + 1)\, \hat{u} + n\beta a^{(n-1)} a' = 0. \tag{2.50}$$

Taking a suitable linear combination of the above two equations then leads to the following requirement,

$$\left(\hat{u}^2 - n\beta a^n\right) a' = 0. \tag{2.51}$$

The option $a' = 0$ is discarded as this corresponds to a trivial solution (velocity and cross-sectional area being constants). Instead, taking $\hat{u}^2 = n\beta a^n$ and differentiating gives $\frac{2}{n}\hat{u}\hat{u}' = n\beta a^{(n-1)}a'$. Substituting for a in equation (2.50) and discarding the possibility $\hat{u} = 0$ it is found that

$$\left(\frac{2}{n} + 1\right)\hat{u}' = -1. \tag{2.52}$$

Upon integrating to find a solution for $\hat{u}$ the relation between $\hat{u}$ and a can be used to find the solution for a. After transforming back to the original variable u there is now a solution to equations (2.47) and (2.48) of the form

$$u = \frac{2}{2+n}\eta + c, \tag{2.53}$$

$$a = \left(\frac{1}{n\beta}\right)^{\frac{1}{n}} \left(c - \frac{n}{2+n}\eta\right)^{\frac{2}{n}}. \tag{2.54}$$

Here c is a constant of integration to be determined. In order to maintain the condition $a > 0$, which is required for a realistic solution corresponding to the biology (i.e. the urethra is open), the solution is valid only in the range $0 \leqslant \eta \leqslant \frac{2+n}{n}c$ and this acts to determine the length of opened tube: we can identify $\eta_1 = \frac{2+n}{n}c$ as the speed of the front. Then, as $\eta \to \eta_1$, $u \to \eta_1$ (the fluid velocity is equal to the front velocity) and $a \to 0$ (i.e. closure of the gap occurs at the moving front position) as expected.

It is found by substituting equations (2.53) and (2.54) into the full governing equations (2.41) to (2.42) that they are valid for all time and are therefore full solutions of the nonlinear partial differential system, of the form

$$u(x,t) = \frac{1}{2+n}\left(2\frac{x}{t} + n\dot{x}_f\right), \tag{2.55}$$

$$a(x,t) = \left(\frac{n}{\beta\left(2+n\right)^2}\left(\dot{x}_f - \frac{x}{t}\right)^2\right)^{\frac{1}{n}}, \tag{2.56}$$

where $0 \leqslant x \leqslant x_f(t)$ gives the vessel's open length at any time and $u = \dot{x}_f(t) = \eta_1$ at the front $x = x_f(t) = \eta_1 t$, reconfirming that the flow speed of the fluid and the front speed of the opening vessel are the same. Here $x_f(t)$ gives the position of the moving front and hence the length of the opened tube.

The similarity solutions for the cases $n = 1/2$, $n = 2$ and $n = 100$ are presented in figures 2.2 - 2.4 where a value of $a(0,t) = 1$ is fixed, thus setting $u(0,t)$ and $\dot{x}_f$. The results are much the same as each other with the continued opening of the urethra as x_f increases with time clearly seen. The effect of the n parameter can be seen affecting the wall response and front speed. The results also lead into the studies in depth below on the influences of gradual or rapid opening (the k effect) and fast- or slow- response vessel walls (the n effect).

2.3.2 Similarity solutions for gradual openings.

It is possible to follow the same method outlined above (in section 2.3.1) for the case of the cross-sectional area being comparable to a general power of time; in terms of micturition, this is equivalent to stating that the tube opens on a lateral scale which is of the order of t^k. So, starting from the assumption that the effective tube width $a \sim t^k$ (for k some given positive value say), it follows from the orders of magnitude in equations (2.41) to (2.43) that the following balances hold: $a \sim t^k$, $u \sim t^{(kn/2)}$ and $x \sim t^{(kn/2+1)}$. This implies the use in the axial direction of the similarity variable

$$\eta = x t^{-\left(\frac{kn}{2}+1\right)} = O\left(1\right). \tag{2.57}$$

Now solutions of the form

$$a = a_1(\eta) t^k + O(t^m), \tag{2.58}$$

$$u = u_1(\eta) t^{\frac{kn}{2}} + O(t^M), \tag{2.59}$$

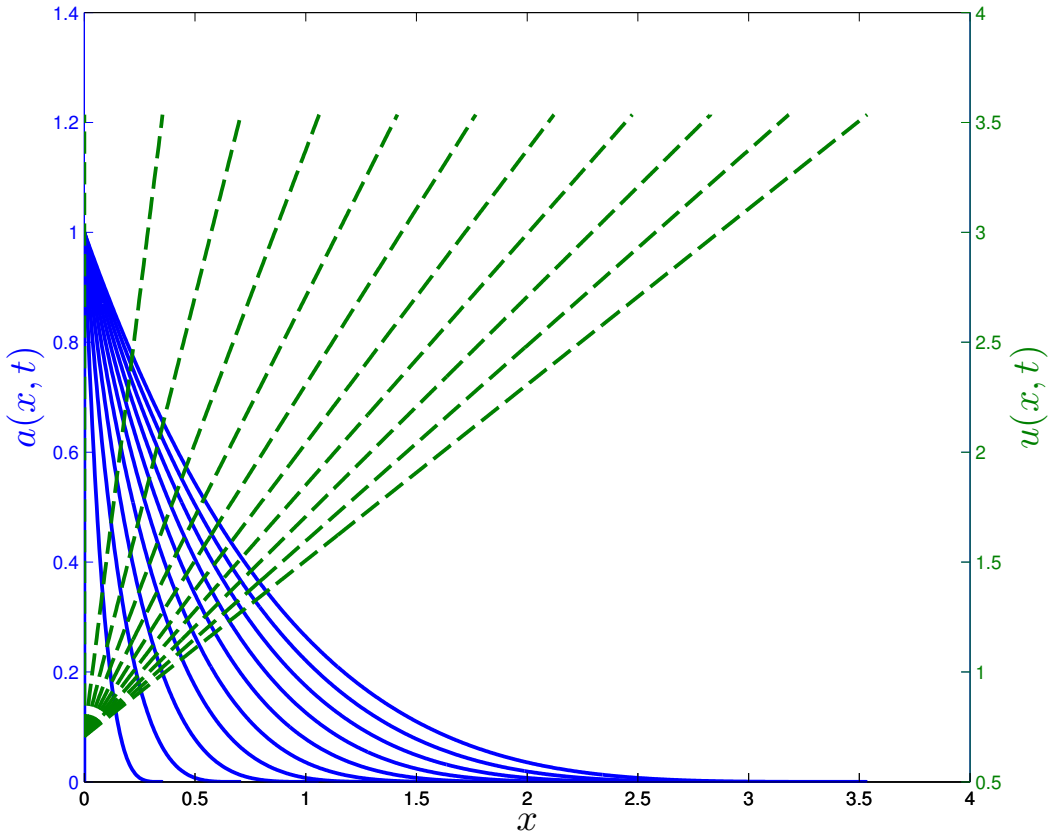

Figure 2.2: Similarity solution showing gradual opening of an initially closed vessel for $n = \frac{1}{2}$ and $\beta = 1$ showing velocity (dashed line) and cross-sectional area (solid line) for $t = 0, 0.1, 0.2, \ldots, 1$. Values at the vessel opening are $a(0,t) = 1$ and $u(0,t) = \frac{1}{\sqrt{2}}$ and are found from equations (2.55) and (2.56).

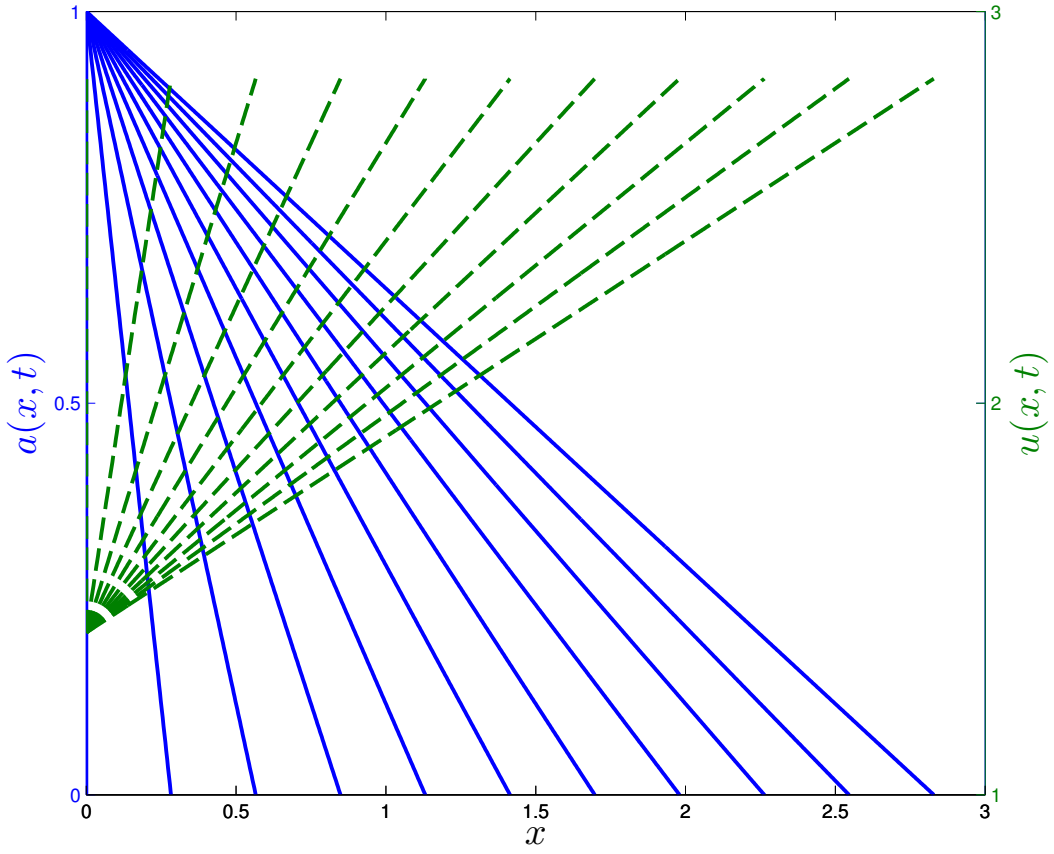

Figure 2.3: Similarity solution showing gradual opening of an initially closed vessel for $n = 2$ and $\beta = 1$ showing velocity (dashed line) and cross-sectional area (solid line) for $t = 0, 0.1, 0.2, \ldots, 1$. Values at the vessel opening are $a(0,t) = 1$ and $u(0,t) = \sqrt{2}$ and are found from equations (2.55) and (2.56).

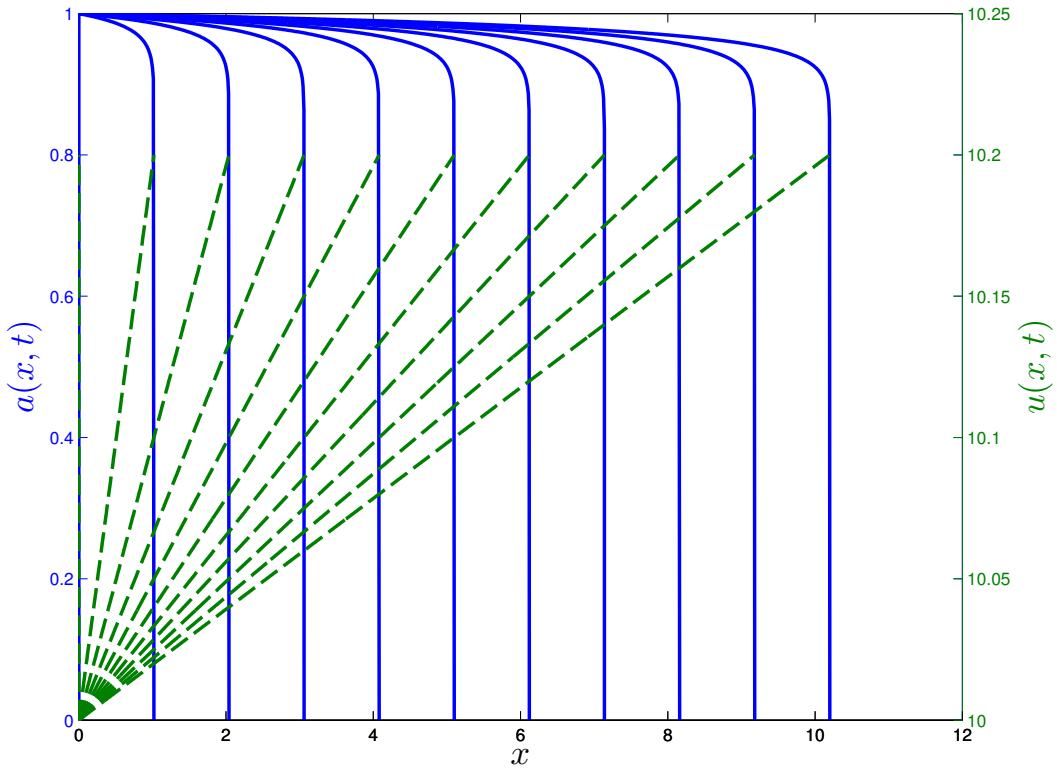

Figure 2.4: Similarity solution showing gradual opening of an initially closed vessel for $n = 100$ and $\beta = 1$ showing velocity (dashed line) and cross-sectional area (solid line) for $t = 0, 0.1, 0.2, \ldots, 1$. Values at the vessel opening are $a(0,t) = 1$ and $u(0,t) = 10$ and are found from equations (2.55) and (2.56).

are sought, where $m > k$ and $M > kn/2$.

Substituting back into equations (2.41) to (2.43) and dropping subscripts, there is now to leading order the coupled pair of ordinary differential equations

$$ka - \left(\frac{kn}{2} + 1\right)\eta a' + ua' + au' = 0, \tag{2.60}$$

$$\frac{kn}{2}u - \left(\frac{kn}{2} + 1\right)\eta u' + uu' + n\beta a^{n-1}a' = 0, \tag{2.61}$$

where the primes denote differentiation with respect to η. One solution may be found for the special case $n = 2$ with $u = a$. In this case it remains to solve

$$ka - k\eta a' + 2aa'\left(1 - \frac{\eta}{2a}\right) = 0, \tag{2.62}$$

from which it is found

$$\eta = 2a\left(1 - ca^{1/k}\right), \tag{2.63}$$

an implicit equation for $a(\eta)$. Here c is a constant, which we may set as unity if we take $a(0) = 1$. This gives, as can be seen in figure 2.5, a solution $a(\eta)$ which encounters a square root singularity and never reaches zero. The solution here is clearly not realistic physically but it is interesting in that it highlights the mixed-boundary-value nature of the mathematical problem for the evolving flow, in addition to the effects of the parameter k. No closed-form solutions of interest seem to exist in the general case however. The system (2.60), (2.61) is examined in greater detail in chapter 3.

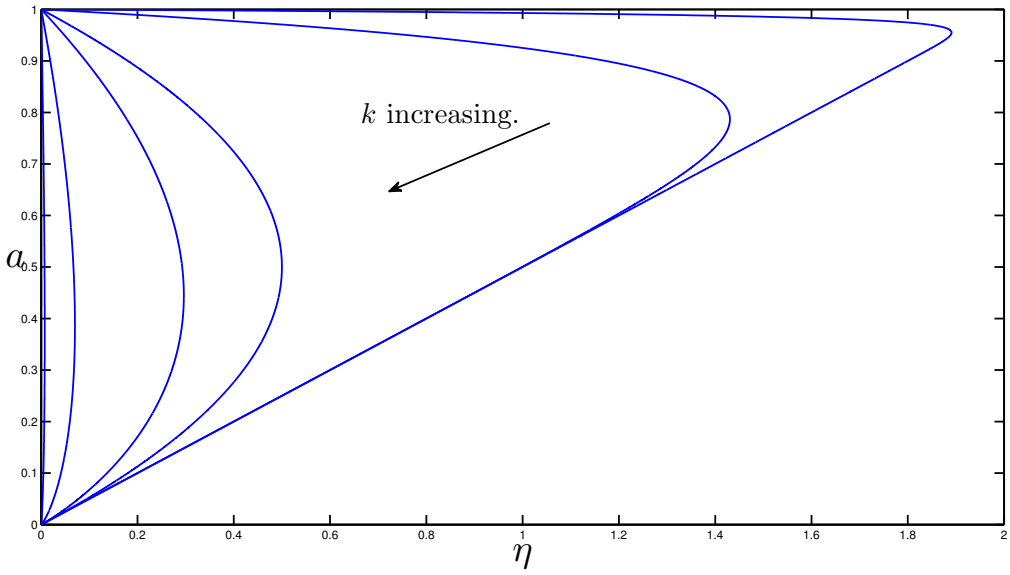

Figure 2.5: Plot of a against η for the special case $n = 2$ with $u = a$ for values of $k = \{0.01, 0.1, 1, 2, 10, 100\}$.

2.4 Short-scale alterations in tube properties and discontinuities in the long-scale

An abrupt alteration in tube properties, such as at a sudden bend or change in distensibility, can be incorporated into the long-scale theory through the implementation of jump conditions. This is achieved by assuming that the alteration occurs over a much shorter length scale than the characteristic length scale of the tube, $L \gg 1$, as follows.

From the long-scale governing equations (2.25), (2.28) a balance $\frac{U}{T} \sim \frac{U^2}{L}$ is observed, where U is the characteristic axial velocity and T is the characteristic time-scale. From this it is given that $T \sim \frac{L}{U}$.

The short-scale flow is taken to be governed by the two-dimensional Euler

equations,

$$u_x + v_y = 0, \tag{2.64}$$

$$u_t + uu_x + vu_y = -P_x, \tag{2.65}$$

$$v_t + uv_x + vv_y = -P_y, \tag{2.66}$$

if we now consider (x, y) of $O(1)$. We have that the flow is driven by an input $u \sim U$ over a time-scale $T \sim \frac{L}{U}$. Comparison of the time dependent and convective terms in equations (2.65) and (2.66) gives, for the left hand sides of the equations, $O(U^2/L, U^2)$ and $O(U/L, U)$ respectively. This indicates that the system may be taken to be quasi-steady. After dropping the time dependent terms, equations (2.64)-(2.66) thus become

$$u_x + v_y = 0, \tag{2.67}$$

$$uu_x + vu_y = -P_x, \tag{2.68}$$

$$uv_x + vv_y = -P_y. \tag{2.69}$$

To these equations are added now the conditions that far upstream and downstream of the bend the flow returns to long-scale flow of the previous kind (sections 2.3.1, 2.3.2). The lower and upper walls of the vessel are given by $f_1(x)$ and $f_2(x)$ respectively.

The first jump condition is obtained by integration of the continuity equation with respect to the lateral variable, y. Thus

$$\int_{f_1(x)}^{f_2(x)} (u_x + v_y)\, \mathrm{d}y = 0, \tag{2.70}$$

giving

$$\begin{aligned} \int_{f_1(x)}^{f_2(x)} u_x dy &= -\int_{f_1(x)}^{f_2(x)} v_y \, \mathrm{d}y \\ &= v(x, f_1(x)) - v(x, f_2(x)). \end{aligned} \tag{2.71}$$

Applying an impermeable boundary condition at the walls, such that for the upper wall we have

$$v(x, f_2(x)) = f_2'(x)u(x, f_2(x)),$$

and similarly for the lower wall, (2.71) becomes

$$\int_{f_1(x)}^{f_2(x)} u_x dy = f_1'(x)u(x, f_1(x)) - f_2'(x)u(x, f_2(x)), \tag{2.72}$$

to which we can apply Leibnitz's integral rule and then integrate with respect to x to give the mass-conservation requirement

$$\int_{f_1(x)}^{f_2(x)} u \, \mathrm{d}y = const, \quad \forall x. \tag{2.73}$$

In the case where the axial velocity both far upstream and far downstream is independent of the lateral variable this simply reduces to the requirement

$$u_0 A_0 = u_1 A_1, \tag{2.74}$$

where the subscript 0 denotes upstream variables and 1 denotes the downstream.

The second jump condition is given by Bernoulli's principle and is obtained through integration of the momentum equations, (2.68) and (2.69), along a streamline. Integrating the x-momentum, equation (2.68), we have in effect

$$uu_x\delta x + vu_y\delta x = -P_x\delta x.$$

We now note that along a streamline, $\frac{\delta y}{\delta x} = \frac{v}{u}$. Therefore

$$uu_x\delta x + uu_y\delta y = -P_x\delta x,$$

which may be rewritten as

$$\frac{1}{2}\delta(u^2) = -P_x\delta x. \tag{2.75}$$

This is done similarly for the y-momentum to give

$$\frac{1}{2}\delta(v^2) = -P_y\delta y. \tag{2.76}$$

Addition of equations (2.75) and (2.76) then leads to

$$\frac{1}{2}\int \mathrm{d}(u^2) + \frac{1}{2}\int \mathrm{d}(v^2) = \int \mathrm{d}P,$$

yielding

$$P + \frac{1}{2}\left(u^2 + v^2\right) = H(\Psi), \tag{2.77}$$

where Ψ denotes the stream function. The Bernoulli quantity $P+1/2\,(u^2+v^2)$ is therefore preserved along a streamline. Relating upstream and downstream variables equation (2.77) then gives the jump condition

$$P_0 + \frac{1}{2}(u_0^2 + v_0^2) = P_1 + \frac{1}{2}(u_1^2 + v_1^2). \tag{2.78}$$

The final condition that is needed is simply the wall law, (2.27). On substitution of the wall law into equation (2.78) we have

$$\beta_0 A_0^{n_0} + \frac{1}{2}\left(u_0^2\right) = \beta_1 A_1^{n_1} + \frac{1}{2}\left(u_1^2\right). \tag{2.79}$$

The full jump conditions for the axial velocity and the cross-sectional area are thus given by equations (2.74) and (2.79). Rearranging equation (2.74) and then substituting for u_1 in equation (2.79) there is obtained an equation for A_1:

$$\beta_1 A_1^{n_1+2} - \left(\beta_0 A_0^{n_0} + \frac{1}{2}\left(u_0^2\right)\right) A_1^2 + \frac{1}{2}\left(u_0 A_0\right)^2 = 0. \tag{2.80}$$

The value of u_1 can then found via equation (2.74).

There are two difficulties that can arise in the use of the preceding jump conditions. Firstly, the solution may not be unique. In many instances there are two viable solutions; two positive solutions for A. We note that similar

results were found by Griffiths [40] for which he was concerned with pressure and two possible values of flow rate. Currently the solution is chosen by its proximity to the value of A before the jump, the "closest" value being taken. The second potential difficulty is that no real solutions may exist. In that event it is likely that there are no steady solutions in the short-scale alteration region and so the jump conditions are no longer valid. These matters are illustrated in figures (2.6), (2.7) and (2.8), for the case $n_0 = n_1 = 2$ with the values (A_0, u_0) found using the similarity solutions. The roots of the quartic, (2.80) for $n_0 = n_1 = 2$, represent the values of A given by the jump conditions; the negative roots are not shown as these are physically unrealistic. The dotted curves in each represent $\beta_0 = \beta_1$ with the value before the jump given by the root $A \approx 0.65$. This curve shows that even with no change in distensibility the jump conditions allow a new value of A to be taken. Given a fixed value of β_0, the value of β_1 is varied. The figures illustrate that as β_1 increases there is a definite critical value (given β_0) above which no real valued solutions exists indicating a cut-off, after which unsteady solutions are expected. Further examination is made in section 4.2 and also in appendix A.

2.4.1 Forward marching RK scheme

Such a scheme was tried initially on the system (2.60), (2.61) of interest but this soon proved to be not completely satisfactory. The reasons are connected with an issue of upstream influence essentially, as will become clear in the next chapter.

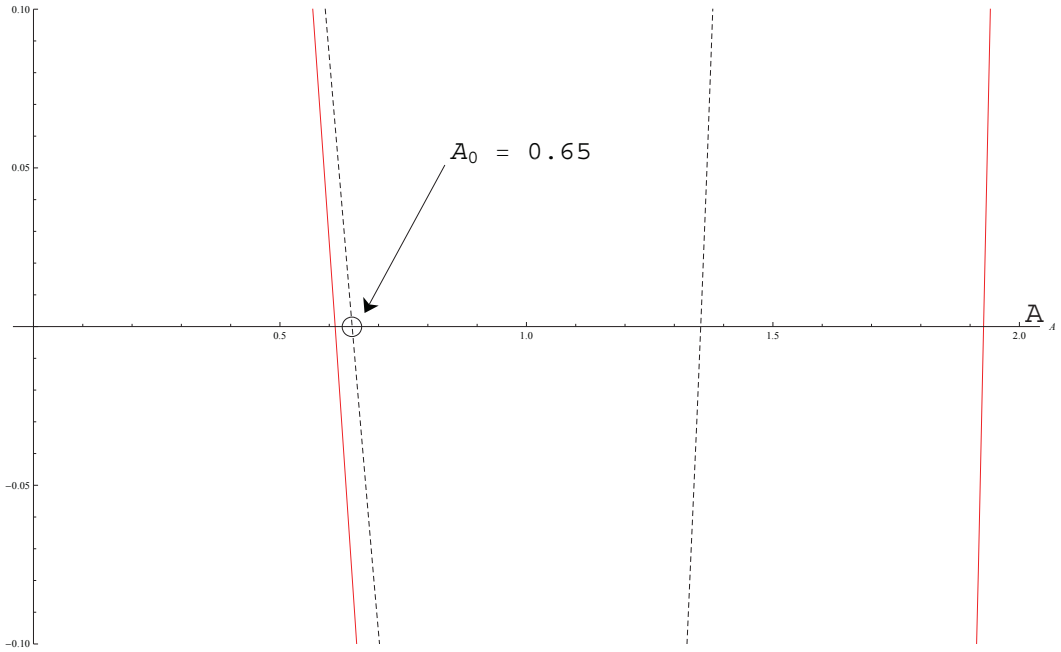

Figure 2.6: Plot of the left hand side of equation (2.80). Here $n_0 = n_1 = 2$, $\beta_0 = 1$, $\beta_1 = 0.55$. Roots of the solid line indicate possible solutions A_1 with the closest root indicating a decrease in cross-sectional area. Values (u_0, A_0) are taken from similarity solutions (2.55), (2.56) for $t = 1$, $x = 1$.

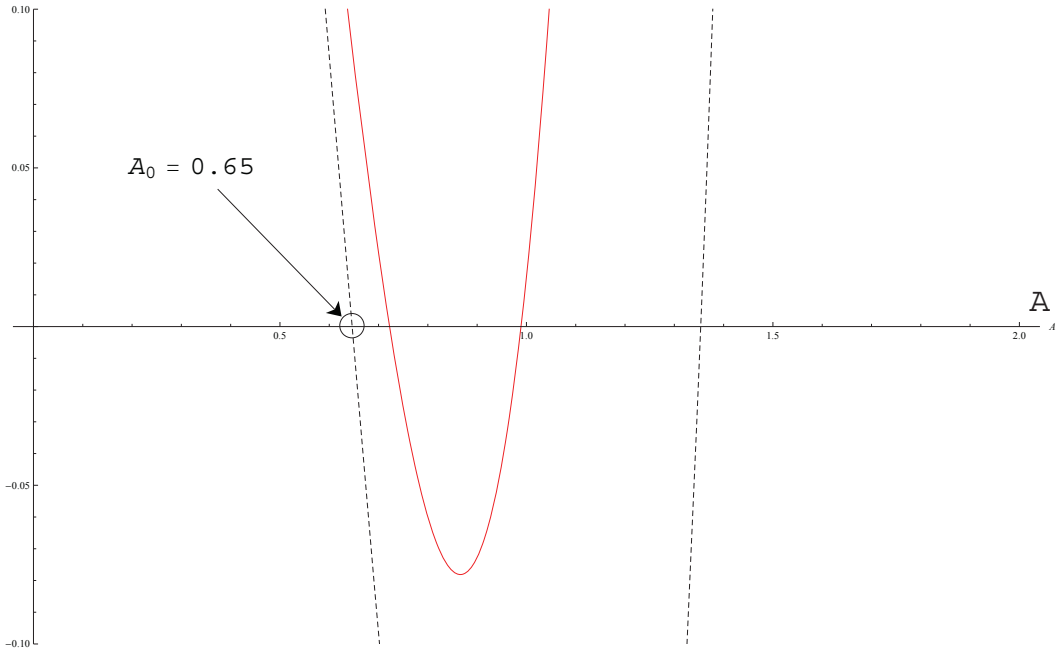

Figure 2.7: Plot of the left hand side of equation (2.80). Here $n_0 = n_1 = 2$, $\beta_0 = 1$, $\beta_1 = 1.5$. Roots of the solid line indicate possible solutions A_1. The closest root indicates an increase in cross-sectional area. Values (u_0, A_0) are taken from similarity solutions (2.55), (2.56) for $t = 1$, $x = 1$.

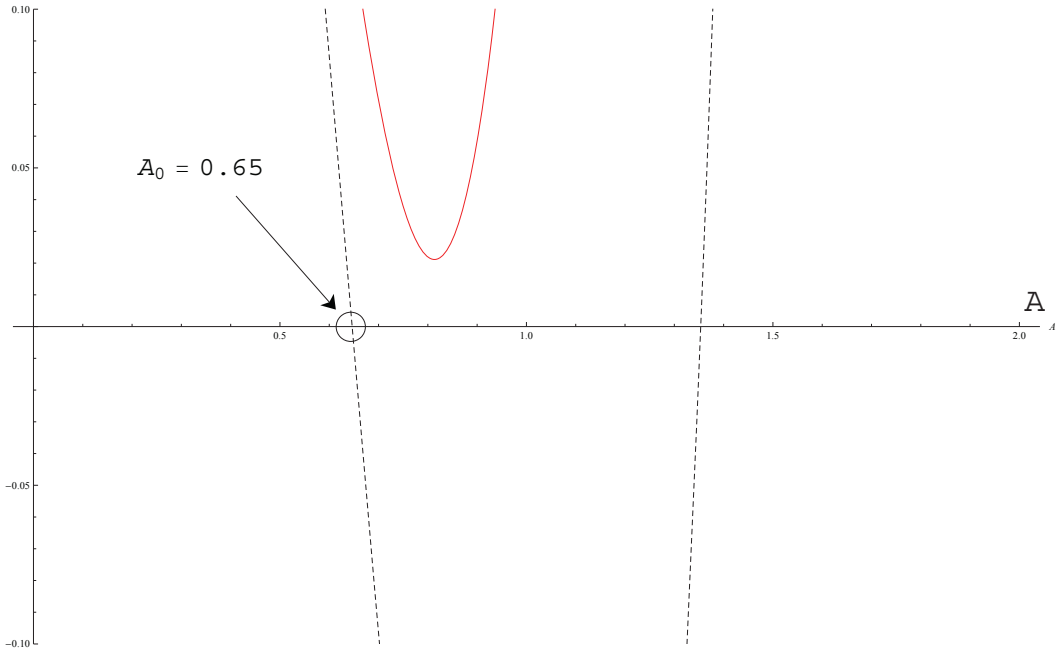

Figure 2.8: Plot of the left hand side of equation (2.80). Here $n_0 = n_1 = 2$, $\beta_0 = 1$, $\beta_1 = 1.7$. Notice that there are now no real roots of the solid line, indicating no possible solutions of A_1. Values (u_0, A_0) are taken from similarity solutions (2.55), (2.56) for $t = 1$, $x = 1$.

2.5 Summary of chapter

In brief summary, the two-dimensional model has now been described in its original dimensional terms and this has led on to a nondimensional version of the governing equations and boundary conditions. The latter version is ready for subsequent investigation.

Although this initial model is relevant only for inviscid flow, this seems a reasonable first guess considering the estimated magnitude of the Reynolds number. The ability to accommodate any cross-sectional shape in principal is quite appealing and the analytical abrupt opening solutions are encouraging. This model seems most appropriate close to the bladder neck and given an estimate for the distensibility of the vessel there, could serve to demonstrate the expected vessel opening shape, pressure and cross-sectionally averaged fluid velocity.

Chapter 3

Fast and slow responses

The primary governing equations for the two-dimensional modelling of the fluid flow through the flexible tube along with appropriate boundary and initial conditions have been set out already in, or at least are clear from, the previous chapter in effect. The aim now is to move towards deriving some helpful and physically interesting solutions and more basic properties of the nonlinear system, given that there is no general exact solution as far as is known to date. Of particular concern is the behaviour of the system when extreme parameters are present such as in fast or slow responses of the wall shape for instance where limiting analyses can be applied to describe the flow properties. These investigations can yield increased insight into the dynamics involved and hence more understanding of the fluid-structure interactions, which in turn may lead on to easier handling for various extensions of the theory in due course. The investigations can also provide guidelines for computational studies of the system (see below and chapter 4) and for the important extensions into three-dimensional modelling (see chapter 5). In the present chapter it is assumed that the scaled distensibility factor β is a constant. This assumption is chosen as the urethra can be seen to be comprised of a number of discrete sections, see chapter 1. So we are able to assume β to be piecewise constant at least, but at any rate

within a section we take β constant.

3.1 Behaviour of the PDE system near the front.

In order to gain insight into the behavior near the moving front $x = x_f(t)$ we now return to the partial differential equations (PDEs) system (2.41) to (2.43). We begin by rescaling a such that $a = \breve{a}\,(n\beta)^{-1/n}$ in order to absorb the constants n and β. In the following we then drop the superscript for convenience. Next we change variables $(x,t) \mapsto (\epsilon,t)$ for convenience where $\epsilon = 1 - x/x_f(t) \ll 1$ near the front. The system therefore becomes

$$a_t + \frac{\dot{x_f} - u - \epsilon\dot{x_f}}{x_f} a_\epsilon - \frac{a}{x_f} u_\epsilon = 0, \tag{3.1}$$

$$u_t + \frac{\dot{x_f} - u - \epsilon\dot{x_f}}{x_f} u_\epsilon - \frac{a^{n-1}}{x_f} a_\epsilon = 0, \tag{3.2}$$

for u, a as unknown functions of ϵ, t. Solutions of the following form are now sought,

$$u(\epsilon,t) = \epsilon^l u_0(t) + \epsilon^{l+1} u_1(t) + \dots \quad ,$$
$$a(\epsilon,t) = \epsilon^m a_0(t) + \epsilon^{m+1} a_1(t) + \dots \quad ,$$

where the powers l, m are to be determined but for biological relevance u, a must remain finite as $\epsilon \to 0^+$. We thus take $l, m \geqslant 0$ with $u_0, a_0 \neq 0$. We would expect u to remain order one at the front in order to drive the front velocity which itself is of order one in general and so $l = 0$. Substitution into

(3.1) and (3.2) then gives

$$\begin{aligned} &\epsilon^{m-1}\left(\dot{x}_f - u_0\right) m a_0 + \\ &+\epsilon^m \left\{x_f a_0' + \left(\dot{x}_f - u_0\right)(m+1)\, a_1 - a_0\left((m+1)\, u_1 + m\dot{x}_f\right)\right\} + \\ &+O\left(\epsilon^{m+1}\right) = 0, \end{aligned} \tag{3.3}$$

$$\begin{aligned} &x_f u_0' + \left(\dot{x}_f - u_0\right) u_1 + \epsilon\left\{x_f u_1' + 2\left(\dot{x}_f - u_0\right) u_2 - \left(u_1 + \dot{x}_f\right) u_1\right\} - \\ &-\epsilon^{mn-1} m a_0^n + \ldots = 0, \end{aligned} \tag{3.4}$$

in turn .

At leading order in equation (3.3) we obtain

$$u_0 = \dot{x}_f,$$

a result which has been seen in the previous chapter, so that close to the front the fluid velocity and the front speed match exactly. This is equivalent to a kinematic boundary condition.

There are now two possibilities to consider, the first of which is that $u_0' \neq 0$. In such a case, which is the general one, equation (3.4) requires that

$$m = \frac{1}{n} > 0 \tag{3.5}$$

be satisfied. The following equations are then left to solve for a_0, u_1,

$$x_f a_0' - a_0\left(\frac{n+1}{n} u_1 + \frac{\dot{x}_f}{n}\right) = 0, \tag{3.6}$$

$$\ddot{x}_f - \frac{a_0^n}{n x_f} = 0. \tag{3.7}$$

Rearranging equation (3.7) to obtain a_0 and then substituting into equation (3.6), the following results are found:

$$a_0 = \left(n x_f \ddot{x}_f\right)^{1/n}, \tag{3.8}$$

$$u_1 = \frac{x_f \dddot{x}_f}{(n+1)\,\ddot{x}_f}. \tag{3.9}$$

The solution is therefore given by

$$u(\epsilon,t) = \dot{x}_f(t) + \epsilon\frac{x_f\dddot{x}_f}{(n+1)\,\ddot{x}_f} + O(\epsilon^2), \tag{3.10}$$

$$a(\epsilon,t) = (\epsilon n x_f \ddot{x}_f)^{1/n} + O(\epsilon^{\frac{1+n}{n}}), \tag{3.11}$$

near the front in the general case.

We now consider the second possibility of $u_0' = 0$, which corresponds to the situation of the front speed being constant so that $\ddot{x}_f = 0$ and is indeed the same situation as for the similarity solution (2.55),(2.56). We will see now that this is in fact a special case as regards the behaviour close to the front. Seeking a solution with $u_1' = 0$ and taking

$$m = \frac{2}{n}$$

so that u_1 and a_0 terms balance within equation (3.4), there is now the system

$$x_f a_0' - a_0\left(\frac{2+n}{n}u_1 + \frac{2\dot{x}_f}{n}\right) = 0, \tag{3.12}$$

$$(u_1 + \dot{x}_f)\,u_1 + \frac{2}{n}a_0^n = 0, \tag{3.13}$$

to be considered. It is clearly possible to rearrange equation (3.13) in order to obtain a_0 in terms of u_1. This may be substituted back into equation (3.12), solving for u_1 to give

$$a_0 = \left(\frac{n}{2+n}\dot{x}_f\right)^{2/n}, \tag{3.14}$$

$$u_1 = -\frac{2}{2+n}\dot{x}_f. \tag{3.15}$$

The solution in the special case is therefore given by

$$u(\epsilon,t) = \frac{1}{2+n}\left(2\left(1-\epsilon\right)+n\right)\dot{x}_f + O(\epsilon^2), \tag{3.16}$$

$$a(\epsilon,t) = \left(\frac{n}{2+n}\dot{x}_f\epsilon\right)^{2/n} + O(\epsilon^{\frac{2+n}{n}}), \tag{3.17}$$

a pair of results which we notice match the similarity solution given by equations (2.56) and (2.55), as we would hope.

The findings in the general case appear to make reasonable physical sense, with for instance the shape coefficient a_0 in (3.11) increasing with the scaled front acceleration $\ddot{x}_f$ but being dependent on the response factor n. The acceleration here has to be positive according to (3.11), or zero in the special scenario (3.17), a scenario which also makes good sense physically. By contrast, deceleration with $\ddot{x}_f$ being negative is inadmissable within the framework of (3.1) - (3.4) it seems, and instead the formation of shock-like effects in the tube flow seems likely then. The findings (3.10), (3.11) are local to the front but are reflected in the global solutions investigated within the remainder of the chapter.

3.2 Front behaviour for gradual openings.

We now turn our attention to equations (2.60) and (2.61) and begin here by re-scaling or re-normalising according to $\eta = \eta_0\eta_b$, $u = \eta_0 u_b$ and $a = \{(n\beta)^{-1}\eta_0^2\}^{1/n} a_b$. The re-scaling has the main effect of normalising the length of interest to be unity in terms of the new longitudinal coordinate η_b while at the same time removing the factor $n\beta$ from the system. Here η_0 is a constant such that $a(\eta_0) = 0$ and thus gives the scaled unknown position of the front for an opening tube. Substitution yields the coupled nonlinear ordinary differential system as

$$ka_b - \left(\frac{kn}{2} + 1\right)\eta_b a_b' + u_b a_b' + a_b u_b' = 0, \tag{3.18}$$

$$\frac{kn}{2}u_b - \left(\frac{kn}{2} + 1\right)\eta_b u_b' + u_b u_b' + a_b^{n-1}a_b' = 0, \tag{3.19}$$

governing $u_b(\eta_b)$, $a_b(\eta_b)$, the effective velocity and gap width respectively, with $0 \leqslant \eta_b \leqslant 1$.

Guided by the findings of the previous section, it is possible to examine the behaviour close to the front position with $\eta_b = 1 - \sigma$ where σ is small. This is with a view to analysis (first) and numerical computation (second) capturing accurately the interactive flow/wall response near the front where singular behaviour of the solution holds in general as will become clear below; see also section 3.1. The variables are then scaled $a_b = \sigma^m B$, $u_b = U$ for convenience where m is a power to be defined. Equations (3.18) and (3.19) become

$$B'\left\{\left(\frac{kn}{2}+1\right)(1-\sigma)-U\right\}+B\left\{k+\left(\frac{kn}{2}+1\right)(1-\sigma)\frac{m}{\sigma}-\frac{mU}{\sigma}-U'\right\}=0, \tag{3.20}$$

$$U'\left\{\left(\frac{kn}{2}+1\right)(1-\sigma)-U\right\}+U\frac{kn}{2}-\sigma^{mn}B^n\left\{\frac{m}{\sigma}+\frac{B'}{B}\right\}=0, \tag{3.21}$$

where m is identified with n^{-1} due to the analysis of the preceding section and given by equation (3.5) in the general situation, while the primes denote differentiation with respect to σ now. Hence we have two equations for U, B.

Further, equation (3.20) can be rearranged next to give

$$\frac{B'}{B}=-\frac{1}{n\sigma}+\frac{U'-k}{\left(\frac{kn}{2}+1\right)(1-\sigma)-U}. \tag{3.22}$$

Inserting (3.22) into (3.21) then yields, after some working,

$$U'=\frac{-k\left\{\frac{nU}{2}\left(\left(\frac{kn}{2}+1\right)(1-\sigma)-U\right)+\sigma B^n\right\}}{D}, \tag{3.23}$$

where the denominator D is defined by

$$D=\left(\left(\frac{kn}{2}+1\right)(1-\sigma)-U\right)^2-\sigma B^n.$$

Finally here, it is possible to obtain a more helpful equation for B' or B'/B from equation (3.23) by eliminating U' using equation (3.22), which results in

$$\frac{B'}{B}=-\frac{1}{n\sigma}-\frac{k\left\{\left(\frac{kn}{2}+1\right)(1-\sigma)+U\left(-1+\frac{n}{2}\right)\right\}}{D}. \tag{3.24}$$

The system (3.23), (3.24) is suitable for numerical study. Also conditions at the front are now obtained by allowing $s \to 0^+$. An $O(1/\sigma)$ balance in equation (3.24) yields

$$U(0) = \frac{kn}{2} + 1, \tag{3.25}$$

and finally an $O(\sigma)$ balance from equation (3.23) gives

$$B(0) = \left\{ \frac{kn^2}{2} \left(\frac{kn}{2} + 1 \right) \right\}^{\frac{1}{n}}, \tag{3.26}$$

which we notice, upon scaling back to the original u and a variables defined by (2.58) and (2.59), match exactly the leading order terms of equations (3.10),(3.11) within the PDE framework when the latter is also scaled back to the original variables.

Thus the nonlinear system of interest now is given by (3.23), (3.24) for (U, B) or (U, B, D). Its properties are examined below.

3.3 Numerically marching backwards in the U, B System

It has already been found in chapter 2 that forward-marching a numerical scheme in terms of η can be difficult in practice for the present cases. The exact solution (2.63) also falls into line with such a finding of difficulty in the forward direction. Hence there arises the need for or at least the desirability of a scheme that marches in the backward direction in η, and thus forward in terms of σ. Another problem is then apparent since the flow/shape solution is irregular close to the front as established in section 3.1 but this is addressed as follows.

In an attempt to find numerical solutions to the potentially problematic (U, B) system (3.23), (3.24) it is convenient to scale in the following manner,

so that we avoid a region arbitrarily close to the front. We take $B^n = b^2\tilde{C}$, $U = b\tilde{U}$, $D = b^2\tilde{D}$ with $\sigma = \exp z$ and define $b \equiv (kn/2 + 1)$. Our system then becomes

$$b\tilde{U}_z = -\frac{k \exp z}{\tilde{D}} \left\{ \frac{n\tilde{U}}{2} \left(1 - \exp z - \tilde{U}\right) + \tilde{C} \exp z \right\}, \tag{3.27}$$

$$\frac{b\tilde{C}_z}{\tilde{C}} = -b - \frac{kn \exp z}{\tilde{D}} \left\{ 1 - \exp z + \left(\frac{n}{2} - 1\right) \tilde{U} \right\}, \tag{3.28}$$

where

$$\tilde{D} = \left(1 - \exp z - \tilde{U}\right)^2 - \tilde{C} \exp z. \tag{3.29}$$

Front conditions are obtained from (3.25) and (3.26) and are given by

$$\tilde{U}(z_{-\infty}) = 1, \tag{3.30}$$

$$\tilde{C}(z_{-\infty}) = \frac{kn^2}{2} \left(\frac{kn}{2} + 1\right)^{-1}, \tag{3.31}$$

where $z = z_{-\infty}$ is a finite large negative value of z and gives the approximate position of the front (strictly the front corresponds to $z_{-\infty} \to -\infty$). This system is tackled numerically using a Runge-Kutta 4 method which marches from $z = z_{-\infty}$, the effective front position, up to $z = 0$, the opening of the vessel.

3.3.1 Rapid entrance openings (small k)

Previously in section 3.1 we noticed from the full partial differential equation system that in the general case equation (3.9) will fail if $\ddot{x}_f = 0$, as the expansion for u breaks down and also $a_0 = 0$. Since the special case $k = 0$ results in a system with exactly zero acceleration $\ddot{x}_f = 0$ this leads us to expect some singular behaviour close to the front when k is small.

We examine this near-front region in the following for small k values. Taking our current system (3.27), (3.28) it is expected, by examination of the conditions close to the front, that $\tilde{U}$ is $O(1)$ and $\tilde{C}$ is $O(k)$. We set $\tilde{C} = k\bar{C}$ and

also $\exp(z) = \Theta \exp(\bar{z})$ for some constant Θ to be found and $\bar{z}$ of $O(1)$. The orders of magnitude from (3.27), (3.28) and (3.29) then suggest attempting the expansions

$$\tilde{U} = 1 + k\bar{U} + O(k^2), \tag{3.32}$$

$$\tilde{C} = k\bar{C} + O(k^2), \tag{3.33}$$

with

$$z = \log(k) + \bar{z} \tag{3.34}$$

and thus

$$\tilde{D} = k^2\bar{D} + O(k^3). \tag{3.35}$$

Thus, when substituted into the governing system, (3.27)-(3.29) produce the reduced form

$$\bar{U}_{\bar{z}} = \frac{n\exp(\bar{z})}{2\bar{D}}\left(\exp(\bar{z}) + \bar{U}\right), \tag{3.36}$$

$$\frac{\bar{C}_{\bar{z}}}{\bar{C}} = -1 - \frac{n^2\exp(\bar{z})}{2\bar{D}}, \tag{3.37}$$

$$\bar{D} = \left(\exp(\bar{z}) + \bar{U}\right)^2 - \bar{C}\exp(\bar{z}), \tag{3.38}$$

to leading order. Here $-\infty < \bar{z} < \infty$ for arbitrarily small k in order to cover the region of the vessel which is open. To solve we now make the transformation $\exp(\bar{z}) = r$ so that $0 < r < \infty$ and (3.36) - (3.38) become

$$\bar{U}_r = \frac{n}{2\bar{D}}\left(r + \bar{U}\right), \tag{3.39}$$

$$\frac{r\bar{C}_r}{\bar{C}} = -1 - \frac{n^2 r}{2\bar{D}}, \tag{3.40}$$

$$\bar{D} = \left(r + \bar{U}\right)^2 - r\bar{C}, \tag{3.41}$$

with boundary conditions

$$\bar{U}(0) = 0, \tag{3.42}$$

$$\bar{C}(0) = \frac{n^2}{2}, \tag{3.43}$$

taken from (3.30) and (3.31).

If we now take

$$V = \bar{U} + r, \tag{3.44}$$

$$G = r\bar{C}, \tag{3.45}$$

$$B = 2\bar{D}, \tag{3.46}$$

after some work we obtain the ordinary differential equation

$$\frac{\mathrm{d}V}{\mathrm{d}G} = \frac{-2(V + \frac{n}{4})^2 + 2G + \frac{n^2}{8}}{n^2 G}. \tag{3.47}$$

A phase plot of $V(G)$ given by equation (3.47) for the case $n = 2$ can be seen in figure 3.1 which may indicate solutions given different starting conditions. In order to find relevant starting conditions for this case, however, we now allow $r \to 0$ in the following.

Approaching the front.

As we approach the front we have $r \to 0$. Using boundary conditions (3.42) and (3.43) we find from (3.41) that

$$\bar{D} \to -\frac{rn^2}{2}, \tag{3.48}$$

which we may then use to find

$$\bar{U}_r \sim -\frac{r + \bar{U}}{nr}, \tag{3.49}$$

$$\frac{r\bar{C}_r}{\bar{C}} \sim 0, \tag{3.50}$$

from (3.39) and (3.40). Equations (3.49) and (3.42) then imply that we take $\bar{U} = O(r)$. Letting $\bar{U} = \mu r$ we then have

$$\mu = \frac{-1}{n+1}.$$

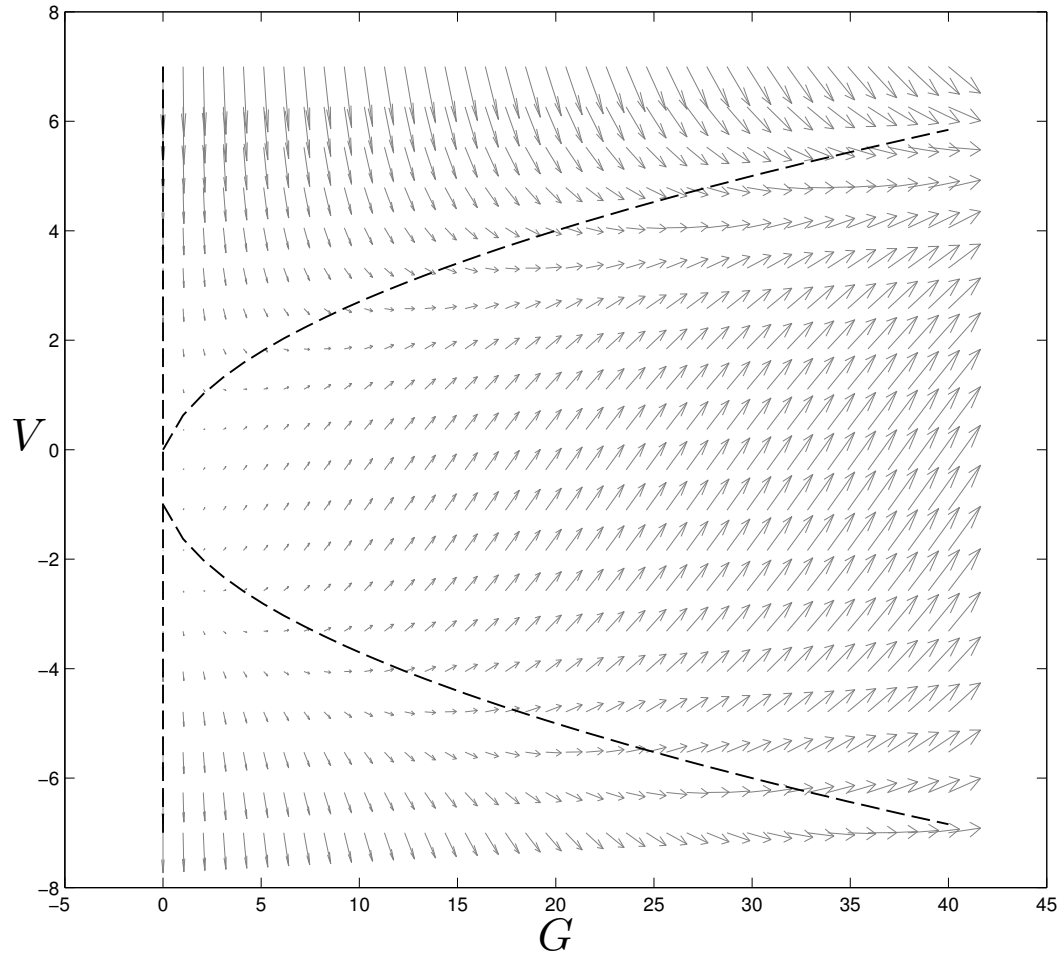

Figure 3.1: Phase plane using equation (3.47) for $n = 2$. Shown are nullclines (dashed) and vectors indicating gradients with their associated magnitudes. It is possible to trace out solutions of equation (3.47) given the starting condition.

Finally (3.50) and (3.43) give $\bar{C}$ so that

$$\bar{U} \to \frac{-r}{n+1}, \tag{3.51}$$

$$\bar{C} \to \frac{n^2}{2}. \tag{3.52}$$

Converting these results to the variables V and G, we obtain starting conditions for numerically solving (3.47). Starting conditions are given as

$$V \sim \frac{n}{n+1} r, \tag{3.53}$$

$$G \sim \frac{n^2}{2} r, \tag{3.54}$$

for $r \ll 1$. Equivalently this may also be written

$$V \sim \frac{2}{n(n+1)} G, \tag{3.55}$$

for $G \ll 1$. We note also that converting back to the original $(u(\eta), a(\eta))$ variables we find that limits (3.51), (3.52) correspond to

$$a \to \eta_0, \tag{3.56}$$

$$u \to 0, \tag{3.57}$$

as $\eta \to \eta_0$ as we expected.

Approaching the opening.

In order to ensure that matching to the main region near to the vessel opening is possible we now investigate $r \to \infty$. Here we have

$$\bar{U} = rU_1 + \cdots, \tag{3.58}$$

$$\bar{C} = rC_1 + \cdots, \tag{3.59}$$

$$\bar{D} = rD_1 + \cdots, \tag{3.60}$$

where the scalings were found in order to balance (3.39) to (3.41). From these we have

$$U_1 = -\frac{2}{n+2}, \tag{3.61}$$

$$C_1 = \left(\frac{n}{n+2}\right)^2, \tag{3.62}$$

$$D_1 = -\frac{n^2}{4}, \tag{3.63}$$

and also the relation

$$U_1 = \sqrt{C_1} - 1. \tag{3.64}$$

This relation, when scaled back to V,G variables, gives

$$V \sim \sqrt{G} \text{ as } G \to \infty, \tag{3.65}$$

which can be seen quite clearly emerging in the numerical results of figure (3.1). In the original variables of (2.55) and (2.56) this means

$$u^2 \to n\beta a^n, \tag{3.66}$$

which we notice matches the solution (2.55) and (2.56) from which we may obtain the same result. Furthermore, scaling (3.61) and (3.62) back to the original variables and letting $k \to 0$ we obtain

$$u(x,t) = \frac{1}{2+n}\left(2\frac{x}{t} + n\eta_0\right), \tag{3.67}$$

$$a(x,t) = \left(\frac{n}{\beta\left(2+n\right)^2}\left(\eta_0 - \frac{x}{t}\right)^2\right)^{\frac{1}{n}}, \tag{3.68}$$

where we may identify η_0 with $\dot{x}_f$ and so obtain the original solutions (2.55) and (2.56) for $k = 0$. These results confirm that matching is possible and in fact that the solutions obtained near the front for small k apply throughout the whole open region of the vessel.

Numerical results obtained from a Runge Kutta 4 scheme applied to equation (3.47), or equivalently the system (3.39)-(3.41), using the starting conditions (3.53),(3.54) in order to avoid the delicate front region can be seen in figures 3.2 and 3.3. Here figure 3.2 shows the small k result for three values of n where the asymptotic solutions are also displayed for comparison. We note the qualitatively similar results but mention that in fact the parameter n cannot be scaled out of the ordinary differential equation (3.47). Figure 3.3 shows the numerical solution for values $k = 0.0001$ and $n = 1$ compared against the analytical result of the $k = 0$ case given by equations (2.55) and (2.56) where we have scaled back to the original variables. We see the close agreement between the small k and $k = 0$ cases where the numerical value of η_0 is found to be 2.998, while the analytical solution for the $k = 0$ case gives $\eta_0 = 3$.

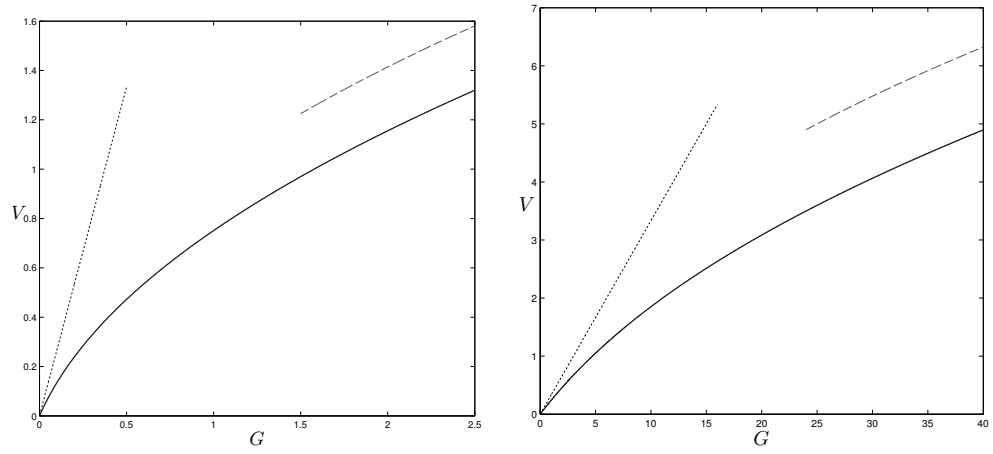

(a)

(b)

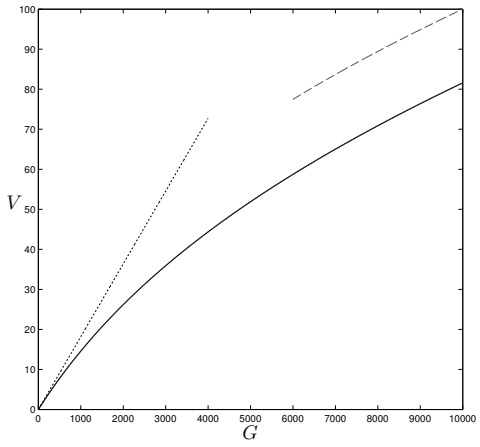

(c)

Figure 3.2: Numerical results (solid lines) for small values of parameter k in V,G variables. Shown are results for (a) $n = 1/2$ with step-sizes $\Delta G = 0.001$ and $k = 0.0005$, (b) $n = 2$ with step-sizes $\Delta G = 0.01$ and $k = 0.005$ and (c) $n = 10$ with step-sizes $\Delta G = 0.1$ and $k = 0.05$. Very good agreement between grid-sizes can be seen in the figures. Also shown are the asymptotic solutions for $G \ll 1$ (dotted) given by equation (3.55) and $G \to \infty$ (dashed) given by equation (3.65). From equation 3.47 it can be seen that n cannot be scaled out, by the way.

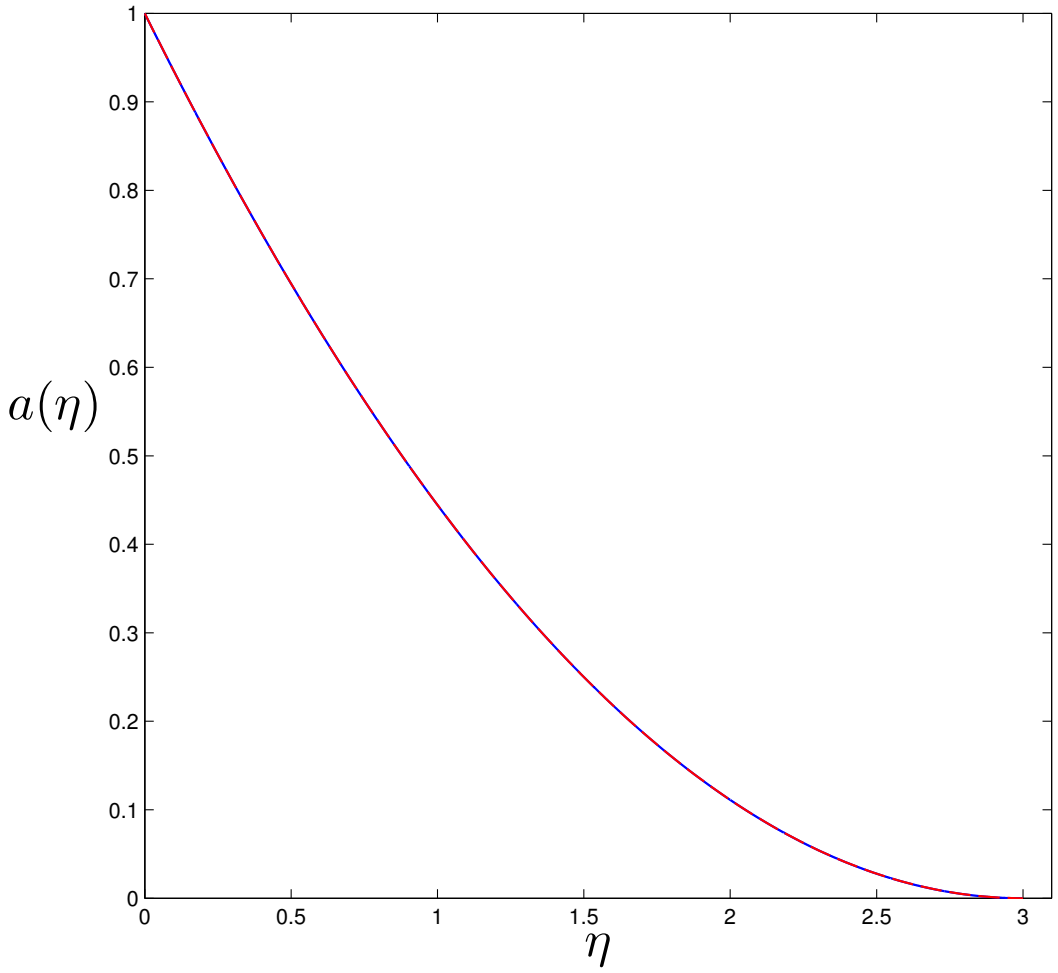

Figure 3.3: Numerical results (solid lines) for $k = 0.0001$ with $n = 1$ showing a against η. This is compared against the $k = 0$ analytical solution 2.56) (dashed) found in the previous chapter.

3.3.2 Fast-response vessels (large n)

In order to define what we mean by a fast-response vessel we return to the non-dimensional pressure-area relation as given by equation (2.43). Removing β by a suitable scaling as in section 3.1, differentiation with respect to area a and rearranging we have

$$\int \frac{\mathrm{d}p}{p} = \int \frac{n\mathrm{d}a}{a}, \tag{3.69}$$

from which we can see that for large values of n a relative change in a produces a larger relative change in pressure p. We thus refer to this $n \gg 1$ regime as fast-response. Likewise for small values of n, we refer to such vessels as slow-response.

For large values of the parameter n, equations (3.27) to (3.29) suggest the expansion

$$\tilde{C} = nc_0(z) + \dots \quad , \tag{3.70}$$

$$\tilde{U} = u_0(z) + \dots \quad , \tag{3.71}$$

$$\tilde{D} = nd_0(z) + \dots \quad , \tag{3.72}$$

with order one variables c_0,u_0,d_0,k and z. Substitution back into (3.27) to (3.29) then gives the leading order system

$$u_0' = 0, \tag{3.73}$$

$$c_0' = -c_0\left(1 + \frac{u_0 \exp(z)}{d_0}\right), \tag{3.74}$$

$$d_0 = -c_0 \exp z, \tag{3.75}$$

with initial conditions

$$u_0(z_{-\infty}) = 1, \tag{3.76}$$

$$c_0(z_{-\infty}) = 1. \tag{3.77}$$

Integrating (3.73) and (3.74), applying initial conditions (3.76) and (3.77) and scaling back to $\tilde{C}$ and $\tilde{U}$ variables gives the remarkably simple solution

$$\tilde{C} = n + \dots \quad , \tag{3.78}$$

$$\tilde{U} = 1 + \dots \quad , \tag{3.79}$$

for large n values. Rescaling back to the original variables, this gives

$$a = \left\{ \eta_0^2 \left(\frac{kn}{2} \right)^2 \left(1 - \frac{\eta}{\eta_0} \right) \right\}^{1/n} , \tag{3.80}$$

$$u = \eta_0 \left(\frac{kn}{2} \right) , \tag{3.81}$$

from which we may find

$$\eta_0 = \frac{2}{kn} \tag{3.82}$$

This result may be seen in the numerical results.

3.3.3 Slow-response vessels (small n)

Here we find required scalings are

$$\exp(z) \sim n^2, \tag{3.83}$$

$$\tilde{C} \sim n^2, \tag{3.84}$$

$$\tilde{U} = 1 + O(\exp(z)), \tag{3.85}$$

$$\tilde{D} \sim n^4, \tag{3.86}$$

so that $z = 2\log(n) + \bar{z}$. This leads into section 3.5 below

3.4 Large-n properties in any two-dimensional vessel.

The aim here is to investigate whether the large-n response of previous sections generalises or not and can apply globally, i.e. throughout an entire vessel. This

is done first of all in the two-dimensional setting. We begin by considering a two-dimensional vessel with compliant walls. The system is taken to be symmetric about the vessel centre-line for convenience and so we need only consider the upper half of the vessel. We again let x denote the horizontal distance along the tube (as in figure 2.1) and y the vertical, with t representing time. The unknown position of the upper wall is given by $y = A(x,t)$ and the centre-line by $y = 0$. We consider the scaled pressure P within the vessel to be dependent on x and t only.

The governing equations for this system are simply the usual conservation of mass and momentum coupled with kinematic boundary conditions at the walls and a relationship between the pressure and cross-sectional area, as defined previously in chapter 2. We note here that A, in this case, represents something like a radius rather than the previous cross-sectional area. As such we should really have a power $2n$ as well as a factor π in the pressure function. In any case, it is possible to scale so that we consider only n again and may absorb the factor π into β. The non-dimensional equations of the two-dimensional flow-structure interaction are as follows,

$$u_x + v_y = 0, \tag{3.87}$$

$$u_t + uu_x + vu_y = -p_x, \tag{3.88}$$

$$v = A_t + uA_x \text{ on } y = A(x,t), \tag{3.89}$$

$$v = 0 \text{ on } y = 0, \tag{3.90}$$

$$p = p_0 + \beta(A^n - A_0^n). \tag{3.91}$$

Here β is again the measure of the distensibility of the tube, with a higher value corresponding to a less distensible tube. For now it is taken to be constant. Also p_0 and A_0 are the values of the resting pressure and cross-sectional area respectively.

By differentiating equation (3.88) with respect to y and using equation (3.87)

to replace v_y, we obtain the equation $\frac{\mathrm{D}\lambda}{\mathrm{D}t} = 0$, where $\lambda = \frac{\partial u}{\partial y}$ is the shear stress and $\frac{\mathrm{D}}{\mathrm{D}t}$ denotes the material derivative following a fluid particle. So shear stress is conserved. We now integrate and set the constant of integration to zero, taking the fluid to be initially shear-free, which leaves u independent of y, as assumed earlier.

We now make a substitution $E = A^n$ for convenience. Equations (3.89) and (3.91) become

$$vE^{\frac{n-1}{n}} = \frac{1}{n}E_t + \frac{1}{n}uE_x \quad \text{on} \quad y = E^{\frac{1}{n}}(x,t), \tag{3.92}$$

$$p = C_0 + \beta E. \tag{3.93}$$

where $C_0 = p_0 - \beta A_0^n$ is a constant.

With n taken to be a parameter which is very large we set y and E to be $O(1)$ as we do not expect the cross-sectional area to vary much over the length-scale of the front, given our earlier findings. We scale $x = lX$, $t = \tau T$, $u = U\bar{u}$, $p = \gamma\bar{p}$ and $v = \alpha\bar{v}$ with X, T, $\bar{u}$, $\bar{p}$ and $\bar{v}$ being $O(1)$ and the constant factors l,τ,U,γ,α to be determined. The governing equations are now

$$\frac{U}{l}\bar{u}_X + \alpha\bar{v}_y = 0, \tag{3.94}$$

$$\frac{U}{\tau}\bar{u}_T + \frac{U^2}{l}\bar{u}\bar{u}_X = -\frac{\gamma}{l}\bar{p}_X, \tag{3.95}$$

$$\alpha\bar{v}E^{\frac{n-1}{n}} = \frac{1}{n\tau}E_T + \frac{U}{nl}\bar{u}E_X \quad \text{on} \quad y = E^{\frac{1}{n}}(x,t), \tag{3.96}$$

$$\bar{v} = 0 \quad \text{on} \quad y = 0, \tag{3.97}$$

$$\gamma\bar{p} = C_0 + \beta E. \tag{3.98}$$

From equation (3.98) we deduce that $\gamma = 1$. Balancing the inertia and pressure terms of equation (3.95) then leads to $\frac{U}{\tau} = \frac{1}{l}$. Finally, considering equation (3.96) gives us $\alpha = \frac{1}{n\tau} = \frac{U}{nl}$. That leaves us with four equations for five unknowns. We obtain $\gamma = 1$, $L = \tau$, $\alpha = \frac{1}{n\tau}$ and $U = 1$. We now take $\tau = 1$ in order to cover the main timescale. Writing again x and t rather than X, T

to represent axial distance and time, we take the following large-n expansions

$$\begin{aligned} u &= u_0(x,t) + \delta u_1(x,t) + \cdots, \\ v &= n^{-1}\left(\bar{v}_0(x,y,t) + \epsilon\bar{v}_1(x,y,t) + \cdots\right), \\ E &= E_0(x,t) + \delta E_1(x,t) + \cdots, \\ p &= p_0(x,t) + \gamma_1 p_1(x,t) + \cdots, \end{aligned}$$

which we now substitute into equations (3.87), (3.88), (3.90), (3.92), (3.93). Thus we have

$$u_{0x} + \delta u_{1x} + \cdots + n^{-1}\bar{v}_{0y} + \cdots = 0, \tag{3.99}$$

$$\begin{aligned} u_{0t} + \delta u_{1t} + \cdots \\ + \left(u_0 + \delta u_1 + \cdots\right)\left(u_{0x} + \delta u_{1x} + \cdots\right) = -P_{0x} - \gamma_1 P_{1x} + \cdots, \end{aligned} \tag{3.100}$$

$$n^{-1}\bar{v}_0 + \cdots = 0 \quad \text{on} \quad y = 0, \tag{3.101}$$

$$\begin{aligned} n^{-1}\left(\bar{v}_0 + n^{-1}\bar{v}_1\right)\left(E_0 + n^{-1}E_1\right) + \cdots = n^{-1}\left(E_{0t} + u_0 E_{0x} + \cdots\right) \\ \text{on} \quad y = 1, \end{aligned} \tag{3.102}$$

$$P_0 + \gamma_1 P_1 + \cdots = C_0 + \beta\left(E_0 + \delta E_1 + \cdots\right). \tag{3.103}$$

At $O(1)$ in equation (3.99) there is simply the balance $u_{0x} = 0$, giving

$$u_0 = u_0(t) \tag{3.104}$$

as the leading order velocity, dependent on time alone. At leading order, equation (3.100) now has $u_{0t} = -\beta E_{0x}$ which integrates to give

$$E_0 = -\frac{1}{\beta}u_{0t}x + f(t), \tag{3.105}$$

a function linear in x. So at $x = 0$ there is $E_0 = f(t)$. If we take the tube opening as a known function of time then we may take

$$E_0(0,t) = f(t) \tag{3.106}$$

along with

$$E_1(0,t) = E_2(0,t) = \ldots = 0 \tag{3.107}$$

as boundary conditions. Examination of equation (3.99) reveals that $\delta = n^{-1}$ in order that the next two terms balance. We know also, from previous work (section 3.1), that at the position of the front $x = x_f(t)$ we must have

$$u(x_f,t) = \dot{x}_f, \tag{3.108}$$

$$E(x_f,t) = 0, \tag{3.109}$$

where dots denote differentiation with respect to t. We therefore take

$$x_f = x_f^0 + n^{-1}x_f^1 + O(n^{-2}) \tag{3.110}$$

which upon substitution into the front conditions (3.108), (3.109) and expanding in powers of n yields

$$u_0(x_f^0,t) = \dot{x}_f^0, \tag{3.111}$$

$$u_1(x_f^0,t) = \dot{x}_f^1, \tag{3.112}$$

$$E_0(x_f^0,t) = 0, \tag{3.113}$$

$$E_1(x_f^0,t) = -x_f^1\frac{\partial E_0}{\partial x}(x_f^0,t), \tag{3.114}$$

up to $O(n^{-1})$. As u_0 is a function of time alone, this implies that $u_0(t) = \dot{x}_f^0$. It then follows from (3.105) and (3.113) that

$$f(t) = \frac{1}{\beta}\ddot{x}_f^0 x_f^0, \tag{3.115}$$

which gives an equation for x_f^0 since $f(t)$ is known from (3.106). We have in fact

$$E_0(x,t) = \frac{1}{\beta}\ddot{x}_f^0\left(x_f^0 - x\right) \tag{3.116}$$

globally with the front position x_f^0 given by

$$\ddot{x}_f^0 x_f^0 = \beta E_0(0,t) = \beta E(0,t). \tag{3.117}$$

This simple-looking nonlinear equation controls the evolution of the front position x_f^0 for a given opening development $E(0,t)$.

Further, integrating equation (3.99) at $O(n^{-1})$ with respect to y gives us

$$\bar{v}_0 = -u_{1x} y, \tag{3.118}$$

where the constant of integration is taken to be zero in order to satisfy the condition (3.102). Equation (3.102) at $O(n^{-1})$ is therefore effectively an equation for the correction velocity u_1,

$$u_{1x} E_0 = -E_{0t} - u_0 E_{0x}. \tag{3.119}$$

Rewriting E_0 and u_0 in terms of x_f, $\dot{x}_f$ and $\ddot{x}_f$, integrating and applying (3.112) we obtain

$$u_1(x,t) = \frac{\dddot{x}_f^0}{\ddot{x}_f^0}\left(x_f^0 - x\right) + \dot{x}_f^1. \tag{3.120}$$

We then find from (3.118)

$$\bar{v}_0 = \frac{\dddot{x}_f^0}{\ddot{x}_f^0} y. \tag{3.121}$$

We now find E_1 from the $O(n^{-1})$ terms of equation (3.100). There we have, after substituting for P_1 by use of equation (3.103), $u_{1t} + u_0 u_{1x} = -\beta E_{1x}$. We then need to solve the following equation for E_1,

$$\ddot{x}_f^1 + \left(x_f^0 - x\right)\left(\frac{\ddddot{x}_f^0}{\ddot{x}_f^0} - \left(\frac{\dddot{x}_f^0}{\ddot{x}_f^0}\right)^2\right) = -\beta E_{1x}.$$

Integrating and applying the condition at the front, E_1 is thus given by

$$E_1 = \frac{1}{\beta}\left\{ x_f^1 \ddot{x}_f^0 + \left(x_f^0 - x\right)\ddot{x}_f^1 + \frac{\left(x_f^0 - x\right)^2}{2}\left(\frac{\ddddot{x}_f^0}{\ddot{x}_f^0} - \left(\frac{\dddot{x}_f^0}{\ddot{x}_f^0}\right)^2\right)\right\}.$$

Applying the condition that $E_1(0,t) = 0$ we obtain an equation for x_f^1, the correction to the front-position prediction, namely

$$x_f^1 \ddot{x}_f^0 + x_f^0 \ddot{x}_f^1 = -\frac{\left(x_f^0\right)^2}{2}\left(\frac{\dddot{x}_f^0}{\ddot{x}_f^0} - \left(\frac{\dddot{x}_f^0}{\ddot{x}_f^0}\right)^2\right) \tag{3.122}$$

After using equation (3.103) to find P_0 and P_1 we have now determined the system explicitly up to $O(n^{-1})$, giving the pattern

$$u = \dot{x}_f^0 + n^{-1}\left(\dot{x}_f^1 + \frac{\dddot{x}_f^0}{\ddot{x}_f^0}\left(x_f^0 - x\right)\right) + \cdots, \tag{3.123}$$

$$v = n^{-1}\left(\frac{\dddot{x}_f^0}{\ddot{x}_f^0} y\right) + \cdots, \tag{3.124}$$

$$\begin{aligned} \beta E = {} & \ddot{x}_f^0\left(x_f^0 - x\right) + n^{-1}\left\{x_f^1 \ddot{x}_f^0 + \left(x_f^0 - x\right)\ddot{x}_f^1\right\} + \\ & n^{-1}\left\{\frac{\left(x_f^0 - x\right)^2}{2}\left(\frac{\ddddot{x}_f^0}{\ddot{x}_f^0} - \left(\frac{\dddot{x}_f^0}{\ddot{x}_f^0}\right)^2\right)\right\} + \cdots, \end{aligned} \tag{3.125}$$

$$\begin{aligned} P = {} & C_0 + \ddot{x}_f^0\left(x_f^0 - x\right) + n^{-1}\left\{x_f^1 \ddot{x}_f^0 + \left(x_f^0 - x\right)\ddot{x}_f^1\right\} + \\ & n^{-1}\left\{\frac{\left(x_f^0 - x\right)^2}{2}\left(\frac{\ddddot{x}_f^0}{\ddot{x}_f^0} - \left(\frac{\dddot{x}_f^0}{\ddot{x}_f^0}\right)^2\right)\right\} + \cdots. \end{aligned} \tag{3.126}$$

We may ask under which conditions do the approximations $u_x = 0$, $u_t = -p_x$ obtained from continuity and momentum apply for any pressure-area relation. We see that in such a case the axial velocity is given simply as a function of time, having no spatial dependence at all. Then momentum gives $p = xq_1(t) + q_2(t)$, a function of axial position and time, which varies linearly with position.

3.4.1 Opening the gap with a general power law in time.

An exact solution to the large-n two-dimensional problem (3.123) to (3.126) can be derived if the vessel opens with time dependence on the order t^k, say $E(0,t) = Bt^k$ for B a constant and the general power $k \neq 0$. Equation (3.117)

then becomes

$$\ddot{x}_f^0 x_f^0 = Bt^k, \tag{3.127}$$

with solution given by

$$x_f^0 = \sqrt{\frac{4B}{k\,(k+2)}}\; t^{\frac{k}{2}+1}. \tag{3.128}$$

We may then solve (3.122) for x_f^1 which has

$$t^2\ddot{x}_f^1 + \frac{k(k+2)}{4}x_f^1 = \frac{k-2}{4}\sqrt{\frac{4B}{k(k+2)}}\; t^{\frac{k}{2}+1} \tag{3.129}$$

an Euler-Cauchy ordinary differential equation with general solution

$$\begin{aligned} x_f^1 = {} & D_1\,|t|^{1/2}\cos\left(\sqrt{\frac{k(k+2)-1}{4}}\log|t|\right) + \\ & + D_2\,|t|^{1/2}\sin\left(\sqrt{\frac{k(k+2)-1}{4}}\log|t|\right) + \\ & + \frac{k-2}{2k(k+2)}\sqrt{\frac{4B}{k(k+2)}}\; t^{\frac{k}{2}+1}, \end{aligned} \tag{3.130}$$

where D_1 and D_2 are constants to be found. However, in order to ensure that there is no overtake by x_f^1 of x_f^0 so that the expansions remain valid, we require that $D_1 = D_2 = 0$. Substitution of x_f^0 and x_f^1 into equations (3.123) to (3.126) yields full solutions up to $O(n^{-1})$. Comparison between these analytical solutions and numerical results can be seen in a later chapter.

3.5 Slow-response vessels (small values of n)

3.5.1 Two-dimensional case

We begin with $n = O\,(1)$ as in chapter 2 and so have the two equations,

$$a_t + au_x + ua_x = 0, \tag{3.131}$$

$$u_t + uu_x = -p_x, \tag{3.132}$$

as in (2.41), (2.41); where a is the cross-sectional area of the tube, u is the velocity of fluid within the tube and x is the distance in the axial direction. Here pressure $p\left(x,t\right)=p_0+\beta\left(x\right)\left(a^n\left(x,t\right)-a_0^n\right)$. The coefficient β appearing in the pressure-area relation is a measure of distensibility, which for the time being is taken to be constant. We now take $a=E^{\frac{1}{n}}$ but with $n\ll 1$, $E=O(1)$ and $u=O(1)$ to obtain to leading order

$$E_t+uE_x=0, \tag{3.133}$$

$$u_t+uu_x=-\beta E_x, \tag{3.134}$$

where we have lost the dependence on the spatial gradient of u in equation (3.133) which now comes in at the next order. A quick consideration of characteristics here indicates that E is advected along the characteristic given by $\mathrm{d}x/\mathrm{d}t=u$, however u is forced by the spatial gradient of E. A numerical scheme can be seen in chapter 4.

Of more interest is an exact solution of the system (3.133) - (3.134). We seek an exact solution that is linear in x so that $E(x,t)=\bar{a}(t)x+B(t)$ say and $u(x,t)=C(t)x+D(t)$ with the functions $\bar{a}(t)$, $B(t)$, $C(t)$, $D(t)$ to be specified. Other forms of solution may exist, of course, involving other powers of x or summation of such terms. However, we examine the exact solutions here as they allow the front position and other properties to be identified closely. Substituting into equations (3.133) and (3.134) and equating powers of x gives the requirements

$$\bar{a}'+C\bar{a}=0, \tag{3.135}$$

$$B'+D\bar{a}=0, \tag{3.136}$$

$$C'+C^2=0, \tag{3.137}$$

$$D'+CD=-\beta\bar{a}. \tag{3.138}$$

Solving equations (3.137),(3.135),(3.138) and (3.136) in that order yields the

solutions

$$C = \frac{1}{t - t_0}, \tag{3.139}$$

$$\bar{a} = \frac{-c_1}{t - t_0}, \tag{3.140}$$

$$D = \frac{\beta c_1 (t - t_1)}{(t - t_0)}, \tag{3.141}$$

$$B = \beta c_1^2 \left(\ln |t - t_0| - \frac{t_0 - t_1}{t - t_0} \right) + \gamma. \tag{3.142}$$

where c_1, t_0, t_1 and γ are unknown constants.

We now use the conditions that $E = 0$ on $x = x_f$ (the front), E and u are known at $x = 0$ (the opening) and $x_f = 0$ at $t = 0$ (initial condition). The first condition gives us an equation for x_f,

$$x_f (t) = \frac{(t - t_0)\gamma}{c_1} + \beta c_1 \{ (t - t_0) \ln |t - t_0| - t_0 + t_1 \},$$

and applying the second condition determines γ. We notice that $u = \frac{dx_f}{dt}$ at $x = x_f$, as we would hope. We have therefore that

$$E (x, t) = -\frac{c_1 x}{t - t_0} + \beta c_1^2 \left(\ln \left| \frac{t - t_0}{t_0} \right| - \frac{t (t_0 - t_1)}{t_0 (t - t_0)} \right), \tag{3.143}$$

$$u (x, t) = \frac{x}{t - t_0} + \beta c_1 \frac{t - t_1}{t - t_0}, \tag{3.144}$$

$$x_f (t) = \beta c_1 \left((t - t_0) \ln \left| \frac{t - t_0}{t_0} \right| - \frac{t (t_0 - t_1)}{t_0} \right), \tag{3.145}$$

as the exact solution. In order to avoid singularities within equations (3.143) and (3.144) that would lead to unphysical behaviour we note the requirement that $t \neq t_0$, for $t \geqslant 0$. We must therefore have $t_0 < 0$. We also note that if $c_1 = 0$ then we have a trivial solution for E and x_f and so we take $c_1 \neq 0$. We also require that $\frac{dx_f}{dt} \geqslant 0$ so that the front remains a monotonically increasing function. Differentiating equation (3.145) and imposing this inequality we see that $t_1 \leqslant 0$ if $c_1 > 0$ and $t_1 \geqslant 0$ if $c_1 < 0$. We may set the constants to satisfy desired $E(0, t)$ and $u(0, t)$, i.e. we satisfy desired velocity and cross-sectional area profiles at the opening.

These solutions have similarities to previous ones including numerical solutions, but they also provide exact test cases, see comparisons in the next chapter. In addition we have also found solutions holding for general nonzero n.

3.6 Summary of chapter

A most useful approach to solving the mathematical system of current concern, for general cases and/or over a wide range of settings, has been found to be associated with the properties holding for fast and slow responses. The advantage gained is both analytical and computational. The approach has been explored so far for several aspects. Further aspects are to be addressed later.

It appears, in general, that for healthy individuals we might expect an almost linear relationship between cross-sectional area and pressure [53] with larger values of n being found in individuals exhibiting pathologies such as bladder outlet obstruction [36], [78]. The large-n solutions are therefore of great interest. With the use of voiding cystourethrogram (contrast agent x-ray videos of the urinary system) it is possible to make estimates of the front position and velocities and so it should, in principal, be possible to make comparisons to the results in this chapter.

Chapter 4

Numerical studies, introduction of jumps and tortuosity

4.1 Finite-difference scheme

We now turn to a numerical treatment of the partial differential system (2.41)-(2.43) where we introduce $E(x,t) = \beta a(x,t)^n$ in a similar fashion to section 3.5. Here we have assumed β to be constant and so obtain the system

$$E_t + uE_x + nEu_x = 0, \tag{4.1}$$

$$u_t + uu_x + E_x = 0, \tag{4.2}$$

for $E(x,t)$, $u(x,t)$, with initial conditions given at $t = 0$, while entrance and front conditions are prescribed at $x = 0$, $x = x_f$ (unknown) respectively. We assume throughout that $u(x,t)$ remains positive. We note that the term nEu_x in equation (4.1) may require some caution when dealing with large values of n but otherwise a finite difference scheme should suffice.

A simple finite-difference scheme is applied using first-order backward-difference approximations. Here we approximate the solution numerically at a node given

by $(i\delta x, t_0 + j\delta t)$ for $i, j = 0, 1, 2, \ldots$ with

$$u(i\delta x, t_0 + j\delta t) = u(x_i, t_j) = u_{i,j}, \tag{4.3}$$

$$E(i\delta x, t_0 + j\delta t) = E(x_i, t_j) = E_{i,j}, \tag{4.4}$$

where t_0 is the initial time for which the solution is known and δx and δt are the constant spatial and temporal steps respectively. The scheme is developed as follows. Taking equation (4.2), first-order backward-differences are applied to the derivatives and then rearranged to form an equation for u at the present spatial and time-step in terms of u, E at the previous spatial and time-step,

$$u_{i,j}\left(\frac{1}{\delta t} + \frac{\bar{u}}{\delta x}\right) = \frac{-E_{i,j}}{\delta x} + \frac{E_{i-1,j}}{\delta x} + \frac{u_{i,j-1}}{\delta t} + \frac{\bar{u}u_{i-1,j}}{\delta x}, \tag{4.5}$$

The same method is then applied to equation (4.1) in order to give

$$E_{i,j}\left(\frac{1}{\delta t} + \frac{\bar{u}}{\delta x}\right) = \frac{E_{i,j-1}}{\delta t} + \frac{\bar{u}E_{i-1,j}}{\delta x} - \frac{n\bar{E}}{\delta x}\left(u_{i,j} - u_{i-1,j}\right), \tag{4.6}$$

Here the values $\bar{u}$, $\bar{E}$ are known and in this case are set as the values of u and E at the previous time-step so that

$$\bar{u} = u_{i,j-1},$$
$$\bar{E} = E_{i,j-1};$$

however it should be noted that it is possible to use an iterative technique in order to give approximate values at the current space and time-steps. Substituting (4.5) into (4.6) in order to remove $u_{i,j}$ and then rearranging we obtain an equation for $E_{i,j}$ in terms of known quantities at the previous space and time-steps,

$$\begin{aligned} E_{i,j}\left(\Lambda - \frac{n\bar{E}}{(\delta x)^2\Lambda}\right) = \frac{E_{i,j-1}}{\delta t} + E_{i-1,j}\left(\frac{\bar{u}}{\delta x} - \frac{n\bar{E}}{(\delta x)^2\Lambda}\right) \\ + \frac{n\bar{E}}{\delta x\Lambda}\left(\frac{u_{i-1,j} - u_{i,j-1}}{\delta t}\right), \end{aligned} \tag{4.7}$$

where $\Lambda = (1/\delta t + \bar{u}/\delta x)$ is known. The finite-difference equations are thus given by

$$E_{i,j} = \bar{A}_1 E_{i,j-1} + \bar{A}_2 E_{i-1,j} + \bar{A}_3 u_{i,j-1} + \bar{A}_4 u_{i-1,j}, \tag{4.8}$$

$$u_{i,j} = \bar{B}_0 E_{i,j} + \bar{B}_2 E_{i-1,j} + \bar{B}_3 u_{i,j-1} + \bar{B}_4 u_{i-1,j}, \tag{4.9}$$

where we solve equation (4.8) for $E_{i,j}$ followed by (4.9) for $u_{i,j}$ and the coefficients are given by

$$\bar{A}_1 = \frac{1}{\delta t\left(\Lambda - \frac{n\bar{E}}{(\delta x)^2\Lambda}\right)}, \qquad \bar{A}_2 = \frac{\left(\frac{\bar{u}}{\delta x} - \frac{n\bar{E}}{(\delta x)^2\Lambda}\right)}{\left(\Lambda - \frac{n\bar{E}}{(\delta x)^2\Lambda}\right)},$$

$$\bar{A}_3 = \frac{-n\bar{E}}{\delta x\Lambda\delta t\left(\Lambda - \frac{n\bar{E}}{(\delta x)^2\Lambda}\right)}, \qquad \bar{A}_4 = \frac{n\bar{E}}{\delta x\Lambda\delta t\left(\Lambda - \frac{n\bar{E}}{(\delta x)^2\Lambda}\right)},$$

$$\bar{B}_0 = \frac{-1}{\delta x\Lambda}, \qquad \bar{B}_2 = \frac{1}{\delta x\Lambda},$$

$$\bar{B}_3 = \frac{1}{\delta t\Lambda}, \qquad \bar{B}_4 = \frac{\bar{u}}{\delta x\Lambda}.$$

4.1.1 Front tracking

In order to track the front position, denoted by x_f as in sections 3.4 and 3.5, an interpolation technique is employed. This works by allowing the time step δt to vary at each temporal step so that the position of the front will coincide with a node. We begin by setting $\delta t^{(0)} = \delta x$ as the initial guess for the time step. Using (4.8) and (4.9) we then obtain an approximation to the solution at time-step $j+1$ given by $E^{(0)}_{i,j+1}$, $u^{(0)}_{i,j+1}$ for $i = 1, \ldots, I+1$. We then linearly extrapolate the solution for $E^0_{I+2,j+1}$ at a new spatial node $(I+2)$ using the values at the two previous spatial steps

$$E^{(0)}_{I+2,j+1} = 2E^{(0)}_{I+1,j+1} - E^{(0)}_{I,j+1}. \tag{4.10}$$

Following this we then rerun using the halved time step $\delta t^{(1)} = \delta t^{(0)}/2$. Again we extrapolate to obtain

$$E^{(1)}_{I+2,j+1} = 2E^{(1)}_{I+1,j+1} - E^{(1)}_{I,j+1}. \tag{4.11}$$

Having found these two values we then interpolate to find an improved value for the time-step which is given by

$$\delta t^{(2)} = \frac{E^{(0)}_{I+2,j+1}\delta t^{(1)} - E^{(1)}_{I+2,j+1}\delta t^{(0)}}{E^{(0)}_{I+2,j+1} - E^{(1)}_{I+2,j+1}}. \tag{4.12}$$

This new time-step value is then used to find values $E_{i,j+1}$, $u_{i,j+1}$ for $i = 1, \ldots, I+1$ with values at $i = I+2$ again found by extrapolation. It can be seen that at each time-step a new spatial node is added. This method may be extended to a full iterative technique by allowing $\delta t^{(0)} = \delta t^{(2)}$ and repeating the steps until a desired level of accuracy is achieved which would be useful when replacing the finite differences with a more accurate scheme. In our method, which uses only a linear scheme, we stop after finding $\delta t^{(2)}$.

An alternative method to the one above is to use the characteristics given by equation (2.32) along with the corresponding Riemann invariants (2.37) as a basis for a numerical method as in [71], [72].

Finally we may also consider piecewise constant values of β by implementing the jump conditions found in section 2.4. In any section of the vessel the method above will be unchanged, whereas at a point of change we would use the jump conditions (2.80) and (2.74) in order to find the correct a and u at the next node.

4.1.2 Numerical results

Numerical results are now shown using exact test cases found previously in sections 2.3.1 and 3.5. Other exact solutions may be possible, but these were chosen to test the numerical method developed above.

Order one values of n

We present a number of numerical results based on the parameter n being of order one. We take $\beta = 1$ throughout. Analytical results are given by equations (2.55), (2.56) where the constant $\dot{x}_f$ is chosen so that at the vessel opening, given by position $x = 0$, we maintain $a(0,t) = 1$. Results are calculated for $n = 1/2$, $n = 2$ and $n = 10$ with plots for $E(x,t)$ and $a(x,t)$ shown in figures 4.1 to 4.6. Front positions are shown in figure 4.7 for each of the cases with solid lines showing analytical solutions and the dashed lines showing the numerical front positions. The errors seen in figures 4.4 and 4.6 are a result of scaling from E back to a where powers of $n > 1$ result in amplifying small errors of order δx in the solutions for E.

Small n-values

Small-n solutions of the form given in section 3.5 were attempted for the case $n = 0.01$. These are shown in figures 4.8 to 4.10 which are plots of E, $a = E^{1/n}$ and x_f respectively. The E and a plots show various times from the initial conditions given by equations (3.143)-(3.145) at $t = 0.1$ where we have taken the constants to be $t_0 = -1$, $t_1 = -1$ and $c_1 = 1/\sqrt{\log 2}$ up to a finishing time of $t = 1$. Unlike the order one case above, $E(0,t)$ is now a known function of time.

Large n-values

In the case of large-n values we attempted solutions of the form given in section 3.4 with boundary and initial conditions given by the leading order terms. The opening function was taken to be $E(0,t) = t^2$ for the case $n = 100000$. Results are shown in figures 4.11 to 4.14 which are plots of E, $a = E^{1/n}$ and x_f respectively. The E and a plots show various times with initial conditions given by leading order terms of equations (3.123)-(3.126) at $t = 1$ with x_f^0 given

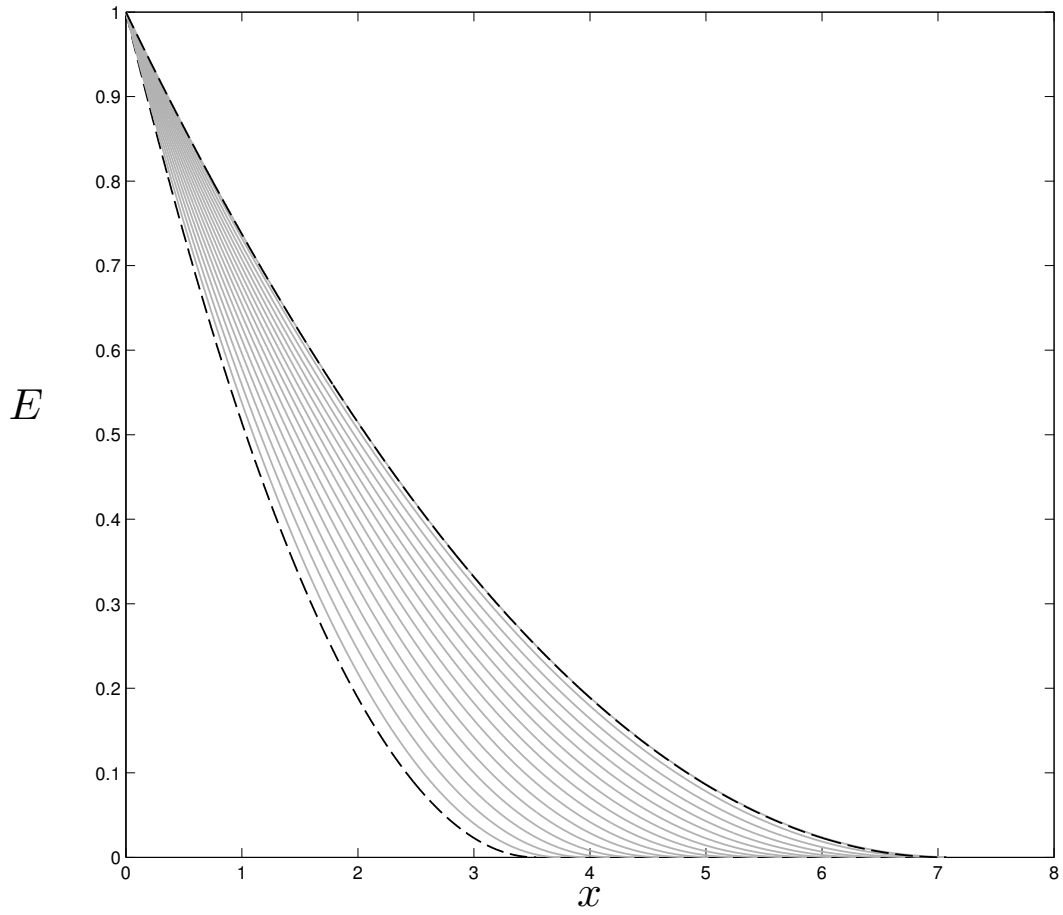

Figure 4.1: Numerical results (solid lines) for $E(x,t)$ with $n = 0.5$ and a spatial step size $\delta x = 0.0035$. The initial condition (at $t = 1$) and the analytical solution for the end time $t = 2$ are both shown as dashed lines. We can see a good agreement at $t = 2$ between the numerical and analytical solutions.

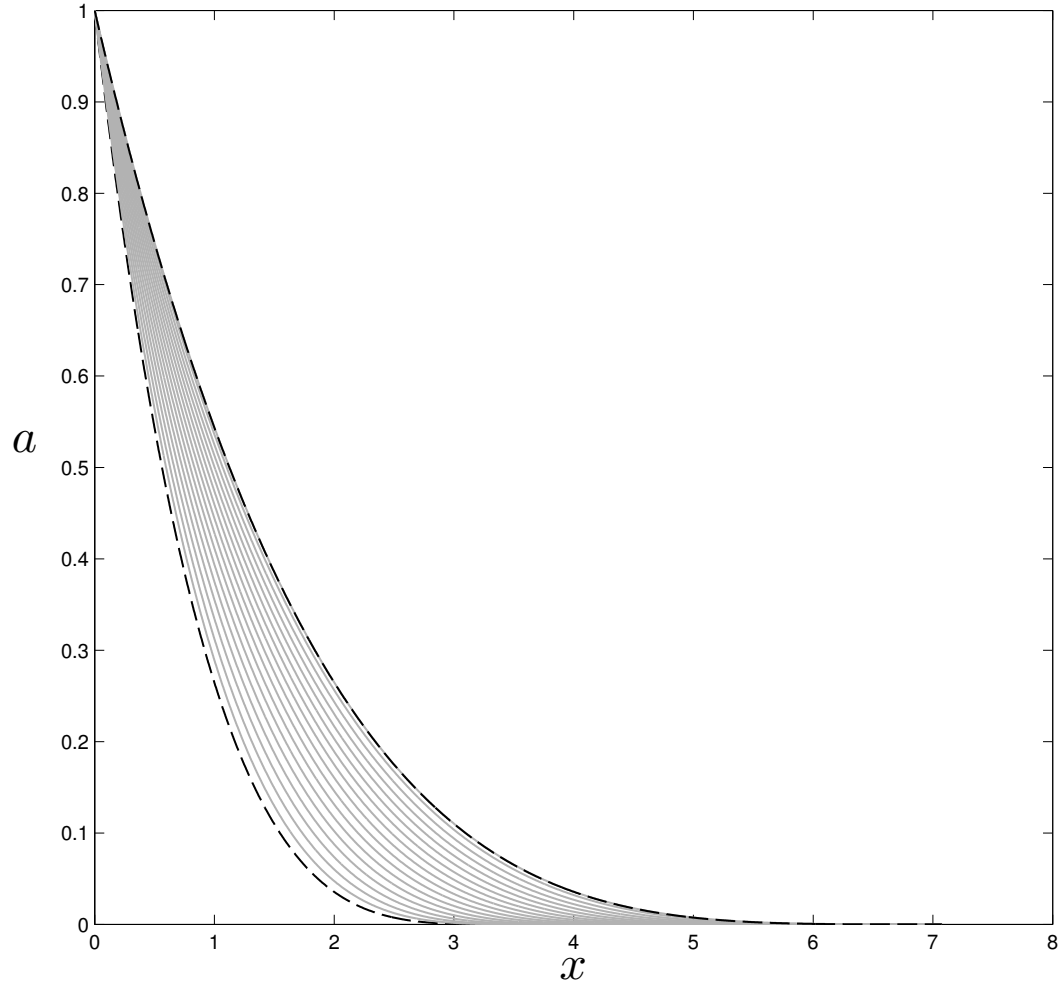

Figure 4.2: Numerical results (solid lines) for $a(x,t)$ with $n = 0.5$ and a spatial step size $\delta x = 0.0035$. The initial condition (at $t = 1$) and the analytical solution for the end time $t = 2$ are both shown as dashed lines. We can see a good agreement at $t = 2$ between the numerical and analytical solutions. Here a is recovered from the numerical E solution by $a(x,t) = E(x,t)^{1/n}$.

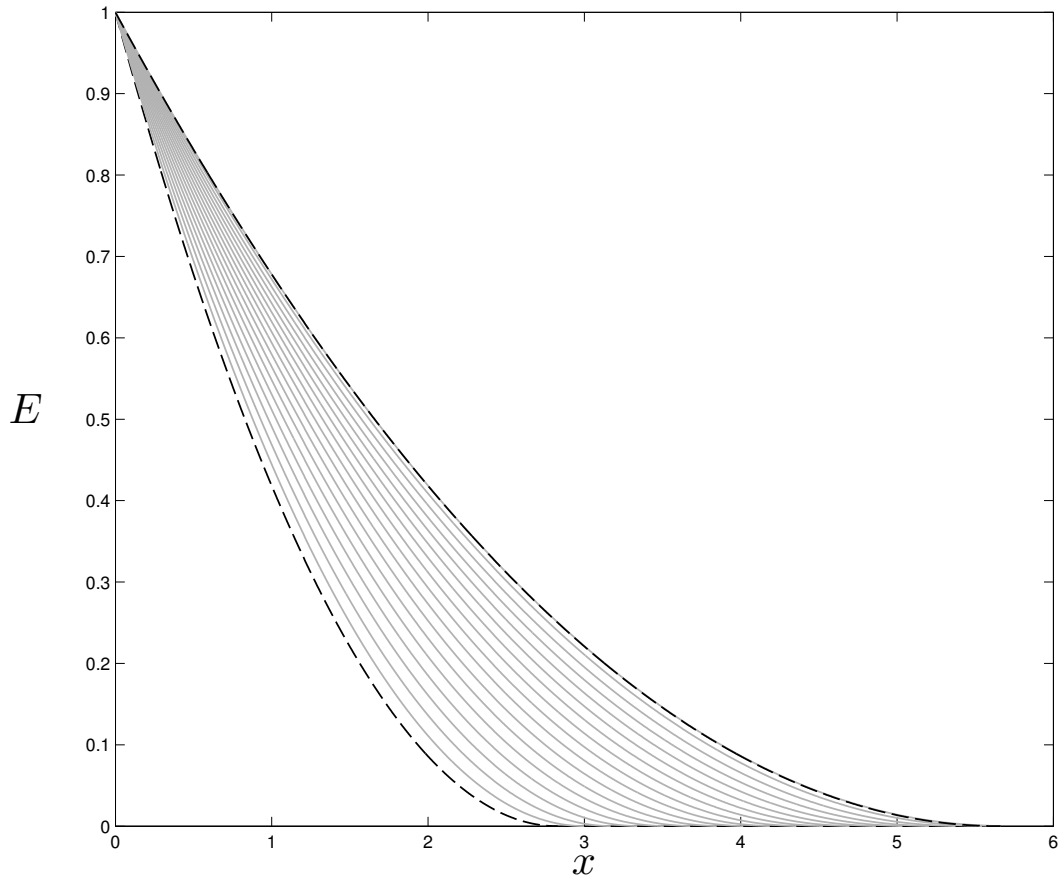

Figure 4.3: Numerical results (solid lines) for $E(x,t)$ with $n = 2$ and a spatial step size $\delta x = 0.0028$. The initial condition (at $t = 1$) and the analytical solution for the end time $t = 2$ are both shown as dashed lines. We can see a good agreement at $t = 2$ between the numerical and analytical solutions.

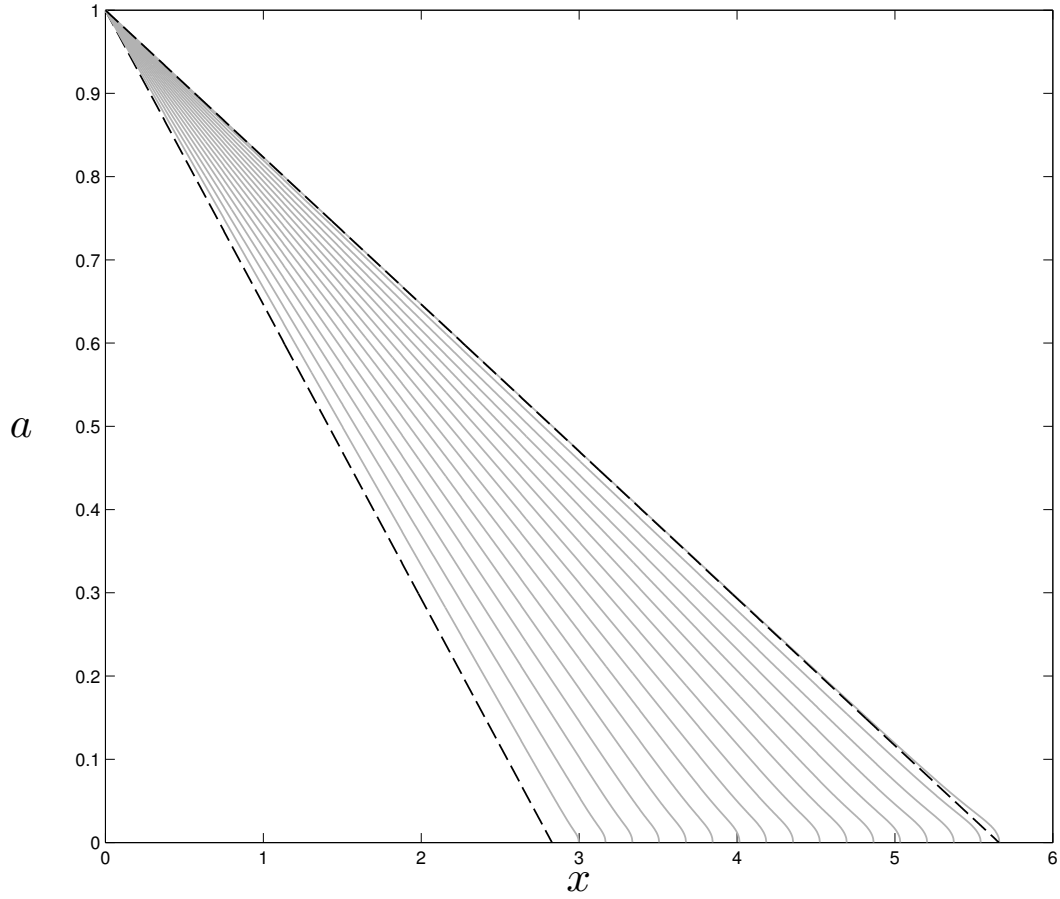

Figure 4.4: Numerical results (solid lines) for $a(x,t)$ with $n = 2$ and a spatial step size $\delta x = 0.0028$. The initial condition (at $t = 1$) and the analytical solution for the end time $t = 2$ are both shown as dashed lines. We can see a good agreement at $t = 2$ between the numerical and analytical solutions. Here a is recovered from the numerical E solution by $a(x,t) = E(x,t)^{1/n}$.

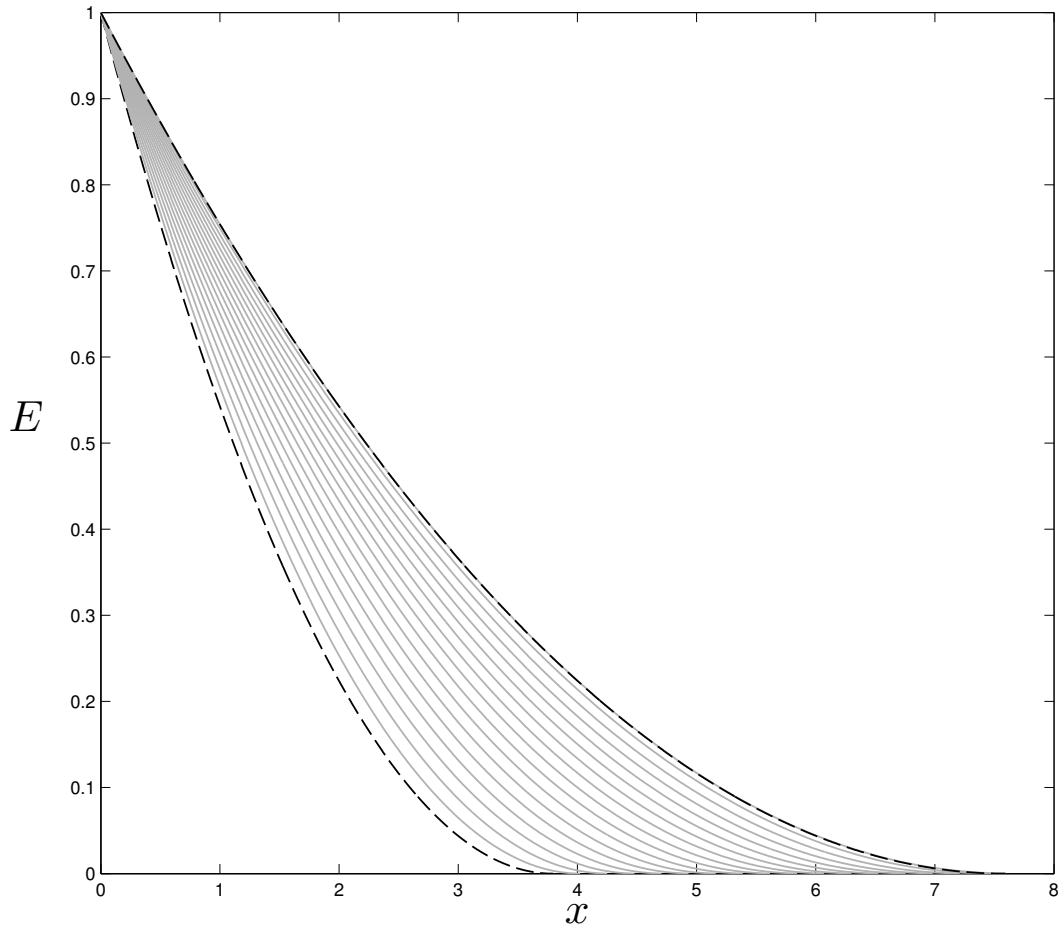

Figure 4.5: Numerical results (solid lines) for $E(x,t)$ with $n = 10$ and a spatial step size $\delta x = 0.0038$. The initial condition (at $t = 1$) and the analytical solution for the end time $t = 2$ are both shown as dashed lines. We can see a good agreement at $t = 2$ between the numerical and analytical solutions.

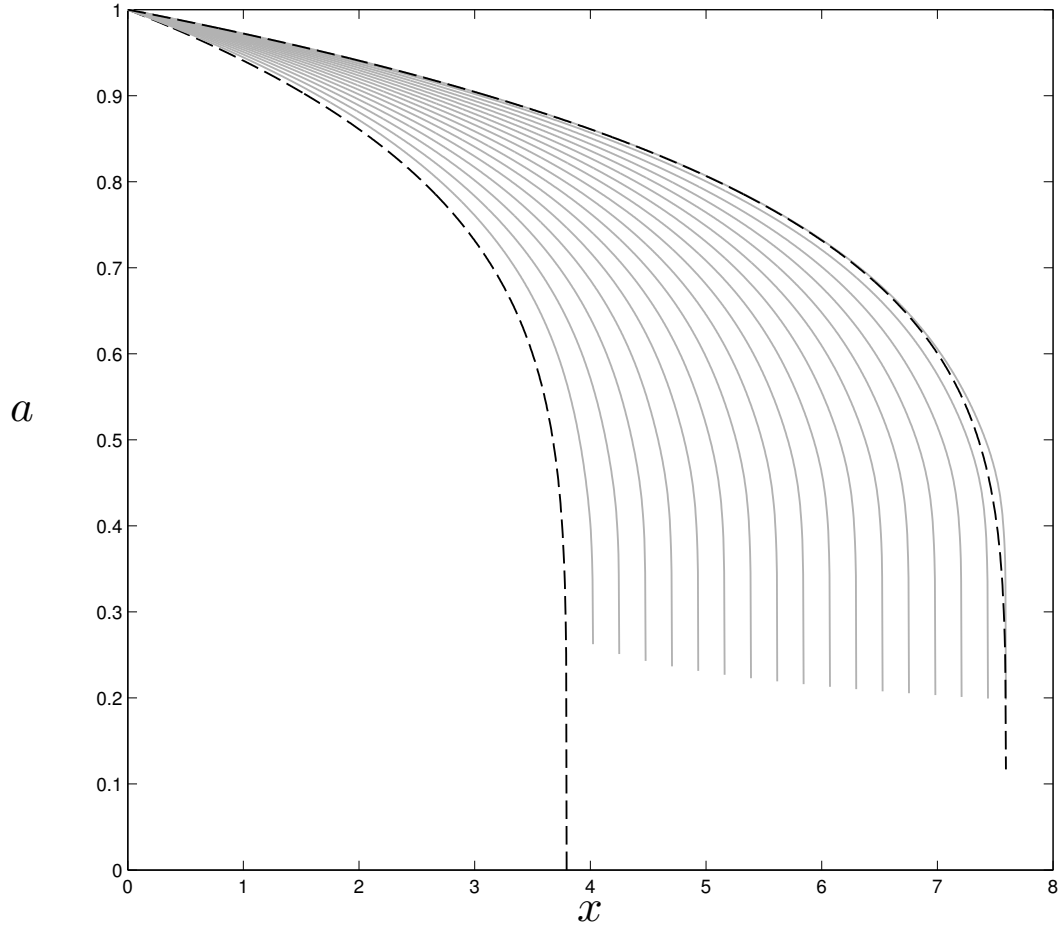

Figure 4.6: Numerical results (solid lines) for $a(x,t)$ with $n = 10$ and a spatial step size $\delta x = 0.0038$. The initial condition (at $t = 1$) and the analytical solution for the end time $t = 2$ are both shown as dashed lines. We can see a good agreement at $t = 2$ between the numerical and analytical solutions. Here a is recovered from the numerical E solution by $a(x,t) = E(x,t)^{1/n}$.

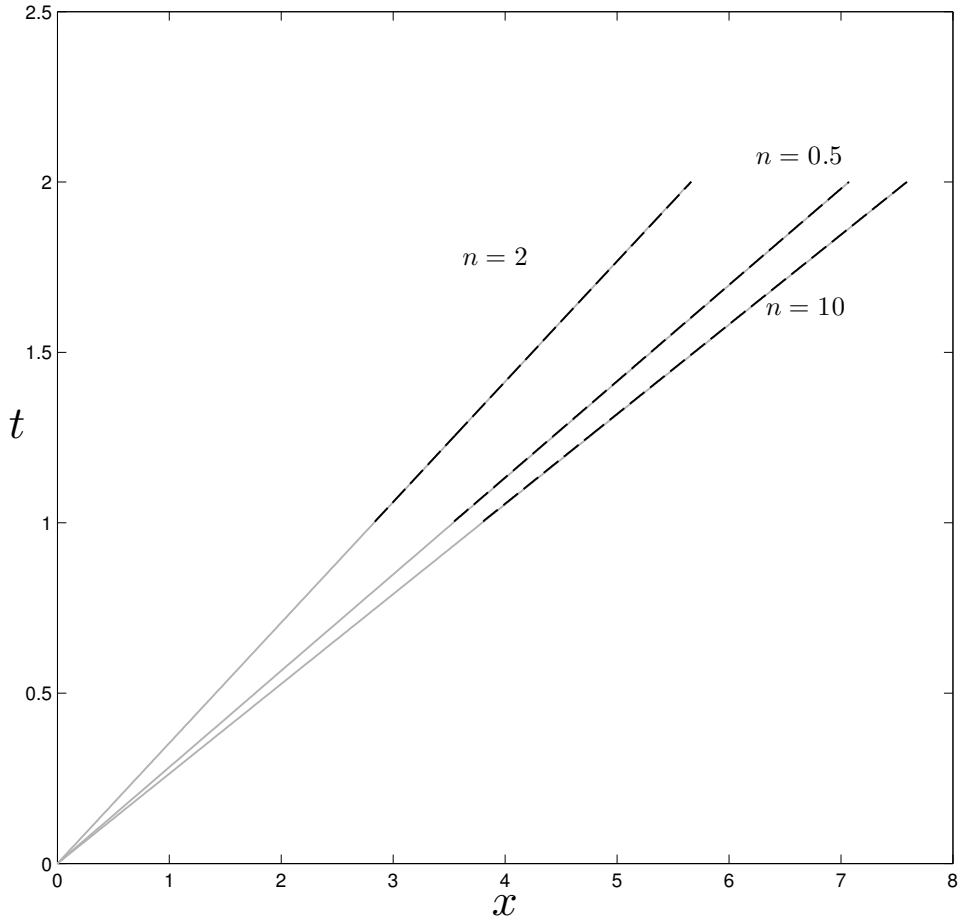

Figure 4.7: Numerical results (dashed lines) showing the front positions for each of the cases $n = 0.5, 2, 10$. Analytical solutions are shown as solid lines. We can see good agreement between numerical and analytical results.

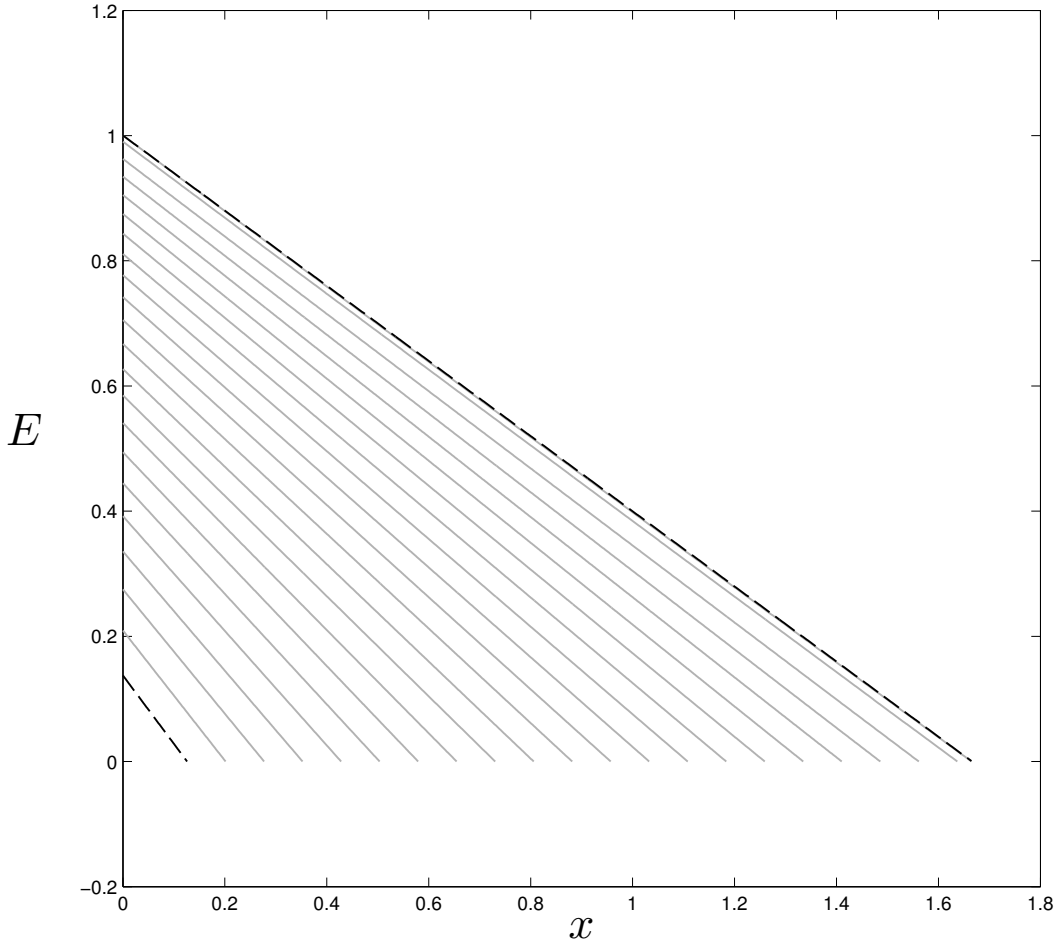

Figure 4.8: Numerical results (solid lines) for $E(x,t)$ with $n = 0.001$ and a spatial step size $\delta x = 0.0013$. The initial condition (at $t = 0.1$) and the analytical solution for the end time $t = 1$ are both shown as dashed lines. We can see a good agreement at $t = 1$ between the numerical and analytical solutions.

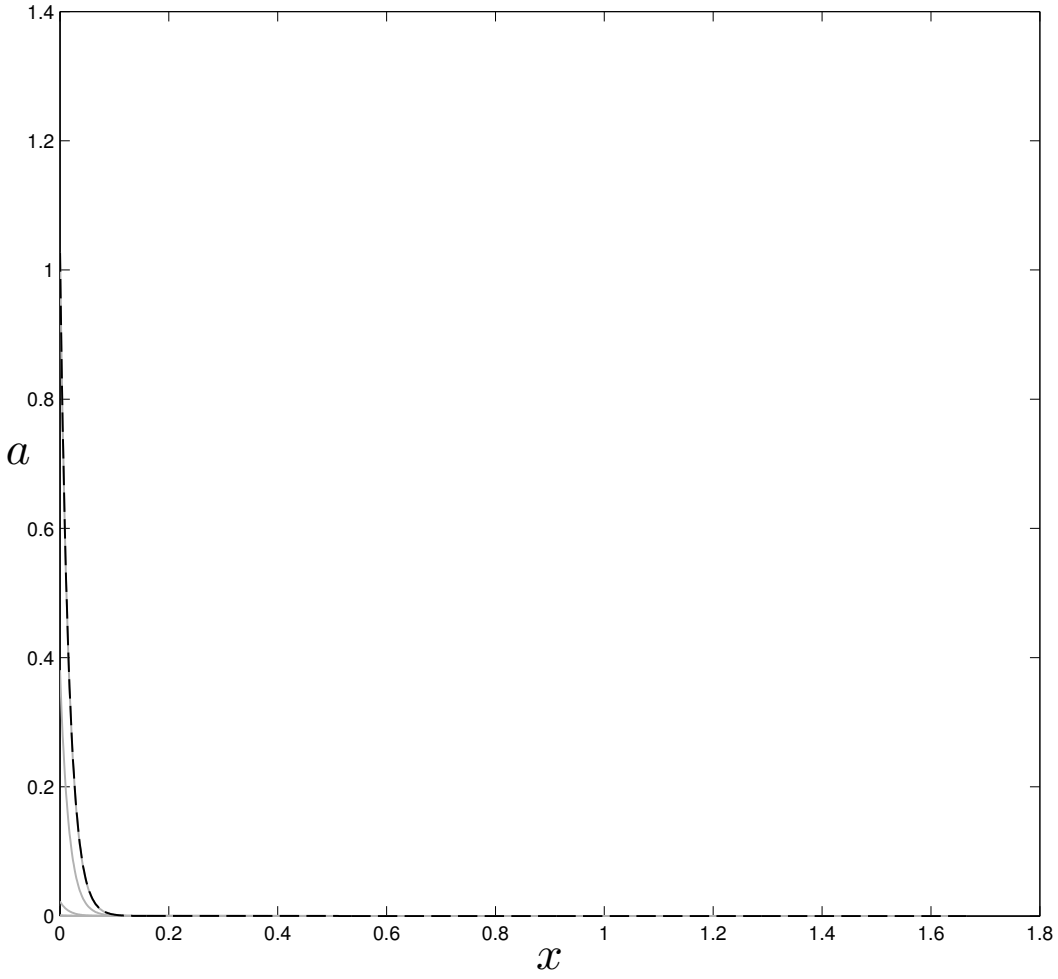

Figure 4.9: Numerical results (solid lines) for $a(x,t)$ with $n = 0.001$ and a spatial step size $\delta x = 0.0013$. The initial condition (at $t = 0.1$) and the analytical solution for the end time $t = 1$ are both shown as dashed lines. We can see a good agreement at $t = 1$ between the numerical and analytical solutions. Here a is recovered from the numerical E solution by $a(x,t) = E(x,t)^{1/n}$.

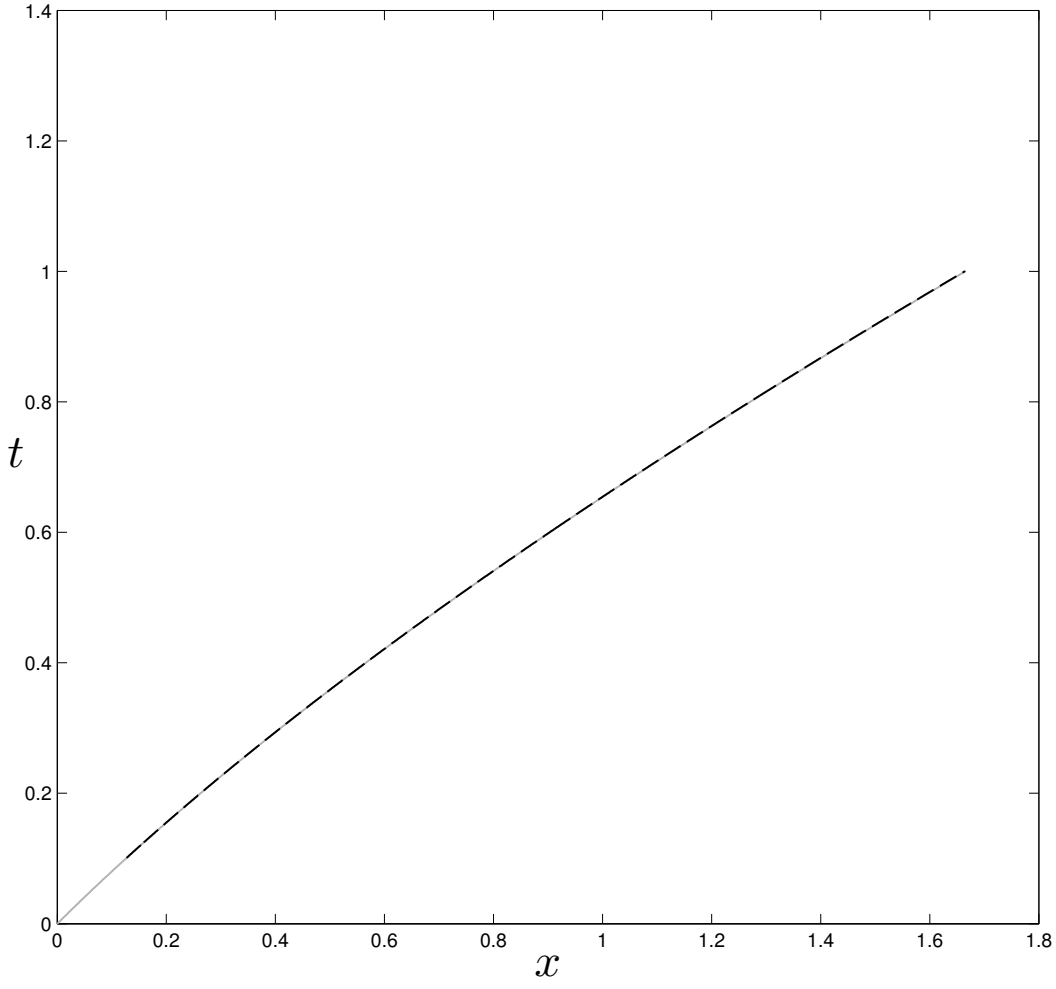

Figure 4.10: Numerical results (dashed lines) showing the front position for $n = 0.001$. We see good agreement between numerical and analytical (solid line) results. Note that unlike the results above, here x_f is not a linear function of time.

by equation (3.128) for $B = 1$ and $k = 2$. The results run up until $t = 2.5$. An important thing to note is that when scaling back to a from E small errors at the front tend to be blown up due to the large value of n, this combined with small negative values producing imaginary numbers means that it is difficult to reach zero in the (x, a) plots. Also connected with difficulties in taking n to be large, as we expected, was an increase in sensitivity to the step-size. This is evident in figure 4.14 where we see some backward movement of the front.

Grid-tests

Grid tests are shown in figures 4.15, 4.16 and 4.17. One for the n of order one case, one for n small and one for n large. Comparisons are made for different spatial step sizes which we see match well in all cases. The time-step is not shown as this may change between each time stepping as a result of the front tracking method.

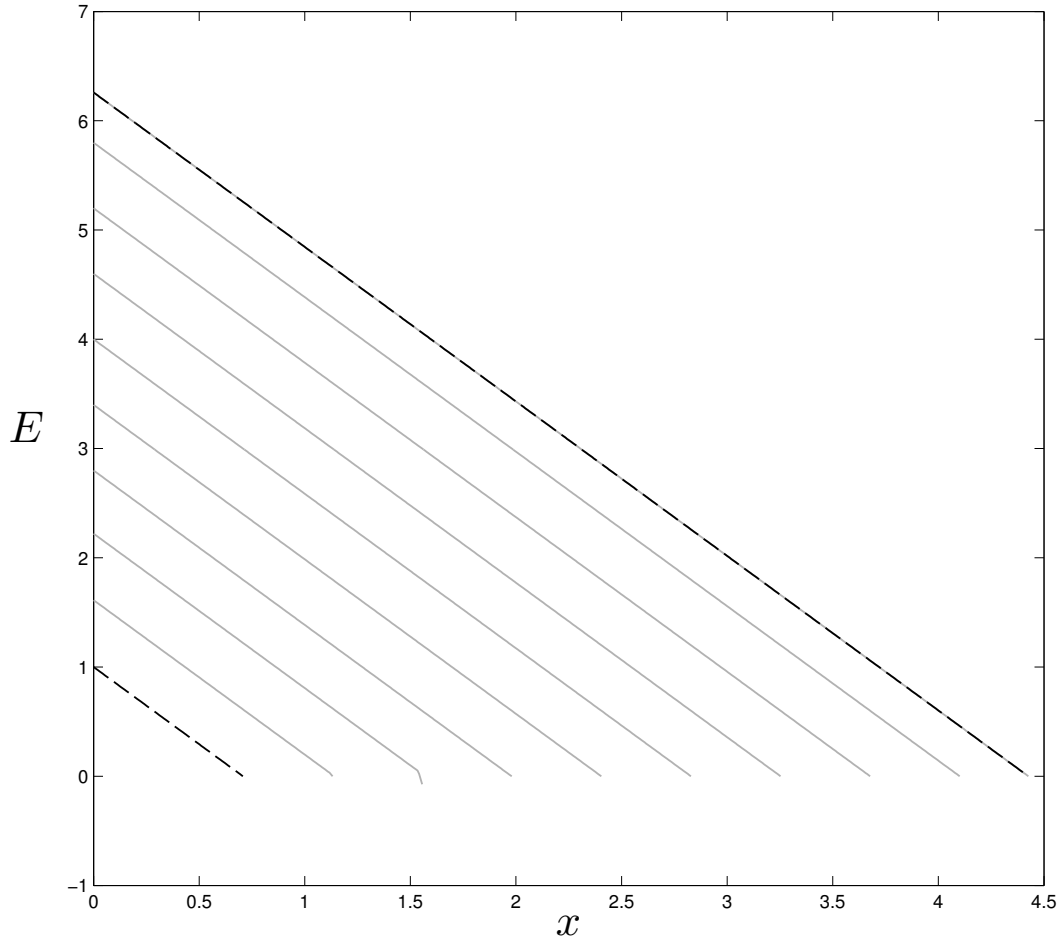

Figure 4.11: Numerical results (solid lines) for $E(x,t)$ with $n = 100000$ and a spatial step size $\delta x = 0.0071$. The initial condition (at $t = 1$) and the analytical solution for the end time $t = 2.5$ are both shown as dashed lines. We can see a good agreement at $t = 2.5$ between the numerical and analytical solutions.

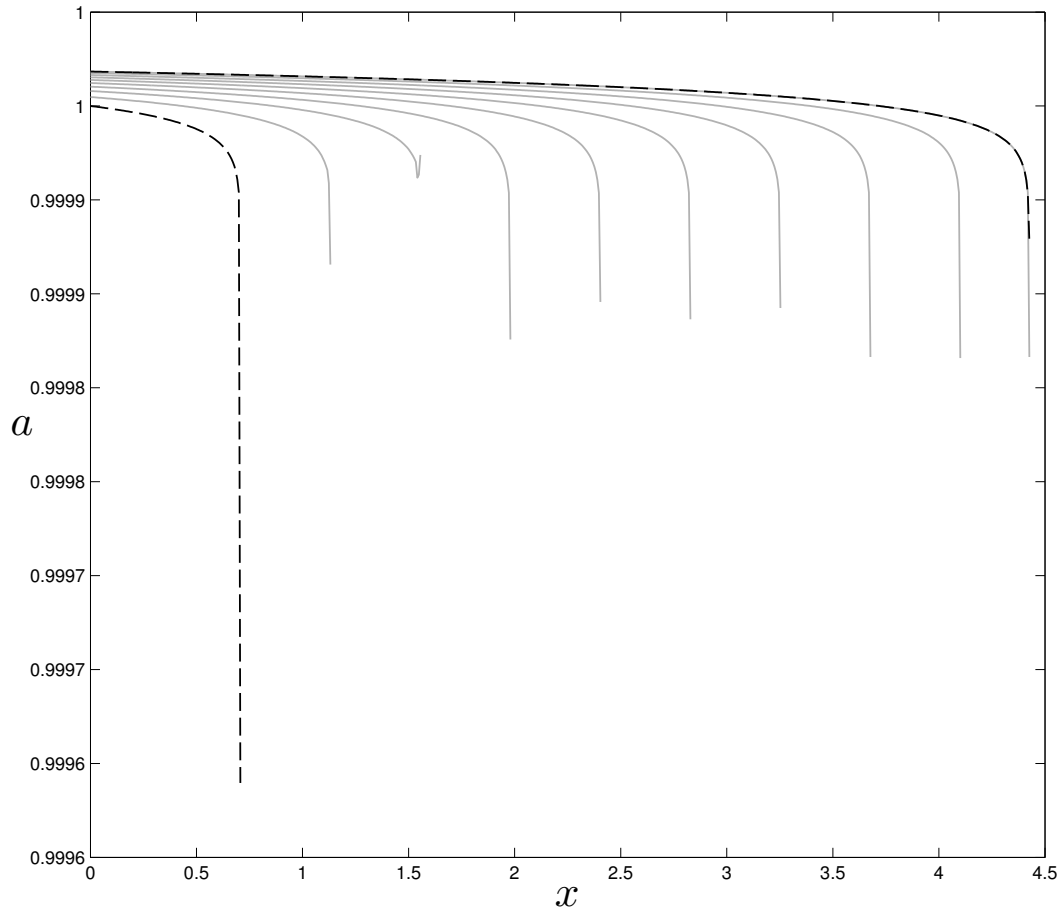

Figure 4.12: Numerical results (solid lines) for $a(x,t)$ with $n = 100000$ and a spatial step size $\delta x = 0.0071$. The initial condition (at $t = 1$) and the analytical solution for the end time $t = 1$ are both shown as dashed lines. We can see a good agreement at $t = 2.5$ between the numerical and analytical solutions. Here a is recovered from the numerical E solution by $a(x,t) = E(x,t)^{1/n}$ however we see that we are unable to reach zero as small errors at the front produce imaginary numbers when scaling E back to a. A companion plot showing $a(x,t)$ can be seen in figure 4.13 where we remove errors of size $O(dx)$ at the front and replace by the correct value of $E(x_f,t) = 0$.

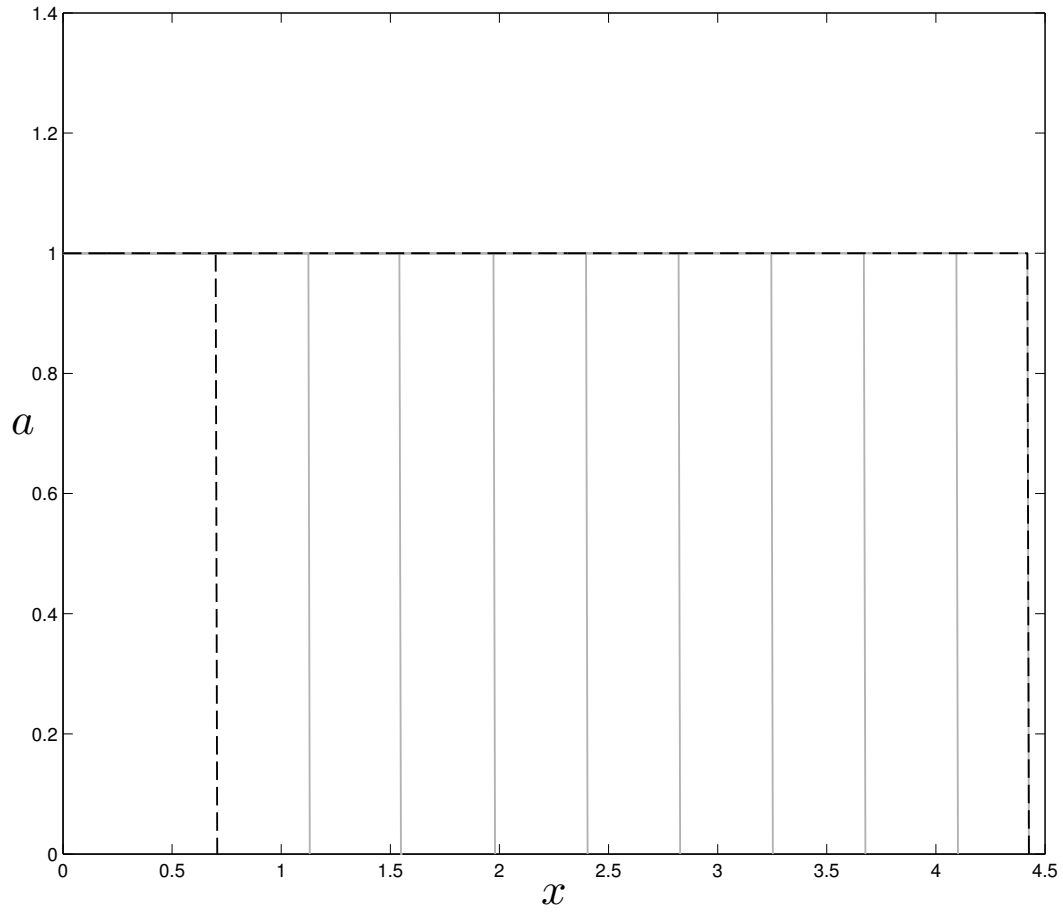

Figure 4.13: Numerical results (solid lines) for $a(x,t)$ with $n = 100000$ and a spatial step size $\delta x = 0.0071$ as shown in figure 4.12. The analytical solutions (dashed lines) at $t = 1$ and $t = 2.5$ are also shown. Here we have replaced errors of order δx in the front value $E(x_f, t)$ by the correct value of zero in order to demonstrate their effect when scaling back to $a(x,t)$.

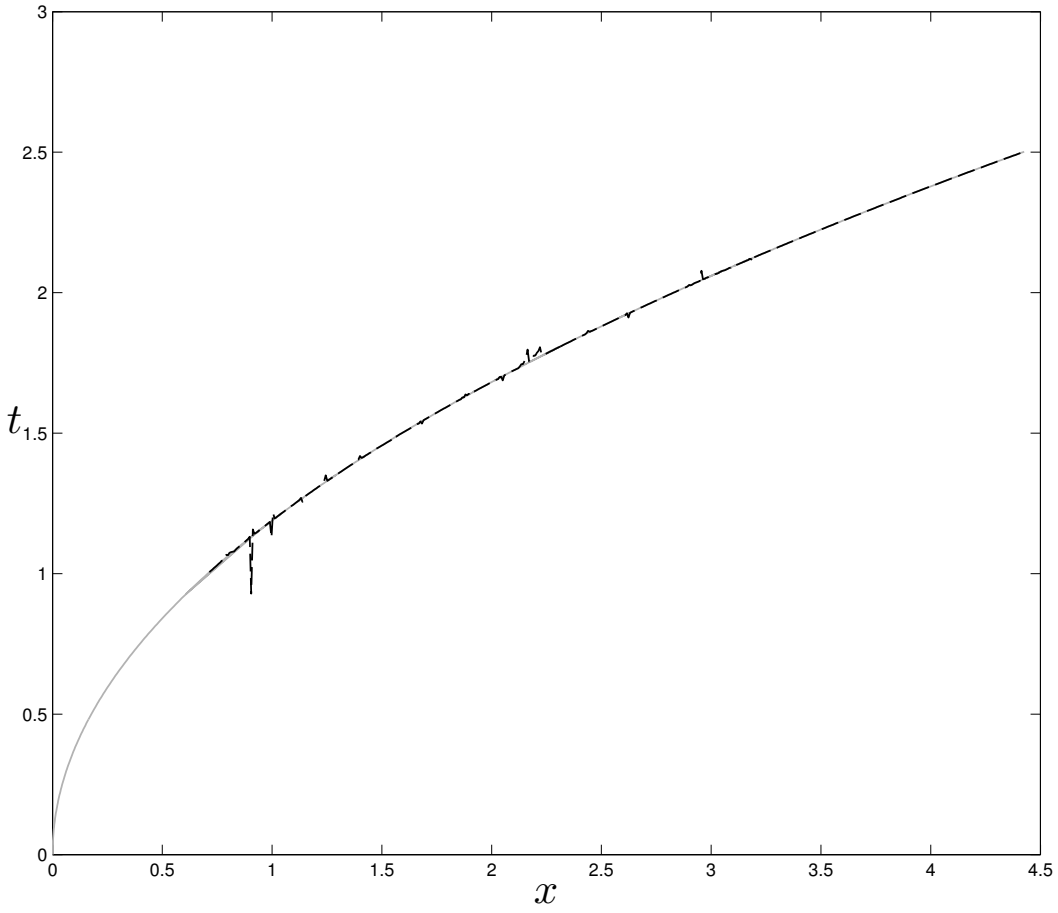

Figure 4.14: Numerical results (dashed lines) showing the front position for $n = 100000$. The analytical solution is shown as a solid line. We can see good agreement between numerical and analytical results, however there is some backward movement of the front seen in the numerical results. This may be due to difficulties in choosing a suitable step-size due to the large value of n.

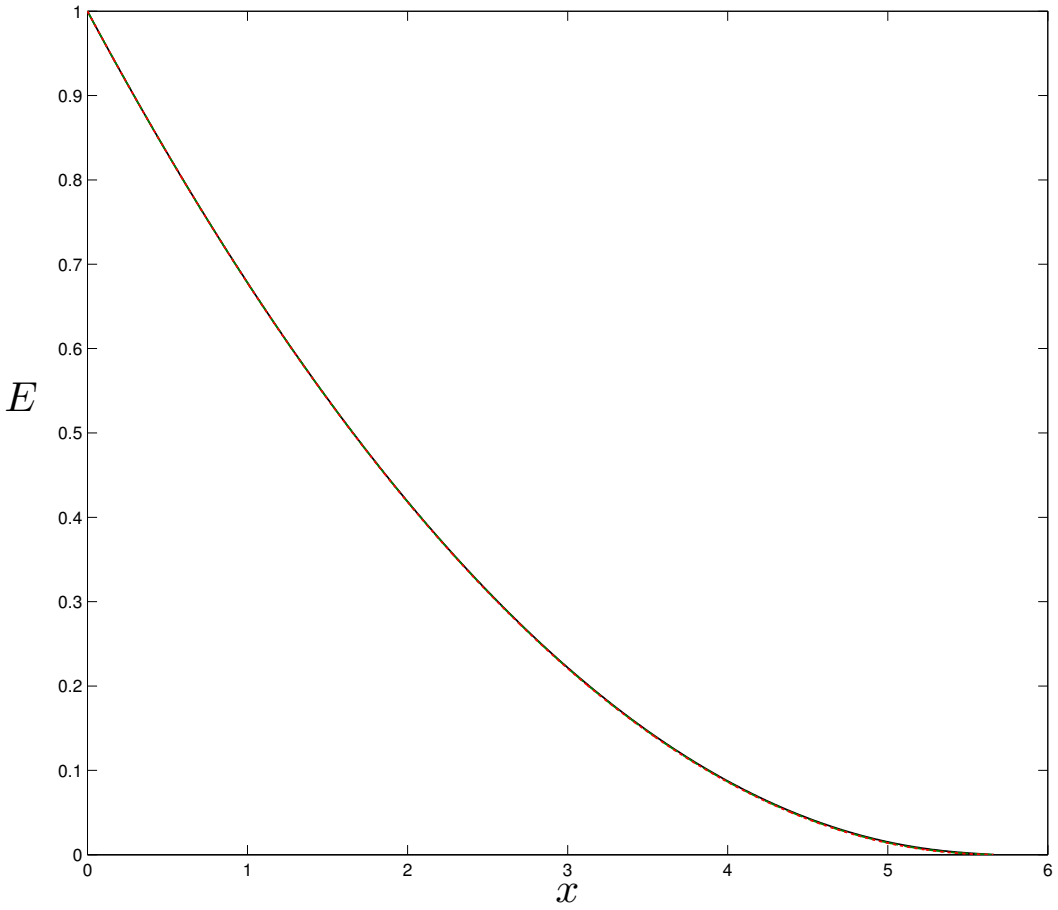

Figure 4.15: Grid tests for the case $n = 2$ as shown in figure 4.3. Spatial step sizes are $\delta x = 0.0071$ (solid), $\delta x = 0.0028$ (dashed) and $\delta x = 0.0014$ (dotted). Agreement between the step sizes is very good.

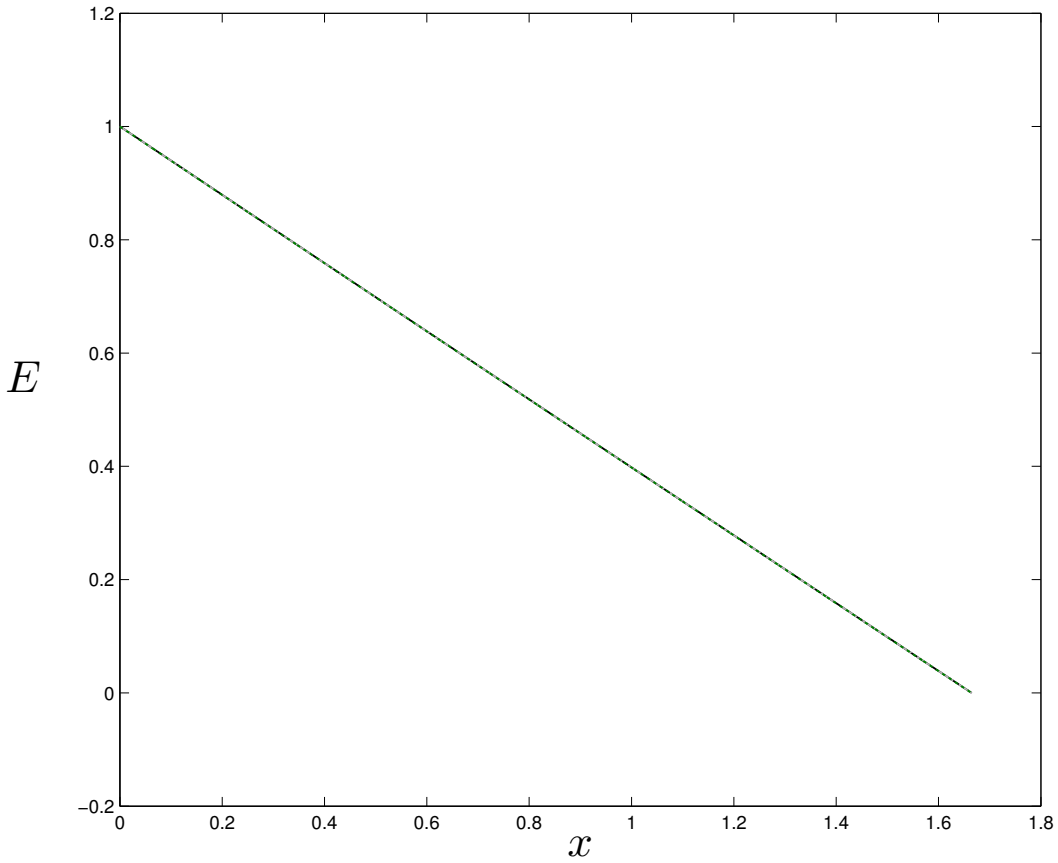

Figure 4.16: Grid tests for the case $n = 0.001$ as shown in figure 4.8. Spatial step sizes are $\delta x = 0.0013$ (solid), $\delta x = 0.0006$ (dashed) and $\delta x = 0.0003$ (dotted). Agreement between the step sizes is very good.

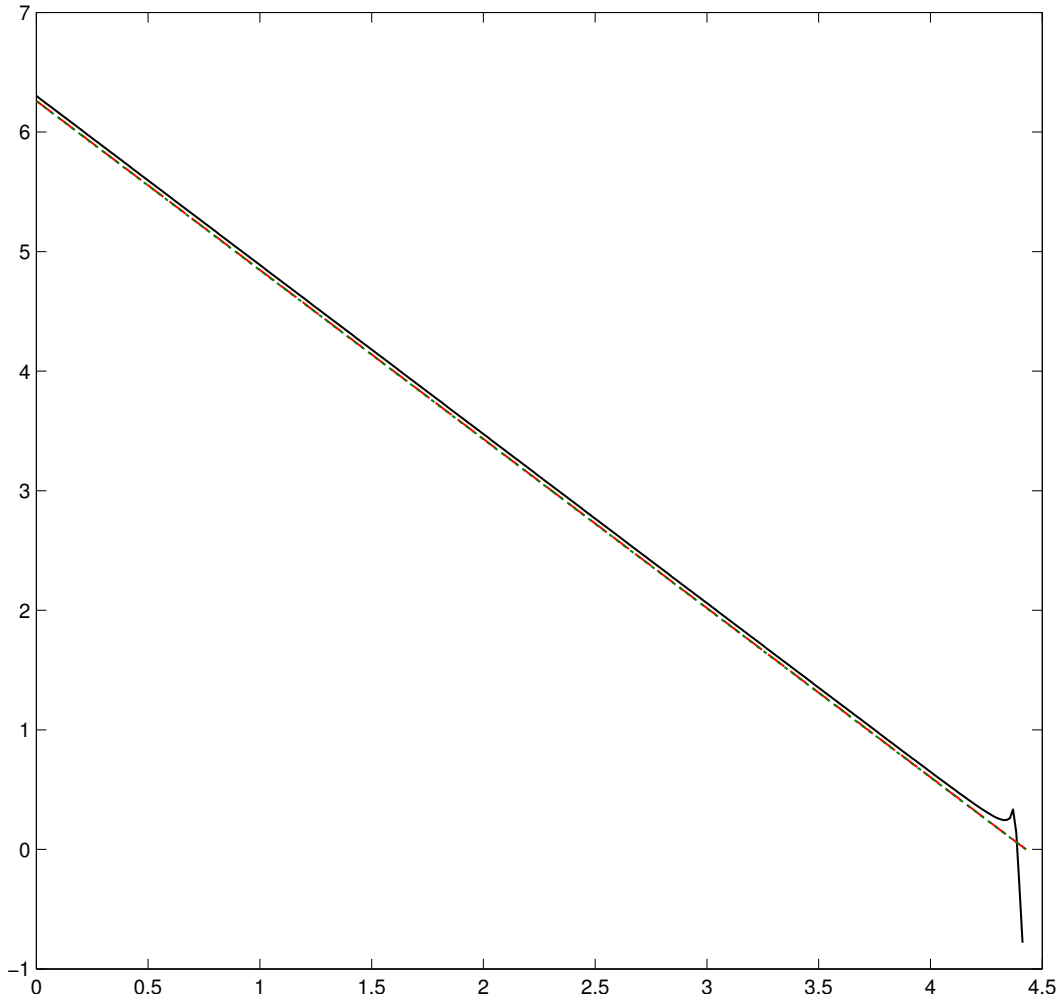

Figure 4.17: Grid tests for the case $n = 100000$ as shown in figure 4.8. Spatial step sizes are $\delta x = 0.0141$ (solid), $\delta x = 0.0081$ (dashed) and $\delta x = 0.0071$ (dotted). Agreement between the two smaller step sizes is very good.

4.2 Long scale approximation with short scale change in distensibility.

Beginning from the usual long scale equations, (2.41) - (2.43), which we rewrite below,

$$a_t + (au)_x = 0, \tag{4.13}$$

$$u_t + uu_x = -p_x, \tag{4.14}$$

$$p - p_0 = \beta(a^n - a_0^n), \tag{4.15}$$

we aim to allow the distensibility β to alter over a relatively short length scale $\lambda \ll 1$ i.e. short compared with the length scales previously considered. Physically this represents the changing of distensibility from one region of the urethra to another, or perhaps due to constriction by, for example, the prostate in men (see chapter 1). This is with a relatively far upstream value of $\beta = \beta_1$ and relatively far downstream $\beta = \beta_2$. We scale therefore as $x - x_1 = \lambda\hat{x}$, $t = \lambda\hat{t}$ and $(a, u, p, \beta) = O(1)$. Here x_1 is the point at which the alteration in distensibility occurs or is centred. On introducing the change in scales we obtain the same equations as previously,

$$a_{\hat{t}} + (au)_{\hat{x}} = 0, \tag{4.16}$$

$$u_{\hat{t}} + uu_{\hat{x}} = -p_{\hat{x}}, \tag{4.17}$$

$$p - p_0 = \beta(a^n - a_0^n), \tag{4.18}$$

provided p_0, a_0 also remain of order unity but with β allowed to vary axially.

Previously in section 2.4 it was found that there exist critical cross-over points $\beta_1 = \beta_2 = \beta_c$ where solutions may cease to exist. These findings were in terms of the Euler balance operating within the shorter length scale, and we note that an alternative KdV-like balance is investigated in appendix A. For now in order to examine the behaviour of the present system in these

circumstances we pick one such point and expand a solution about it in the form

$$(a, u, p) = (a_c, u_c, p_c) + \epsilon^{\frac{1}{2}} (a_1, u_1, p_1) + \epsilon (a_2, u_2, p_2) + \dots, \tag{4.19}$$

$$\beta(\hat{x}) = \beta_c + \epsilon\hat{\beta}(\hat{x}) + \dots \quad , \tag{4.20}$$

where a_c, u_c, p_c and β_c are constants.

In order to obtain a global solution we utilise the method of multiple scales [43], taking the time derivative to scale as

$$\partial_{\hat{t}} \to \partial_{\hat{t}} + \epsilon^{\frac{1}{2}}\partial_{\tilde{t}} + \dots \tag{4.21}$$

where $\hat{t}$ is the faster time scale and $\tilde{t}$ the slower. Substituting the expansions into equations (4.16) - (4.18) we obtain at leading order the requirement

$$p_c - p_0 = \beta_c \left(a_c^n - a_0^n\right), \tag{4.22}$$

as we might expect from examination of equations (4.16)-(4.18). At $O(\epsilon^{\frac{1}{2}})$ we obtain

$$a_{1\hat{t}} + u_c a_{1\hat{x}} + u_{1\hat{x}} a_c = 0, \tag{4.23}$$

$$u_{1\hat{t}} + u_c u_{1\hat{x}} = -p_{1\hat{x}}, \tag{4.24}$$

$$p_1 = \beta_c n a_c^{n-1} a_1, \tag{4.25}$$

while at $O(\epsilon)$ we have

$$a_{2\hat{t}} + a_{1\tilde{t}} + u_c a_{2\hat{x}} + u_{2\hat{x}} a_c + (u_1 a_1)_{\hat{x}} = 0, \tag{4.26}$$

$$u_{2\hat{t}} + u_{1\tilde{t}} + u_c u_{2\hat{x}} + u_1 u_{1\hat{x}} = p_{2\hat{x}}, \tag{4.27}$$

$$\begin{aligned} p_2 = {} & \beta_c n a_c^{n-1} a_2 \\ & + \beta_c \frac{n(n-1)}{2} a_c^{n-2} a_1^2 \\ & + \hat{\beta}(\hat{x})(a_c^n - a_0^n). \end{aligned} \tag{4.28}$$

A solution is sought such that $a_{1\hat{t}} = u_{1\hat{t}} = 0$, i.e. one in which unsteady effects are suppressed until at least the level (4.26)-(4.28) is encountered. The $O(\epsilon^{\frac{1}{2}})$ equations (4.23) - (4.24) then give us after some integration

$$u_c a_1 + u_1 a_c = 0, \tag{4.29}$$

$$u_c u_1 = -p_1, \tag{4.30}$$

$$p_1 = \beta_c n a_c^{n-1} a_1. \tag{4.31}$$

We have taken, without loss of generality, the constants of integration to be zero. Substitution of equations (4.31) and (4.29) into equation (4.30) now yields

$$u_c^2 = \beta_c n a_c^n, \tag{4.32}$$

in agreement with equation (2.51) and section 2.1.5. It still remains to find the unknown functions a_1, u_1 and p_1 in full and for this an appeal is made to the $O(\epsilon)$ equations. Similarly to before we seek a quasi-steady solution with $a_{2\hat{t}} = u_{2\hat{t}} = 0$. Equations (4.26) to (4.28) now give

$$a_{1\tilde{t}} + u_c a_{2\hat{x}} + u_{2\hat{x}} a_c + (u_1 a_1)_{\hat{x}} = 0, \tag{4.33}$$

$$u_{1\tilde{t}} + u_c u_{2\hat{x}} + u_1 u_{1\hat{x}} = -p_{2\hat{x}}, \tag{4.34}$$

$$\begin{aligned} p_2 = \beta_c n a_c^{n-1} a_2 + \beta_c \frac{n(n-1)}{2} a_c^{n-2} a_1^2 \\ + \hat{\beta}(\hat{x})(a_c^n - a_0^n). \end{aligned} \tag{4.35}$$

Multiplying (4.33) by u_c and subtracting a_c lots of (4.34) in order to remove u_2 terms and then removing $p_{2\hat{x}}$ by means of equation (4.35) and u_1 by means of equation (4.29) leaves us with the inviscid Burgers equation for a_1 with a spatially dependent forcing term,

$$a_{1\tilde{t}} - \frac{(n+2)u_c}{2a_c} a_1 a_{1\hat{x}} = \frac{a_c}{2u_c}(a_c^n - a_0^n)\hat{\beta}'(\hat{x}) \tag{4.36}$$

where the prime denotes the full derivative with respect to $\hat{x}$. Once the thickness effect a_1 is found the pressure effect p_1 may be obtained via equation (4.25) and finally the velocity effect u_1 by equation (4.24).

It is possible to check that the cut-off in solutions encountered previously (see section 2.4) can be seen again here. This is done by examining the steady case of equation (4.36). Setting $a_{1\tilde{t}} = 0$ and then integrating once with respect to $\hat{x}$ gives

$$a_1^2 = -\frac{2a_c^2}{(n+2)\,u_c^2}\,(a_c^n - a_0^n)\,\hat{\beta}. \tag{4.37}$$

The constant of integration is set to zero to satisfy the expansions (4.19) and (4.20) so that $a = a_c$ when $\beta = \beta_c$. It is clear that a change in sign of $\hat{\beta}$ determines whether solutions exist for a_1 or not. In fact, so long as $p - p_0$ remains always non-negative (so that $(a_c^n - a_0^n) > 0$), solutions of equation (4.37) exist only when $\hat{\beta} \leqslant 0$.

4.2.1 Numerical solutions

Numerical approaches are normally the most useful treatments for a forced evolution equation such as the Burgers case (4.36). We begin here by making the following substitutions, $a_1 = -\frac{2a_c}{(n+2)u_c}a^*$ and $\hat{\beta} = -\frac{4}{(a_c^n - a_0^n)(n+2)}\beta^*$, where both a^* and β^* are order one variables, and substitute into equation (4.36). This leaves us

$$a^*_{\tilde{t}} + a^* a^*_{\hat{x}} = \beta^{*\prime}(\hat{x}). \tag{4.38}$$

where the prime denotes the full derivative with respect to $\hat{x}$.

We would like to examine a simple case of jumping β^* from one value to another smoothly and so choose the function $\beta^* = \frac{1}{2}\,(\tanh(\hat{x}) + 1)$, where we have ensured that β^* remains non-negative in accordance with the condition found previously from equation (4.37). The equation to solve is then

$$a^*_{\hat{t}} + a^* a^*_{\hat{x}} = \frac{1}{2}\operatorname{sech}(\hat{x})^2. \tag{4.39}$$

An analogous case of jumping downward, $\beta^* = \frac{1}{2}(-\tanh(\hat{x}) + 1)$, need not be computed as a simple transformation $a^* \to -a^*$ as $\hat{x} \to -\hat{x}$ applied to equation (4.39) results in exactly the equation that we would have in the upward jump example.

A steady state to equation (4.39) is found simply via omission of the temporal derivative term and then integration with respect to $\hat{x}$. The constant of integration is chosen such that the right hand side remains non-negative so that solutions exist:

$$a^*_0(\hat{x}) = \sqrt{\tanh(\hat{x}) + 1} \tag{4.40}$$

is thus the steady-state solution.

4.2.2 Numerical method

The numerics are carried out using a very simple finite-differencing scheme incorporating reduced truncation viscosity in order to obtain local stability [51]. This type of scheme is known as the first order local stability scheme and has been studied in [79] who also discuss truncation error, stability and monotonicity. The scheme uses backward differencing in time and central differencing spatially giving $O(\delta\tilde{t})$ accuracy in $\tilde{t}$ and $O(\delta\hat{x}^2)$ accuracy in $\hat{x}$. Here the $\delta\tilde{t}$ and $\delta\hat{x}$ are the grid step sizes in $\tilde{t}$ and $\hat{x}$ respectively for a uniform grid. Thus we use

$$\begin{aligned} a_i^{j+1} = a_i^j - \frac{\delta\tilde{t}}{2\delta\hat{x}}\left(F_{i+1}^j - F_{i-1}^j\right) + \\ + \frac{1}{2}\left(\frac{\sigma_{i+1}^2 + \sigma_i^2}{2}\left(a_{i+1}^j - a_i^j\right) - \frac{\sigma_i^2 + \sigma_{i-1}^2}{2}\left(a_i^j - a_{i-1}^j\right)\right). \end{aligned} \tag{4.41}$$

Here superscript j represents the time station and subscript i represents the x-station. Also σ_i is the local Courant number and F is the conserved quantity given by rewriting equation (4.39) in conservative form. The asterisk of (4.38) is dropped here for convenience.

It is possible to adapt the scheme to better handle shocks by allowing extra diffusion in these regions. This is done by switching to the van Leer scheme [63] when appropriate; we replace terms σ_k^2 in the scheme (4.41) by

$$\sigma_k^2 + \left(\frac{\omega}{\sigma}\sigma_k^2 - \sigma_k^2\right)\left(\frac{|a_k - a_{k+1}|}{\max\limits_l |a_l - a_{l+1}|}\right)^n \tag{4.42}$$

When close to a shock this term tends to the value $\frac{\omega}{\sigma}\sigma_k^2$ of the van Leer scheme and when far from a shock tends to our original value σ_k^2. In the van Leer scheme, σ is the global Courant number and ω is a parameter to be set but for monotonicity must be greater than unity. In this work we set $\omega = 1.1$. For the switching function a value of $n = 2$ is chosen. Within this numerical work the modified scheme is employed only in regions where compression occurs, where infinite gradients (shocks) will tend to form i.e. where the gradient is negative for $a_i^j > 0$ and where the gradient is positive for $a_i^j < 0$. The maximum is taken only over these areas.

4.2.3 Case 1: Starting from an undisturbed cross-section.

We study the development of a^* when beginning from an initially undisturbed state, $a^*(\hat{x}, 0) = 0$ with the far upstream and downstream thickness or area held constant and undisturbed such that $a^*\left(-\infty, \tilde{t}\right) = 0$ and $a^*\left(\infty, \tilde{t}\right) = 0$. Effects of grid-refinement are shown in figure 4.18 which demonstrates good agreement between various step-sizes. The evolution of the solution may be seen in figure 4.19 which demonstrates the development of a shock and it's subsequent translation downstream.

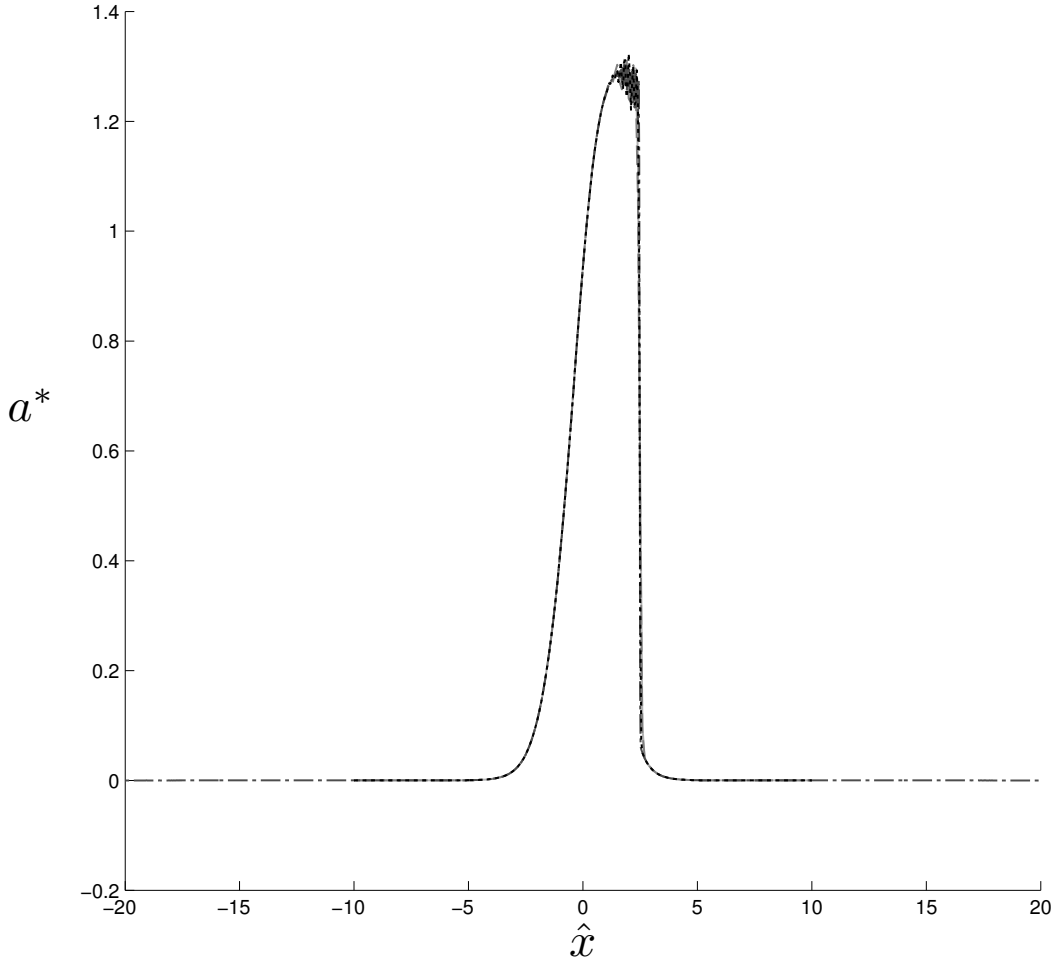

Figure 4.18: Grid refinement at $\tilde{t} = 4$ for case 1 where we initially begin with an undisturbed solution $a^*(\hat{x}, 0) = 0$. Shown are results for $\delta\hat{x} = 0.1$ with $\delta\tilde{t} = \delta\hat{x}^2$ (solid), $\delta\hat{x} = 0.1$ with $\delta\tilde{t} = \delta\hat{x}^3$ (dashed), $\delta\hat{x} = 0.02$ with $\delta\tilde{t} = \delta\hat{x}^2$ (dash-dotted) and $\delta\hat{x} = 0.05$ with $\delta\tilde{t} = \delta\hat{x}^3$ (dotted). Good agreement can be seen between the refinements.

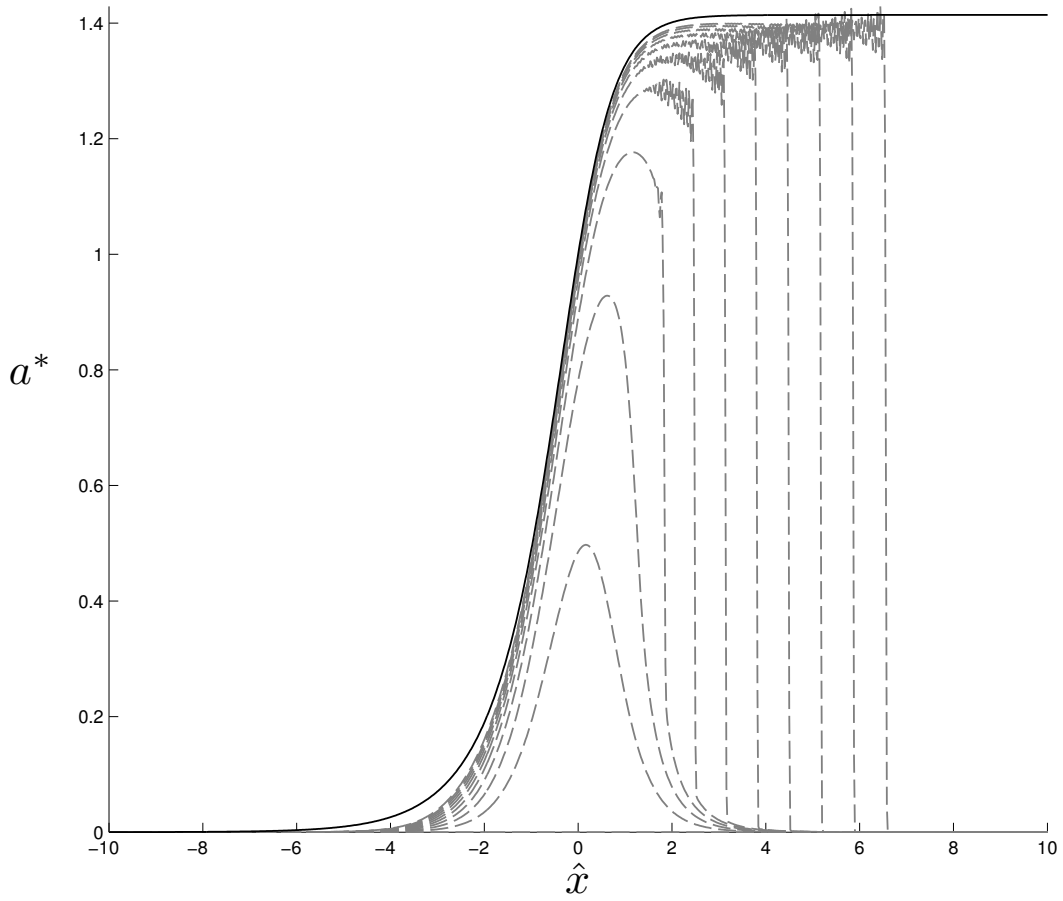

Figure 4.19: Evolution of the numerical solution (dashed) of $a^*(\hat{x}, \tilde{t})$ for case 1. Results are shown for step-sizes $\delta\hat{x} = 0.02$ and $\delta\tilde{t} = \delta\hat{x}^2$. The development and translation of a shock can be seen. Also shown is the steady-state solution given by equation 4.40 (solid).

4.2.4 Case 2: Perturbation about the theoretical steady state.

Having failed to obtain smooth, shock free solutions in case 1, an attempt is made to begin from a state which is a perturbation from the theoretical steady state. As such the initial condition is taken to be

$$a^*(\hat{x}, 0) = a_0(\hat{x}) + \frac{1}{100} e^{-\hat{x}^2}. \tag{4.43}$$

Boundary conditions $a^*\left(-\infty, \tilde{t}\right) = 0$ and $a^*\left(\infty, \tilde{t}\right) = \sqrt{2}$ are also imposed. This initial condition along with the steady state can be seen plotted together in figure (4.20), for comparison.

Effects of grid refinement at $\tilde{t} = 4$ can been seen in figure (4.21) and also in figure (4.22). It can be seen that due to the initial perturbation a hump is formed which propagates downstream in figure (4.23). An estimate of speed, using the highest point of the hump at each time step, can be made and was found to tend to approximately $\sqrt{2}$.

4.2.5 Examining disturbances such as those seen in Case 2.

In case 2 the computations began with an initial condition close to the steady state; given by equation (4.43). Our solution, seen numerically, had the form

$$a^*\left(\hat{x}, \tilde{t}\right) = a_0\left(\hat{x}\right) + \gamma a_1^*\left(\hat{x}, \tilde{t}\right) + \ldots \tag{4.44}$$

with $\gamma \ll 1$ in effect. We note that equation (4.39) may be rewritten as

$$a_{\tilde{t}}^* + a^* a_{\hat{x}}^* = a_0 a_0' \tag{4.45}$$

and so upon substitution of equation (4.44) we obtain at $O(\gamma)$

$$a_{1\tilde{t}}^* + \left(a_0 a_1^*\right)_x = 0, \tag{4.46}$$

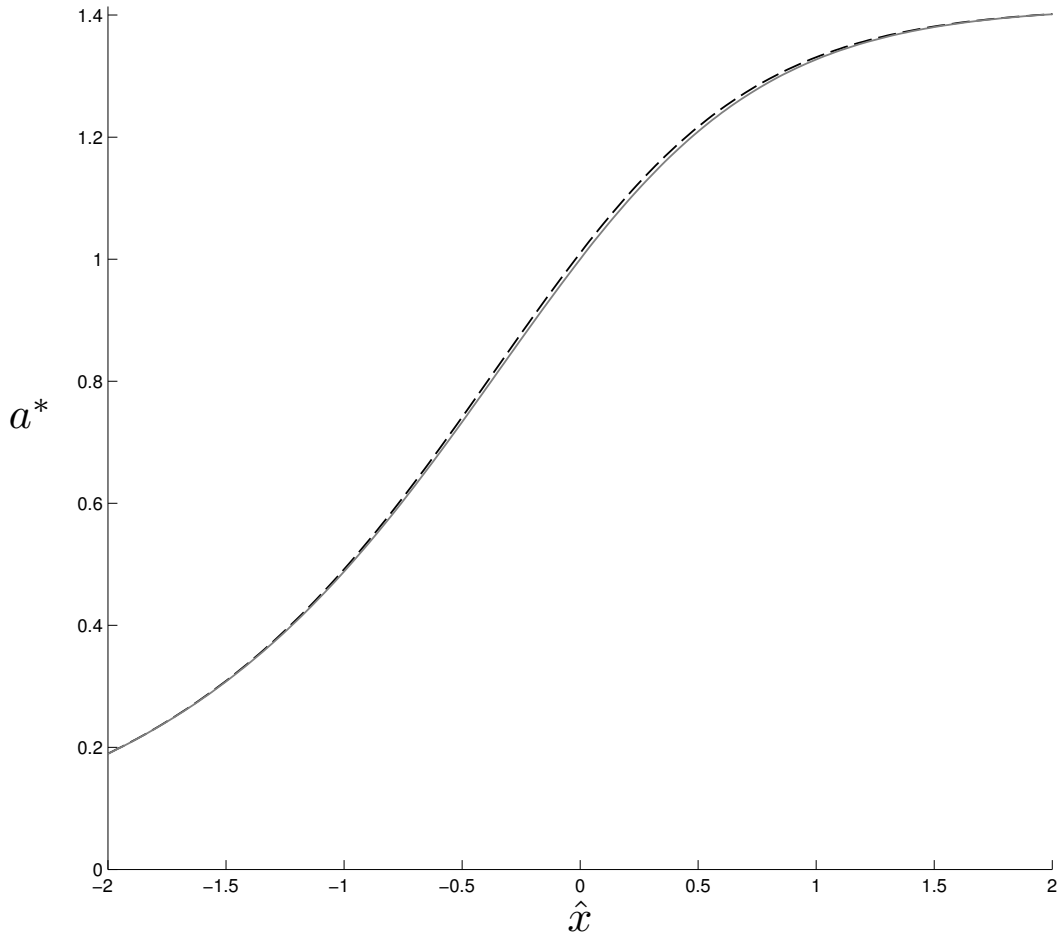

Figure 4.20: Comparison of initial condition (4.43) (dashed) to steady state (4.40) (solid) for case 2.

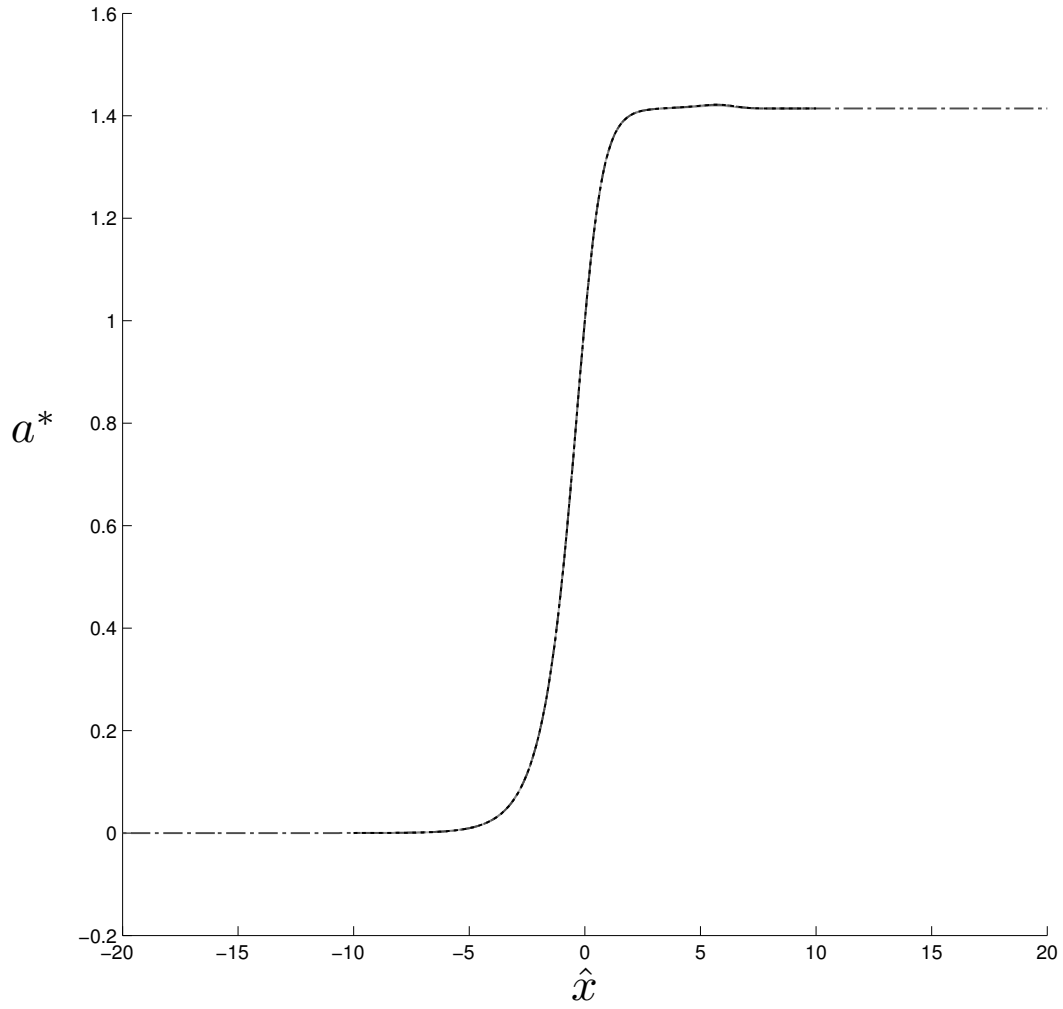

Figure 4.21: Effects of grid refinement for case 2 at $\tilde{t} = 4$ where we begin from a perturbation away from the steady state. Shown are results for $\delta\hat{x} = 0.1$ with $\delta\tilde{t} = \delta\hat{x}^2$ (solid), $\delta\hat{x} = 0.1$ with $\delta\tilde{t} = \delta\hat{x}^3$ (dashed), $\delta\hat{x} = 0.02$ with $\delta\tilde{t} = \delta\hat{x}^2$ (dash-dotted) and $\delta\hat{x} = 0.05$ with $\delta\tilde{t} = \delta\hat{x}^3$ (dotted). At this scale good agreement can be seen between the refinements.

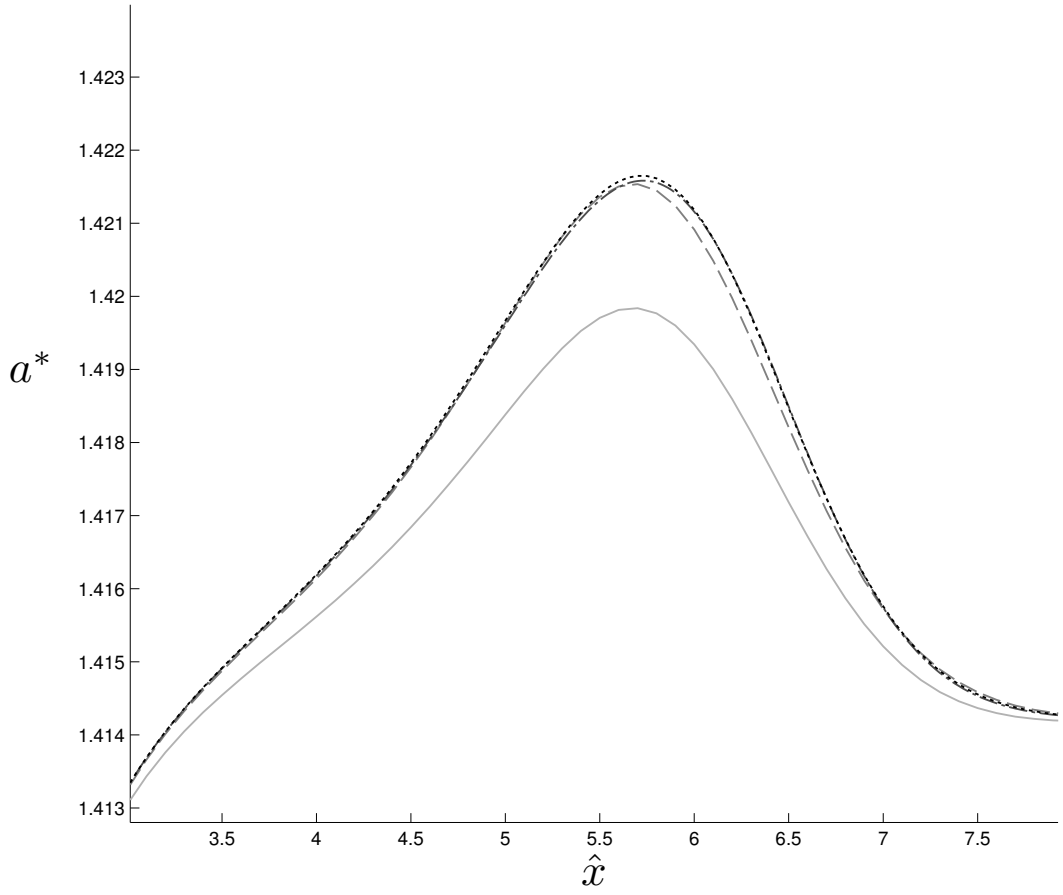

Figure 4.22: A closer view of the hump formation for various grid refinements at $\tilde{t} = 4$ in case 2 as seen in figure 4.21. Again results for $\delta\hat{x} = 0.1$ with $\delta\tilde{t} = \delta\hat{x}^2$ (solid), $\delta\hat{x} = 0.1$ with $\delta\tilde{t} = \delta\hat{x}^3$ (dashed), $\delta\hat{x} = 0.02$ with $\delta\tilde{t} = \delta\hat{x}^2$ (dash-dotted) and $\delta\hat{x} = 0.05$ with $\delta\tilde{t} = \delta\hat{x}^3$ (dotted) are shown. Excellent agreement can be seen between the latter three refinements.

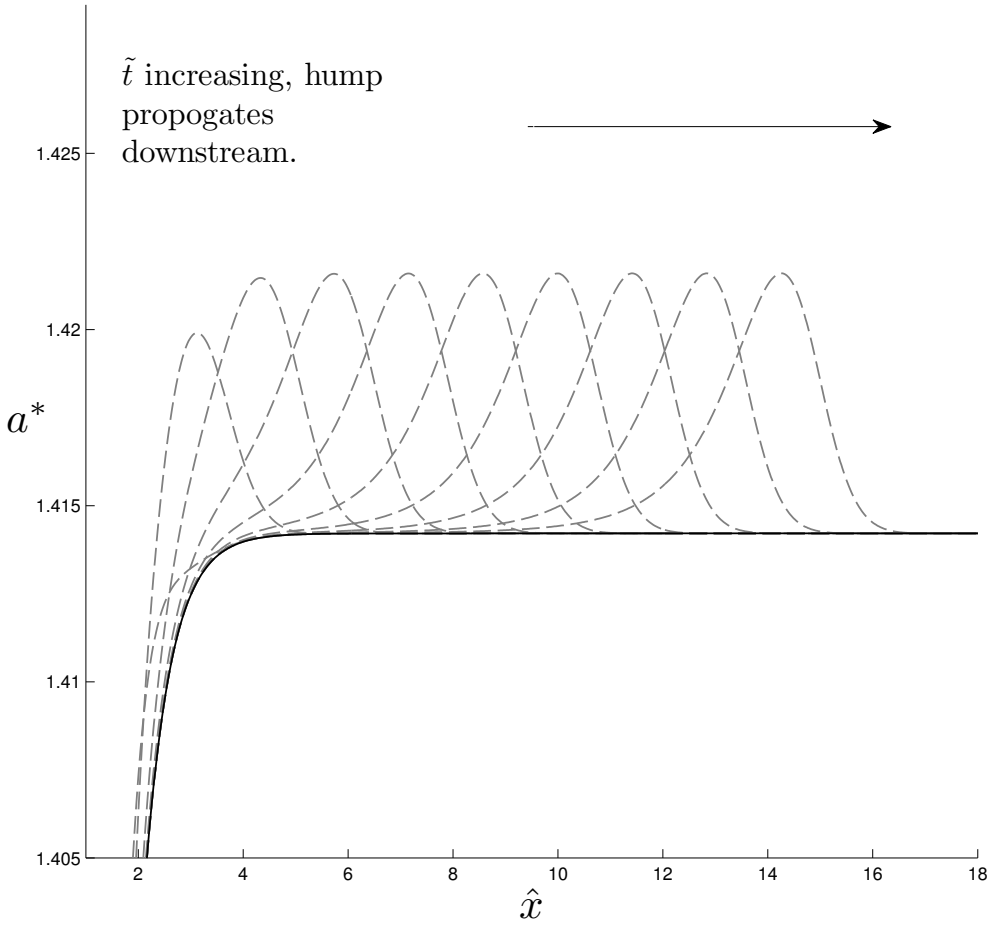

Figure 4.23: Evolution of the formed hump of case 2. Shown are the analytical steady state given by equation 4.40 (solid) and the numerical results for increasing $\tilde{t}$ with $\delta\hat{x} = 0.02$, $\delta\tilde{t} = \delta\hat{x}^2$. Various $\tilde{t}$ are shown up to $\tilde{t} = 10$. An estimated propagation speed of $\sqrt{2}$ is found by tracking the point of greatest height of the hump.

with $a_1^*(\hat{x}, 0)$ known.

By considering characteristics we can see that along curves

$$\frac{d\hat{x}}{d\tilde{t}} = a_0, \tag{4.47}$$

the quantity $a_0 a_1^*$ is conserved, as shown by

$$\begin{aligned} \int d(a_0 a_1^*) &= \int (a_0 a_1^*)_{\tilde{t}} d\tilde{t} + \int (a_0 a_1^*)_{\hat{x}} d\hat{x} \\ &= \int a_0 a_{1\tilde{t}}^* d\tilde{t} + \int (a_0 a_1^*)_{\hat{x}} d\tilde{t} a_0 \\ &= 0. \end{aligned} \tag{4.48}$$

Therefore effects from $a_1^*(\hat{x}, 0)$ will be almost stationary far upstream where a_0 is small but move with speed $\sqrt{2}$ far downstream. As we saw numerically.

It follows that a_1^* will decrease in magnitude as it travels downstream in order to conserve the quantity $a_0 a_1^*$. This can be seen in figure (4.23) in which humps can be seen to form and propagate downstream.

It is possible to integrate equation (4.47) in order to get

$$\frac{1}{\sqrt{2}} \tanh^{-1}\left(\sqrt{\frac{1+\tanh(\hat{x})}{2}}\right) - \frac{1}{\sqrt{1+\tanh(\hat{x})}} = \tilde{t} - \tilde{t}_0, \tag{4.49}$$

which gives characteristic curves with $\hat{x}$ given as an implicit function of $\tilde{t}$. Several of these curves are plotted in figure (4.24). It can be seen that upstream quantities $a_0 a_1^*$ remain stationary, whereas further downstream they quickly tend to a constant speed of $\sqrt{2}$, as stated previously. This can be seen in figure (4.23).

4.2.6 Finite time singularities.

The possible development of shocks due to a finite-time singularity, as illustrated in figures 4.18, 4.23, may be examined analytically in the same manner

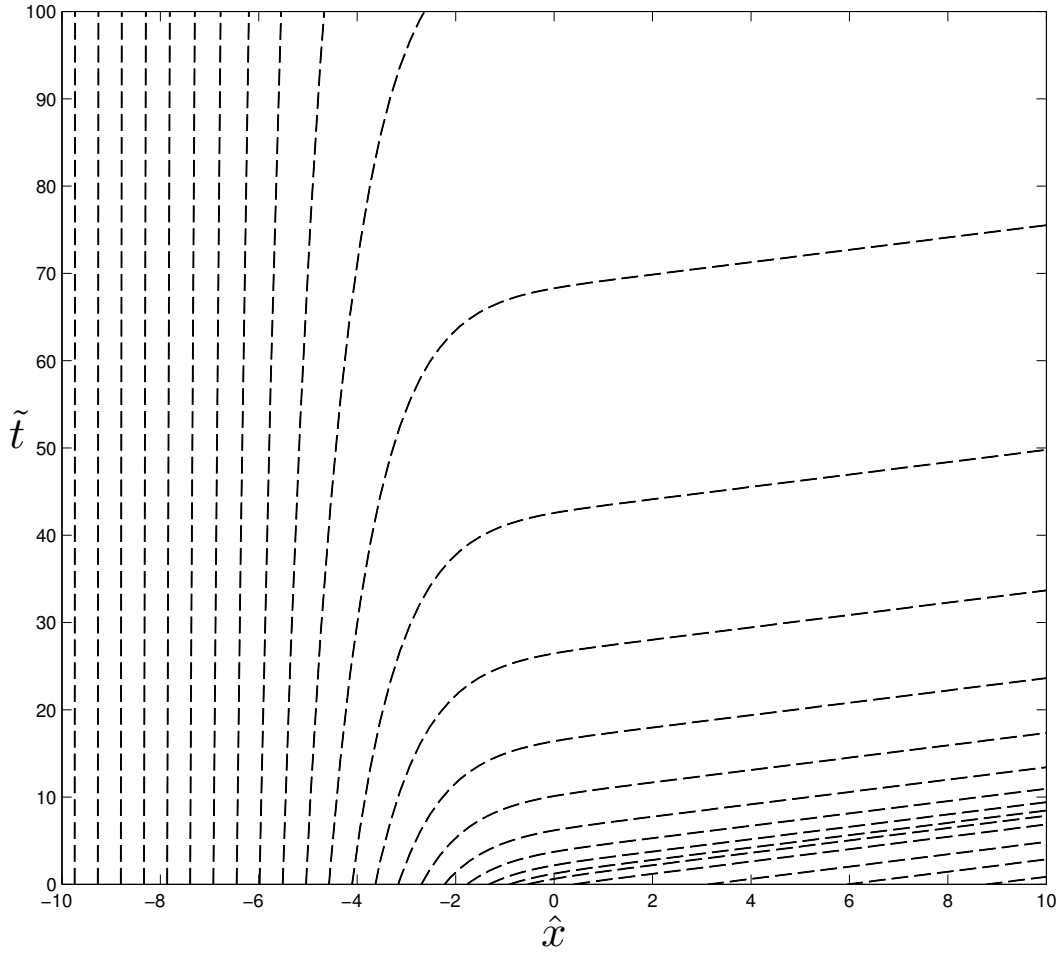

Figure 4.24: Plot of characteristic curves given by equation (4.49). From this figure we can see that disturbances far upstream are essentially stationary, while those further downstream tend to a constant speed of $\sqrt{2}$.

as [15], [75]. In the case of smooth initial conditions there is a collapse about the point $\hat{x} = \bar{x}$, $\tilde{t} = \bar{t}$ say given by the form

$$a^* = \bar{a}_0 + \left(\bar{t} - \tilde{t}\right)^{\frac{1}{2}} \bar{a}_1(\xi) + \left(\bar{t} - \tilde{t}\right)^{\frac{3}{4}} \bar{a}_2(\xi) + \left(\bar{t} - \tilde{t}\right) \bar{a}_3(\xi) + \ldots, \tag{4.50}$$

as time $\tilde{t} \to \bar{t}-$, where the local spatial coordinate is defined by

$$\hat{x} - \bar{x} = c_0 \left(\tilde{t} - \bar{t}\right) + \left(\bar{t} - \tilde{t}\right)^{\frac{3}{2}} \xi, \tag{4.51}$$

with c_0, $\bar{a}_0$ constant and $\xi = O(1)$. Substitution of (4.50) and (4.51) into equation (4.39) yields $c_0 = \bar{a}_0$ in order to maintain the balance of terms on the left hand side of equation (4.39) along with

$$3\xi \bar{a}_1' - \bar{a}_1 + 2\bar{a}_1 \bar{a}_1' = 0, \tag{4.52}$$

$$3\xi \bar{a}_2' - \frac{3}{2}\bar{a}_2 + 2\left(\bar{a}_1 \bar{a}_2\right)' = 0, \tag{4.53}$$

$$3\xi \bar{a}_3' - 2\bar{a}_3 + 2\left(\bar{a}_1 \bar{a}_3\right)' + 2\bar{a}_2 \bar{a}_2' = \operatorname{sech}(\bar{x})^2, \tag{4.54}$$

where primes denote differentiation with respect to ξ. Multiplying equation (4.52) by $(\bar{a}_1)^{-4}$, integrating with respect to ξ and then multiplying by $\bar{a}_1^3$ we obtain an implicit solution for $\bar{a}_1$ given by

$$\xi = -\bar{a}_1 - c_1 \bar{a}_1^3, \tag{4.55}$$

with c_1 a positive constant. A possible solution to equation (4.53) is simply $\bar{a}_2 = 0$ and so it then remains to solve equation (4.54), in which effects from the forcing term of equation (4.39) come into play. By using equation (4.55), equation (4.54) may be rewritten as,

$$\left(\frac{\bar{a}_3\left(3\xi + 2\bar{a}_1\right)}{\bar{a}_1^5}\right)' \bar{a}_1^5 = \operatorname{sech}(\bar{x})^2. \tag{4.56}$$

This is then integrated to give an equation for $\bar{a}_3$ in terms of $\bar{a}_1$:

$$\bar{a}_3(\xi) = \frac{\bar{a}_1(\xi)^5 \operatorname{sech}(\bar{x})^2}{3\xi + 2\bar{a}_1(\xi)} \int_0^{\xi} \bar{a}_1(q)^{-5} \, \mathrm{d}q. \tag{4.57}$$

From equations (4.55) and (4.57) it can be seen that as $\xi \to \pm\infty$ we have $|\bar{a}_1| \propto |\xi|^{\frac{1}{3}}$ and $|\bar{a}_3| \propto |\xi|^{\frac{2}{3}}$. So just outside of the local breakdown region there are terms $O(|\hat{x} - \bar{x}|^{\frac{1}{3}})$ and $O(|\hat{x} - \bar{x}|^{\frac{2}{3}})$ respectively, in a^*. An infinite slope thus develops at the collapse point $(\bar{x}, \bar{t})$. So for a large enough disturbance the governing equation (4.39) will break down in finite time, as was found to be the case numerically when our initial condition was set to zero, see section 4.2.3.

4.3 Summary of chapter

The main progress in the present chapter has been in the context of numerical methodology and fully nonlinear results, as well as allowing for discontinuities in the vessel-wall properties and short-scale phenomena. An alternative approach to section 4.2, which instead considers KdV effects can be found in appendix A.

Perhaps of interest is the possibility of pressure jumps along with associated shedding of pressure pulses downstream. It is questionable, however, whether, these would be detectable in practice due to their comparatively small amplitude. However, the theoretical constant speed of this disturbance could aid in the determination of location of possible distensibility changes.

Chapter 5

Three-dimensional modelling

The study moves on now to the more difficult but more realistic scenario of spatially three-dimensional behaviour. This is first for a slightly three-dimensional case with rigid walls in section 5.1 and second returning to flexible walls with a fast-response case in section 5.2.

5.1 Three-dimensional effects over a relatively long length scale.

As in [82], a slender flow model is examined in order to consider a small three-dimensional perturbation about a two-dimensional solution. The length and velocity scales involved are shown in figure (5.1). The non-dimensional tube length scale is taken to be l, such that $1 \ll l \ll Re$, with l in particular being much larger than the cross-sectional length scales which are of $O(1)$.

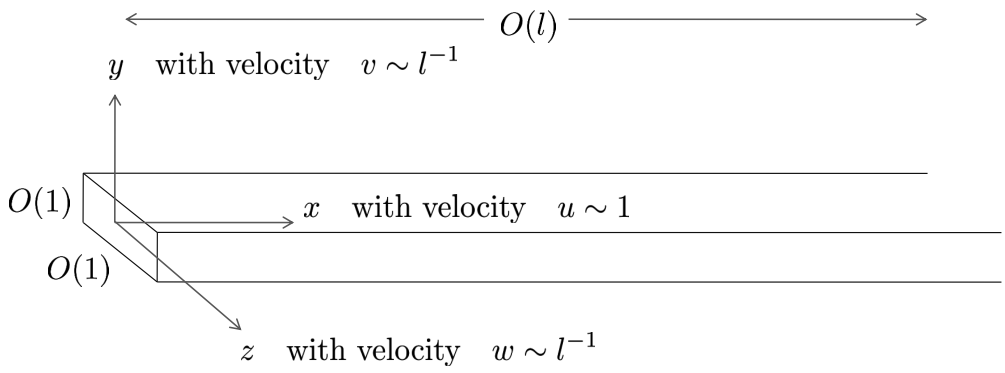

Figure 5.1: A schematic of the nondimensional long-scale approximation. A duct-like cross-section in shown, although in principal the vessel could have any general cross-section satisfying y, z of order one with x being of order $l \gg 1$.

The flow solution of the three-dimensional Euler equations,

$$u_x + v_y + w_z = 0, \tag{5.1}$$

$$u_t + uu_x + vu_y + wu_z = -p_x, \tag{5.2}$$

$$v_t + uv_x + vv_y + wv_z = -p_y, \tag{5.3}$$

$$w_t + uw_x + vw_y + ww_z = -p_z, \tag{5.4}$$

is thus expanded as

$$(u, v, w) = (\bar{u}, l^{-1}\bar{v}, l^{-1}\bar{w}) + \cdots,$$

$$p = \bar{p} + l^{-2}\tilde{p} + \cdots,$$

as far as the slender three-dimensional model is concerned with $x = lX$. Here the effective coordinates X, y, z are order one, as are the velocity components $\bar{u}, \bar{v}, \bar{w}$ and the pressure components $\bar{p}$ and $\tilde{p}$. Balancing the momentum equations leads to $\bar{p} = \bar{p}(X, t)$ being dependent only on X,t. Then the governing

equations are a set of the time-dependent Euler type equations. Dropping bars on the velocity variables we have

$$u_X + v_y + w_z = 0, \tag{5.5}$$

$$u_t + uu_X + vu_y + wu_z = -\bar{p}_X, \tag{5.6}$$

$$v_t + uv_X + vv_y + wv_z = -\tilde{p}_y, \tag{5.7}$$

$$w_t + uw_X + vw_y + ww_z = -\tilde{p}_z, \tag{5.8}$$

which represent a longitudinal vortex-type flow response. See figure (5.1).

5.1.1 Three-dimensional perturbation about a two-dimensional solution.

A first attempt to model effects of tortuosity in three-dimensions is contained in the following. Starting from a two-dimensional solution a three-dimensional perturbation is taken in the form

$$u = u_0(X,t) + \epsilon u_1(X,y,z,t) + \cdots, \tag{5.9}$$

$$v = v_0(X,y,t) + \epsilon v_1(X,y,z,t) + \cdots, \tag{5.10}$$

$$w = 0 + \epsilon w_1(X,y,z,t) + \cdots, \tag{5.11}$$

$$\bar{p} = \bar{p_0}(X,t) + \epsilon \bar{p_1}(X,t) + \cdots, \tag{5.12}$$

$$\tilde{p} = \tilde{p_0}(X,y,z,t) + \epsilon \tilde{p_1}(X,y,z,t) + \cdots. \tag{5.13}$$

Where $(u_0, v_0, \bar{p}_0)$ forms the two-dimensional solution with three-dimensionality coming in at the next order (subscript 1 terms) and in the $\tilde{p}$ pressure correction term.

Substituting these back into equations (5.5)-(5.8) the $O(1)$ governing equa-

tions are given by

$$u_{0X} + v_{0y} = 0, \tag{5.14}$$

$$u_{0t} + u_0 u_{0X} = -\bar{p}_{0X}, \tag{5.15}$$

$$v_{0t} + u_0 v_{0X} + v_0 v_{0y} = -\tilde{p}_{0y}, \tag{5.16}$$

$$0 = -\tilde{p}_{0z}. \tag{5.17}$$

These correspond to a two-dimensional flow $(u_0, v_0, \bar{p}_0)$ as expected, with $\tilde{p}_0$ giving secondary pressure effects independent of z.

For the current plug flow with u_0 independent of y in principle we can say that $u_0, \bar{p}_0$ and $\tilde{p}_0$ are known, from chapter 2. It remains to find v_0. This is accomplished by assuming that the lower and upper walls of the vessel are given by $y = f_1(X,t)$ and $y = f_2(X,t)$ respectively and then integrating the continuity equation (5.14),

$$\int_{f_1}^{y} (u_{0X} + v_{0y'})\, dy' = 0. \tag{5.18}$$

This leads to an expression for v_0 in terms of u_0 and f_1,

$$v_0 = -u_0(y - f_1) + f_{1t} + u_0 f_{1X}, \tag{5.19}$$

and also to the relationship

$$(f_2 - f_1)_t + (u_0 (f_2 - f_1))_X = 0, \tag{5.20}$$

as in most shallow-layer theories.

At order ϵ the governing equations are those for a three-dimensional linear disturbance,

$$u_{1X} + v_{1y} + w_{1z} = 0, \tag{5.21}$$

$$u_{1t} + u_0 u_{1X} + u_1 u_{0X} + v_0 u_{1y} = -\bar{p}_{1X}, \tag{5.22}$$

$$v_{1t} + u_0 v_{1X} + u_1 v_{0X} + v_0 v_{1y} + v_1 v_{0y} = -\tilde{p}_{1y}, \tag{5.23}$$

$$w_{1t} + u_0 w_{1X} + v_0 w_{1y} = -\tilde{p}_{1z}. \tag{5.24}$$

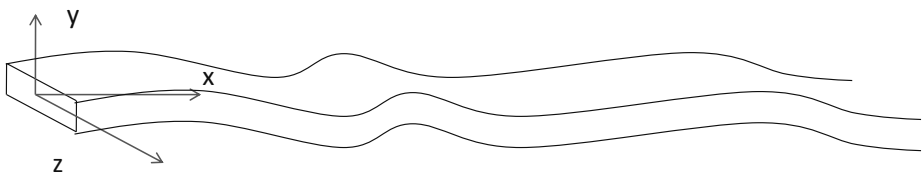

Figure 5.2: Addition of tortuosity through variation of the centreline in the y-direction. Although a duct like cross-section is shown, any general cross-section satisfying y,z of order one with x order $l \gg 1$ is possible.

A general method of solution can be seen immediately. With the pressure $\bar{p}_1$ taken to be known, equation (5.22) can be solved for u_1. Then cross differentiating equations (5.23) and (5.24) and defining the cross-plane vorticity $\zeta = v_{1z} - w_{1y}$ the following equation for v_1 and w_1,

$$\zeta_t + u_0\zeta_X + v_0\zeta_y + v_{0y}\zeta + u_{1z}v_{0X} = 0, \tag{5.25}$$

is obtained. Combining this with equation (5.21) gives two equations for two unknowns, which in principle can be solved. The work here is taken further in the next subsection.

5.1.2 Adding tortuosity.

Starting again from equations (5.5) - (5.8) a more tortuous physical path of the slender vessel may be modelled by introducing a change in "height" or position of the centreline of the tube, say, as the longitudinal distance X increases.

A diagram is presented in figure (5.2). A change of variables is now introduced such that

$$y - F(X, z, t) = \bar{y}, \tag{5.26}$$

where F represents the tube centreline position. The y velocity is then given by

$$v = F_t + uF_X + wF_z + \bar{v} \tag{5.27}$$

for convenience, with $\bar{v}$ to be found. The partial derivatives transform as

$$\begin{aligned}
\frac{\partial}{\partial X} &\to \frac{\partial}{\partial X} - F_X \frac{\partial}{\partial \bar{y}}, \\
\frac{\partial}{\partial y} &\to \frac{\partial}{\partial \bar{y}}, \\
\frac{\partial}{\partial z} &\to \frac{\partial}{\partial z} - F_z \frac{\partial}{\partial \bar{y}}, \\
\frac{\partial}{\partial t} &\to \frac{\partial}{\partial t} - F_t \frac{\partial}{\partial \bar{y}}.
\end{aligned}$$

The governing equations incorporating a tortuous path are therefore

$$u_X + \bar{v}_{\bar{y}} + w_z = 0, \tag{5.28}$$

$$u_t + uu_X + \bar{v}u_{\bar{y}} + wu_z = -\bar{p}_X, \tag{5.29}$$

$$\begin{aligned}
\bar{v}_t + u\bar{v}_X + \bar{v}\bar{v}_{\bar{y}} + w\bar{v}_z = &-(1+F_z^2)\tilde{p}_{\bar{y}} + F_X\bar{p}_X + F_z\tilde{p}_z - \\
&- F_{tt} - 2uF_{Xt} - 2wF_{zt} - \\
&- u^2F_{XX} - 2uwF_{Xz} - w^2F_{zz},
\end{aligned} \tag{5.30}$$

$$w_t + uw_X + \bar{v}w_{\bar{y}} + ww_z = -\tilde{p}_z + F_z\tilde{p}_{\bar{y}}. \tag{5.31}$$

In a fixed geometry depending only on the variable X, that is $F = F(X)$, these equations are simplified to

$$u_X + \bar{v}_{\bar{y}} + w_z = 0, \tag{5.32}$$

$$u_t + uu_X + \bar{v}u_{\bar{y}} + wu_z = -\bar{p}_X, \tag{5.33}$$

$$\bar{v}_t + u\bar{v}_X + \bar{v}\bar{v}_{\bar{y}} + w\bar{v}_z = -\tilde{p}_{\bar{y}} - u^2F_{XX} + F_X\bar{p}_X, \tag{5.34}$$

$$w_t + uw_X + \bar{v}w_{\bar{y}} + ww_z = -\tilde{P}_z. \tag{5.35}$$

The term F_{XX} here acts as an effective Görtler number [67] or Dean number [9], by the way.

For simplicity and hopefully more realistic application these equations may be recast in cylindrical polar coordinates such that $\bar{y} = r\cos\theta$, $z = r\sin\theta$, $\bar{v} = V\cos\theta - W\sin\theta$ and $w = V\sin\theta + W\cos\theta$. Here V and W represent the radial and azimuthal velocities respectively. The partial derivatives are transformed as follows,

$$\begin{aligned}
\frac{\partial}{\partial X} &\to \frac{\partial}{\partial X}, \\
\frac{\partial}{\partial \bar{y}} &\to \cos\theta\frac{\partial}{\partial r} - \frac{\sin\theta}{r}\frac{\partial}{\partial \theta}, \\
\frac{\partial}{\partial z} &\to \sin\theta\frac{\partial}{\partial r} + \frac{\cos\theta}{r}\frac{\partial}{\partial \theta}, \\
\frac{\partial}{\partial t} &\to \frac{\partial}{\partial t}.
\end{aligned}$$

This leads us to the equations

$$u_X + \frac{1}{r}(rV)_r + \frac{1}{r}W_\theta = 0, \tag{5.36}$$

$$u_t + uu_X + Vu_r + \frac{1}{r}Wu_\theta = -\bar{p}_X, \tag{5.37}$$

$$\begin{aligned}
V_t + uV_X + VV_r + \frac{1}{r}WV_\theta - \frac{W^2}{r} &= -\tilde{p}_r + \\
&\quad + (\bar{p}_X F_X - u^2 F_{XX})\cos\theta,
\end{aligned} \tag{5.38}$$

$$\begin{aligned}
W_t + uW_X + VW_r + \frac{1}{r}WW_\theta + \frac{1}{r}VW &= -\frac{1}{r}\tilde{p}_\theta + \\
&\quad - (\bar{p}_X F_X - u^2 F_{XX})\sin\theta.
\end{aligned} \tag{5.39}$$

A solution is now sought as a three-dimensional perturbation about an axisymmetric solution in the form

$$u(X,t) = u_0(X,t) + \epsilon u_1(X,t) + \cdots, \tag{5.40}$$

$$V(X,r,\theta,t) = V_0(X,r,t) + \epsilon V_1(X,r,\theta,t) + \cdots, \tag{5.41}$$

$$W(X,r,\theta,t) = 0 + \epsilon W_1(X,r,\theta,t) + \cdots, \tag{5.42}$$

$$\bar{p}(X) = \bar{p_0}(X) + \epsilon\bar{p_1}(X) + \cdots, \tag{5.43}$$

$$\tilde{p}(X,r,\theta) = \tilde{p_0}(X,r) + \epsilon\tilde{p_1}(X,r,\theta) + \cdots. \tag{5.44}$$

The variables with subscript 0 correspond to a basic axisymmetric flow solution and are taken to be known, as is $\bar{P}_1$. The order ϵ equations obtained by substitution of equations (5.40)-(5.44) into the governing equations (5.36)-(5.39) are

$$u_{1X} + \frac{1}{r}(rV_1)_r + \frac{1}{r}W_{1\theta} = 0, \tag{5.45}$$

$$u_{1t} + u_0 u_{1X} + u_1 u_{0X} = -\bar{p}_{1X}, \tag{5.46}$$

$$V_{1t} + u_0 V_{1X} + u_1 V_{0X} + V_0 V_{1r} + V_1 V_{0r} = -p_r, \tag{5.47}$$

$$W_{1t} + u_0 W_{1X} + V_0 W_{1r} + \frac{1}{r}V_0 W_1 = -\frac{1}{r}p_\theta, \tag{5.48}$$

where

$$p = \tilde{p}_1 - r(\bar{p}_{0X} F_{1X} - u_0^2 F_{1XX})\cos\theta. \tag{5.49}$$

To solve we proceed by analogy with the previous subsection. Equation (5.46) can be solved for u_1 leaving only V_1 and W_1 unknown. The vorticity,

$$\zeta = V_{1\theta} - (rW_1)_r, \tag{5.50}$$

is introduced and equations (5.47) and (5.48) are cross differentiated to leave us with

$$\zeta_t + u_0 \zeta_X + (V_0 \zeta)_r = 0. \tag{5.51}$$

This leads to an equation for V_1 and W_1 which, along with equation (5.45), can be solved in order to obtain V_1 and W_1. The main point here however is that it can be seen that in fact the tortuosity does not drive any cross-plane motion at this order. The tortuosity has influence only on the induced pressure, specifically by means of the depletion of the pressure effect P. To capture the influence of tortuosity or three-dimensionality more fully leads us into the study of three-dimensional behaviour in the following sections and in chapter 6.

5.2 Large-n properties in three-dimensional vessels.

We now move on to investigating the possible three-dimensional effects of having large-n values, i.e. the fast-response regime. The over-riding motivation here is that in practical applications three-dimensional effects could well be important, with the flow unlikely to be axisymmetric, especially given that in reality the cross-section of the urethra is rarely circular.

5.2.1 Three-dimensional effects over a relatively long length scale.

Again we consider the slender flow model obtained in section 5.1 and so begin from the longitudinal vortex flow response equations given by (5.5)-(5.8), which we repeat here for convenience:

$$u_X + v_y + w_z = 0, \tag{5.52}$$

$$u_t + uu_X + vu_y + wu_z = -\bar{p}_X, \tag{5.53}$$

$$v_t + uv_X + vv_y + wv_z = -\tilde{p}_y, \tag{5.54}$$

$$w_t + uw_X + vw_y + ww_z = -\tilde{p}_z. \tag{5.55}$$

We assume symmetry about the $y = 0$ plane and so consider, without loss of generality, the upper half-plane only. As such, our lower boundary condition is simply that no fluid penetrates this plane. The upper wall remains the flexible tube wall and so the usual kinematic boundary condition applies there. The boundary conditions are given as

$$v = f_t + uf_X + wf_z \quad \text{on} \quad y = f(X, z, t), \tag{5.56}$$

$$v = 0 \quad \text{on} \quad , y = 0, \tag{5.57}$$

together with appropriate conditions on the sides $z = z_{\pm a}$ which we take as $w = 0$. Here $f(X, z, t)$ gives the unknown scaled shape of the upper wall. The starting conditions at $X = 0$ are analogous to those in two dimensions. Finally we introduce the main pressure-wall relationship for this three-dimensional configuration,

$$\bar{p}(X, z, t) = \beta(X, z) \left(f(X, z, t)\right)^n \tag{5.58}$$

which we notice is as before with the exception that we now allow the distensibility coefficient β to vary with X and z. The form of β is such that its z dependence cancels with that of f^n. We may choose β to be piecewise constant over the X-z plane, giving different pressure-wall relations in essence within each different region of the X-z plane.

Putting $E = f^n$ and allowing $n \gg 1$ the boundary condition (5.56) becomes

$$v = \frac{E_t + uE_X + wE_z}{nE}, \tag{5.59}$$

and the pressure $\bar{p}$ is given by

$$\bar{p} = \beta(X, z)E(x, z, t). \tag{5.60}$$

Guided by the two-dimensional results (3.123) to (3.126) we now seek a solution

$$u = u_0(t) + n^{-1}u_1 + \cdots, \tag{5.61}$$

$$v = n^{-1}v_0 + \cdots, \tag{5.62}$$

$$w = n^{-1}w_0 + \cdots, \tag{5.63}$$

$$E = E_0 + n^{-1}E_1 + \cdots, \tag{5.64}$$

$$\bar{p} = \bar{p}_0 + n^{-1}\bar{p}_1 + \cdots, \tag{5.65}$$

$$\tilde{p} = n^{-1}\tilde{p}_0 + \cdots, \tag{5.66}$$

for large values of the parameter n.

Substitution into the longitudinal system (5.52) to (5.55) yields

$$u_{1X} + v_{0y} + w_{0z} + O(n^{-1}) = 0, \tag{5.67}$$

$$u_{0t} + n^{-1}u_{1t} + n^{-1}u_0u_{1X} + O(n^{-2}) = -\bar{p}_{0X} - n^{-1}\bar{p}_{1X}, \tag{5.68}$$

$$n^{-1}v_{0t} + n^{-1}u_0v_{0X} + O(n^{-2}) = -n^{-1}\tilde{p}_{0y}, \tag{5.69}$$

$$n^{-1}w_{0t} + n^{-1}u_0w_{0X} + O(n^{-2}) = -n^{-1}\tilde{p}_{0z}, \tag{5.70}$$

along with boundary conditions

$$n^{-1}v_0 + O(n^{-2}) = \frac{1}{nE_0}\left(E_{0t} + u_0E_{0X} + n^{-1}w_0E_{0z}\right) \text{ on } y = 1, \tag{5.71}$$

$$v_0 + O(n^{-1}) = 0 \text{ on } y = 0, \tag{5.72}$$

$$w_0 + O(n^{-1}) = 0 \text{ on } z = z_{\pm a}, \tag{5.73}$$

and with the main pressure

$$\begin{aligned}\bar{p}_0(X,t) + n^{-1}\bar{p}_1(X,t) + O(n^{-2}) = \beta(X,z)E_0(X,z,t) \\ + n^{-1}\beta(X,z)E_1(X,z,t).\end{aligned} \tag{5.74}$$

At leading order it follows from equation (5.68) that $u_{0t} = -\bar{p}_{0X}(X,t)$. This we now integrate to give the pressure as linear in X,

$$\bar{p}_0 = -u_{0t}(t)\left(X - X_0(t)\right), \tag{5.75}$$

where $X_0(t)$ is to be determined. Using equation (5.74) then gives

$$\beta(X,z)E_0(X,z,t) = -u_{0t}(t)\left(X - X_0(t)\right). \tag{5.76}$$

As in the section 3.4 we expect to have a front which we expand $X_f(t) = X_{f0}(t) + n^{-1}X_{f1}(t) + \cdots$ and provides us the condition that $E_0 = 0$ at $X = X_{f0}(t)$. We therefore have $X_0 = X_{f0}$. We also require a condition at the opening, and again we proceed as in section 3.4. Here we assume that $\beta(0,z) = \beta^0$ is a constant for definiteness and so have a known opening $E_0(0,z,t) = E^0(t)$ which is independent of z. We finally require, as previously, the kinematic

balance $u_0(t) = \dot{X}_{f0}(t)$ as a result of the front condition. Hence equation (5.76) acts to govern the evolution of the front position X_{f0} in the form

$$\beta^0 E^0(t) = \ddot{X}_{f0} X_{f0}, \tag{5.77}$$

a nonlinear ordinary differential equation for $X_{f0}(t)$. Once $X_{f0}(t)$ is known we are then able to find u_0 from

$$u_0(t) = \dot{X}_{f0}, \tag{5.78}$$

from which we may find E_0 at arbitrary X by using equation (5.76) and then the pressure effect $\bar{p}_0$ by using equation (5.74) at leading order. Thus we have

$$E_0(X, z, t) = \frac{\ddot{X}_{f0}(t)}{\beta(X, z)} \left(X_{f0}(t) - X\right), \tag{5.79}$$

which we notice matches the earlier result (3.116) from the two-dimensional case, with the exception that β here is not usually constant.

We now turn to the next order of the system (5.67) to (5.70) and present it below for convenience,

$$u_{1X} + v_{0y} + w_{0z} = 0, \tag{5.80}$$

$$u_{1t} + u_0 u_{1X} = -\bar{p}_{1X}, \tag{5.81}$$

$$v_{0t} + u_0 v_{0X} = \tilde{p}_{0y}, \tag{5.82}$$

$$w_{0t} + u_0 w_{0X} = \tilde{p}_{0z}, \tag{5.83}$$

with pressure from (5.74) given by

$$\bar{p}_1 = \beta(X, z) E_1(X, z, t), \tag{5.84}$$

and boundary conditions (5.71) to (5.73) giving

$$v_0 = \frac{1}{E_0} \left(E_{0t} + u_0 E_{0X}\right) \text{ on } y = 1, \tag{5.85}$$

$$v_0 = 0 \text{ on } y = 0, \tag{5.86}$$

$$w_0 = 0 \text{ on } z = z_{\pm a}. \tag{5.87}$$

The condition at the opening, $X = 0$ is as (3.107) from the two-dimensional case and so

$$E_1(0, z, t) = E^1(z, t) = 0 \tag{5.88}$$

and hence

$$\bar{p}_1(0, t) = \beta^0 E^1(z, t) = 0. \tag{5.89}$$

Velocity components at the opening are taken as unknown, as is $\tilde{p}_0$. Front conditions are as (3.111) to (3.114) and so

$$u_1(X_{f0}, y, z, t) = \dot{X}_{f1} \tag{5.90}$$

$$E_1(X_{f0}, z, t) = -X_{f1} \frac{\partial E_0}{\partial X}(X_{f0}, z, t). \tag{5.91}$$

In order to solve the system (5.80) to (5.83) we begin by removing the pressure $\tilde{p}_0$ to find an equation for the cross-plane vorticity. This is done via cross-differentiation of (5.82) and (5.83) which yields

$$(\partial_t + u_0 \partial_X) \{v_{0z} - w_{0y}\} = 0, \tag{5.92}$$

which states that the scaled cross-plane vorticity is conserved along the main flow paths and so can be evaluated from its starting value at the opening $X = 0$. Assuming that the cross-plane vorticity is in fact zero at the opening then gives $v_{0z} - w_{0y} = 0$ throughout the flow and allows us to define a velocity potential Φ given by

$$v_0 = \Phi_y, \tag{5.93}$$

$$w_0 = \Phi_z. \tag{5.94}$$

The continuity equation (5.80) may thus be rewritten

$$\nabla^2 \Phi = -u_{1X}, \tag{5.95}$$

a Poisson equation for the velocity potential forced by the axial spatial gradient of the order n^{-1} correction to the axial velocity. Here the operator $\nabla = (\partial_y, \partial_z)$ is two-dimensional in the cross-plane.

It remains to solve the system (5.95), (5.81) along with

$$(\partial_t + u_0\partial_X)\,\Phi_y = -\tilde{p}_{0y}, \tag{5.96}$$

$$(\partial_t + u_0\partial_X)\,\Phi_z = -\tilde{p}_{0z}, \tag{5.97}$$

from (5.82), (5.83), and the boundary conditions

$$\Phi_y = 0 \quad \text{on} \quad y = 0, \tag{5.98}$$

$$\Phi_z = 0 \quad \text{on} \quad z = z_{\pm a}, \tag{5.99}$$

from (5.86), (5.87) and

$$\Phi_y = \frac{\dddot{X}_{f0}}{\ddot{X}_{f0}} - \frac{\beta_X}{\beta}\dot{X}_{f0} \,\text{on}\, y = 1 \tag{5.100}$$

in view of (5.85).

We proceed now by integrating (5.95) over the cross-plane and applying boundary conditions (5.86), (5.87) and (5.100) to find an equation for u_1, which is given by

$$u_{1X} = \frac{1}{C}\int_{z_{-\infty}}^{z_\infty}\left(\dot{X}_{f0}\frac{\beta_X}{\beta} - \frac{\dddot{X}_{f0}}{\ddot{X}_{f0}}\right)\mathrm{d}z, \tag{5.101}$$

where $C = \iint_S \mathrm{d}y\mathrm{d}z$ is the cross-sectional area and S denotes the cross-section. Notice that u_1 is a function of X, t alone as we might expect from examination of equation (5.81). We note that $C = (z_a - z_{-a}) = \bar{z}$, say. Then (5.101) becomes

$$u_{1X} = \frac{\dot{X}_{f0}}{\bar{z}}\frac{d}{dX}\int_{z_{-\infty}}^{z_\infty}\log(\beta)\,\mathrm{d}z - \frac{\dddot{X}_{f0}}{\ddot{X}_{f0}}, \tag{5.102}$$

which is integrated to

$$u_1 = \frac{\dot{X}_{f0}}{\bar{z}}\int_{z_{-\infty}}^{z_\infty}\log(\beta)\,\mathrm{d}z - \frac{\dddot{X}_{f0}}{\ddot{X}_{f0}}X + g(z,t), \tag{5.103}$$

Finding u_{1X} then allows (5.95) to be solved for Φ.

The above establishes that solutions of the assumed three-dimensional form are indeed possible. Rather than looking at these in detail we turn now to another three-dimensional form whose solutions are found to be of much interest.

5.2.2 Three-dimensional thin-region flow.

Having examined the longitudinal vortex structure in the previous section we now turn our attention to another main three-dimensional case, again for n large. Here we begin from the three-dimensional Euler equations (5.1) - (5.4) and assume a thin flow where $(x,\, y,\, z) \sim (1,\, \epsilon,\, 1)$ along with corresponding velocity components $(u,\, v,\, w) \sim (1,\, \epsilon,\, 1)$, i.e. we have height and velocity components vertically much smaller than in the horizontal cross-plane, for parameter values $\epsilon \ll 1$. In actuality we take $\epsilon \sim n^{-1}$. A schematic diagram of the flow configuration is shown in figure (5.3).

Thus we obtain here the nondimensional governing equations

$$u_x + v_y + w_z = 0, \tag{5.104}$$

$$u_t + uu_x + vu_y + wu_z = -p_x, \tag{5.105}$$

$$w_t + uw_x + vw_y + ww_z = -p_z, \tag{5.106}$$

$$0 = -p_y, \tag{5.107}$$

which we notice are of the three-dimensional interactive inviscid boundary layer type [76]; they are equivalent to the three-dimensional shallow-water system [86] or that of three-dimensional internal flows [74]. Coupled to this we also have the wall law

$$p(x,z,t) = p_0 + \beta(x,z)\left(a(x,z,t)^n - a_0^n\right), \tag{5.108}$$

similar to that in equation (2.21), along with a kinematic boundary condition on the vessel surface, $y = a(X,z,t)$, impermeability condition on the flat

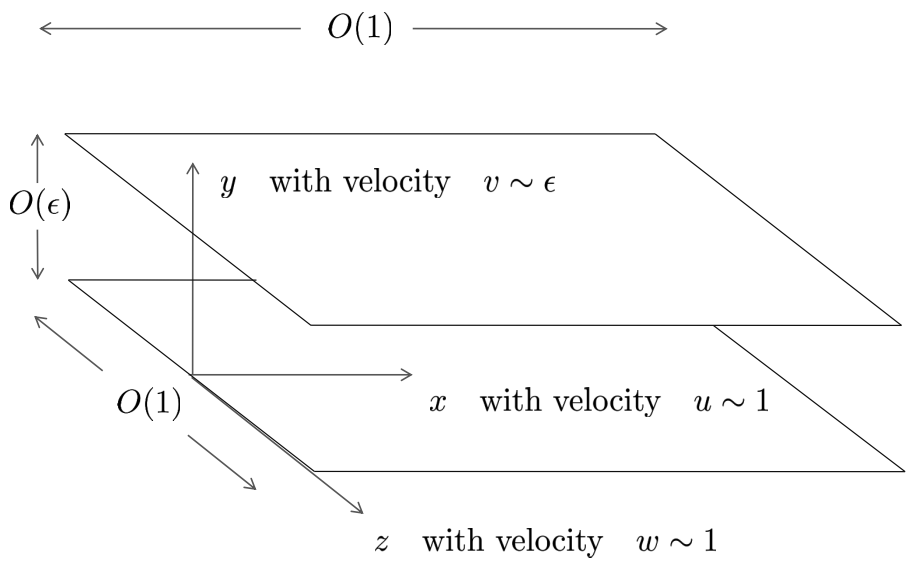

Figure 5.3: A schematic diagram (not to scale) of the nondimensional thin flow approximation. Here x, z are of order one with y being of order $\epsilon \ll 1$, where the small parameter $\epsilon \sim n^{-1}$ for large-n values.

bottom surface, $y = 0$

$$v = a_t + ua_x + wa_z \text{ on } y = a(X, z, t), \tag{5.109}$$

$$v = 0 \text{ on } y = 0, \tag{5.110}$$

and periodic boundary conditions on $z = -D$, D taken as the edges of the system in the z-direction, for a constant D. Notice the pressure is independent of y as indicated by equation (5.107)

We now turn our attention to large values of the parameter n. Following the method of sections 3.4, 3.4.1, 5.2 we introduce the variable $E = a^n$ which we substitute into the governing system (5.104)-(5.107). Taking $n \gg 1$, the kinematic boundary condition (5.109) when rewritten in the form (5.59) then forces the ordering $v \sim n^{-1}$ while u and w remain order one. We therefore introduce the expansions

$$u = u_0 + n^{-1}u_1 + \cdots, \tag{5.111}$$

$$v = n^{-1}v_0 + \cdots, \tag{5.112}$$

$$w = w_0 + n^{-1}w_1 + \cdots, \tag{5.113}$$

$$E = E_0 + n^{-1}E_1 + \cdots, \tag{5.114}$$

$$p = \bar{p}_0 + n^{-1}\bar{p}_1 + \cdots, \tag{5.115}$$

which then give from (5.104)-(5.107), to leading order, the system

$$u_{0x} + w_{0z} = 0, \tag{5.116}$$

$$u_{0t} + u_0u_{0x} + w_0u_{0z} = -\bar{p}_{0x}, \tag{5.117}$$

$$w_{0t} + u_0w_{0x} + w_0w_{0z} = -\bar{p}_{0z}, \tag{5.118}$$

with $\bar{p}_0 = \bar{p}_0(x, z, t) = p_0 + \beta E_0$. Remarkably these are in fact the two-dimensional Euler equations acting in the plane of the x-z surface. We now absorb the constant p_0 into $\bar{p}_0$ for convenience, leaving

$$\bar{p}_0 = \beta E_0, \tag{5.119}$$

as the pressure-shape relation.

Next we consider small values of β within the confines of system (5.116) - (5.119), which although perhaps not entirely realistic is at least not completely unreasonable when considering the proximal urethra in men with bladder outlet obstruction [36]. We require firstly that $n^{-1} < \beta \ll 1$ in order not to violate the expansions (5.111) - (5.115), then the velocities and pressure can be expected to be small, $(u,\, w,\, p) \sim \beta$ so as to balance the pressure terms. The system in such a case reduces still further to

$$u_{0x} + w_{0z} = 0, \tag{5.120}$$

$$u_{0t} = -\bar{p}_{0x}, \tag{5.121}$$

$$w_{0t} = -\bar{p}_{0z}, \tag{5.122}$$

from (5.116) - (5.118), along with (5.119). These are incidentally the equations of linearised unsteady potential flow.

Differentiating (5.121) with respect to x and (5.122) with respect to z and then adding the results together yields, by use of equation (5.120), Laplace's equation for $\bar{p}_0$ in the x-z plane,

$$\nabla^2 \bar{p}_0 = 0. \tag{5.123}$$

The boundary conditions are then:

$$\bar{p}_0 = g(z,t) \quad \text{at} \quad x = 0, \tag{5.124}$$

for $g(z,t)$ a known function found via (5.119) from the given opening $E(0,z,t) \approx E_0$; periodicity on the spanwise edges such that

$$\bar{p}_0(x,-D,t) = \bar{p}_0(x,D,t), \tag{5.125}$$

$$\bar{p}_{0z}(x,-D,t) = \bar{p}_{0z}(x,D,t); \tag{5.126}$$

and two conditions at the unknown moving front $x = x_f(z,t)$. The first condition,

$$\bar{p}_0 = 0 \quad \text{at} \quad x = x_f(z,t), \tag{5.127}$$

is derived from the requirement that $E_0 \sim E(x_f, z, t) = 0$, a consequence of the definition of the front as marking the moving positions where the gap closes. The second is a normal derivative condition (akin to a kinematic boundary condition as in (5.109)), given by

$$-S_x + S_z x_{fz} = x_{ft}, \tag{5.128}$$

where we have taken $\bar{p}_0 = S_t$ for convenience. Here $S = \int_0^t \bar{p}_0(x,z,t^*)\,dt^*$ with $\bar{p}_0(x,z,0) = 0$ so that the vessel is initially closed, by virtue of (5.119). Equations (5.121),(5.122) therefore give that $S_x = -u_0$ and $S_z = -w_0$. The unknown function $-S(x,z,t)$ is clearly equivalent to a velocity potential, in keeping with the original governing equations (5.120)-(5.122). The task here then is to solve (5.123)-(5.128).

The case of an opening shape given with non-uniform z-dependence such that

$$g \propto q_2(t) + a(t)\cos(z) \tag{5.129}$$

is addressed now, with $q_2(t)$, $a(t)$ depending on time only. This admits two exact solutions of much interest.

The $\exp(-x)$ **case**

One exact solution contains a term proportional to $\exp(-x)$ and is given by

$$\bar{p}_0(x,z,t) = xq_1(t) + q_2(t) + a(t)e^{-x}\cos\left(\frac{\pi z}{D}\right), \tag{5.130}$$

where $q_1(t)$, $q_2(t)$ and $a(t)$ are functions of t to be found. This solution satisfies Laplace's equation (5.123) and the periodicity conditions (5.125), (5.126). We

take $D = \pi$ for convenience and without loss of generality consider only the region $z \in [0, \pi]$. We therefore have the pressure

$$\bar{p}_0(x, z, t) = xq_1(t) + q_2(t) + a(t)e^{-x}\cos(z), \tag{5.131}$$

and hence the negative velocity potential

$$S(x, z, t) = xQ_1(t) + Q_2(t) + b(t)e^{-x}\cos(z), \tag{5.132}$$

where the functions of time involved are related by $\frac{d}{dt}\{Q_1, Q_2, b\} = \{q_1, q_2, a\}$. It then remains to satisfy the boundary conditions, which require, from (5.124), (5.127) and (5.128)),

$$q_2(t) + a(t)cos(z) = g(z, t), \tag{5.133}$$

$$x_f q_1(t) + q_2(t) + a(t)e^{-x_f}\cos(z) = 0, \tag{5.134}$$

$$-Q_1(t) + b(t)e^{-x_f}\cos(z) - x_{fz}b(t)e^{-x_f}\sin(z) = x_{ft}. \tag{5.135}$$

Here we treat $Q_1(t)$ and $b(t)$ as known which give $q_1(t)$, $a(t)$ and so we are left to solve (5.133)-(5.133) for $q_2(t)$, $x_f(z, t)$ and $g(z, t)$. We set suitable forms of $Q_1(t)$ and $b(t)$ below to give a reasonable opening pressure function $g(z, t)$.

It is noted immediately in passing that there is a special case for $a(t) = b(t) = 0$ which retrieves from (5.133)-(5.133) the exact two-dimensional solution of section 3.4 namely that $x_f\ddot{x}_f = g(t)$ as in equation (3.117). We refer back to this case later in the working.

Looking at equation (5.135) we consider below both $z = 0$ and $z = \pi$, along which

$$-Q_1(t) + b(t)e^{-x_f} = \frac{dx_f}{dt}, \tag{5.136}$$

$$-Q_1(t) - b(t)e^{-x_f} = \frac{dx_f}{dt}, \tag{5.137}$$

respectively. Since we expect the front to move in the positive x-direction at the start, when $x_f = 0$, then we have both that $b > Q_1$ and $b < -Q_1$. This can only be satisfied if $Q_1 < 0$.

We now consider the particular forms

$$Q_1(t) = -\bar{q}t^n, \tag{5.138}$$

$$b(t) = \bar{b}t^n, \tag{5.139}$$

for n, $\bar{q}$, $\bar{b}$ constants and n, $\bar{q} > 0$. Then along $z = 0$, equation (5.136) becomes

$$t^n \left(\bar{q} + \bar{b}e^{-x_f}\right) = \frac{dx_f}{dt}, \tag{5.140}$$

which integrates to

$$x_f(0,t) = \ln\left|\frac{\bar{b}}{\bar{q}}\left(-1 + k_1 \exp\left(\frac{\bar{q}t^{n+1}}{n+1}\right)\right)\right|. \tag{5.141}$$

If, at $t = 0$, the front starts at $x = 0$ then we have the constant $k_1 = \left(1 + \frac{\bar{q}}{\bar{b}}\right)$.

Similarly, we may look at $z = \pi$ which gives

$$x_f(\pi,t) = \ln\left|\frac{\bar{b}}{\bar{q}}\left(1 + k_2 \exp\left(\frac{\bar{q}t^{n+1}}{n+1}\right)\right)\right|, \tag{5.142}$$

from (5.137), with the constant $k_2 = \left(-1 + \frac{\bar{q}}{\bar{b}}\right)$ if $x_f = 0$ at $t = 0$. In order for both solutions x_f to remain non-negative for physical sense we require $\left|\bar{b}\right| < \bar{q}$. If we now examine $t \to \infty$ we have that $x_f(0,t) \to \frac{\bar{q}t^{n+1}}{n+1}$: the solution is then approaching the two-dimensional state. Comparing this to the two-dimensional solution (3.128) we identify $n = \frac{M}{2}$ and $\bar{q} = \sqrt{\frac{B(M+2)}{M}}$. Comparisons of the two-dimensional front (3.128) and movement of the three-dimensional front along $z = 0$ can be seen in figures (5.4),(5.5) where first we see a comparison for large times showing the close agreement between the results and secondly there is shown more clearly the differences between the two-dimensional and three-dimensional results for front position at smaller times.

Returning to equation (5.135) we now consider general $z \in (0, \pi)$ spanning across (around) the wall. The characteristics of the equation are defined by

$$\frac{dz}{dt} = \bar{b}t^n e^{-x_f} \sin(z), \tag{5.143}$$

and along the characteristics we have from (5.135)

$$\frac{dx_f}{dt} = \bar{q}t^n + \bar{b}t^n e^{-x_f}\cos(z)\,. \tag{5.144}$$

Combining (5.144) and (5.143) gives the result that

$$\frac{dx_f}{dz} = \frac{\bar{q}\exp(x_f)}{\bar{b}\sin(z)} + \cot(z)\,, \tag{5.145}$$

along characteristics. The solution to (5.145) for $x_f(z)$ on the characteristics is found by considering x_f as the sum of two functions of z such that $x_f = F(z) + G(z)$, say. Letting

$$\frac{dG}{dz} = cot(z), \tag{5.146}$$

we find

$$G = \log|\sin(z)|\,, \tag{5.147}$$

where we have taken the constant of integration to be zero without loss of generality. From (5.145) it then remains to solve

$$\frac{dF}{dz} = \frac{\bar{q}\exp(F)\,|sin(z)|}{\bar{b}\sin(z)}, \tag{5.148}$$

which gives, for $\sin(z) > 0$ as in our setting,

$$F = -\log\left(\frac{\bar{q}}{\bar{b}}(z_0 - z)\right), \tag{5.149}$$

with z_0 a constant to be found. We have therefore that

$$x_f = \log\left(\frac{\bar{b}\sin(z)}{\bar{q}(z_0 - z)}\right), \tag{5.150}$$

along the characteristics. If this is substituted into (5.143) we can then find characteristics given by $z(t)$ and corresponding x_f values. We have

$$\frac{dz}{dt} = \bar{b}t^n\left(\frac{\bar{q}(z_0 - z)}{\bar{b}\sin(z)}\right)\sin(z), \tag{5.151}$$

which gives

$$\frac{dz}{dt} = \bar{q}t^n(z_0 - z), \tag{5.152}$$

and integrates to

$$z(t) = z_0 + C\exp\left(-\frac{\bar{q}t^{n+1}}{n+1}\right), \tag{5.153}$$

with C a constant. If we define $z(0) = z_s$ as the starting value of z along the characteristic we find that $z_0 = z_s - C$. Substituting (5.153) into (5.150) and taking $x_f(0) = 0$ we have $C = -\frac{\bar{b}\sin(z_s)}{\bar{q}}$. We thus find characteristics given by

$$z(t; z_s) = z_s + \frac{\bar{b}\sin(z_s)}{\bar{q}}\left(1 - \exp\left(-\frac{\bar{q}t^{n+1}}{n+1}\right)\right), \tag{5.154}$$

along which we have

$$x_f = \log\left(\frac{\bar{b}\sin(z(t))}{\bar{q}\left(z_s + \frac{\bar{b}}{\bar{q}}\sin(z_s) - z(t)\right)}\right). \tag{5.155}$$

Rewriting (5.155) by use of (5.154) there is obtained the front solution

$$x_f(t; z_s) = \frac{\bar{q}t^{n+1}}{n+1} + \log\left(\frac{\sin\left(z_s + \frac{\bar{b}\sin(z_s)}{\bar{q}}\left(1 - \exp\left(-\frac{\bar{q}t^{n+1}}{n+1}\right)\right)\right)}{\sin(z_s)}\right), \tag{5.156}$$

for $0 < z < \pi$. From this we can see that, as in the $z = 0$ and $z = \pi$ cases, as $t \to \infty$, $x_f \to \frac{\bar{q}t^{n+1}}{n+1}$ i.e. the two-dimensional solution is approached at large times.

The corresponding opening pressure function $g(z, t)$ can now be found from (5.133), (5.134) where the procedure would be to find $q_2(t)$ from (5.134) and then substitute into (5.133). The function is thus given by

$$g(z, t) = nt^{n-1}\left(\bar{q}x_f(z, t) + (1 - \exp(-x_f(z, t)))\,\bar{b}\cos(z)\right). \tag{5.157}$$

Again as a check, now letting $t \to \infty$ leads us to the solution $g(z, t) \to \frac{n\bar{q}^2t^{2n}}{n+1}$ for $0 \leqslant z \leqslant \pi$ which we find is identical to the opening pressure function for the two-dimensional solution, defined by (3.127).

Plots of front position and opening function can be seen in figures 5.6, 5.7.

The $\exp(x)$ case

An alternative exact solution is given by

$$\bar{p}_0(x,z,t) = xq_1(t) + q_2(t) + a(t)e^x \cos\left(\frac{\pi z}{D}\right), \tag{5.158}$$

and this exhibits interesting behaviour different to that seen above.

Again we take $D = \pi$ and consider the region given by $z \in [0,\pi]$, following the treatment of (5.130) and so on; thus

$$\bar{p}_0 = xq_1(t) + q_2(t) + a(t)\exp(x)\cos(z), \tag{5.159}$$

and

$$S(x,z,t) = xQ_1(t) + Q_2(t) + b(t)\exp(x)\cos(z), \tag{5.160}$$

for Q_1, Q_2 and b defined as previously.

We are then left to solve, from the boundary conditions, equations

$$q_2(t) + a(t)cos\,(z) = g(z,t), \tag{5.161}$$

$$x_f q_1(t) + q_2(t) + a(t)e^{x_f}\cos(z) = 0, \tag{5.162}$$

$$-Q_1(t) - b(t)e^{x_f}\cos(z) - x_{fz}b(t)e^{x_f}\sin(z) = x_{ft}, \tag{5.163}$$

for $q_2(t)$, $x_f(z,t)$ and $g(z,t)$, with $Q_1(t)$ and $b(t)$ given. Again the special case $a = b = 0$ gives the two-dimensional solution.

Equation (5.163) along $z = 0$ and $z = \pi$ gives

$$-Q_1(t) - b(t)e^{x_f} = \frac{dx_f}{dt}, \tag{5.164}$$

$$-Q_1(t) + b(t)e^{x_f} = \frac{dx_f}{dt}, \tag{5.165}$$

respectively. Expecting the front to move in the positive x-direction, at least initially, requires that both $-Q_1 > b$ and $Q_1 < b$. Again we thus have $Q_1 < 0$ and so take Q_1, b defined as in equations (5.138) and (5.139). It therefore

follows that $\left|\bar{b}\right| < \bar{q}$ with $\bar{q} > 0$. In the following we now take $\bar{b} > 0$, without loss of generality, as we notice that a change $\bar{b} \to -\bar{b}$ results in the same equations (5.161)-(5.162) so long as $z \to (\pi - z)$, i.e. we have the same solution but reversed in the z-direction.

Integrating (5.164) and (5.165) gives

$$x_f(0,t) = \log\left|\frac{\bar{q}}{\bar{b}\left(1+\left(-1+\frac{\bar{q}}{\bar{b}}\right)\exp\left\{\frac{\bar{q}t^{n+1}}{n+1}\right\}\right)}\right|, \tag{5.166}$$

$$x_f(\pi,t) = \log\left|\frac{\bar{q}}{\bar{b}\left(-1+\left(1+\frac{\bar{q}}{\bar{b}}\right)\exp\left\{\frac{\bar{q}t^{n+1}}{n+1}\right\}\right)}\right|, \tag{5.167}$$

respectively. As $t \to \infty$ both solutions tend to a constant value $\log\left(\bar{q}/\bar{b}\right)$. However it is evident from (5.167) that a finite-time singularity occurs along the $z = \pi$ position with the time to this singularity given by

$$t_\infty = \left(\frac{n+1}{\bar{q}}\log\left(1+\frac{\bar{q}}{\bar{b}}\right)\right)^{\frac{1}{n+1}}. \tag{5.168}$$

We will find below that the opening-pressure function exhibits similar behaviour at this time and so note that the solution will only be valid for $0 \leqslant t < t_\infty$ at most.

We can again find a solution for $0 < z < \pi$ if we consider characteristics, now for equation (5.163). Following the same procedure we obtain

$$x_f = \log\left(\frac{\bar{q}\,(z-z_0)}{\bar{b}\sin(z)}\right), \tag{5.169}$$

$$\frac{dz}{dt} = \bar{q}(z-z_0)t^n. \tag{5.170}$$

Integrating (5.170) and applying the condition that at $t = 0$ we have $z = z_s$ for $0 < z_s < \pi$ we find

$$z = z_0 + (z_s - z_0)\exp\left(\frac{\bar{q}t^{n+1}}{n+1}\right). \tag{5.171}$$

We find $z_0 = z_s - \frac{\bar{b}\sin(z_s)}{\bar{q}}$ from equation (5.169) where we have that at $t = 0$, $x_f = 0$. The position of the front is thus given by

$$x_f(t; z_s) = \frac{\bar{q}t^{n+1}}{n+1} - \log\left(\frac{\sin\left(z_s - \frac{\bar{b}}{\bar{q}}\sin(z_s)\left(1 - \exp\left\{\frac{\bar{q}t^{n+1}}{n+1}\right\}\right)\right)}{\sin(z_s)}\right), \quad (5.172)$$

along characteristics

$$z(t; z_s) = z_s - \frac{\bar{b}}{\bar{q}}\sin(z_s)\left(1 - \exp\left\{\frac{\bar{q}t^{n+1}}{n+1}\right\}\right). \quad (5.173)$$

Of course the general solution of (5.123) to (5.128) would have the single term in $\exp(-x)$ in (5.130) replaced by an infinite series of terms containing $\exp(-mx)$ for integers $m \geqslant 1$.

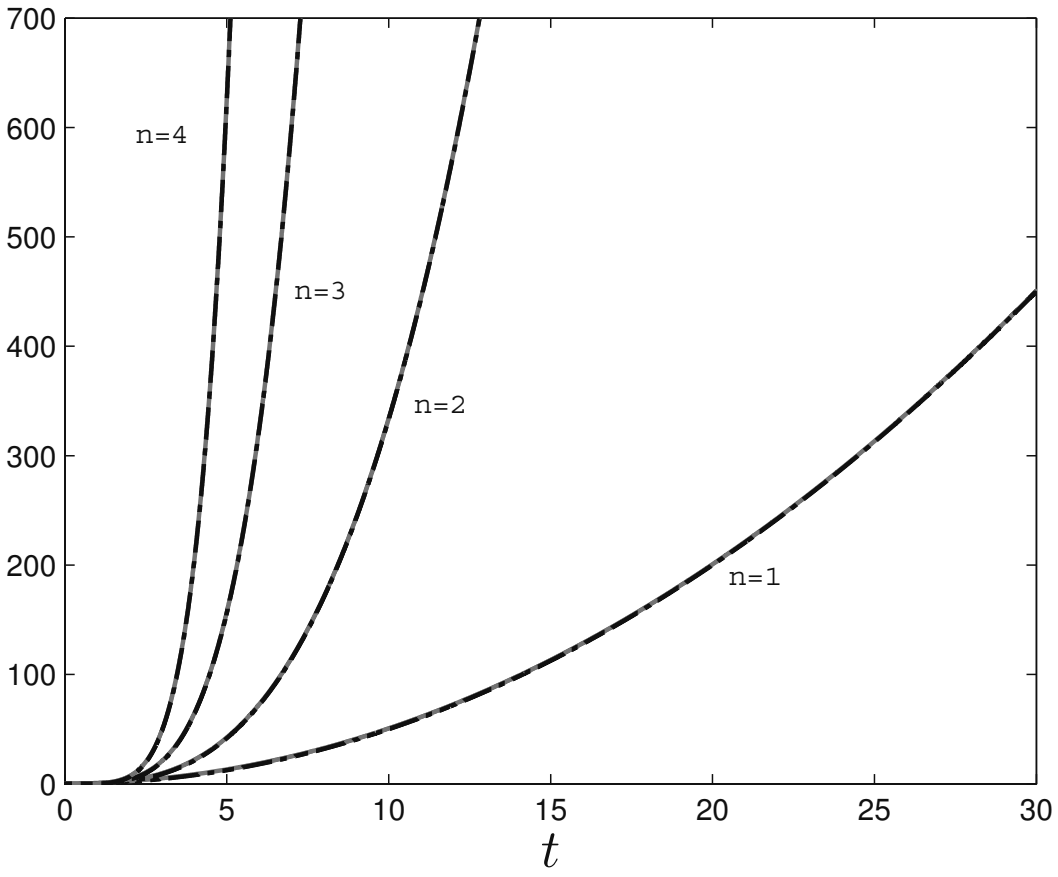

Figure 5.4: For large-n theory in three-dimensions, a comparison between front position x_f as given by equations (5.141) (solid line, for the three-dimensional evolution along $z = 0$) and (3.128) (dotted line, for the two-dimensional evolution) showing close agreement for large values of t. Plots are for $n = 1$, 2, 3, 4. Here $\bar{q} = 1$, $\bar{b} = 0.5$. See also figure 5.5

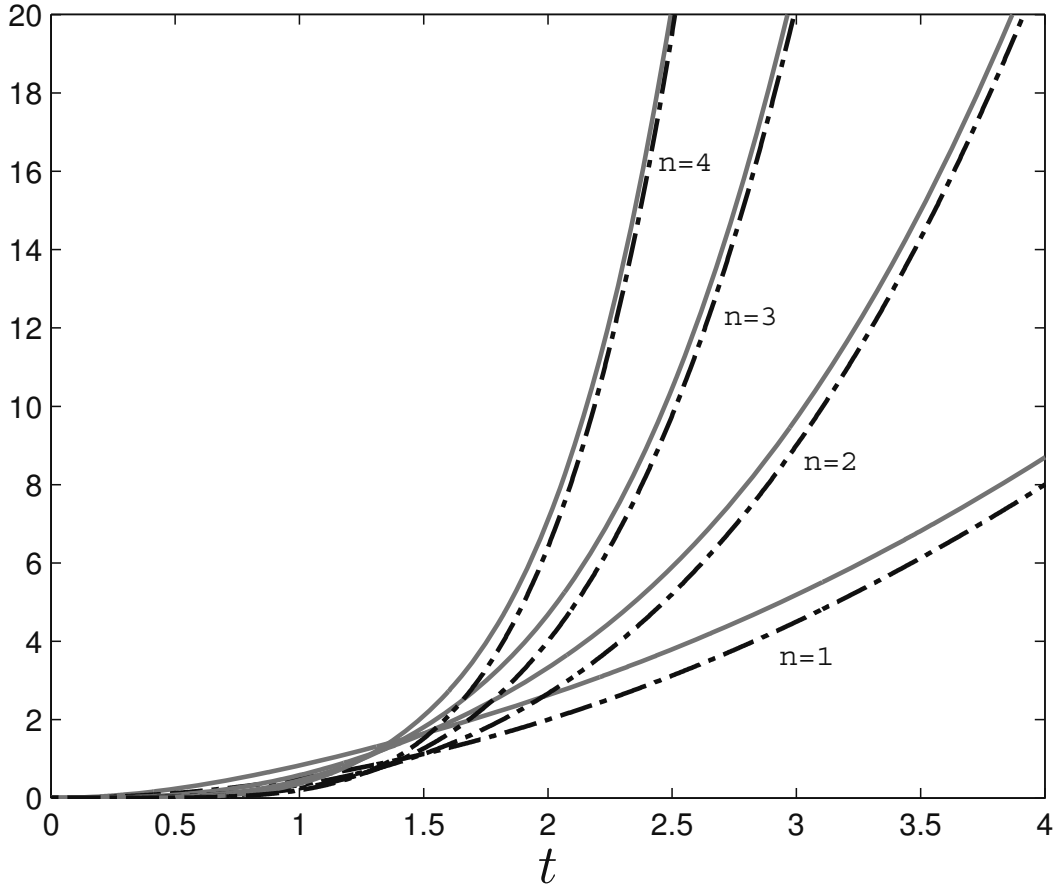

Figure 5.5: For large-n theory in three-dimensions, a comparison between front position x_f as given by equations (5.141) (solid line, three-dimensional case along $z = 0$) and (3.128) (dotted line, two-dimensional case) showing clearly the differences for order-one values of t. Plots are for $n = 1, 2, 3, 4$. Here $\bar{q} = 1$, $\bar{b} = 0.5$. See also figure 5.4

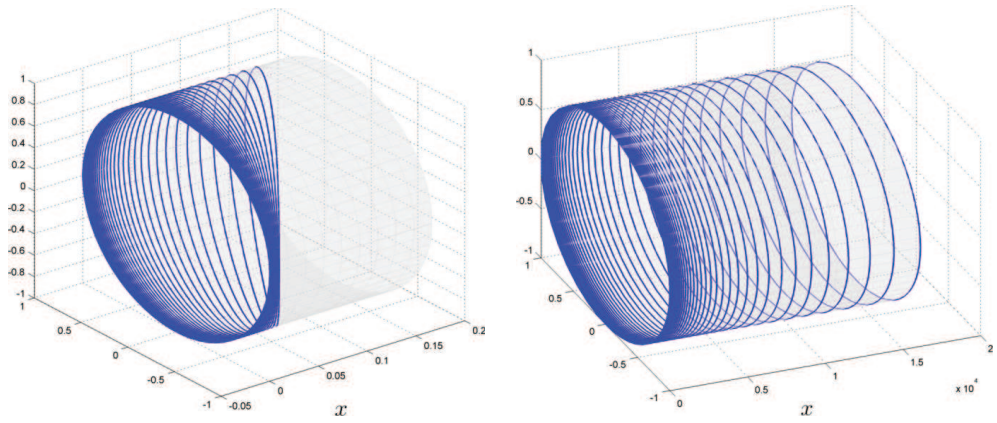

(a) Front position up to t=1 (b) Front position up to t=3

Figure 5.6: Three-dimensional front position plotted onto a tube with a normalised resting radius, for the case of (5.130). Here $n = 10$, $\bar{b} = 0.9$, $\bar{q} = 1$.

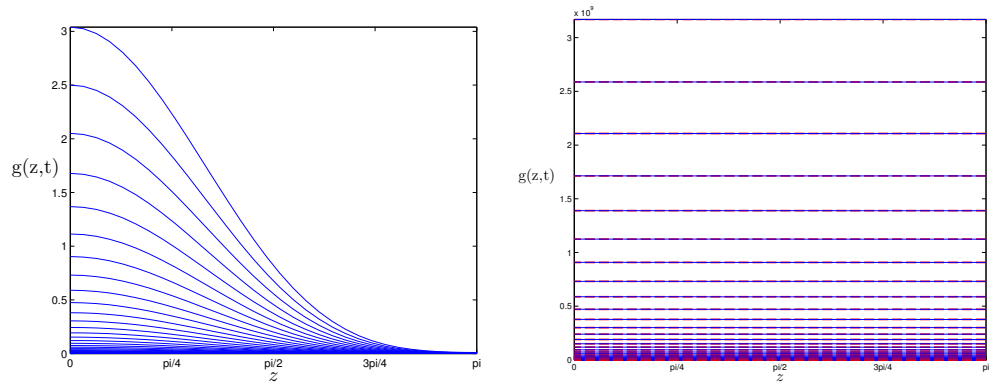

(a) Opening pressure up to t=1 (b) Opening pressure up to t=3

Figure 5.7: Opening pressure in the three-dimensional case of (5.130). Here $n = 10$, $\bar{b} = 0.9$, $\bar{q} = 1$. Dashed lines in (b) are the two-dimensional solution (3.127), showing the agreement between the three-dimensional and two-dimensional solution for larger times.

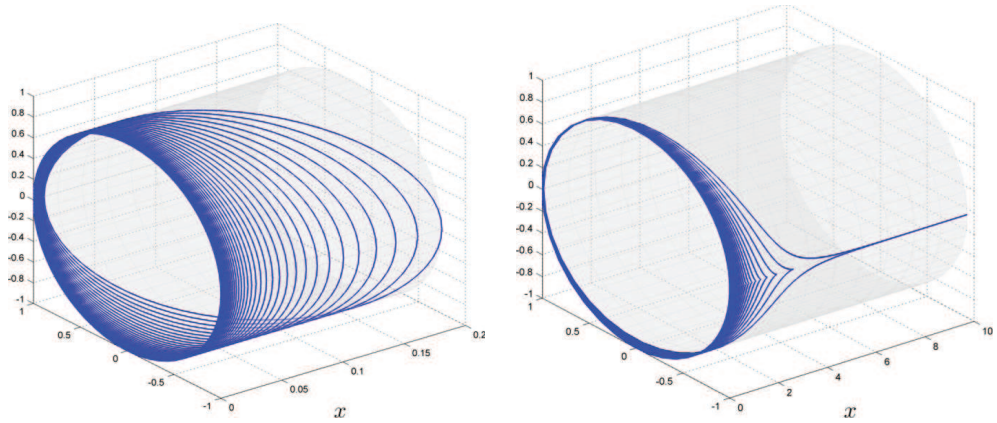

(a) Front position up to $t = 1$ (b) Front position up to $t = t_\infty$

Figure 5.8: Three-dimensional front position plotted onto a tube with a normalised resting radius, for the case of (5.158). Here $n = 10$, $\bar{b} = 0.9$, $\bar{q} = 1$ with t_∞ given by (5.168).

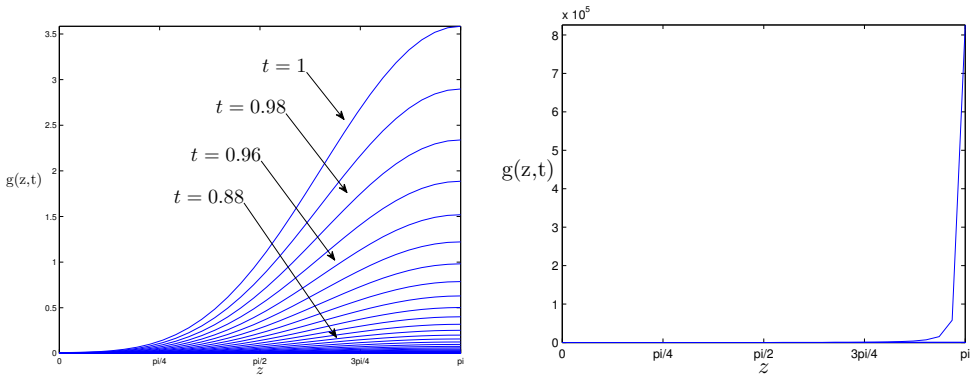

(a) Opening pressure up to $t = 1$ (b) Opening pressure up to $t = t_\infty$

Figure 5.9: Opening pressure in the three-dimensional case of (5.158). Here $n = 10$, $\bar{b} = 0.9$, $\bar{q} = 1$. We notice that on approach to $t = t_\infty$ the opening pressure tends to infinity. Here t_∞ is given by (5.168).

5.3 Summary of chapter

There are many three-dimensional avenues to investigate but perhaps the most helpful one is that connected with the fast-response situation, according to the research in this chapter. The results obtained point towards potentially high relevance to practical situations.

The behaviour found in this chapter is interesting given the connection between large-n values and pathologies of the urethra [36]. Although only a first attempt, the effects of bulging in the vessel with associated finite-time singularity suggest further investigation and demonstrate the possible importance of three-dimensional considerations in urethral modelling.

Chapter 6

Three-dimensional constriction

Following on from the three-dimensional work of the previous chapter we now consider another important case, which is more nonlinear and allows for viscous effects in a steady-flow setting. We begin by taking a long, slender, rigid tube with a smooth constriction formed by a relatively local collapse of the tube walls. The solution method adopted follows that of Bowles et al [12] for tube branching; however in this case the constriction is not severe enough to form two fully developed daughter tubes but only a local deformation in which the vessel shape returns to the undisturbed cross-section downstream. The three-dimensional effects of the constriction on the flow pressure and velocities are to be found, where far upstream a uniform axial flow is imposed. The present investigation which is numerical and analytical includes examining flow properties close to the point of greatest constriction.

6.1 Governing equations

We examine laminar flow of an incompressible fluid in three dimensions through a slender vessel as considered previously and so, going back to basic concepts again, we take an axial length scale L^* along with radial scale R^*. Here

$L^* \gg R^*$. We define an aspect ratio

$$\alpha = \frac{R}{L} \ll 1.$$

Dimensional Cartesian coordinates, (x^*, y^*, z^*), are used with x^* representing the axial direction. We then have corresponding dimensional velocity components (u^*, v^*, w^*) with dimensional pressure p^*. The Reynolds number is thus defined by

$$Re = \frac{U^* L^* \rho^*}{\mu^*} \tag{6.1}$$

where U^* is a representative axial flow velocity fixed by the upstream laminar flow profile, ρ^* is the fluid density and μ^* is the fluid viscosity. Taking now the three-dimensional time-independent Navier-Stokes equations, the following scalings are found from the continuity equation and pressure balance within the momentum equations,

$$(x^*, y^*, z^*) = (L^* x, R^* y, R^* z), \tag{6.2}$$

$$(u^*, v^*, w^*) = (U^* u, U^* \alpha v, U^* \alpha w), \tag{6.3}$$

$$p^* = \rho U^{*2} \left(p(x) + \alpha^2 P(x, y, z) \right), \tag{6.4}$$

to leading orders. Here we have scaled dimensions by their respective length scales, L^* for axial and R^* for the radial plane. The axial velocity and length scale then define a time-scale by $T^* = L^*/U^*$ which we may then use to write the typical radial velocity as $R^*/T^* = U^* R^*/L^* = U^* \alpha^*$. The non-dimensional governing equations are then

$$u_x + v_y + w_z = 0, \tag{6.5}$$

$$u u_x + v u_y + w u_z = -p_x + \bar{R}(u_{yy} + u_{zz}), \tag{6.6}$$

$$u v_x + v v_y + w v_z = -P_y + \bar{R}(v_{yy} + v_{zz}), \tag{6.7}$$

$$u w_x + v w_y + w w_z = -P_z + \bar{R}(w_{yy} + w_{zz}), \tag{6.8}$$

where we define $\bar{R} = \frac{1}{Re\alpha^2}$, which is an order-one parameter so that for fixed α a flow rate is determined. For a discussion on lubrication dominated ($Re \ll \alpha^{-2}$) and inviscid ($1 \ll \alpha^{-2} \ll Re$) flow regimes see [12].

6.2 Analysis close to the point of minimum gap

There are two flow regions to consider close to the point of greatest constriction, which is given by the point $(x, y, z) = (x_c, y_c, z_c)$. One is the core flow in which we take $x - x_c$ small with $y - y_c$ and $z - z_c$ both of order one, and the second is the region very close to the carina where $y - y_c$ and $z - z_c$ are then also small. The particular case considered herein will take a wall that comes in quadratically both in the longitudinal- and cross-planes so that $|z - z_c| \sim |y - y_c|^2$ with $|z - z_c| \sim |x - x_c|^2$ and so $|y - y_c| \sim |x - x_c|$. The powers are a result of the known wall shape.

6.2.1 Core flow

In the core flow region we have $x - x_c = \epsilon X$ say, where ϵ is a small positive parameter. Here (X, y, z) are all order-one variables. We expect a regular expansion in the axial direction with the pressure perturbation being mainly linear in $x - x_c$: thus

$$(u, v, w) = [u_0, v_0, w_0](y, z) + \epsilon X [u_1, v_1, w_1](y, z) + \ldots, \tag{6.9}$$

$$(p, P) = (p_0, P_0(y, z)) + \epsilon X (p_1, P_1(y, z)) + \ldots. \tag{6.10}$$

Substituting (6.9) and (6.10) into equations (6.5)-(6.8) gives the core-flow equations to leading order as

$$u_1 + v_{0y} + w_{0z} = 0, \tag{6.11}$$

$$u_0 u_1 + v_0 u_{0y} + w_0 u_{0z} = -p_1 + \bar{R}\left(u_{0yy} + u_{0zz}\right), \tag{6.12}$$

$$u_0 v_1 + v_0 v_{0y} + w_0 v_{0z} = -P_{0y} + \bar{R}\left(v_{0yy} + v_{0zz}\right), \tag{6.13}$$

$$u_0 w_1 + v_0 w_{0y} + w_0 w_{0z} = -P_{0z} + \bar{R}\left(w_{0yy} + w_{0zz}\right). \tag{6.14}$$

Here the velocity profile u_0, and the pressure constants p_0 and p_1 are found from the upstream flow.

6.2.2 Saddle point of the point of greatest constriction

In this local region the smooth saddle point shape is assumed given at the upper wall $z = z_+(x, y)$ such that $z_+ - z_c = A(x - x_c)^2 + B(y - y_c)^2 + \gamma$ for some constants $A, B, \gamma > 0$. The lower wall is similarly given by $z = z_-(x, y)$ with $z_- - z_c = -A(x - x_c)^2 - B(y - y_c)^2 - \gamma$. Hence we have in this region an axial scaling as in the core section along with $y - y_c = \epsilon Y$ and $z - z_c = \epsilon^2 Z$. Cross-plane variables X and Y are of order one. We expect p to scale as in the core region, in order to match. Then continuity and momentum balances provide the following expansions,

$$(u, v, w) = \left[\epsilon^4 U, \epsilon^4 V, \epsilon^5 W\right](X, Y, Z) + \ldots, \tag{6.15}$$

$$(p, P) = (p_0, Q_0) + \epsilon\left(X p_1, Q_1(X, Y, Z)\right) + \ldots, \tag{6.16}$$

with the X-dependence being more subtle here than in the core, as indicated. Here p_0, Q_0 are constants. Substitution of equations (6.15), (6.16) into the

system (6.5)-(6.8) then yields the lubrication equations

$$U_X + V_Y + W_Z = 0, \tag{6.17}$$

$$0 = -p_1 + \bar{R}U_{ZZ}, \tag{6.18}$$

$$0 = -Q_{1Y} + \bar{R}V_{ZZ}, \tag{6.19}$$

$$0 = -Q_{1Z}. \tag{6.20}$$

These are subject to no-slip on the walls with the walls given by

$$Z_+ = z_+ - z_c = AX^2 + BY^2 + 1, \tag{6.21}$$

$$Z_- = z_- - z_c = -AX^2 - BY^2 - 1, \tag{6.22}$$

where ϵ is defined by the minimum vertical half-gap width, such that $\epsilon = \sqrt{\gamma}$. In general ϵ represents some vertical scale.

Integrating (6.18) and applying the boundary conditions at the walls we obtain a solution for the axial velocity,

$$U(X, Y, Z) = -\frac{p_1}{2\bar{R}}\left(Z_+^2 - Z^2\right), \tag{6.23}$$

where we have used the fact that $Z_- = -Z_+$.

The wall shear stress on the upper wall is then given by

$$U_Z(X, Y, Z_+) = \frac{p_1}{\bar{R}}\left(X^2 + Y^2 + 1\right). \tag{6.24}$$

Next, we find from equation (6.20) that

$$Q_1 = Q_1(X, Y),$$

is independent of Z and so integrating (6.19) with respect to Z there is the balance

$$V(X, Y, Z) = -\frac{Q_{1Y}}{2\bar{R}}\left(Z_+^2 - Z^2\right). \tag{6.25}$$

Finally we integrate the continuity equation (6.17) over the gap width, substituting in (6.24), (6.25) and applying the no-slip condition on the top wall, Z_+, to find W such that

$$2\bar{R}W(X,Y,Z) = p_1\left\{\frac{\partial\left(Z_+^2\right)}{\partial X}\left(Z-Z_+\right)\right\} + Q_{1Y}\left\{\frac{\partial\left(Z_+^2\right)}{\partial Y}\left(Z-Z_+\right)\right\} + \\ + Q_{1YY}\left\{\frac{\left(Z_+^3-Z^3\right)}{3} + Z_+^2\left(Z-Z_+\right)\right\}, \tag{6.26}$$

where we have again used symmetry for simplification.

If we now apply the lower wall no-slip condition and introduce the gap width $H(X,Y) = Z_+ - Z_- = 2Z_+$, then (6.26) becomes

$$0 = p_1\frac{\partial H^3}{\partial X} + Q_{1Y}\frac{\partial H^3}{\partial X} + Q_{1YY}H^3, \tag{6.27}$$

which upon rearranging and integrating with respect to Y becomes the Reynolds lubrication equation

$$Q_{1Y}H^3 = -p_1\int\frac{\partial\left(H^3\right)}{\partial X}\,\mathrm{d}Y, \tag{6.28}$$

allowing the pressure correction $Q_1(X,Y)$ to be found given the known gap width $H(X,Y)$ and the pressure constant p_1.

6.3 Numerical solutions

Numerical results are obtained using the method outlined in [12] where a detailed description can be found.

The system given by equations (6.5)-(6.8) is parabolic and so as long as the axial velocity u remains positive there is no upstream influence. It is therefore possible to apply a forward marching scheme in the axial direction, starting at some point upstream and continuing through the carina. We apply boundary

conditions of no slip on all of the walls and an initial velocity profile at the starting point upstream. Mass flux is fixed with the flow far upstream of the carina taken to be fully developed parallel flow.

As the scheme marches forward toward the carina, a pinching of the vessel wall occurs. This is handled numerically by modification of the grid at each x-station. [77], [82].

Numerical results can be seen in figures (6.1), (6.2), (6.3),(6.4) and were kindly provided by Professor Smith. There are two main cases that we examine. The first being vessels that are symmetric (section 6.3.1) about the plane given by $Z = 0$ and the second being non-symmetric (section 6.3.2) where only the upper wall is allowed to constrict, with the lower wall remaining circular and rigid. Grid effects are shown in section 6.3.3.

6.3.1 Symmetric cases

Results were calculated for symmetric constrictions (about the horizontal plane $Z = 0$) for a widening vessel (figure 6.1), a severe constriction of a non-tapering vessel (figure 6.2) and a mild constriction of a non-tapering vessel (figure 6.3). The velocities along the midline and pressures were found in each case all showing qualitatively similar results in that a pressure drop is observed. In figure (6.2(b)) the zero midline velocity is a result of the constriction completely obscuring that section of vessel. The equation used for the vessel wall here is

$$Z_+ = (1 + rF(X)) \left\{ 1 - \left(\frac{Y}{1 + rF(X)} \right)^2 \right\}^{\frac{1}{2}} - \frac{hF(X)}{1 + 8Y^2}, \tag{6.29}$$

where

$$F(X) = \begin{cases} \left(\frac{X}{X_2} \right)^2 & \text{for} \quad X \leqslant X_2, \\ \frac{2X - X_2}{X_2} & \text{for} \quad X > X_2 \end{cases}, \tag{6.30}$$

and $Z_+ = Z_-$. Here h is a parameter to be set and $X_2 = 1$. In the expanding vessel $r = 1.2$ whereas in the non-tapering vessels $r = 0$.

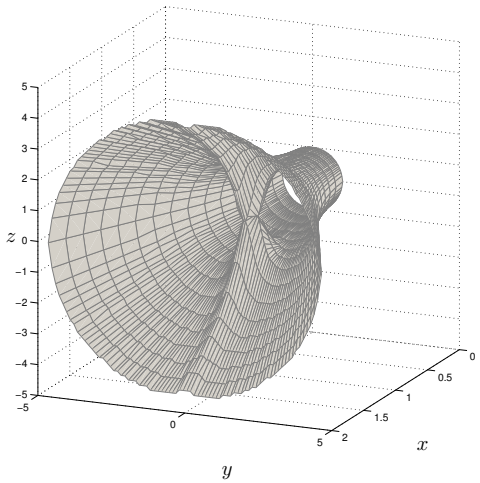

(a) Three-dimensional plot of vessel shape where the positive direction of x is "out of the page".

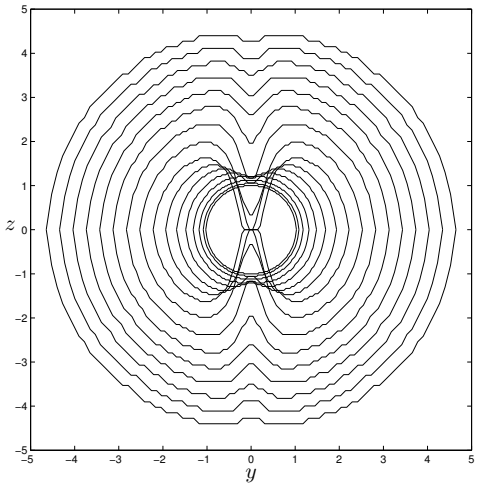

(b) Cross-sectional plot showing the development of two daughter vessels and subsequent rejoining into a single (larger) vessel

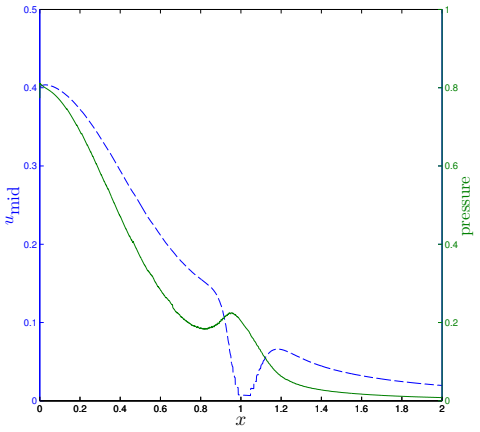

(c) Plot of pressure (solid) and axial velocity (dashed) against x along the midpoint given by $y = z = 0$

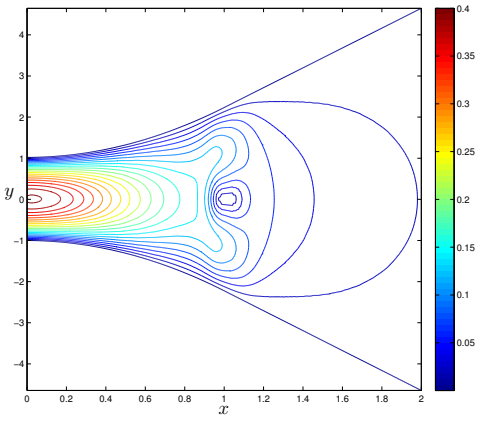

(d) Contour plot showing the axial velocity profile in the plane $z = 0$

Figure 6.1: Widening vessel exhibiting a symmetric constriction that briefly results in two daughter vessels, with the point of greatest constriction taken to be $x = 1$. Here the grid step-sizes are $dy = dz = 2.67^{-2}$ and $dx = 5 \times 10^{-4}$.

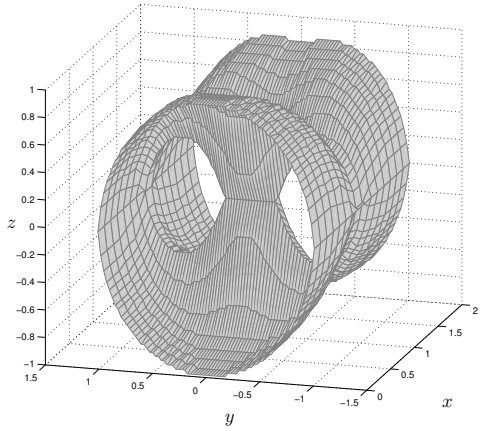

(a) Three-dimensional plot of vessel with severe symmetric constriction resulting in the brief development of two daughter vessels.

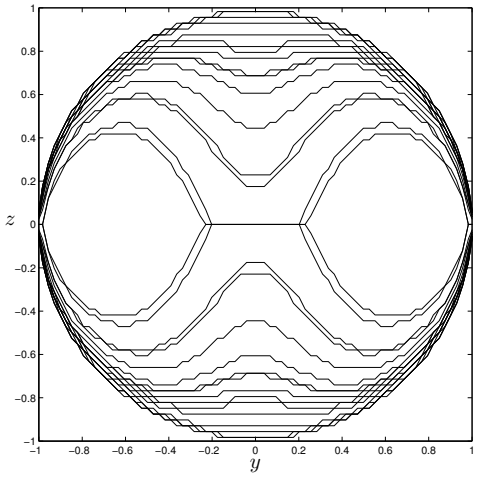

(b) Cross-sectional plot showing the development of the symmetric constriction

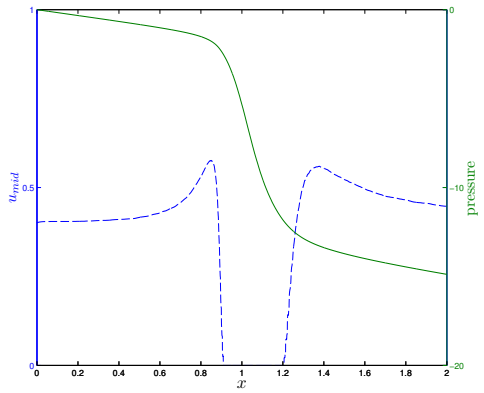

(c) Plot of axial velocity (dashed) and pressure (solid) against x along the midpoint $y = z = 0$.

Figure 6.2: A non-tapering vessel exhibiting a constriction resulting in two daughter vessels which rejoin. The point of greatest constriction is taken to be $x = 1$ where the upper and lower walls first touch (or converge). The cross-section of the vessel is shown. Here the grid step-sizes are $dy = dz = 2.67^{-2}$ and $dx = 5 \times 10^{-4}$.

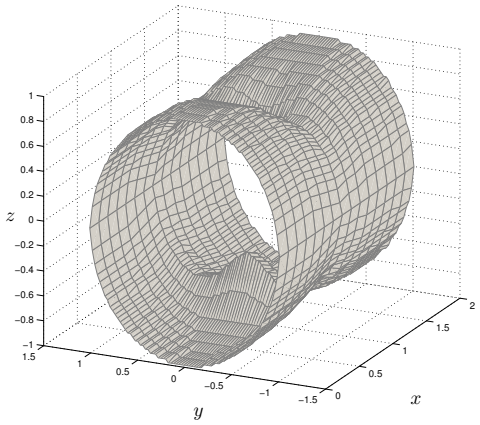

(a) Three-dimensional plot of vessel with a mild symmetric constriction.

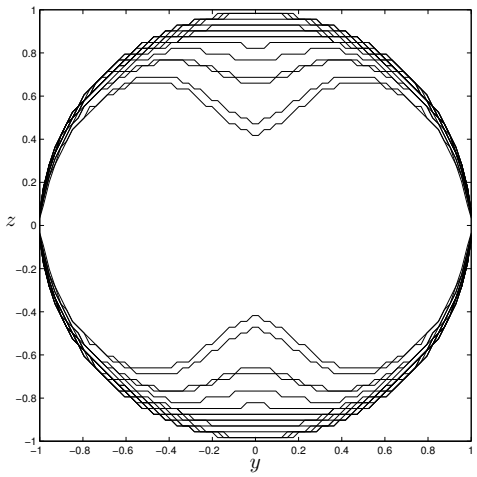

(b) Cross-sectional plot showing the development of the mild symmetric constriction

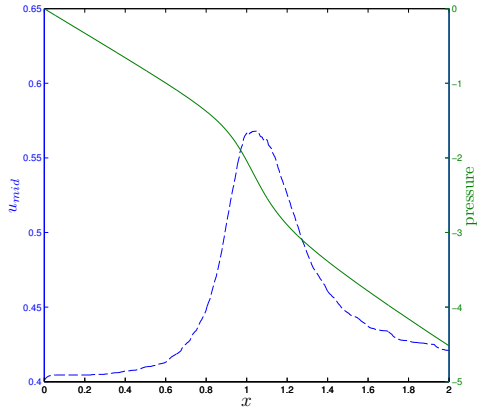

(c) Plot of axial velocity (dashed) and pressure (solid) against x along the midpoint $y = z = 0$.

Figure 6.3: A milder symmetric case. Here the constriction causes partial collapse of the vessel with the walls not touching. The cross-section of the vessel is shown with the the point of greatest constriction taken to be $x = 1$. Here the grid step-sizes are $dy = dz = 2.67 \times 10^{-2}$ and $dx = 5 \times 10^{-4}$.

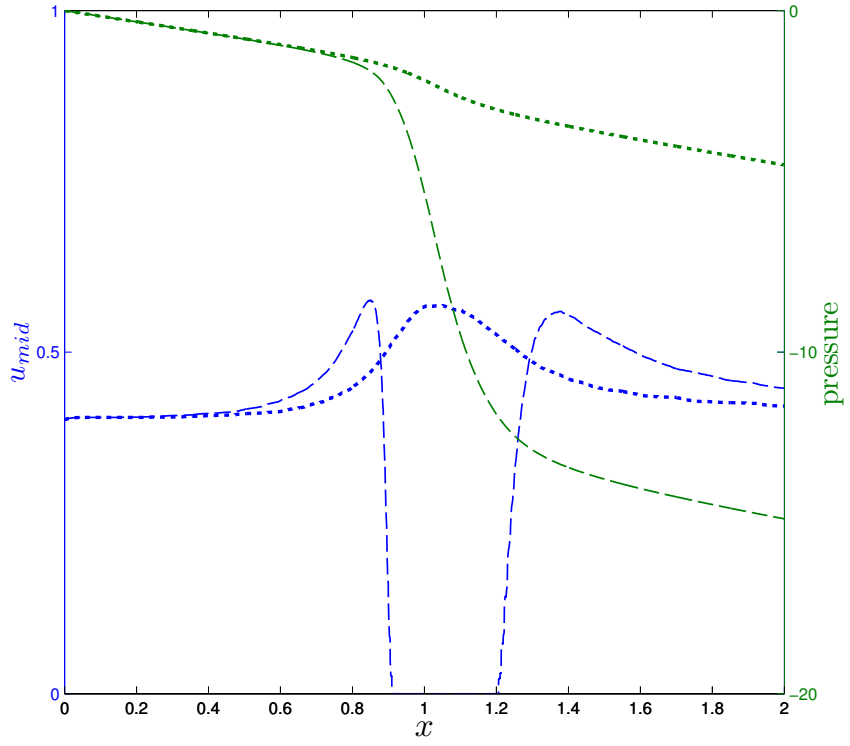

Figure 6.4: Direct comparison of symmetric cases as shown in 6.2(b) (dashed) and 6.3(c) (dotted).

6.3.2 Non-symmetric cases

Non-symmetric cases were tackled with the aim of being closer to the reality of an enlarged prostate (see chapter 1) whereby the constriction tends to intrude on one side of the vessel. Three cases were computed with varying amounts of constriction (figures 6.5 and 6.6). Again, qualitatively similar results can be seen where the vessel sees a pressure drop going through the constriction. The non-symmetric case has walls given by

$$Z_+ = \left\{1 - Y^2\right\}^{\frac{1}{2}} - \frac{hF(X)f(X)}{1+8Y^2}, \tag{6.31}$$

where

$$F(X) = \begin{cases} \left(\frac{X}{X_2}\right)^2 & \text{for} \quad X \leqslant X_2, \\ \frac{2X - X_2}{X_2} & \text{for} \quad X > X_2 \end{cases}, \tag{6.32}$$

$$f(X) = \frac{A_L}{1 + \frac{(X-X_2)^2}{e_L^2}} \tag{6.33}$$

and $Z_- = \sqrt{1-Y^2}$. Here h is a parameter to be set, $e_L = X_2/5$ and $X_2 = 1$. The strength of the constriction is controlled by the parameter A_L.

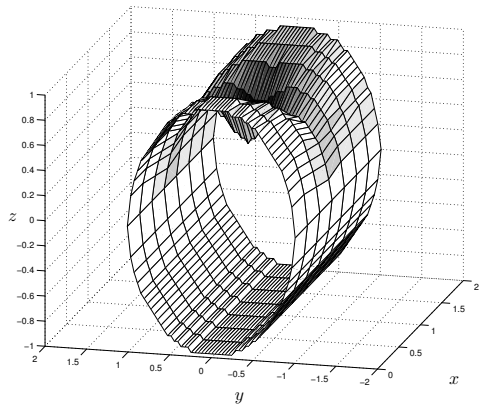

(a) Three-dimensional plot for $A_L = 0.2$ case; a mild non-symmetric constriction. Here $dx = 10^{-3}$, $dy = dz = 4 \times 10^{-2}$

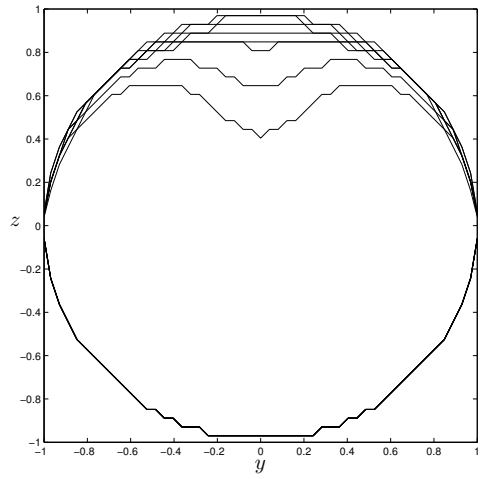

(b) Cross-section of the mild non-symmetric case

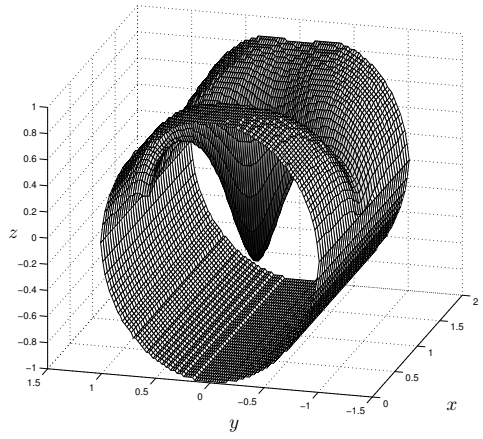

(c) Three-dimensional plot for $A_L = 0.5$ case; a non-symmetric constriction. Here $dx = 10^{-3}$, $dy = dz = 2 \times 10^{-2}$

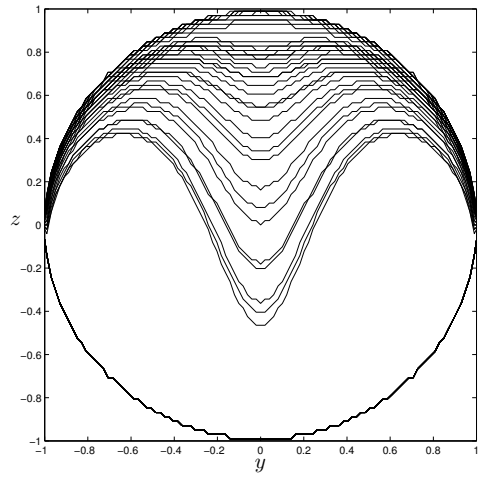

(d) Cross-section of the non-symmetric $A_L = 0.5$ case

Figure 6.5: Non-symmetric constriction cases.

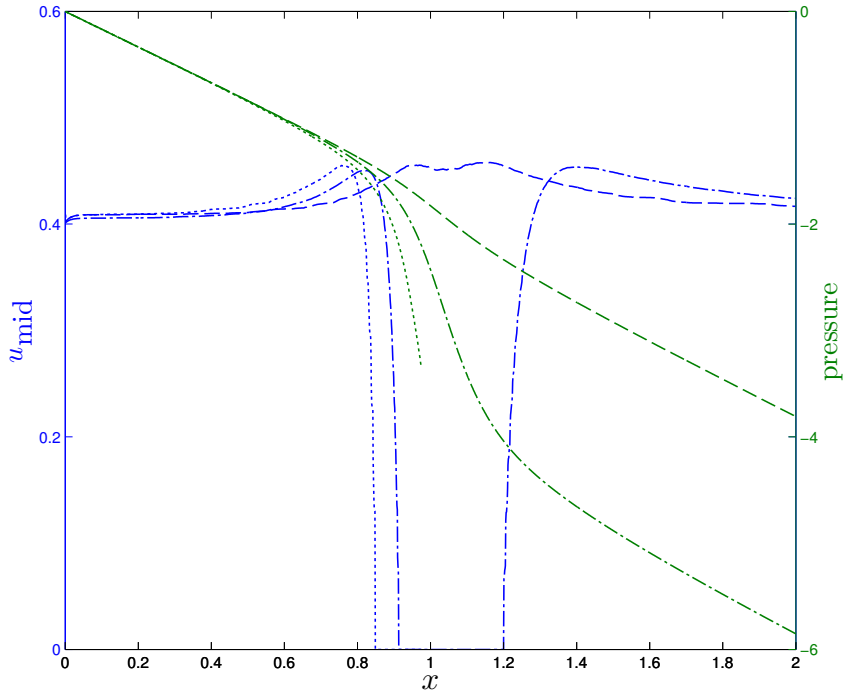

Figure 6.6: Comparison of pressure and axial velocity along the mid-line for the non-symmetric cases $y = z = 0$ for $A_L = 0.2$ (dashed), $A_L = 0.5$ (dash-dotted), $A_L = 0.75$ (dotted).

6.3.3 Grid tests

Grid tests were carried out in order to check for grid effects. The results for two tests are shown in figure 6.7 where we see good agreement between the different grid sizes.

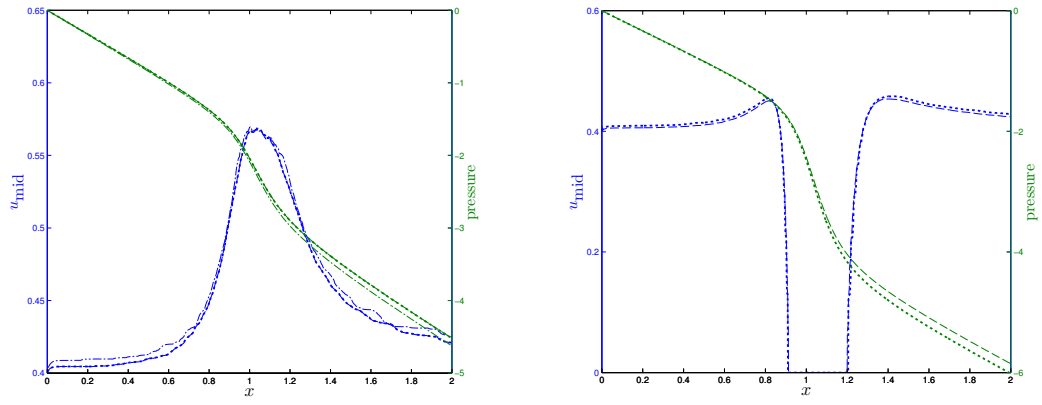

(a) (b)

Figure 6.7: Grid tests with (a) the mild symmetric case showing $dx = 5\times10^{-4}$, $dy = 2.67 \times 10^{-2}$ (dashed); $dx = 10^{-3}$, $dy = 2.67 \times 10^{-2}$ (dotted); $dx = 10^{-3}$, $dy = 4 \times 10^{-2}$ (dash-dotted) and (b) the nonsymmetric $A_L = 0.5$ case showing $dx = 5 \times 10^{-4}$ $dy = 2 \times 10^{-2}$ (dashed); $dx = 5 \times 10^{-4}$, $dy = 4 \times 10^{-2}$ (dotted).

6.4 Summary of chapter

Again the three-dimensional regime appears to produce a model and results which are fairly sensible physically as well as fairly realistic, if only potentially so, in regard to the application to the original medical context. The predictions for the induced internal pressures for example are valuable in principle then. This model is appropriate for urethral strictures which are an abnormal narrowing of the urethra. Typically these exhibit a decreased force of urinary stream, which can be seen here as a pressure drop through the constriction. Some caution should be taken, however, as in general the bladder will attempt

to compensate by increasing the pressure, which is not modelled here. Also to note is the fact that flexible walls have been neglected here and could have a significant affect on the flow.

Part II

Heterogeneous population modelling

Chapter 7

Describing the context

The following work arose from an opportunity of an internship which was taken up by the author in 2008 at Unilever UK, sponsored through the Knowledge Transfer Network in industrial mathematics by EPSRC. The link with the other part of the thesis study was spotted in discussions involving the author and his first supervisor. The present part appeared in an issue of Advances in Complex Systems in 2010 ([68]), joint authored with the industrial supervisor Dr Abhijit Sengupta. The work focused on the heterogeneity of shoppers, its effect on purchasing decisions and possible predictions of purchases.

The relationship between Parts I and II comes from their focus on heterogeneous populations. Since the approaches of this part are quite different from those of Part I, however, the bulk of Part II is placed in an appendix (Appendix B) of the thesis. It is possible to relate the choice of products by shoppers to aspects of Part I by considering, for example, a decision of treatment by a GP or surgeon for individuals who exhibit a set of symptoms (or characteristics in the language of Part II).

It is also possible to find another connection. This is in terms of a conceptual

model with a governing equation

$$\frac{dP}{dt} = gB - hC. \tag{7.1}$$

Here in the context of Part I firstly P represents the probability that a person chooses to have a clinical operation (for instance concerning difficulties with a prostate gland), B stands for the benefits of an operation and C stands for the costs which may include financial costs to the patient, NHS costs as well as more general costs such as physical ones. The terms g, h are coefficients which are generally positive, and we note P could also denote implicitly the number of people taking the option. The values of the contributions B, C in individual cases depend on the typical results shown in Part I in the sense that for example an operation can alter the properties of the urethral walls and hence beneficially affect the urinary flows and pressures. The same equation holds, secondly, in the balance of effects discussed in Part II as described in Appendix B. Additional work in this context has been carried out as an MSc project by Vasundhara Misra at UCL [56].

Part III

Conclusion

Chapter 8

Final Discussion

This thesis has examined through mathematical modelling what we regard as some central issues concerned with the fluid flow in a model of the urethra with the problems of incontinence either in mind or regarded as motivation. This has been done in two parts, firstly via a physical model of the flow through various types of specific distensible vessel and secondly via looking more widely at heterogenous populations who might exhibit certain pathologies which raise the the option of going to surgery. In the following we now summarise each chapter, starting of course with Part I.

- In chapter 2 we derived a one-dimensional mathematical model involving cross-sectional averaged quantities as others have done before in the context of large blood vessels. We introduced a simple representative tube law (i.e. pressure-area relation) and then began analysing the main governing equations and boundary conditions for early opening times and for short-scale alterations in the tube properties. This included for example bends or sudden changes in distensibility.

- Following on from the work in the previous chapter, chapter 3 studied the early time opening in much more detail, seeking special solutions

and inspecting specifically both slow- and fast-response materials (for the vessel wall). In this context, a start was also made on more general two-dimensional modelling. Various solution properties of interest were discussed. Fast-response vessels are of particular interest considering their relevance to pathologies.

- Chapter 4 then introduced numerical methodology and corresponding results, beginning with a relatively simple finite difference scheme applied to the full original partial differential equations found in chapter 2 and allowing accurate and reliable front tracking. Short scale changes within the long scale framework were also examined in greater detail in order to shed light on the non-existence of the quasi-steady solutions in certain circumstances shown in chapter 2. Burgers equation in particular was found to be relevant in certain circumstances; this was solved numerically and the existence of finite-time singularities shown, which imply that short-scale behaviour can emerge eventually in the flexible vessel. The downstream movement of disturbances could be important in detecting and locating changes in the vessel distensibility.

- Three-dimensionality was acknowledged in chapter 5 for relatively mild tortuosity as well as large-n effects associated with fast responses in a longitudinal vortex system and also in a thin-region flow setting. The three-dimensionality was found to yield potentially more realistic responses to the system and demonstrates the potential importance of three-dimensional with regards to pathologies of the urethra.

- Continuing in three dimensions, the fully three-dimensional effects of a constriction were examined in chapter 6, with its importance owing to pathologies such as benign prostatic hyperplasia and strictures. A number of cases were examined and resultant pressure effects found. The

results are quite sensible physically in addition to being fairly realistic for medical applications.

Part II then followed.

- Part II consisted of chapter 7 which considered related features of population modelling through the use of an agent based model in effect. There are reasonably clear links between the choice model presented in chapter 7 (and an appendix) and the probabilities of electing for surgery based on the perceived benefits and disadvantages as seen by the clinician or surgeon.

8.1 Future Work

We may now list some clear possible future extensions and allied areas of work, as follows.

- Addition of network effects in part II - this could include such social dynamics as gossip about friends operations, etc.
- Exploiting the links described above for part II could also be worthwhile.
- Current urodynamics is of much concern - for example the fact of introducing a catheter to measure pressures in itself may alter the pressures or characteristics of the urethra. Further research would seem warrented here.
- Emerging flow at the exit from the urethra- similar to jets from nozzles. Inviscid incompressible fluid falling under gravity is addressed in [24]. Steady and two-dimensional numerical work shows two flows are possible one in which fluid falls down the underside of the nozzle and another where the flows splits into two sheets. Important flow parameters are the

angle above the horizontal at which the nozzle is aimed and the Froude number. Potential flows issuing from a two-dimensional curved nozzle are in [84]. A round jet (axi-symmetric) of inviscid fluid under gravity with a nozzle of slowly varying profile, treated by matching asymptotics, is in [45]. Slender streams are in [32], with astymptotic methods for thin potential flows and a mixture of rigid or free-boundaries in two dimensions. Clearly there are many relevant routes to be explored further.

- Breakup of jets - this is important in some urodynamical tests. A review is given in [52]

- Full numerical three-dimensional simulation could include wall effects on a flexible vessel with viscous flow. This ties in with the eventual emphasis in the present thesis on three-dimensional modelling and the importance of three-dimensionality in terms of the effects produced. This is especially so, we feel, for the potential application to urethral properties.

Appendix A

KdV-like behaviour

The following work is a collaboration with Professor Jean-Marc vanden Broeck who also kindly provided the numerical results. The ideas are similar to those mentioned in sections 2.4 and 4.2 where we allow the vessel distensibility to alter over some region. In this case we work from a KdV perspective and view the distensibility alteration in the context of an applied pressure distribution as seen in free-surface problems.

A.1 Introduction

We begin with a two-dimensional vessel which is assumed symmetric about the horizontal centre-line. We thus consider only the upper half plane, replacing the centre-line by a rigid impermeable wall (or boundary). The upper wall takes the role of an unknown free-surface and we continue in the context of a free-surface problem for an inviscid fluid. We denote the undisturbed depth as h_0 (or perhaps the vessel radius for circular vessels) and assume the horizontal direction to be infinite but with a characteristic length scale $L \gg h_0$. Surface disturbances (or changes in vessel radius) are described by $\eta(x,t)$ and are characterised by an amplitude α. The fluid depth is thus given by $h(x,t) =$

$h_0 + \eta(x,t)$.

We define non-dimensional parameters

$$a = \frac{\alpha}{h_0},$$
$$b = \left(\frac{h_0}{L}\right)^2,$$

which are the characteristic relative disturbance amplitude and the characteristic vessel aspect ratio respectively. In the following we consider small amplitude disturbances on the surface of a slender vessel and so $a, b \ll 1$.

Defining velocity potential $\Phi(x,y,t)$ we have the following governing equations for continuity and momentum along with boundary conditions on a lower fixed wall $y = 0$ and upper free-surface $y = h(x,t)$ given by

$$\Phi_{xx} + \Phi_{yy} = 0, \quad 0 < y < h(x,t), \tag{A.1}$$
$$\Phi_t + \frac{1}{2}\left(\Phi_x^2 + \Phi_y^2\right) + P(x,t) = 0, \quad y = h(x,t), \tag{A.2}$$
$$\Phi_y = 0, \quad y = 0, \tag{A.3}$$
$$h_t + \Phi_x h_x - \Phi_y = 0, \quad y = h(x,t), \tag{A.4}$$

where subscripts denote partial differentiation and $P(x,t)$ is the fluid pressure.

We now define a pressure-wall relation (see section 2.1.3) which we take to be

$$P(x,t) = A_0 + \beta(x) h^n(x,t), \tag{A.5}$$

with A_0 a constant and, as in the previous chapters, β representing the distensibility of the vessel. We allow P to be perturbed by introducing a perturbation to a constant distensibility parameter through

$$\beta(x) = \beta_0 + a^2 \beta_0 \beta_1(x), \tag{A.6}$$

where β_0 is a constant. In the undisturbed state we define $P = 0$ and so have

$$A_0 = -\beta_0 h_0^n. \tag{A.7}$$

Substituting equations (A.6) and (A.7) into (A.5) the pressure becomes

$$P(x,t) = a^2\beta_0\beta_1 h_0^n + \sum_{r=1}^{n} \binom{n}{r} h_0^{n-r}\eta^r\beta_0\left(1+\beta_1 a^2\right), \tag{A.8}$$

where $\binom{n}{r} = \frac{n!}{(n-r)!r!}$ and into which we substitute the non-dimensional constants

$$g = n\beta_0 h_0^{n-1}, \quad c_0 = \sqrt{gh_0}, \tag{A.9}$$

which represent gravity and a characteristic wave speed respectively. We also non-dimensionalise by $x = L\tilde{x}$, $y = h_0\tilde{y}$, $\eta = \alpha\tilde{\eta}$, $t = \frac{L}{c_0}\tilde{t}$, $\Phi = \frac{gL\alpha}{c_0}\tilde{\Phi}$, where tildes denote order one variables. Equation (A.8) is thus

$$P\left(\tilde{x},\tilde{t}\right) = \frac{c_0^2 a^2}{n}\left(\beta_1 + \sum_{r=1}^{n}\binom{n}{r}\tilde{\eta}^r\left(1+\beta_1 a^2\right)a^{r-2}\right) \tag{A.10}$$

and governing equations (A.1)-(A.4) in non-dimensional form are therefore

$$b\Phi_{xx} + \Phi_{yy} = 0, \quad 0 < y < 1 + a\eta \tag{A.11}$$

$$\begin{aligned}\Phi_t + \frac{a}{2}\left(\Phi_x^2 + \frac{1}{b}\Phi_y^2\right) = &-\frac{\beta_1 a}{n} - \\ &-\frac{1}{n}\sum_{r=1}^{n}\binom{n}{r}\eta^r\left(1+\beta_1 a^2\right)a^{r-1}, \quad y = 1 + a\eta\end{aligned} \tag{A.12}$$

$$\Phi_y = 0, \quad y = 0 \tag{A.13}$$

$$\eta_t + a\Phi_x\eta_x - \frac{1}{b}\Phi_y = 0, \quad y = 1 + a\eta. \tag{A.14}$$

where tildes have been dropped for convenience.

Equations (A.11) and (A.13) have solution

$$\Phi = \sum_{m=0}^{\infty}(-1)^m\frac{y^{2m}}{2m!}\frac{\partial^{2m} f(x,t)}{\partial x^{2m}}b^m. \tag{A.15}$$

Substituting this into equations (A.12) and (A.14) we obtain surface condi-

tions

$$f_t + \frac{f_x^2 a}{2} + \frac{\beta_1 a}{n} + \frac{1}{n}\sum_{r=1}^{n}\binom{n}{r}\eta^r\left(1+\beta_1 a^2\right)a^{r-1}$$
$$-\frac{(1+a\eta)^2}{2}\left(f_{xxt} + f_x f_{xxx} a - f_{xx}^2 a\right)b + O\left(b^2\right) = 0, \tag{A.16}$$

$$\eta_t + \left\{(1+a\eta)\, f_x\right\}_x$$
$$-\left(\frac{1}{6}(1+a\eta)^3 f_{xxxx} + \frac{1}{2}a(1+a\eta)^2\eta_x f_{xxx}\right)b + O\left(b^2\right) = 0. \tag{A.17}$$

Letting $w = f_x$, which is the leading order horizontal velocity, and substituting into the partial derivative of (A.16) with respect to x and equation (A.17) there is

$$w_t + aww_x + \frac{\beta_{1x}a}{n} + \frac{1}{n}\sum_{r=1}^{\min(3,n)}\binom{n}{r} r\eta_x\eta^{r-1}a^{r-1}$$
$$+\frac{1}{n}\sum_{r=1}^{\min(1,n)}\binom{n}{r}\left(r\eta_x\eta^{r-1}\beta_1 + \eta^r\beta_{1x}\right)a^{r+1} - \frac{w_{xxt}b}{2} = 0, \tag{A.18}$$

$$\eta_t + \left\{(1+a\eta)\, w\right\}_x - \frac{b}{6}w_{xxx} = 0. \tag{A.19}$$

Terms of $O\left(a^3, ab, b^2\right)$ have been dropped.

A.2 KdV approximation.

Keeping terms up to $O(a, b)$ of equations (A.18) and (A.19) leaves

$$w_t + aww_x - \frac{1}{2}bw_{xxt} + \eta_x + (n-1)\,\eta\eta_x a + \frac{1}{n}\beta_{1x}a = 0, \tag{A.20}$$

$$\eta_t + \left\{(1+a\eta)\, w\right\}_x - \frac{b}{6}w_{xxx} = 0, \tag{A.21}$$

which to leading order are

$$w_t + \eta_x = 0, \tag{A.22}$$

$$\eta_t + w_x = 0. \tag{A.23}$$

These two equation reduce to

$$\eta_t + \eta_x = 0 \tag{A.24}$$

for

$$w = \eta. \tag{A.25}$$

Having found the leading order relationship between w and η we now substitute a solution of the form

$$w = \eta + aA\left(x,t\right) + bB\left(x,t\right) + O\left(a^2 + b^2\right), \tag{A.26}$$

into equations (A.20) and (A.21) which become

$$\eta_t + \eta_x + \left(A_t + n\eta\eta_x + \frac{1}{n}\beta_{1x}\right)a + \left(B_t - \frac{1}{2}\eta_{xxt}\right)b = 0, \tag{A.27}$$

$$\eta_t + \eta_x + \left(A_x + 2\eta\eta_x\right)a + \left(B_x - \frac{1}{6}\eta_{xxx}\right)b = 0, \tag{A.28}$$

respectively. By use of the leading order equations (A.24), (A.25) the following relations are found $A_t = -A_x$, $B_t = -B_x$ and $\eta_{xxt} = -\eta_{xxx}$ which we substitute into equation (A.27) to leave

$$\eta_t + \eta_x + \left(-A_x + n\eta\eta_x + \frac{1}{n}\beta_{1x}\right)a + \left(-B_x + \frac{1}{2}\eta_{xxx}\right)b = 0. \tag{A.29}$$

Comparing a and b terms of equations (A.28) and (A.29) provides equations for A and B,

$$A = \frac{(n-2)}{4}\eta^2 + \frac{1}{2n}\beta_1, \tag{A.30}$$

$$B = \frac{1}{3}\eta_{xx} \tag{A.31}$$

where the constants of integration have been taken to be zero.

Combining equations (A.26), (A.30) and (A.31) we obtain the relation

$$w = \eta + \left(\frac{(n-2)}{4}\eta^2 + \frac{1}{2n}\beta_1\right)a + \frac{b}{3}\eta_{xx} + O\left(a^2 + b^2\right), \tag{A.32}$$

along with

$$\eta_t + \eta_x + \frac{(n+2)}{2}\eta\eta_x a + \frac{b}{6}\eta_{xxx} = -\beta_{1x}\frac{a}{2n}, \tag{A.33}$$

a forced KdV equation for $\beta_{1x} \neq 0$.

It is convenient to rewrite (A.33) in terms of the dimensional variables and so using $\hat{x} = Lx$, $\hat{\eta} = \alpha\eta$, $\hat{t} = \frac{L}{c_0}t$ along with $a = \frac{\alpha}{h_0}$ and $b = \left(\frac{h_0}{L}\right)^2$ where hats denote dimensional veriable, we obtain

$$\eta_t + c_0\eta_x + \frac{(n+2)}{2}\frac{c_0}{h_0}\eta\eta_x + \frac{c_0 h_0^2}{6}\eta_{xxx} = -c_0 h_0\beta_{1x}\frac{a^2}{2n}, \tag{A.34}$$

where hats have been dropped for convenience. Equation (A.34) has been studied intensively. When its right hand side is zero, it models waves propagating at the surface of a fluid of small depth. Classical solutions are then periodic cnoidal waves and solitary waves (see [90] for a review and other references). When the right hand side is different from zero, (A.33) describes free surface flows past a disturbance in shallow water. The disturbance can be a submerged object or a prescribed distribution of pressure. There are then various types of solutions which are classified as subcritical, supercritical and critical flows (see [7], [10], [23], [29], [48], [70] and the references therein). We shall here concentrate on the equivalent to our model of the critical solutions.

NOTE let $\eta = pz + q$, with $q - -\frac{2}{a(n+2)}$, $p = -\frac{u_c}{aa_c}$, cf eqn 4.36 having $a_0 = 0$. (considering full depth - same Burger approximation 4.2).

We assume that the flow is steady in a frame of reference moving at the velocity c. Therefore we write

$$\eta(x,t) = f(X) \quad \text{where} \quad X = x - ct \tag{A.35}$$

Substituting (A.35) into (A.34) gives the ordinary differential equation

$$\left(1 - \frac{c}{c_0}\right)\eta_x + \frac{(n+2)}{2}\frac{1}{h_0}\eta\eta_x + \frac{h_0^2}{6}\eta_{xxx} = -h_0\beta_{1x}\frac{a^2}{2n} \tag{A.36}$$

Integrate (A.36) with respect to x gives

$$\left(1-\frac{c}{c_0}\right)\eta+\frac{(n+2)}{2}\frac{1}{2h_0}\eta^2+\frac{h_0^2}{6}\eta_{xx}=-h_0\beta_1\frac{a^2}{2n}+A \tag{A.37}$$

where A is a constant of integration.

We assume, without loss of generality, that

$$\beta_1(x)\to 0 \quad \text{and} \quad \eta(x)\to 0 \quad \text{as} \quad x\to-\infty, \tag{A.38}$$

representing the undisturbed vessel radius before the change in distensibility. It follows from (A.37) that $A=0$.

For the purpose of numerical computations we introduce dimensionless variables by taking c_0 as the reference velocity and h_0 as the reference length. Then (A.37) becomes

$$(1-F)\eta+\frac{(n+2)}{4}\eta^2+\frac{1}{6}\eta_{xx}=-\beta_1\frac{a^2}{2n} \tag{A.39}$$

where

$$F=\frac{c}{c_0}=\frac{c}{(gh)^{1/2}}, \tag{A.40}$$

the Froude number.

Specific calculations will be presented for the choice

$$a^2\beta_1(x)=e[\frac{1}{4}+\frac{1}{2\pi}\tan^{-1}x] \tag{A.41}$$

where e is a given constant.

We seek flows which are characterised by different constant levels of the the free surface as $x\to\pm\infty$.

Relation (A.41) shows that

$$a^2\beta_1(x)\to\frac{e}{2} \quad \text{as} \quad x\to\infty \tag{A.42}$$

It then follows from (A.39) that

$$\eta(x)\to B \quad \text{as} \quad x\to\infty \tag{A.43}$$

where

$$F = 1 + \frac{1}{B}\left(\frac{e}{4n} + \frac{n+2}{4}B^2\right). \tag{A.44}$$

The right hand side of (A.44) has a local minimum at

$$B_{min} = [\frac{e}{n\,(n+2)}]^{1/2} \tag{A.45}$$

and a local maximum at

$$B_{max} = -[\frac{e}{n\,(n+2)}]^{1/2} \tag{A.46}$$

The corresponding values of F are

$$F_{min} = 1 + \left(\frac{(n+2)\,e}{4n}\right)^{1/2} \quad \text{and} \quad F_{max} = 1 - \left(\frac{(n+2)\,e}{4n}\right)^{1/2} \tag{A.47}$$

There are no solutions of the type considered here for $F_{max} < F < F_{min}$. For each value of $F < F_{max}$ or $F > F_{min}$ there are two possible values of B. These findings are illustrated in Figure A.1 where we plot B versus F for $n = 2$ and $e = 0.5$. The values F and B at the minimum and maximum are then $F_{min} = 1.5$, $F_{max} = 0.5$, $B_{min} = 0.25$ and $B_{max} = 0.25$. We note that the solid curves in Figure A.1 give values of F and B for which solutions 'might' exist. It does not imply the existence of solutions. Indeed as we shall see only a portion of the solid curves of Figure A.1 correspond to solutions for $y = \eta\,(x)$.

We now show some computed solutions for $\eta\,(x)$. Those were obtained by solving (A.33) numerically by finite differences. We first define the mesh points

$$x_i = -R + \frac{2R\,(i-1)}{N-1} \tag{A.48}$$

and the corresponding unknowns

$$\eta_i = \eta\,(x_i) \tag{A.49}$$

Here the values of x are truncated at $x = -R$ and $x = R$ where R is large. We satisfy (A.39) at the mesh points x_i, $i = 2, \ldots, N-1$. The derivative

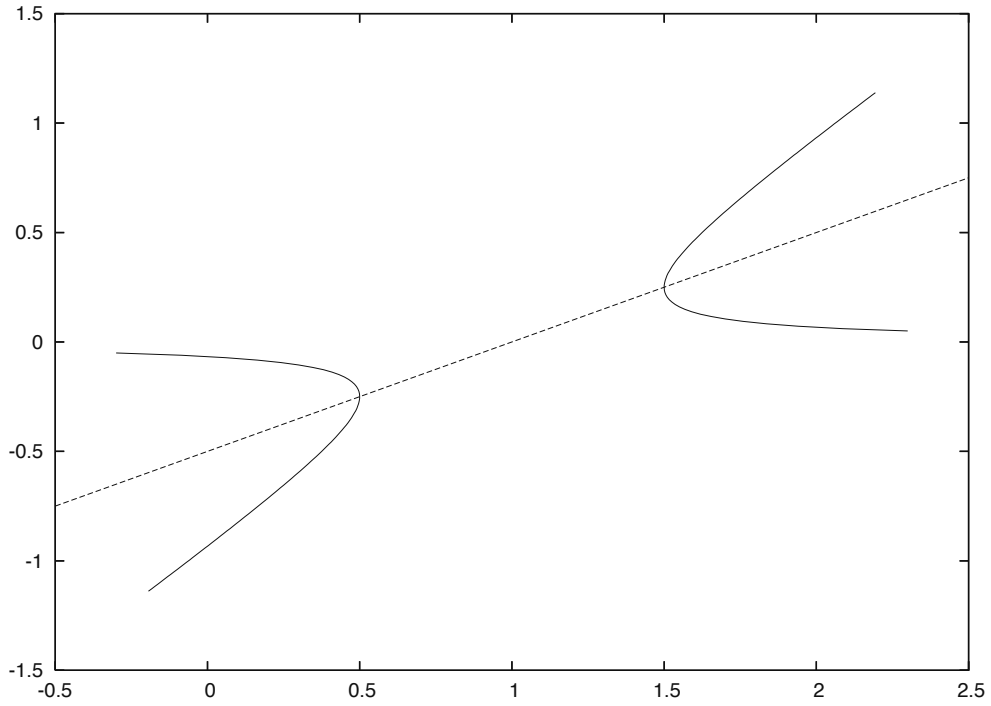

Figure A.1: Values of B versus F for which potential solutions might exist. Here $e = 0.5$ and $n = 2$. The broken curve is the line (A.53).

η_{xx} is evaluated by centred differences. This leads $N - 2$ .equations for the N unknowns η_i, $i = 1, \ldots, n$. The last two equations are obtained by imposing $\eta_1 = 0$ and $\eta_n = B$. The resulting system of N nonlinear algebraic equations with N unknowns is solved by Newton's method for given values of n, e and B. The value of F is defined by (A.44).

We used the numerical schemes to try to compute free surface profiles corresponding to the two solid curves in Figure A.1. Therefore we chose $n = 2$ and $e = 0.5$. We found that no converged solution could be obtained for the values of F and B corresponding to the left solid curve and to the portion $B > B_{max} = 0.25$ of the right solid curve. The only reliable numerical solutions correspond to the values $B < B_{max}$ on the right solid curve. A typical

free surface profile corresponding to $F = 1.7$ and $B = 0.105$ is shown if Figure A.2.

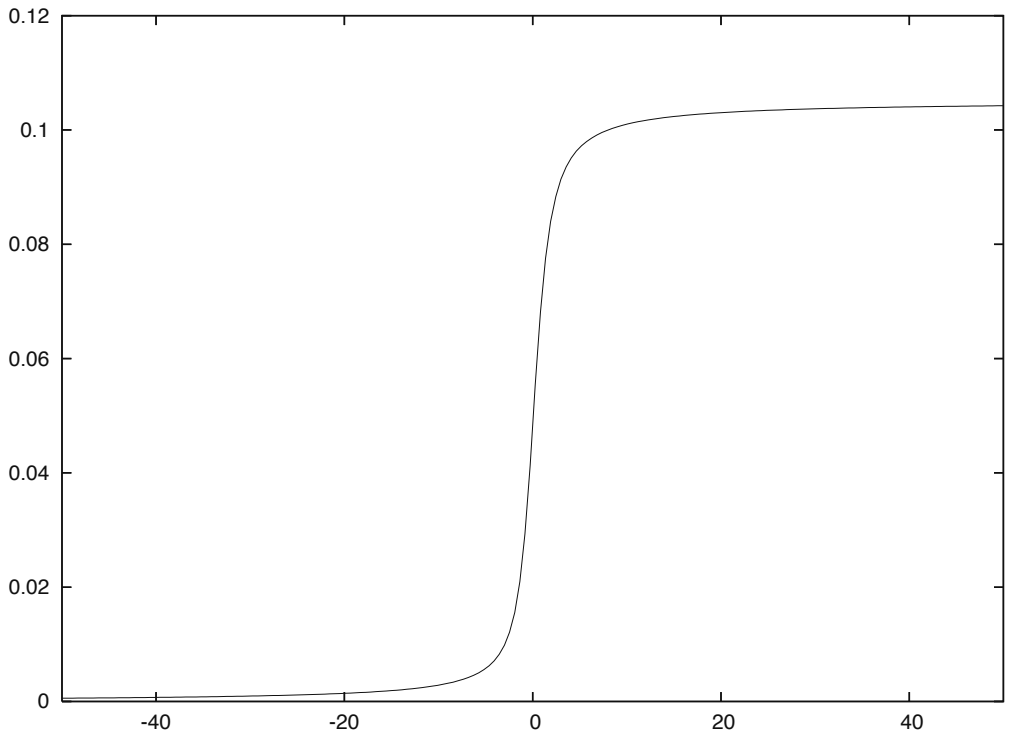

Figure A.2: Free surface profile for $e = 0.5$, $n = 2$, $F = 1.7$ and $B = 0.105$

The reason for which only the lowest portion of the right curve in Figure A.1 gives numerical solutions can be explained analytically as follows. Since $\eta(x) \to 0$ as $x \to -\infty$ we can linearise (A.39) around $\eta = 0$ for large negative values of x by writing $\eta(x) = s(x)$ dropping nonlinear terms in s. This leads

$$(1 - F)\, s + \frac{1}{6} s_{xx} = 0 \tag{A.50}$$

Similarly, since $\eta(x) \to B$ as $x \to \infty$, we can linearise (A.39) around $\eta = B$ for large positive values of x by writing $\eta(x) = B + s(x)$ and dropping nonlinear terms in s. This leads

$$\left(1 - F + \frac{n+2}{2} B\right) s + \frac{1}{6} s_{xx} = 0 \tag{A.51}$$

Equations (A.50) and (A.51) have oscillatory solutions when

$$F < 1 \quad \text{and} \quad 1 - F + \frac{n+2}{2} B > 0 \tag{A.52}$$

In the (B, F)-plane the second of the conditions (A.52) is satisfied in the half plane on top of the line

$$1 - F + \frac{n+2}{2} B = 0 \tag{A.53}$$

The line (A.53) is shown in Figure A.1. It can easily be checked that the line (A.53) goes through the points (B_{min}, F_{min}) and (B_{max}, F_{max}). Therefore the only portion of the solid curves of Figure A.1 for which the conditions (A.52) are not satisfied is the lowest portion of the right curve. Along that portion there are no oscillatory behaviour if the far field. This is precisely where we obtained reliable numerical solutions.

Appendix B

Volatility in the consumer packaged goods industry - a simulation based study.

B.1 Introduction

Software based simulation techniques have become a popular tool in the analysis of populations and societies in recent years. Social scientists have repeatedly pointed out that human societies, groups and organizations usually comprise of multiple heterogenous agents who often interact with each other as well as with the environment they are placed in. Such "complex systems" do not lend themselves to analysis using traditional top-down analytical/quantitative techniques. These systems typically exhibit *emergent behaviour* of some kind, and simulations seem to be one of the best tools to use for study ([25], [34], [83]). Consequently, bottom-up approaches such as agent based modelling/agent based computational economics (ABM/ACE) have increasingly been used in analyzing such systems. This paper uses such a bottom-up approach in building a simple but effective behavioral model of a typical consumer packaged

goods (CPG) market, whose volatile and heterogenous nature makes it very suitable for a simulation based study.

Consumer markets are usually characterized by noisy dynamics and instability [46]. Such volatility may arise due to multiple factors, for instance, large variations in tastes/preferences [5] and/or intense competitive market interventions by firms such as discounts and pricing campaigns, competitive packaging, advertising etc. ([11], [4]). Moreover, potential lateral effects such as word-of-mouth can become important as well in consumers' decision making and as a result lead to non-linearities in the system. Hence CPG markets possess many key characteristics of a complex system and consequently, lend themselves readily to agent based modelling techniques [33].

This paper takes the first step in building and validating a model of CPG markets using a combination of theory, simulation and real life data. We model the fresh fruit juices category and the choices made therein by a set of supermarket consumers facing a large variety of competing products. We focus on consumers' tastes and preferences for various attributes inherent in a product, as well as their reactions towards pricing and promotions in order to build a behavioral model of choice. This behavioral model is subsequently used as the template for running simulations where we attempt to replicate the choices made by real life consumers in an online retail supermarket. This is a multi-agent model analyzing a dynamic system from the bottom-up. Independent virtual agents, each of which represents an individual unit in the real population, are incorporated into the simulation. However, at this stage of the analysis we do not incorporate agent to agent interactions and social networks. This model should be treated as the *first step* towards a fully developed ABM incorporating potential social interactions, and for use as the benchmark for further analysis. The main aim here is to demonstrate that a simple enough model incorporating multiple heterogenous agents can pre-

dict a volatile and noisy CPG market with a high degree of accuracy. Once the underlying theoretical model of choice has been suitably validated, further compounding factors can be introduced in the model for more theoretical and/or empirical experimentation.

This paper's primary aim is to address the twin issues of individual heterogeneity and volatility, and illustrate the relationship between the two. To demonstrate this link, a model based on random choice is used as a benchmark, which does not incorporate agent level heterogeneity in tastes and preferences. The choice probabilities in the random model are generated from the data. The data consists of customer transactions within the fresh juice category from LeShop (www.leshop.ch), an online supermarket based in Switzerland. The simulations within the main model and the corresponding validation strategy results in a good fit of the out-of-sample predictions in comparison to the benchmark, particularly the direction and frequency of changes in market shares of product groups (where products are grouped on the basis of brands and flavors). At the micro level, a remarkably good out of sample fit is achieved for individual households, which drives the accuracy of the model at the macro level. The model significantly outperforms the benchmark at all levels.

Over and above the stated aim of demonstrating the link between volatility and heterogeneity in consumer goods markets, this paper has two overarching objectives. The first is to establish a simulation based approach which is not only able to estimate market share movements over time but also predict individual choices of products and features with a reasonable degree of accuracy. And the second is to provide a validated benchmark model which can be used to explore abstract scenarios, carry out "what if" exercises and more generally, explore theoretical constructs which can in turn explain a variety of complex phenomena. Examples of potential directions of theoretical exploration are numerous, with multiple motivations ([26]) and are discussed later. Such nor-

mative exploration necessitates the existence of a benchmark which has been tested and validated, against which reasonable comparisons can be made and this is precisely what a model like the one presented here may be used for.

The time period considered here is one calendar year, but both the simulation methodology and the behavioral model are flexible enough to be used for examining the short term and medium to long term dynamics. The latter, especially the medium term, can be studied with using small modifications to the current model, and a brief discussion on this is provided in the concluding section of this paper. Tackling the longer term using a similar methodology might be complicated, given that the environment and consumers might "drift" away from the calibrated model and this needs to be incorporated into the main model itself or addressed separately. Household level choice within a CPG context also involves additional aspects which are outside the scope – timing of purchase, quantity bought, product portfolio etc. being a few of them. In spite of these shortcomings, the model stands out from the rest for its simplicity, and hence implementation and extensions are easy.

B.1.1 Background

It is important to note that there exists a substantial amount of prior literature on quantitative analysis of CPG markets, especially with relevance to the effect of pricing and promotions on the evolution of market shares. Multinomial logit, nested and mixed logit and probit models have been heavily used in this area (see [6], [30] for details). Factors such as brand choice, purchase quantity, category incidence have usually been the focus of these studies (see for instance [8], [42] and [20]). Most of the analysis has been carried out almost exclusively using a static framework, where the temporal element was ignored. These models performed well in picking out short term responses to marketing mix policies. However, not as widespread and not as successful, are a few papers

dealing with the issue of the long term evolution of markets in response to multiple marketing strategies ([55], [21], [60]). A handful of papers have used dynamic programming as well to analyze the impact of promotions ([81], [80]), citing that discrete choice models overestimate promotion effects.

In spite of all the research done in this area, some questions remain unanswered which researchers and practitioners alike find very hard to tackle. For instance, what are the key differentiating factors which lead to variation in behavior within the population and how does this heterogeneity affect market dynamics? Is it possible to model the evolution of a market over time? Additionally, they lack the ability to take into account a number of compounding factors which may have important implications with regard to market behavior. For instance, potential non-linearities (such as social networks), disruptive changes (paradigm shifting innovations in products and technologies), dynamic nature of market fundamentals (shifts in consumer preferences), changing nature of how firms and consumers interact in today's world (effect of the internet and viral marketing techniques for instance) are just a few examples of such factors. This is where a simulation based model such as the one presented here is useful ([46]), forming the basis of further experimentation and analysis.

Model validation using real life data is an important component of any simulation based study. Although various definitions of validation exist in the literature, there is one common theme among all: A validated model will possess a satisfactory range of accuracy matching the simulated model to the real world phenomenon [89, 31, 27]. Most authors also stress that in typical models which study large complex entities such as markets, validation should be carried out at multiple levels. For instance, with a model of a market such as the one presented in this paper, not only should the simulation model mimic the macro-level dynamics of the real market (macro-level validation), individual agents should also suitably mimic the behaviour of the real households or

consumers they represent (micro-level validation).

One important aspect of validation is calibration of model parameters in order to match the simulation output to real data. The Fagiolo and Windrum survey [27] proposed three alternative calibration strategies - the indirect calibration approach, the Werker-Brenner approach and the history friendly approach. While the first two involves more rigorous quantitative techniques, the third encompasses a more general qualitative method. For more details on all three, please see the following: [28], [88] for indirect calibration and Werker-Brenner approaches respectively; [54] and [31] for the history friendly approach. This paper does not focus on any of these approaches exclusively, although the model specification lends itself more towards a direct quantitative approach rather than a qualitative one.

The choice model presented here has been developed specifically with the CPG industry in mind – where consumers make frequent purchases, tastes and preferences have an important role to play and firms engage in frequent price/promotion led marketing strategies. Additionally, it lends itself to a novel validation technique. Since our methodology validates the model both at the macro and the micro levels, two different fitness metrics are used for the two separate levels. At the macro level, the performance is judged by how closely market shares of product groups evolve over time in the simulation vis-a-vis the real data. At the micro level, we focus on household level preferences relating to individual products and product attributes. We divide the data into *three* sets – the first used for initialization of agents, the second for direct calibration and the third for testing out of sample predictions.

The rest of the paper is organized as follows. Section B.2 characterizes the underlying model which forms the basis of the agent level behavior in the simulation. The data used in validating the simulation results is described in Section B.3 while the actual validation methodology is described in Section

B.4. Next we present the results from the modelling and validation exercise in Section B.6 while the paper concludes in Section B.7 with a brief discussion and directions for future research.

B.2 The Market Model

A theoretical ABM framework is developed in [46], which incorporates the "4 P"s of marketing mix (product, price, placement and promotion) within a simulation framework. Our approach is similar to the extent that we start at the level of an individual shopper – a linear ordinal utility based behavioral model is used to characterize the choice mechanism. However, we deviate in the model specification itself. Following are the key assumptions made in our model.

Assumption 1 *Consumers act rationally and are able to rank the available alternatives in a consistent manner given their preference.*

Assumption 2 *All products and product characteristics remain unchanged during the given time period under consideration.*

Assumption 3 *Consumers' tastes and preferences remain unchanged in the given period.*

Consider an industry with K distinct products and a consumer base of size N. Each product is endowed with a set of M attributes, which makes it unique for a consumer. In order to define the preferences of consumers in such a framework, we borrow from traditional discrete choice theory in which a product is consumed, not for its own sake, but for the set of attributes or characteristics it embodies ([49], [22], [69]). Hence we make the following final assumption in our model of consumer choice:

Assumption 4 *Each consumer ranks alternatives based on a subjective ordinal utility measure, which is a function of the product specific price and characteristics as well as consumer specific preferences.*

The product specific characteristics are quantified as a M-dimensional vector belonging to a *characteristic space*, where each dimension represents one attribute. This vector is then called the *address* of the product. Each consumer's preference is defined using a complementary *ideal point*, a vector of characteristics that he would ideally like to see in a product. The closer this ideal point is to the actual mix of characteristics of a commodity, the higher the subjective utility of the consumer from purchasing it.

For $k \in K$, let $X_k = (x_k^1, x_k^2, \ldots, x_k^M)$ be the product address for k. For any consumer $i \in N$, consider $\lambda_i = (\lambda_i^1, \lambda_i^2, \ldots, \lambda_i^M)$ as i's ideal point. Let P_k be the price of the product k. In order to characterize the "distance" of consumer i's ideal point with a given product k, we use the 1-norm distance[1] measure, defined as,

$$D_k^i = \sum_{j=1}^{M} |x_k^j - \lambda_k^j|.$$

This is simply the sum of *absolute distances*, along each dimension of the characteristic space, between the two vectors. Consumer i's subjective utility from product k is hence characterized as,

$$\begin{gathered} U_i(k) = \omega_1^i d_k^i + \omega_2^i p_k \\ \text{where, } \omega_2^i = 1 - \omega_1^i, \quad 0 \leqslant \omega_1^i \leqslant 1. \end{gathered} \tag{B.1}$$

Identity B.1 refers to the parameterized utility function where,

$$d_k^i = -\frac{D_k^i}{\max\limits_{j \in K} D_j^i} \quad \text{and} \quad p_k = -\frac{P_k}{\max\limits_{j \in K} P_j},$$

[1] Any distance norm applicable to the Euclidean space $\mathbb{R}^n$ can be used here, without any change in the results. Our use of this particular distance measure was entirely based on simplicity of form.

and ω_1^i, ω_2^i are the weights place by individual i on d_k^i and p_k respectively, in determining the utility from product k[2]. Note that P_k is the *per unit* price of product k and not the listed price.

Next we consider price based promotions, where prices of specific products are reduced (discounted) for individual or groups of consumers. Consequently, we need to differentiate between the *gross* and *net* prices, i.e. P_k^{gross} and P_k^{net} respectively where the discount on the product k is, $\Delta P_k = P_k^{gross} - P_k^{net}$. Identity B.1 is redefined as,

$$\begin{aligned} U_i^{net}(k) &= \omega_1^i d_k^i + \omega_2^i p_k^{net} \\ \text{where, } \omega_2^i &= 1 - \omega_1^i, \quad 0 \leqslant \omega_1^i \leqslant 1, \end{aligned} \tag{B.2}$$

in order to incorporate promotions, where p_k^{net} is the relative price defined as above, but now in net terms. Note that identity B.2 is the simplest possible characterization of an utility function incorporating promotions implicitly. A more complete characterization should explicitly take into account the incidence of promotion itself as well as the quantity bought as a result.

B.3 Data

The data used in the current analysis consists all transactions within the fresh fruit juice category from LeShop, for the period of January 2006 to December 2006. Given the nature of the fruit juice category and available data, we consider three dimensions of product characteristics for the analysis – brand, flavor and pack size. Table B.1 gives a break up of the products in terms of

[2]The relative measures are used in order to normalize each component between 0 and 1, so that no single one dominates the function *numerically* although either one of them might dominate *functionally*, for instance if ω_1^i is equal to or very close to 0 or 1. In such a case, the individual agent's choice is based purely on either price or characteristics, and not on a convex combination of both.

the identified brands and flavors. The third characteristic dimension – that of pack size – is expressed in grams, which ranges from 280g to 12552g.

Table B.1: *Product break up by brand and flavors*

Brand	No. of Products	Flavor	No. of Products
Isola	2	Kid's Drink	3
Danone	2	Grape fruit	2
Mickey's Adventures	2	Nectar	7
Oasis	1	Pineapple	2
Capri Sonne	2	Apple	11
Granini	5	Multi-fruit	12
Michel	5	Orange	12
Obi	2	Other fruit	6
Nectar	8		
Hohes C	4		
Ramseier	5		
Max Havelaar	1		
Actilife	3		
M	8		
Gold	5		
Total	55		55

Each recorded transaction contains the following items: a household ID, product ID(s) of the product(s) purchased, the week number (indexed from 1 to 52) when the transaction was made, the net price paid, the discount applied if any, and finally the quantity of the product purchased. The time-line of transactions is indexed by weeks. An associated data table provides information about each product sold in that year and which has the following items: the product ID, the pack size, the flavor of the product, and the brand selling the product.

Each household ID represents a unique user of the LeShop website, and forms the basis of the agents in the simulation. Each product ID, similarly represents a unique product (Stock Keeping Unit or SKU), and hence is part of the set of alternatives available to the consumer. A few households had to be eliminated from the analysis given that they were infrequent purchasers. As a result, only those households were considered who had at least three or more transaction points over the whole time period, with at least two of those transactions within the weeks 25-52. The final data comprised of 55 unique SKUs, 2435 households and 28179 transactions for all of the 52 weeks.

B.4 Validation

For the purpose of validation, the full year's transactions data is split into three sets along the temporal dimension – weeks 1 to 24, 25 to 38 and 38 to 52. The first set is used for initialization of individual ideal points in the characteristics space, the second for calibration of the choice model, and the third for testing the predictions made by the simulation.

1. *Initialization.* The *first* partition is used for initialization of agent specific taste and preferences in the simulation. We initialized the product specific characteristic vectors and the agent specific ideal points using the transaction history covering weeks 1 to 24 in the data set.

2. *Calibration.* The parameter space is partitioned in a suitable manner. Simulations are run for all partitions of the parameter space. The results are recorded for every individual agent for every time step. Using the *second* partition of the data set, we calibrate each agent individually, i.e. obtain the intersection of parameters which provide the best in-sample predictions for that particular agent. The optimum parameter set is then

recorded for each agent. The optimization method is described in more detail below.

3. *Testing*. The final step involves the use of the parameterized agents to make out of sample predictions. We use the *third* data partition for this purpose. A Monte-Carlo type of method is used, where multiple runs of the simulation are made where each run corresponds to a random draw from the optimized parameter set of each agent. The results are collated and statistically compared against the data under consideration..

B.4.1 Initialization

The characteristics space is defined as the subset $[0,1]^3 \in \mathbb{R}^3$, i.e. numerically, the maximum and minimum values attached to any one dimension are 1 and 0 respectively. For each characteristic, the unique categories were assigned a value based on their total sales volume in the weeks 1-24, normalized by the maximum within that dimension. For instance, within the dimension representing brand, the one with the highest total sales volume (Gold) is assigned the value 1 while the one with the lowest (Isola) is assigned 0. All other brands were placed equi-spaced within (0,1), with each brand's position proportional to the relative sales volume (for eg., M has the second highest sales volume and hence is placed at 0.86 in the brand dimension). All ties were resolved randomly. The relative positions of brands and flavors in the characteristics space for the given data, correspond to the ordering in Table B.1.

Next we estimated a proxy for the ideal point of each agent using the transactions history within weeks 1 to 24 of the specific household which the agent represents. For a given characteristic dimension and for a given household, we calculate the weighted average of all categories purchased, with the purchase frequency used as the weight. This is repeated for every dimension. Given the

household and its transaction history, we generate a three dimensional vector in the characteristics space, which represents its ideal point[3].

This method does have a drawback when we consider households whose purchases concentrate on the two ends of the scale, in which case the weighted average falls somewhere in the middle, which is *not* representative of its preferences and happens only for a minority of cases. This can be seen from the spread of distances of agents' ideal points to their actual purchases (within partition 1 of the data), the mean and standard deviation of the spread over all agents is 0.285 and 0.149 respectively. Figure B.4 shows this distribution in a histogram. The ideal points remain static for the rest of the analysis (given Assumption 3).

B.4.2 Calibration

Calibration is done on both the macro and micro levels separately. For the macro level, we aim to fit the evolution of *market shares of product groups* to the actual data, while for the micro level validation, the corresponding aim is to fit *household specific choice of SKU and product characteristics*. And because each level requires a different fitness metric over which agent specific parameters are calibrated, we carry out the calibration exercise *twice* – once for each level of validation. We use *binary matching* of simulated versus real take-up of SKUs to calibrate at the market share (macro) level and use the *city-block metric* to calibrate characteristic take-up at the household (micro) level.

[3]For example, suppose household i purchases the brands M and Gold 2 and 3 times respectively in the first half of the year. M's and Gold's position in the [0, 1] interval along the brand dimension of the characteristics space is given by 0.86 and 1 respectively. Hence, household i's ideal point coordinate along the brand dimension is $\frac{2*0.86+3*1}{5} = 0.94$. The coordinates along the remaining two dimensions are computed similarly.

For calibrating agent i's specific ω_1 (the superscript i is dropped for notational convenience), the simulation is run for time steps (weeks) 25 to 38. The parameter space is discretized into 25 equi-spaced points, $0 = \omega_1^0 < \omega_1^1 < \omega_1^2 < \ldots < \omega_1^{24} = 1$ and the simulation is run 25 times for each agent, with each run corresponding to one value of ω_1 within the discretized space. Since there are no non-linearities involved in terms of social influences and feedback in the model, we can run the simulation sequentially for each agent in turn without having to carry it out simultaneously for all agents. Moreover, given that we have considered deterministic rational choice here, the number of runs for each agent for a specific parameter value is limited to one. Two sets of optimum parameter subsets are constructed per agent i, Ω_b^i using binary matching and Ω_c^i using the city-block metric, defined in detail below. The results of the calibration exercise is provided in Figure B.8.

Binary Matching

The binary matching calibration is done to optimize each virtual agent's utility function for optimum *SKU* choice. For each agent and each parameter value, the simulated and actual data are compared. In each purchase week a binary matching score is found in the following way. Let K be the set of all products and let the simulated choice by agent i at week t be $S_t^i \in K$. That is, for any give week t,

$$S_t^i(k) = \arg\max_{k \in K} \{U_i^{net}(k)\}$$

is the product chosen by agent i after a comparison of utility from all available products (SKUs). The binary matching score for agent i at week t is then

defined as,

$$\begin{aligned} b_t^i(S_t^i) &= \frac{1}{N_t^i}\sum_{k=1}^{K} n_{t,k}^i \delta(k, S_t^i), \\ \text{where,} \quad \delta(k, S_t^i) &= \begin{cases} 1, & \text{if } k = S_t^i \\ 0, & \text{otherwise.} \end{cases} \end{aligned} \tag{B.3}$$

In the above definition, $n_{t,k}^i$ is the quantity of product k purchased by household i in week t and N_t^i is the total number of purchases by the household in that week, so that $N_t^i = \sum_{k=1}^{K} n_{t,k}^i$. For agent i, and for each parameter value ω_1^p, $p = 0, 1, 2, \ldots, 24$ (the superscript i is suppressed), the binary matching score is averaged over all of the purchase weeks to obtain an overall score,

$$B^i(\omega_1^p) = \frac{1}{|T^i|}\sum_{t \in T^i} b_t^i(S_t^i(\omega_1^p)), \tag{B.4}$$

where T^i is the set of weeks where household i made a purchase and $|T^i|$ is the cardinality of set T^i.

The set of best parameter values for agent i, Ω_b^i is then constructed as,

$$\Omega_b^i = \left\{ \omega_i^p \,\middle|\, B^i(\omega_1^p) = \max_p \left(B^i(\omega_i^p)\right), p = 0, 1, \ldots, 24 \right\}. \tag{B.5}$$

Identities B.3, B.4 and B.5 spells out the macro level calibration strategy. For any agent i, every match with corresponding household's purchase in the real data is given a score of 1 for the particular parameter value ω_i^p and 0 otherwise. The total score per weak is summed up and normalized for the total number of purchases made that week (to account for multiple purchase instances within the week). Weekly scores are averaged for all weeks per parameter value and the parameter value(s) with the highest score added to set Ω_b^i. See Figure B.8(a) for a distribution of calibrated ω_1 across all agents in the binary matching case.

City-block Metric

We use the city-block metric[4] in order to calibrate the utility function of agents for optimum choice of *product characteristics*. Once again, let $S_t^i \in K$ be the simulated choice made by agent i in week t. Following section B.2, let x_k^m be the m^{th} characteristic of product k, where M is the total number of relevant characteristics. A city-block metric assigns a score of 0 per characteristic where it matches with the real data and 1 for a mismatch. The characteristic matching score for agent i in week t is then defined as,

$$\begin{aligned} c_t^i(S_t^i) &= \sum_{m=1}^{M} \min_{\substack{k \in K \\ n_{t,k}^i \neq 0}} \Delta^m(k, S_t^i) \\ \text{where} \quad \Delta^m(k, S_t^i) &= \begin{cases} 0, & \text{if } x_k^m = x_{S_t^i}^m \\ 1, & \text{otherwise.} \end{cases} \end{aligned} \tag{B.6}$$

Here $0 \leqslant c_t^i \leqslant M$. Since $M = 3$ for our data, a score of 0 would mean that each of the characteristics of the simulated product S_t^i matched with a corresponding characteristic in household i's actual product purchases in week t; a score of 1 would mean that any two out of three were matched (i.e. 1 mismatch); 2 that only one could be matched (2 mismatches) and 3 that none of S_t^i's characteristics matched with any of the actual purchases. Note that a score of 0 in most cases imply an exact SKU match as well (except when multiple products are purchased within a week).

The set of best parameter values for agent i, Ω_c^i is found in the following manner. First, we define a binary variable $\psi_t^i(\omega_1^p)$, which is used to judge

[4]The name derives from the commonly used concept of city-block distance which measures the absolute distance between two points in Euclidean space, by measuring along each dimension independently. In the calibration exercise presented here, each dimension over the 3-dimensional characteristic space is checked independently for a match and the results added up for the overall score – similar to the distance measure – and hence the name.

whether a characteristic matching score is "good" enough, which in turn is used to determine the optimal ω_1^p.

Definition 1 *The parameter value ω_1^p is considered optimal for agent i in week t, if it is less than the mean city-block distance over all parameter values in week t, i.e.*

$$\psi_t^i(\omega_1^p) = \begin{cases} 1, & \text{if, } c_t^i\big(S_t^i(\omega_1^p)\big) \leqslant \dfrac{1}{25}\displaystyle\sum_{p=0}^{24} c_t^i\big(S_t^i(\omega_1^p)\big) \\ 0, & \text{otherwise.} \end{cases}$$

As before, an overall score $C^i(\omega_1^p)$ is obtained for each parameter setting by averaging over all purchase weeks:

$$C^i(\omega_1^p) = \frac{1}{|T^i|}\sum_{t\in T^i}\psi_t^i(\omega_1^p). \tag{B.7}$$

Finally, the set of optimal parameter values for agent i is defined as,

$$\Omega_c^i = \Big\{\omega_i^p \Big|\ C^i(\omega_1^p) = \max_p\big(C^i(\omega_i^p)\big), p = 0, 1, \ldots, 24\Big\}. \tag{B.8}$$

See Figure B.8(b) for a distribution of calibrated ω_1 across all agents for the city-block metric case. Once the Ω_b^i and Ω_c^i sets have been identified for each agent/household, we proceed with the final stage in the analysis – that of testing our model with the out of sample data.

B.4.3 Testing

The model testing exercise is carried out on out of sample transactions data covering weeks 39 to 52. For each agent i, we now use both the sets Ω_b^i and Ω_c^i in multiple runs. The use of either set Ω_b^i or Ω_c^i is dependant on the type of validation being carried out, i.e whether macro or micro level respectively. By definition, $\Omega_b^i \subseteq \Omega_c^i$ and we could have just used the former for prediction. However, given that the objective of micro-validation is to parameterize the

utility function on the basis of individual preferences, ignoring elements in $\Omega_c^i - \Omega_b^i$ is essentially loss of agent specific information.

It is very likely that the cardinality of these sets is greater than one, and so, for each agent one parameter value $\omega_1 \in \Omega_{b,c}^i$ is selected at random. As before, at each purchase week the agent makes a choice from that week's product choice set using the parameterized utility function. The variability that is introduced through random choice of suitable parameter values necessitates the need for a Monte-Carlo type analysis and so the simulation is run 100 times for each agent. We select the *modal value*, or the product that is purchased the *maximum number of times* in a week among the 100 runs, as that week's predicted choice.

Since choice of quantity is not a part of the behavioral model, it is matched from the actual data in the testing phase. If the simulated choice is identical to the actual choice, the quantity bought by the agent is copied from the data. If however, the simulated and actual choices do not match, then agent is made to purchase a quantity, q of the product. Quantity q is calculated using the average liquid volume (pack size) per transaction of the household vol^i, which is calculated on the first six months of data. Define,

$$q = \min \left\{ n \in Z \middle| \; n \geqslant \frac{vol^i}{x_S^1} \right\}$$

where x_S^1 is the pack size of product S (the simulated purchase of i), implying that the purchase for that week satisfies the household's average liquid volume purchase per transaction. In the characteristic matching (micro-level) validation, purchase quantities need not be considered.

B.4.4 The benchmark

A random choice model is used as a benchmark to compare the results of the model described above. This random model is based on probability distribu-

tions generated from the data itself. All transactions from week 1 to week 38 are jointly used to generate the vector of probabilities ($P_1, \ldots, P_j, \ldots, P_{55}$), such that,

$$P_j = \frac{N_j}{N} \quad \forall j \in [1, 55]$$

where N_j is the number of transactions in which SKU j was purchased, and N is the total number of transactions. As defined above, P_j represents the *average market share* of SKU j within weeks 1 to 38. Note that this random model disregards the effect of heterogeneity in individual consumer preferences as well as specific price effects. By definition, it captures the *observed* market level preferences, without considering any underlying factors which led to the observations.

As part of the experimental procedure, each agent is then made to choose from all SKUs based on the probability distribution generated above. The choice of purchased quantity by each agent is decided in the same manner as defined in B.4.3. As before, the experiments are run a 100 times for each agent and the modal value considered as the simulated/predicted choice.

B.4.5 Notes on validation

A caveat is necessary to clarify some aspects of the validation methodology developed for the model.

First of all, a single data set has been used in the whole exercise to initialize, calibrate and test the model. The authors acknowledge the need to carry out some form of "cross-validation" with related data sets in order to test the robustness of this methodology. Several possibilities arise in this regard. The most straight forward one is to establish this method within a different product category from the same source (i.e. transactions from another group of products within LeShop in this case). The set of consumers would most likely be a different one, with some intersection between the two. It would

also be possible to establish the same methodology using transactions data from a different source as long as the data structure is more or less similar (i.e. transactions carry information about individuals' purchase of products, which link up with standardized product characteristic descriptions). An interesting deviation from the above would be to track consumer households across *different* shopping channels to test for the consistency of the model – assuming that most consumers are largely consistent in their shopping habits across channels. This would involve initialization and calibration of households within one data set and testing it in another.

All three methods of cross validation are currently being tested and comparable results have been achieved in most product categories with a few specific exceptions (an interesting and open research question remains on why this is so). Unfortunately, current restrictions on the dissemination of the results based on some of this data prevents us from discussing them any further here.

Additionally, a simplifying procedure is followed with regard to the quantity chosen by agents in the testing phase of the model, although market share – the key component in macro validation – is a function of quantity. This work specifically focusses on the choices of product and product characteristics made by households, and modelling quantity choice is beyond scope here. Predicting the quantity of products bought by any household involves a number of household specific factors (size, storage capacity, durability of the product etc.) which are not available in the current data. More information regarding the households themselves and their shopping habits are required in order to incorporate this into the model.

B.5 Simulation Setup

The simulation is designed such that each virtual agent represents one consumer household in the data within a Matlab environment. The simulation consists of 2435 agents whose behavior is defined by the model described above. Each agent represents an unique household in the data, with parameter set (λ_i, ω_1^i), where $\lambda_i = (\lambda_i^1, \lambda_i^2, \lambda_i^3)$. Note that, $\lambda_i \in [0,1]^3$ and $\omega_1^i \in [0,1]$. As mentioned earlier, ideal point λ_i is initialized using the first partition of the data, which leaves ω_1^i as the only parameter to be calibrated using the second partition.

At every time step in the simulation, agents choose *one* product from a subset of 55 total products. We do not make the assumption that all products were available at all weeks covering the simulation but use the transactions table to determine the *available* choices.

Definition 2 *A product $k \in K$ is considered to be within the available set in any week t, if there is at least one transaction in the real data involving k in week t.*

Moreover, the only information that we have from the transaction table is which product was bought at what price/discount in a certain week by a customer, but not what the prices and discounts were of all *alternatives* that were available to him. Given that this information is required to evaluate the relative utility of all products by the representative agent, we once again compute this from the transactions table.

Definition 3 *For any product k, the price (discount) listed in time step t is the average price (discount) corresponding to* all *the transactions involving k in that particular week t.*

An agent, when facing the set of available choices, simply looks up the corresponding prices and discounts from a table for that particular week.

If a household made a purchase within a given week, then the agent representing the household is provided with a choice set of products which includes those that were purchased in reality plus all the "available" alternatives. The agent evaluates the prices, discounts, product characteristics and selects the one product which maximizes its utility. The following rules are implemented in the simulation:

- The quantity of fruit juice purchased by the household in the data determines the quantity purchased by the agent.
- If the household made no purchases that week then no purchase is made by the agent.

These rules are essentially simplifying the model but as mentioned before, we are not modelling incidence or quantity bought, just the choice itself. Once the purchase decision has been made by an agent in a given week, the simulation then progresses by one time-step to the next week. The purchase made by the agent is recorded at each time-step.

B.6 Results

Out of sample (weeks 39 to 52) predictions and goodness of fit results are presented separately for the market (macro) and household (micro) levels. Results from the random model are used for comparison. In order to differentiate between the main model and the benchmark, we refer to them as the ABM and the Random model respectively.

B.6.1 Market Level

At the level of the market as a whole, the models are tested on the basis of a comparison between predicted and actual *market shares*. Given the large number of products, we group them on the basis of brands and flavors. Table B.2 reports the degree of accuracy with which the simulated market shares match the actual ones in the data. We provide two measures – the average *relative difference* between the actual and simulated market shares per brand/flavour ($r_{b/f}$) and the correlation coefficient ($c_{b/f}$) between the two. For each brand b, r_b and is computed as:

$$r_b = \frac{1}{14} \sum_{t=1}^{14} \frac{|S_t^b - A_t^b|}{A_t^b}$$

where S_t^b and A_t^b are the simulated and actual market shares of b in week t. r_f is computed similarly for each flavor f. Both measures considered together indicate how well the models perform in terms of capturing the volatility in the market.

The key results from the macro-level validation is presented in Table B.2 can be summarized as follows. First, for most brands and flavors, the ABM predicts the *direction of change* of market shares very well. It performs reasonably well with regard to the *magnitude* of market shares, although not as accurately as the prediction of direction. Second, both the correlation coefficient as well as the relative difference is significantly better in the ABM for brands/flavors which have high market shares overall than those which are in the lower end. Generally, brands with market shares consistently less than 2% of the market are difficult to predict whereas the others are well predictable either in direction or both in direction and magnitude. The pattern within flavors is similar as well (with the threshold around 8% of market share), but with one important difference - as compared to brands, the average prediction is better in magnitude (0.44 against 0.53) but worse in direction (0.45 against

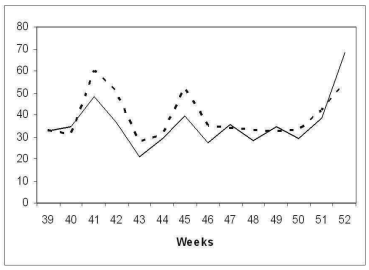

(a) Brand: Gold

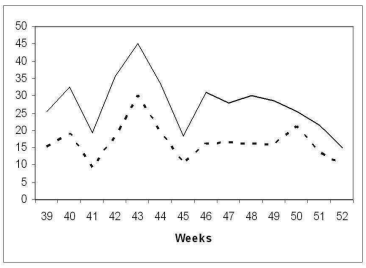

(b) Brand: M

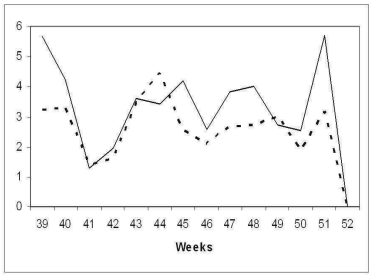

(c) Brand: Hohes C

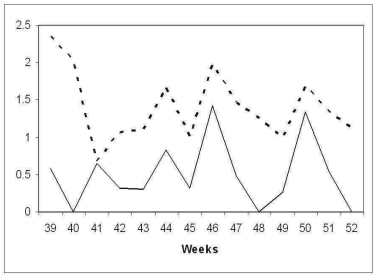

(d) Brand: Danone

Figure B.1: Weekly market share predictions of ABM versus actuals of selected brands. Solid line - predicted; dotted - actual

0.57). Equivalent values for the Random model are far worse, for most brands and flavors (Mickey's Adventure in brands and Kid's Drink, Grape Fruit and Other fruit are the only exceptions). Overall, the ABM significantly outperforms the Random model in predicting the volatility in the market. Note that choice of quantity (number of SKU's being purchased) is not endogenous in the model, that is, it is not a decision variable for the agents although pack size is. Figures B.1 and B.2 show the predictions of the ABM versus actual market shares of a selected set of brands and flavors over weeks 39 through 52. The rest of the brands and flavors can be found in Figures B.5, B.6 and B.7 in the Appendix.

Table B.3 presents the number of weeks a brand or a flavor has been on promotion within the 14 week period. As can be seen, incidences of promotions

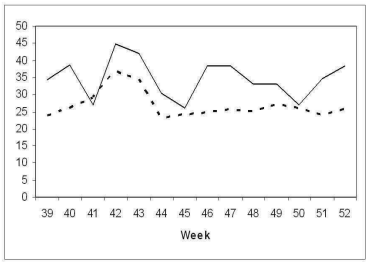

(a) Flavor: Other

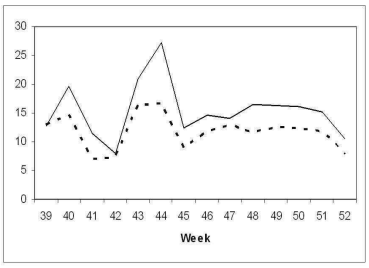

(b) Flavor: Multi-fruit

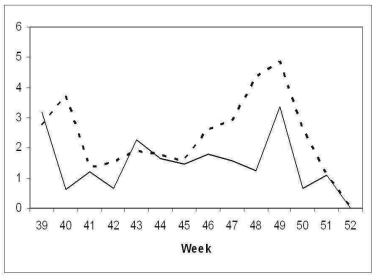

(c) Flavor: Nectar

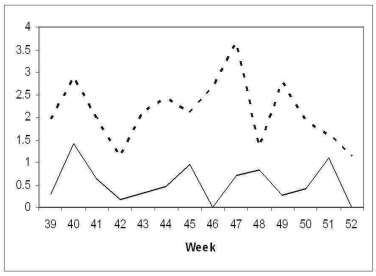

(d) Flavor: Kid's Drink

Figure B.2: Weekly market share predictions of ABM versus actuals of selected flavors. Solid line - predicted; dotted - actual

in the form of price discounts were quite rare for most brands, but not so when product groups are grouped as flavors. Yet actual market shares of both product groupings exhibit high volatility, *which is also picked up by the ABM simulation*, driven through SKU level choices. Agents differ from one another in terms of how strongly they react to price changes and inherent preferences. Since different attribute combinations are under promotion at different times, varying responses to promotions by any one agent as well as across agents lead to the high volatility in the simulations. On the other hand, the Random model, which disregards individual level preferences and price responses, is unable to pick up on market share movements either in direction or magnitude both at the level of attributes as well as on the average. However, as mentioned before, examination of the household/micro level choices made by individual

households is necessary in order to establish the validity of the model.

B.6.2 Household Level

The performance of the models at the micro level provides the basis of their performance at the macro level. A counting scheme similar to that of the city-block metric is used to test the model at the micro level. The accuracy of predictions in household's choice of characteristics is measured, in each dimension of the characteristic space independently, as well as jointly along subsets of dimensions. Given a particular dimension within the characteristic space and for any given household, the number of times a correct prediction is made along that dimension, is estimated. And for measuring the joint predictions along all dimensions, the number of times the simulation respectively predicts 3, 2, 1 and 0 characteristics correctly is also estimated for every household, irrespective of what those characteristics are. The former implies finding the proportion of times the model correctly predicts the choice along a dimension, independent of other characteristic dimensions. The latter implies a joint prediction "score" per household per transaction (as defined in (B.6)). Note that a score 0 for agent i implies that, i's choices in the simulation matched the corresponding real household's purchase in *all* dimensions, while a score of r, where $0 < r \leqslant 3$, implies only $3 - r$ characteristics matched correctly. Table 4 and Figure B.3 summarizes the results for the ABM and Random models.

Part 1 of Table 4 indicates that the household specific SKU choice was predicted correctly 35.74% of the times in the ABM and 2.1% in the Random model, from a pool of 8213 transactions in total. The total 8213 transactions incorporate households for whom all 100% of the transactions were correctly predicted, as well as households for whom none were correct and those for whom predictions were only partially correct. This distribution is presented in Part 2 of Table 4 for ABM, which describes the break up of households in terms

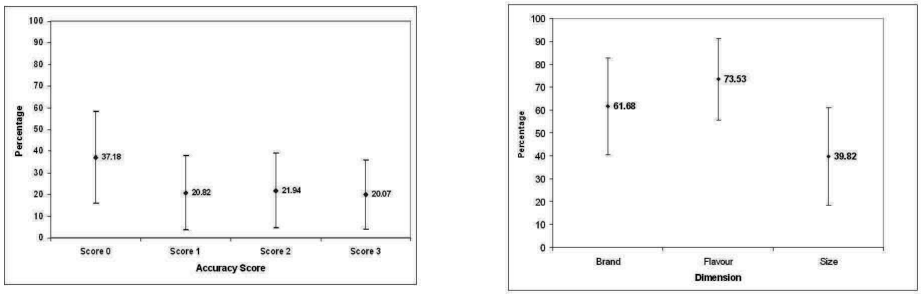

(a) Joint Predictions - Mean & Standard Deviation

(b) Per Dimension Prediction - Mean & Standard Deviation

Figure B.3: Household level prediction mean and variation in the characteristics space.

of accuracy of predictions jointly across subsets of characteristic dimensions. Each column indicates the distribution of households under a particular score. For instance, and importantly as well, for 24.43% of the households, all product characteristics from all their transactions were correctly predicted. For the small percentage of cases where multiple brands/flavors and/or sizes are bought by the same household in the same transaction, we might be able to match all characteristics but not the product. This explains why the accuracy in SKU prediction (35.74%) is slightly less than the mean of the proportion of Score 0 for all households (37.18%). Also, it is only a minority of households (8.25% as seen in the Score 3 column), that predictions are inaccurate in all dimension for all transactions. Figure B.3(a) summarizes mean and standard deviations graphically.

Part 3 of Table 4 and Figure B.3(b) summarize the accuracy of household level predictions within each characteristic dimension individually. Flavor is definitely the characteristic which is most predictable, followed by the brand and finally the size, for both the ABM and the Random models. However, the ABM significantly outperforms the Random model in all three. The low

degree of predictability of size is understandable given that it is likely to be influenced by individual consumption rates, frequency of visits to the shop, the incidence and size of promotions etc. - which have not been included in the behavioral model currently. Note that it is the low level of predictability of size which is pulling down the overall SKU prediction figure as well. If we discount product size, these results definitely indicate that ranking products based on attribute specific preferences and prices is able to mimic household level choice behavior significantly – thus establishing the overall validity of the simulation model.

Table B.2: *Comparison of mean relative distance (r_b) and correlation coefficient (c_b) between predicted and actual market shares for ABM versus random model.*

	ABM		Random			ABM		Random	
Brand	r_b	c_b	r_b	c_b	Flavor	r_f	c_f	r_f	c_f
Isola	0.56	0.75	0.82	0.37	Kid's Drink	0.73	0.22	0.66	0.29
Danone	0.63	0.36	0.72	-0.28	Grape fruit	0.97	0	0.49	-0.20
Mickey's Adventures	0.83	0	0.80	-0.23	Nectar	0.32	0.50	0.69	0.14
Oasis	0.67	0.23	0.68	0.39	Pineapple	0.42	0.30	0.52	0.14
Capri Sonne	0.20	0.78	0.46	0.38	Apple	0.36	0.59	0.42	0.16
Granini	0.55	0.64	0.80	0.41	Multi-fruit	0.30	0.88	1.37	-0.33
Michel	0.31	0.36	0.57	0.57	Orange	0.12	0.59	0.47	-0.56
Obi	0.73	0.24	0.65	0.26	Other fruit	0.31	0.55	0.27	0.49
Nectar	0.41	0.46	0.52	0.20					
Hohes C	0.33	0.76	0.59	0.24					
Ramseier	0.23	0.86	0.71	0.36					
Max Havelaar	0.33	0.95	0.51	0.46					
Actilife	0.29	0.43	0.69	-0.41					
M	0.70	0.89	1.05	-0.23					
Gold	0.14	0.76	0.43	-0.06					
Average	0.53	0.57	0.67	0.16	Average	0.44	0.45	0.61	0.01

Table B.3: *Number of weeks within weeks 39 to 52, when brands and flavors are in promotion*

Brand	No. of weeks	Flavor	No. of weeks
Isola	0	Kid's Drink	0
Danone	0	Grape fruit	7
Mickey's Adventures	0	Nectar	1
Oasis	0	Pineapple	5
Capri Sonne	0	Apple	4
Granini	4	Multi-fruit	10
Michel	2	Orange	11
Obi	0	Other fruit	2
Nectar	1		
Hohes C	2		
Ramseier	1		
Max Havelaar	1		
Actilife	0		
M	6		
Gold	5		

Table B.4: *Prediction Results at the Household Level for the ABM model. Numbers in parenthesis indicate the corresponding values for the Random model.*

1. SKU Predictions		
Exact Matches	2936	
Number of Transactions	8213	
Accuracy	35.74%	(2.1%)

2. Characteristics Predictions *Joint across dimensions*				
Percentage Accuracy (%)	Score 0	Score 1	Score 2	Score 3
100	24.43%	11.21%	10.14%	8.25%
75 - 100 (excl.)	4.56%	1.89%	2.75%	1.97%
50 - 75 (excl.)	11.13%	9.20%	10.88%	11.66%
25 - 50 (excl.)	7.97%	8.13%	9.16%	10.06%
0 - 25 (excl.)	51.83%	69.53%	66.98%	67.97%
	$\sim 100\%$	$\sim 100\%$	$\sim 100\%$	$\sim 100\%$
Mean across hh.	37.18%	20.82%	21.94%	20.07%
Standard Deviation	21.21	17.17	17.01	15.94

3. Characteristics Predictions *Per dimension*			
	Brand	Flavor	Size
Mean across hh.	61.68%	73.52%	39.81%
	(5.9%)	(9.5%)	(3.7%)
Standard Deviation	42.1425	35.6669	42.6331

B.7 Conclusion

This paper used a bottom-up simulation based approach in order to model the volatile fresh juice market within the CPG industry, using checkout data from an online supermarket as the basis for empirical validation. Virtual agents were designed using a simple behavioral model, were initialized, calibrated and finally tested on the basis of predictions made out of sample. The behavioral model took account of both the heterogeneity in preferences for product attributes as well as the heterogeneity in individual responses to pricing. A random choice model was used as a benchmark to compare the performance of the multi-agent model.

The validation methodology tested the model and its predictions at both macro and micro levels. The volatility seen in the market at the macro level, in terms of week to week market share movements of product groupings (brands and flavors), were captured by the model with high degree of accuracy – both in terms of direction of change and to a slightly lesser degree, the magnitude of change. The accuracy in predicting the volatile market at the macro level is driven by the accuracy in the prediction of choices of SKUs and various product attributes by individual households at the micro level. On the other hand, once the heterogeneity in the behavioral model is removed, as in the case of the benchmark, predictions at the micro level fall dramatically in accuracy and consequently, it is unable to capture the volatile market.

Although the approach used in the simulation is bottom up and multi-agent based, it lacks one key feature of a full fledged agent based model – agent to agent interactions through social networks. The data set used here does not allow us to go any further, for example to test the presence of networking effects. This might be possible with a different data set within a different market, and is part of ongoing research. However, what the current model is effective for, is in running *what if* scenarios – for instance, testing the efficacy

of alternative pricing/promotion strategies, alternative product offerings and even imposing agent to agent interactions within the current model to analyze levels of deviation from current behavior.

The behavioral model itself can and should be enhanced in a number of ways. Instances of promotions can be incorporated explicitly into the analysis instead of being implicitly considered through the net price. Also, rationality is a strong assumption to impose on the agents and this can be relaxed in varying degrees to test for effects on market share evolution. The current model allows the researcher to incorporate cognitive elements explicitly within agent level behavior as well (such as static or shifting attitudes towards specific characteristics or characteristic dimensions), in line with [66]. Additionally, allowing for introduction of new products and exit of existing ones would be an interesting extension within the current framework. The last would be especially important when examining the longer term dynamics of markets. Within this context, it would be interesting to analyze the effects of changing preferences (instead of static ideal points), changing attitudes and even development of social norms with regard to shopping behavior.

All in all, the current model's simplicity, parsimony and ability to combine theory, simulation and real life data seamlessly should make it very appealing for researchers and practitioners alike. Moreover, the possibilities of enhancing this model in many directions makes it an exciting starting point and benchmark for future experimentation and analysis.

B.8 Figures

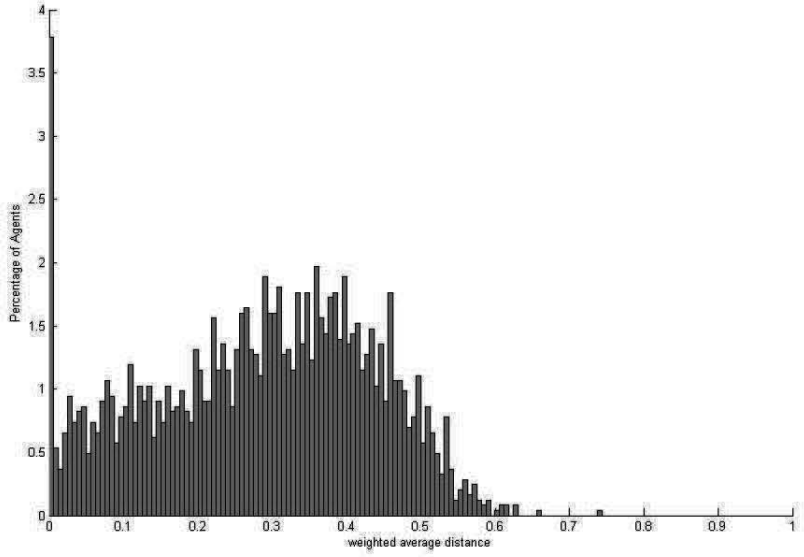

Figure B.4: Spread of distances of agents' ideal points from the purchases with which the ideal points are calculated.

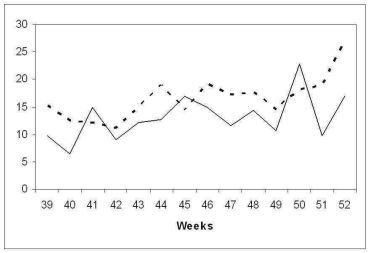

(a) Brand: Actilife

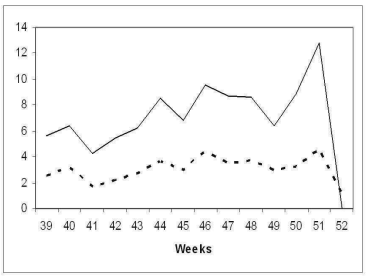

(b) Brand: Max Havelaar

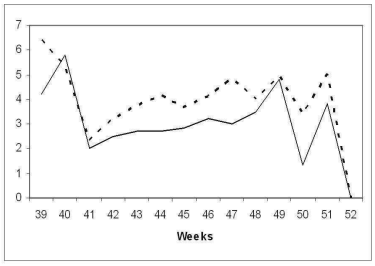

(c) Brand: Ramseier

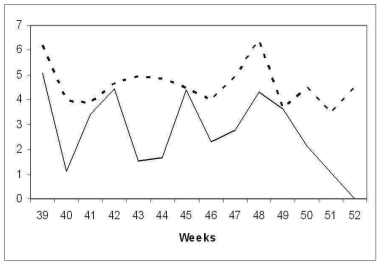

(d) Brand: Nectar

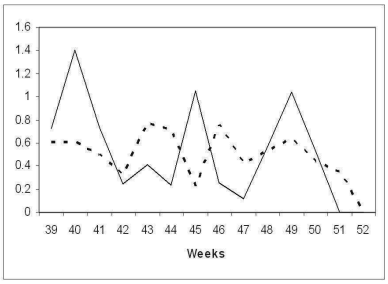

(e) Brand: Obi

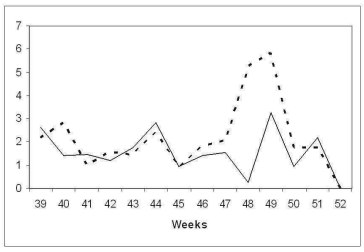

(f) Brand: Michel

Figure B.5: Predicted and actual weekly market shares of brands. Solid line - predicted; dotted - actual

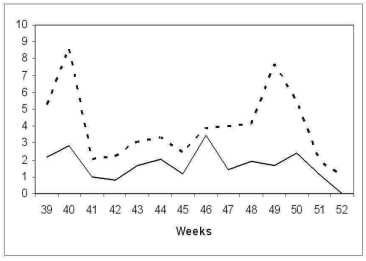

(a) Brand: Granini

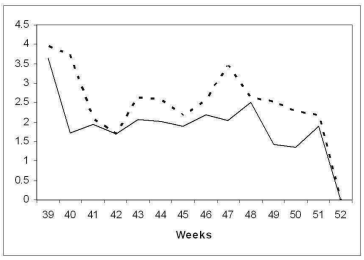

(b) Brand: Capri Sonne

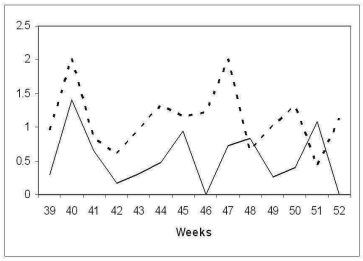

(c) Brand: Oasis

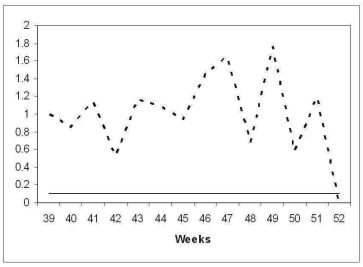

(d) Brand: Mickey's Adventure

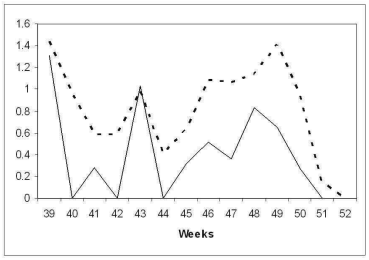

(e) Brand: Isola

Figure B.6: Predicted and actual weekly market shares of brands (Cont.). Solid line - predicted; dotted - actual

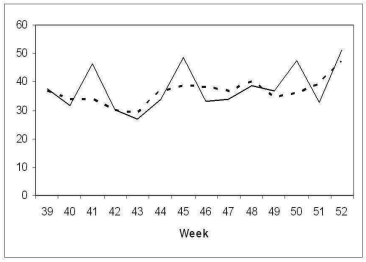

(a) Flavor: Orange

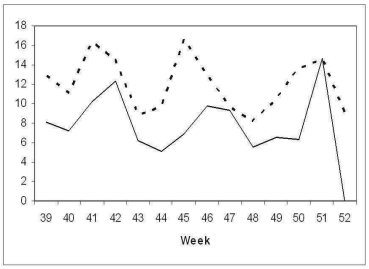

(b) Flavor: Apple

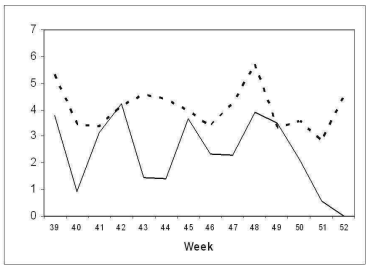

(c) Flavor: Pineapple

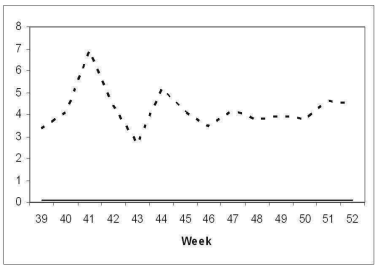

(d) Flavor: Grape Fruit

Figure B.7: Predicted and actual weekly market shares of flavors. Solid line - predicted; dotted - actual

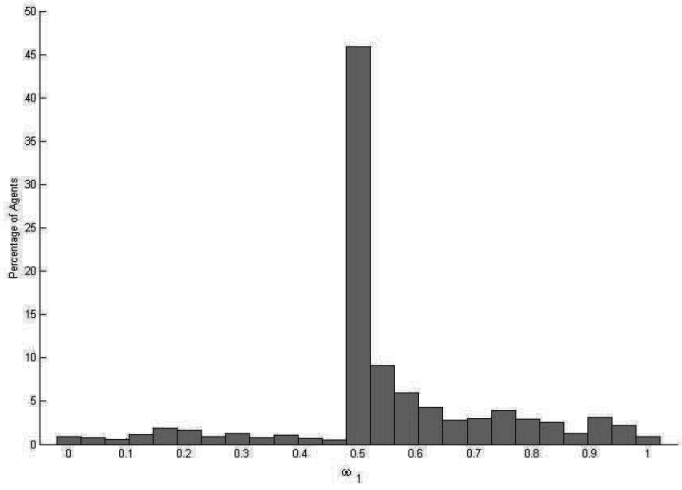

(a) Binary Matching

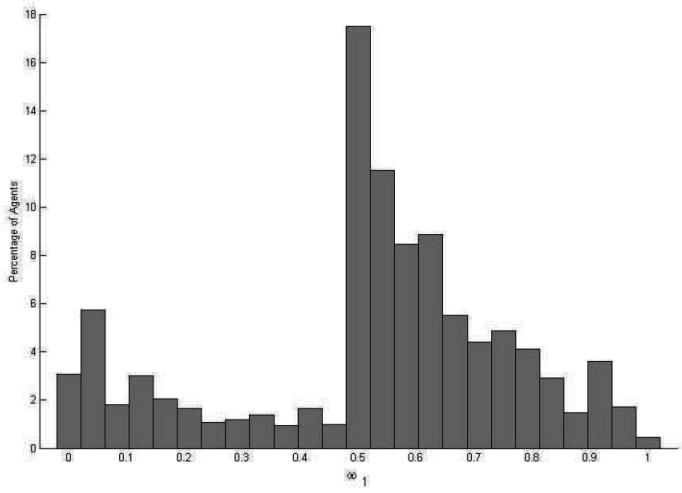

(b) City Block Metric

Figure B.8: Distribution of optimal ω_1 across all agents for each calibration type. For agents with multiple optima, the average is considered.

Bibliography

[1] P. Abrams. *Urodynamics*. Springer Verlag, 2006.

[2] P. Abrams. *Incontinence: 4th International Consultation on Incontinence, Paris, July 5-8, 2008*. Health Publications Ltd., 2009.

[3] P. Abrams and I. C. on incontinence. *Incontinence: 2nd International Consultation on Incontinence, Paris July 1-3, 2001*. Plymbridge Distributors Ltd., 2002.

[4] K. Ailawadi, D. Lehmann, and S. Neslin. Market response to a major policy change in the marketing mix: Learning from procter and gamble's value pricing strategy. *Journal of Marketing*, 65(January):44–61, 2001.

[5] G. M. Allenby and P. E. Rossi. Marketing models of consumer heterogeneity. *Journal of Econometrics*, 89(1-2):57–78, November 1998.

[6] S. P. Anderson, A. de Palma, and J.-F. Thisse. *Discrete Choice Theory of Product Differentiation*. (Cambridge: The MIT Press), 1992.

[7] J. Asavanant and J. Vanden-Broeck. Nonlinear free-surface flows emerging from vessels and flows under a sluice gate. *Journal of the Australian Mathematical Society-Series B*, 38(1):63–86, 1996.

[8] D. Bell, J. Chiang, and V. Padmanabhan. The decomoposition of promotional response: an empirical generalization. *Marketing Science*, 18(4):504–526, 1999.

[9] S. A. Berger, L. Talbot, and L. S. Yao. Flow in curved pipes. *Annual Review of Fluid Mechanics*, 15:461–512, 1983.

[10] B. Binder and J. Vanden-Broeck. The effect of disturbances on the flows under a sluice gate and past an inclined plate. *Journal of Fluid Mechanics*, 576:475, 2007.

[11] R. Blattenberg and K. J. Wisniewski. Price induced patterns of competition. *Marketing Science*, 8(4):291–309, 1989.

[12] R. I. Bowles, N. C. Ovenden, and F. T. Smith. Multi-branching three-dimensional flow with substantial changes in vessel shapes. *Journal of Fluid Mechanics*, 614, 2008.

[13] A. Brading. The physiology of the mammalian urinary outflow tract. *Experimental physiology*, 84(1):215, 1999.

[14] J. Brocklehurst, M. Amess, M. Goldacre, A. Mason, E. Wilkinson, A. Eastwood, and J. Coles. Health outcome indicators: Urinary incontinence. report of a working group to the department of health, 1999.

[15] R. V. Brotherton-Ratcliffe and F. T. Smith. Complete breakdown of an unsteady interactive boundary-layer (over a surface distortion or in a liquid layer). *Mathematika*, 34(67, Part 1):86–100, Jun 1987.

[16] N. Bullock, R. H. R. H. Whitaker, and G. Sibley. *Essential urology*. Churchill Livingstone, Edinburgh ; New York :, 2nd ed. edition, 1994.

[17] R. Burton-Opitz and R. Dinegar. The viscosity of urine. *American Journal of Physiology–Legacy Content*, 47(2):220, 1918.

[18] A. Bykova and S. Regirer. Mathematical models in urinary system mechanics (review). *Fluid Dynamics*, 40(1):1–19, 2005.

[19] S. Canic, Suncica Canic. Mathematical analysis of the quasilinear effects in a hyperbolic model blood flow through compliant axi-symmetric vessels. *Mathematical Methods in the Applied Sciences*, 26:1161–1186, 2003. 10.1002/mma.407.

[20] T. Chan, C. Narasimhan, and Q. Zhang. Decomposing promotional effects with a dynamic structural model of flexible consumption. *Journal of Marketing Research*, 45(4):487–498, 2008.

[21] M. DeKimpe, D. Hanssens, and J. Silva-Risso. Long-run effects of price promotions in scanner markets. *Journal of Econometrics*, 89:269–291, 1999.

[22] G. DeSoete, J. D. Carroll, and W. S. DeSarbo. The wandering ideal point model: A probabilistic multidimensional unfolding model for paired comparisions data. *Journal of Mathematical Psychology*, 30:28–41, 1986.

[23] F. Dias and J. Vanden-Broeck. Open channel flows with submerged obstructions. *Journal of Fluid Mechanics*, 206(1):155–170, 1989.

[24] F. Dias and J. Vanden-Broeck. Flows emerging from a nozzle and falling under gravity. *Journal of Fluid Mechanics*, 213:465–477, 1990.

[25] J. Epstein and R. Axtell. *Growing Artificial Societies – Social Science from the Bottom UP*. MIT Press, Cambridge, MA, 1996.

[26] J. M. Epstein. Why model? *Journal of Artificial Societies and Social Simulation*, 11(412), 2008.

[27] G. Fagiolo, M. A., and P. Windrum. Empirical validation of agent-based models: A critical survey. In *International Workshop on Agent-Based*

Modeling and Economic Policy Design, University of Bielefeld, Germany, 2005.

[28] G. Fagiolo, G. Dosi, and R. Gabriele. Matching, bargaining and wage setting in an evolutionary model of labor market and output dynamics. *Advances in Complex Systems*, 14:237–273, 2004.

[29] L. Forbes. On the wave resistance of a submerged semi-elliptical body. *Journal of Engineering Mathematics*, 15(4):287–298, 1981.

[30] P. H. Franses and R. Paap. *Quantitative Models in Marketing Research*. Cambridge University Press, 2001.

[31] R. Garcia, P. Rummel, and J. Hauser. Validating agent-based marketing models through conjoint analysis. *Journal of Business Research*, 60:848–857, 2007.

[32] J. Geer and J. Keller. Slender streams. *Journal of Fluid Mechanics*, 93(01):97–115, 1979.

[33] N. Gilbert, W. Jager, G. Deffuant, and I. Adjali. Complexities in markets: Introduction to the special issue. *Journal of Business Research*, 60(8):813–815, 2007.

[34] N. Gilbert and K. G. Troitzsch. *Simulation for the Social Scientist*. Open University Press, Maidenhead, UK, second edition, 2005.

[35] D. M. Gleason and M. R. Bottaccini. The effect of a fine urethral pressure-measuring catheter on urinary flow in females. *Neurourology and Urodynamics*, 3(3):163–171, 1984.

[36] P. H. Graversen, P. Bagi, H. P. Tofft, H. Colstrup, and J. K. Kristensen. Pressure-to-cross-sectional area relationships in the proximal urethra of

men with bladder outlet obstruction. *The Journal of Urology*, 155(1):267 – 270, 1996.

[37] D. Griffiths. Urethral elasticity and micturition hydrodynamics in females. *Medical and Biological Engineering and Computing*, 7(2):201–215, 1969.

[38] D. Griffiths. Hydrodynamics of male micturitionii measurements of stream parameters and urethral elasticity. *Medical and Biological Engineering and Computing*, 9(6):589–596, 1971.

[39] D. Griffiths and H. Rollema. Urine flow curves of healthy males: a mathematical model of bladder and urethal function during micturition. *Medical and Biological Engineering and Computing*, 17(3):291–300, 1979.

[40] D. J. Griffiths. *Urodynamics : the mechanics and hydrodynamics of the lower urinary tract*. Medical physics handbooks ; 4. Bristol : Hilger in collaboration with the Hospital Physicists Association, c1980.

[41] J. Grotberg and O. Jensen. Biofluid mechanics in flexible tubes. *Annual review of fluid mechanics*, 36(1):121, 2004.

[42] H. Heerde, S. Gupta, and D. Wittink. Is 75 percent of the sales promotion bump due to brand switchig? No, only 33 percent is. *Journal of Marketing Research*, 40(4):481–491, 2003.

[43] E. J. Hinch. *Perturbation methods*. Cambridge University Press, 1991.

[44] H. E. Huppert. The propagation of two-dimensional and axisymmetric viscous gravity currents over a rigid horizontal surface. *Journal of fluid mechanics*, 121(AUG):43–58, 1982.

[45] Y. Iemoto, Y. Miyake, and C. Yamaji. On a round jet of inviscid liquid. *Archive of Applied Mechanics*, 46(4):223–233, 1977.

[46] W. Jager. The four p's in social simulation, a perspective on how marketing could benefit from the use of social simulation. *Journal of Business Research*, 60:868–875, 2007.

[47] O. Jensen. Flows through deformable airways. *Dynamical systems in physiology and medicine course notes, Urbino, Italy*, 2002.

[48] H. Lamb. *Hydrodynamics, 1945*, chapter 9. Dover Publications, New York.

[49] K. J. Lancaster. A new approach to consumer theory. *Journal of Political Economy*, 74:132–157, 1966.

[50] S. W. Lee and J. H. Kim. The significance of natural bladder filling by the production of urine during cystometry. *Neurourology and Urodynamics*, 27(8):772–774, 2008.

[51] R. LeVeque. *Numerical methods for conservation laws*. Birkh "auser, 1992.

[52] S. Lin and R. Reitz. Drop and spray formation from a liquid jet. *Annual Review of Fluid Mechanics*, 30(1):85–105, 1998.

[53] G. Lose. Mechanical properties of the urethra in healthy female volunteers: Static measurements in the resting urethra. *Neurourology and Urodynamics*, 8(5):451–459, 1989.

[54] F. Malerba, R. Nelson, L. Orsenigo, and S. Winter. History-friendly models of industry evolution: the computer industry. *Industrial Corporate Change*, 8(1):3–40, 1999.

[55] C. F. Mela, S. Gupta, and D. R. Lehmann. The long-term impact of promotion and advertising on consumer brand choice. *Journal of Marketing Research*, 34(2):248–261, 1997.

[56] V. Misra. Consumer behaviour modelling using transitional probabilities. Master's thesis, UCL, 2009.

[57] A. R. Mundy, T. P. Stephenson, and A. J. Wein. *Urodynamics : principles, practice and application*. Practice of surgery. Churchill Livingstone, Edinburgh :, 2nd ed. edition, 1994.

[58] G. Oates. Fluid flow in soft-walled tubes part 1: Steady flow. *Medical and Biological Engineering and Computing*, 13(6):773–779, 1975.

[59] G. Oates. Fluid flow in soft-walled tubes part 2: Behaviour of finite waves. *Medical and Biological Engineering and Computing*, 13(6):780–784, 1975.

[60] K. Pauwels, D. M. Hanssens, and S. Siddarth. The long-term effects of price promotions on category incidence, brand choice, and purchase quantity. *Journal of Marketing Research*, 39(November):421–439, 2002.

[61] T. J. Pedley. *The fluid mechanics of large blood vessels*. Cambridge monographs on mechanics and applied mathematics. Cambridge University Press, Cambridge :, 1980.

[62] T. J. Pedley and X. Y. Luo. Modelling flow and oscillations in collapsible tubes. *Theoretical and Computational Fluid Dynamics*, 10:277–294, 1998. 10.1007/s001620050064.

[63] T. Petrila and D. Trif. *Basics of fluid mechanics and introduction to computational fluid dynamics*, volume 3. Springer Verlag, 2005.

[64] B. Pullan, J. Phillips, and D. Hickey. Urethral lumen cross-sectional shape: Its radiological determination and relationship to function. *British Journal of Urology*, 54(4):399–407, 1982.

[65] J. Reynard, C. Lim, S. Swami, and P. Abrams. The obstructive effect of a urethral catheter. *The Journal of Urology*, 155(3):901 – 903, 1996.

[66] J. Richetin, A. Sengupta, M. Perugini, I. Adjali, R. Hurling, D. Greetham, and M. Spence. A micro-level simulation for the prediction of intention and behavior. *Cognitive Systems Research*, 11(2):181–193, 2010.

[67] W. S. Saric. Gortler vortices. *Annual Review of Fluid Mechanics*, 26:379–409, 1994.

[68] A. Sengupta and S. E. Glavin. Volatility in the consumer packaged goods industry - a simulation based study. *Advances in Complex Systems (ACS)*, 13(04):579–605, 2010.

[69] A. Sengupta, D. Greetham, and M. Spence. An evolutionary model of brand competition. In *Proceedings of IEEE SSCI 2007: Symposium on Artificial Life*, pages 100–107, 2007.

[70] S. Shen. On the accuracy of the stationary forced korteweg-de vries equation as a model equation for flows over a bump. *Quarterly of applied mathematics*, 53:701–720, 1996.

[71] S. J. Sherwin, V. Franke, J. Peir, and K. Parker. One-dimensional modelling of a vascular network in space-time variables. *Journal of Engineering Mathematics*, 47:217–250, 2003.

[72] R. Shoucri and M. Shoucri. Application of the method of characteristics for the study of shock waves in models of blood flow in the aorta. *Cardiovascular Engineering*, 7(1):1–6, 2007.

[73] R. Skalak, N. Ozkaya, and T. Skalak. Biofluid mechanics. *Annual review of fluid mechanics*, 21(1):167–200, 1989.

[74] F. T. Smith. On entry-flow effects in bifurcating, blocked or constricted tubes. *Journal of Fluid Mechanics*, 78:709–736, 1976.

[75] F. T. Smith. Finite-time break-up can occur in any unsteady interacting boundary layer. *Mathematika*, 35:256–273, 1988.

[76] F. T. Smith. Steady and unsteady 3-d interactive boundary layers. *Computers & Fluids*, 20(3):243 – 268, 1991.

[77] F. T. Smith, R. Purvis, S. C. R. Dennis, M. A. Jones, N. C. Ovenden, and M. Tadjfar. Fluid flow through various branching tubes. *Journal of Engineering Mathematics*, 47:277–298, 2003.

[78] A. Spangberg, H. Terio, A. Engberg, and P. Ask. Quantification of urethral function based on griffiths' model of flow through elastic tubes. *Neurourology and Urodynamics*, 8(1):29–52, 1989.

[79] K. Srinivas, J. Gururaja, and K. K. Prasad. On the first order local stability scheme for the numerical solution of time-dependent compressible flows. *Computers & Fluids*, 5(2):87 – 97, 1977.

[80] B. Sun. Promotion effect on endogenous consumption. *Marketing Science*, 24(3):430–443, 2005.

[81] B. Sun, S. Neslin, and K. Srinivasan. Measuring the impact of promotions on brand switching when consumers are forward looking. *Journal of Marketing Research*, 40(4):389–405, 2003.

[82] M. Tadjfar and F. T. Smith. Direct simulations and modelling of basic three-dimensional bifurcating tube flows. *Journal of Fluid Mechanics*, 519:1–32, 2004.

[83] L. Tesfatsion. Agent based computational economics: A constructive approach to economic theory. In L. Tesfatsion and K. L. Judd, editors, *Handbook of Computational Economics, Volume 2: Agent-Based Computational Economics*. North-Holland, Amsterdam, 2006.

[84] F. Toison and J. Hureau. Potential flow issuing from a two-dimensional curved nozzle. *Physics of Fluids*, 13:793, 2001.

[85] M. Tziannaros. *Modelling bladder collapse flow*. PhD thesis, UCL, 2010.

[86] J. M. Vanden-Broeck. *Gravity-Capillary Free-Surface Flows*. Cambridge University Press, University College London, 2010.

[87] P. C. Walsh. *Campbell's urology*. Saunders, Philadelphia ; London :, 8th ed. edition, 2002.

[88] C. Werker and T. Brenner. Empirical calibration of simulation tools. In *Papers on Economics and Evolution*, volume 0410. 2004.

[89] P. Windrum, G. Fagiolo, and A. Monneta. Empirical validation of agent-based models: Alternatives and prospects. *Journal of Artificial Societies and Social Simulation*, 10(2):8, 2007.

[90] G. Witham. *Linear and nonlinear waves*. Wiley, New York, 1974.